

Antibacterial Surfaces for Medical Implant Applications

Thesis submitted in accordance with the requirements of

The University of Liverpool

for the degree of

Doctor of Philosophy

By George Fleming

December, 2018



UNIVERSITY OF
LIVERPOOL

Abstract

Implantable medical devices are prone to bacterial and biofilm infection, which can lead to serious complications and fatalities in patients. Bacterial resistance to current antibiotics and increasing emergence of healthcare associated infections drives the urgency to develop new antibacterials that do not induce bacterial resistance.

In this study the surface chemistry and/or topography of medically relevant polymers, poly(ethylene terephthalate) (PET), silicone elastomer (SE), polystyrene (PS), polycaprolactone (PCL), poly(methyl methacrylate) (PMMA) and polydimethylsiloxane (PDMS) were modified, in an attempt to fabricate synthetic polymers with antibacterial surfaces for use in medical implant applications. Surfaces have been modified chemically to release nitric oxide (NO), a potent antibacterial agent. Physical modifications have led to the fabrication of surfaces with micro-/nanotopographical features that can inhibit bacterial adhesion.

In Chapter 4, PET and SE were first aminosilanised to functionalise the surface with amines which facilitate the *in situ* formation of *N*-diazoniumdiolates; a class of NO donor that decompose under physiological conditions to release NO. The modified polymers released low levels of NO, which prevented biofilm formation after 24 hrs.

In Chapter 5, SE substrates were coated with xerogels. Unlike in Chapter 4, *N*-diazoniumdiolates were preformed before incorporation into the xerogel to increase NO storage and release. The *N*-diazoniumdiolated xerogel coatings released high levels of NO, which resulted in the killing of planktonic (free-moving) bacteria after 1, 4 and 24 hrs.

In Chapter 6, PS/PCL, PS/PMMA and PCL/PMMA binary blends were spin coated to form polymer demixed films. By varying the relative concentrations of the polymers in the binary blends, demixed films with island-, ribbon- and pit-like micro-/nanotopographical surface structures were fabricated. When surface structures were smaller than the diameter of the bacterial cell, a reduction in cell adhesion was observed; when the surface structures were comparable in size to the diameter of the bacterial cell no reduction in cell adhesion was observed.

In Chapter 7, *N*-diazoniumdiolate groups were tethered *in situ* to PDMS replicas with structured microtopographies resulting in novel materials with both distinct surface microfeatures and NO releasing capabilities. Bacterial cell adhesion was reduced on non-releasing structured PDMS compared to non-releasing flat PDMS after 24 hrs, but both surfaces were ineffective in killing bacteria. After 24 hrs, novel dual-action NO-releasing structured PDMS surfaces were both bactericidal and reduced cell adhesion.

Acknowledgements

I would firstly like to thank Dr Raechelle D'Sa for her complete devotion, support and guidance, and also providing me with kicks up the backside at all the right times to remind me that this would be no walk in the park, exactly when I needed reminding. Dr Jenny Aveyard has been my mentor throughout this experience. Her commitment and passion in and out of the lab has been paramount to my development as a scientist, and her attention to detail has ensured my figures and schemes no longer look like they were drawn by a developing toddler. Thanks to Dr Jo Fothergill and her group who gave me armbands to survive in the previously unexplored swimming pool of microbiology, and to Professor Rasmita Raval and Dr Fiona McBride in surface science who enabled me to scratch more than just the surface. I would also like to thank EPSRC for funding this work.

To everyone in the D'Sa lab group and all my friends and colleagues that I have shared a lab or workspace with, I want to thank you for providing me with just the right level of distraction to keep my sanity intact without hindering my progress and productivity; a miracle I've got to this point really, considering how much you all enjoy a natter.

I have to dedicate this work to my sister; for persisting to smile through the most turbulent times in the face of adversity; for never failing to astonish and bewilder me; for putting up with 23 years of relentless, brotherly torment and bullying. Thanks Em.

Mum and Carl, you have pretended to be interested in my work at all the right times, even when I have talked over Strictly or Bake Off. But on a serious note, thank you for looking after me. You have allowed me to prolong my time as a student without the lack of food and clean clothes it is so often associated with. I could go on forever, but I know you'd cringe more than me, Mum.

My Nan and Granddad have always given me the confidence to believe I can achieve anything, especially if it means they can tell anyone they see that their grandson is a doctor. This one's for you Nan.

Liv and Ash, you have put up with me for almost two years through this. I don't know whether to congratulate or thank you. I suppose I'll do both. You've been great, cheers.

Ste and James, as I've grown inevitably more unpopular and friendless with age, you two still won't leave me alone. Cheers for everything, lads.

And here's one last line to thank myself... Surely there's nothing wrong with that, is there?

Abstract	i
Acknowledgements	ii
Nomenclature	vii
Chapter 1: Introduction	1
1.1 Aims and Objectives	3
1.2 Publications	4
Chapter 2: Literature Review	5
2.1 Implantable Medical Devices	5
2.1.1 Polymeric Implants.....	6
2.2 Implant-associated Biofilm Infections	7
2.2.1 Biofilm Formation	8
2.2.2 Mechanisms of Antibiotic Resistance in Biofilms	9
2.3 Strategies for Antibacterial Surface Design	11
2.4 Nitric Oxide	12
2.4.1 Endogenous NO Formation.....	13
2.4.2 Antibacterial Behaviour of NO	14
2.5 Nitric Oxide Donors	15
2.5.1 Organic Nitrates	15
2.5.2 Organic Nitrites	16
2.5.3 Metal-nitrosyl Complexes	16
2.5.4 Nitrosothiols (RSNOs).....	17
2.5.5 <i>N</i> -Diazeniumdiolates	18
2.5.6 Comparison of NO Donors as Antibacterial Agents.....	19
2.6 <i>N</i>-diazeniumdiolated NO Storage and Delivery vehicles	21
2.6.1 Polymer-based Strategies	22
2.6.1.1 Physically Dispersed LMW NO Donors.....	22
2.6.1.2 Covalently Bound LMW NO Donors.....	23
2.6.2 Xerogel Coatings	24
2.7 Topographical Control of Bacterial Response	27
2.7.1 Natural Antibacterial Topographies.....	27
2.7.2 Synthetic Materials with Micro-/Nanopatterned Topographies.....	29
2.7.2.1 Patterning at the Micro-/Nanometre Scale	29
2.7.2.2 Antibacterial Behaviour of Micro-/Nanopatterned Materials.....	31
2.7.2.3 Commercial Applications: Sharklet AF™	33
2.8 Summary	34
Chapter 3 - Materials and Methods	36
3.1 Introduction	36

3.2 Polymer Substrates	36
3.3 Silanes.....	37
3.4 Synthesis.....	39
3.4.1 Preparation of Substrates for Analysis.....	39
3.4.2 Plasma treatment of Substrates	39
3.5 Analytical Techniques.....	39
3.5.1 Contact Angle Analysis	39
3.5.2 Fourier-transform Infrared Spectroscopy.....	40
3.5.3 X-ray Photoelectron Spectroscopy	41
3.5.4 Atomic Force Microscopy	43
3.5.5 Nitric Oxide Detection by Chemiluminescence	45
3.5.6 Scanning Electron Microscopy	46
3.6 Biological Assessment	46
3.6.1 Preparation of Bacterial Solutions	46
3.6.2 Planktonic Cell CFU Assay	46
3.6.3 Adhered Cell CFU Assay	47
3.6.4 Fixation of Bacteria	47
3.7 Statistical Analysis.....	47
Chapter 4: Covalently bound <i>N</i>-diazoniumdiolates to Polymer Surfaces for	
Prevention of Biofilm Formation	48
4.1 Introduction	48
4.2 Experimental.....	50
4.2.1 Aminosilanisation	50
4.2.2 <i>N</i> -diazoniumdiolate tethering.....	50
4.3 Results	51
4.3.1 Ageing Test: Contact Angle	51
4.3.2 Wettability: Contact Angle.....	53
4.3.3 Surface Chemistry: XPS	54
4.3.4 Surface Topography: AFM.....	66
4.3.5 NO Release: Chemiluminescent Detection	70
4.3.6 Bacterial Response	74
4.4 Discussion	76
4.4.1 Oxygen Plasma Treatment of Polymeric Surfaces	76
4.4.2 <i>N</i> -Diazoniumdiolate Formation and NO Release	78
4.4.3 Bacterial Response	80
4.5 Conclusion	81
Chapter 5: Nitric Oxide-releasing Xerogels as Antibacterial Coatings	82
5.1 Introduction	82
5.2 Experimental.....	84
5.2.1 Preparation of Preformed <i>N</i> -Diazoniumdiolate Solutions.....	84

5.2.2 Preparation of <i>N</i> -diazoniumdiolated Xerogel Coatings	85
5.2.3 Optimisation of Sol-gel Process	86
5.3 Results: Preformed <i>N</i>-diazoniumdiolate Solutions.....	89
5.3.1 UV-Vis Spectroscopy	89
5.3.2 NO Release: Chemiluminescence Detection.....	90
5.4 Results: <i>N</i>-diazoniumdiolated Xerogel Coatings	93
5.4.1 Wettability: Contact Angle	93
5.4.2 Surface Chemistry: XPS	94
5.4.3 Surface Topography: AFM.....	100
5.4.4 NO release: Chemiluminescence Detection	102
5.4.4.1 Effect of pH.....	102
5.4.4.2 Effect of Temperature.....	105
5.4.4.3 Effect of Bases	107
5.4.5 Bacterial Response	109
5.4.5.1 Adhered Cell CFU Assay (LB Media).....	109
5.4.5.2 Planktonic and Adhered Cell CFU Assays (Phosphate Buffered Saline)	
.....	110
5.4.5.3 Effect of Base on Bactericidal Activity	112
5.5 Discussion	116
5.5.1 Preformed <i>N</i> -Diazoniumdiolate Solutions	116
5.5.2 <i>N</i> -diazoniumdiolated Xerogel Coatings.....	117
5.5.2.1 Formation.....	117
5.5.2.3 NO Release	118
5.5.3 Bacterial Response	119
5.5.3.1 Adhered Cell CFU Assay (LB Media).....	119
5.5.3.2 Planktonic and Adhered Cell CFU Assays (Phosphate Buffered Saline)	
.....	120
5.5.3.3 Effect of Base on Bactericidal Activity.	120
5.6 Conclusion	121
Chapter 6: Polymer Demixed Films with Micro-/Nanotopographies to Control	
Bacterial Response	123
6.1 Introduction	123
6.2 Experimental.....	124
6.2.1 Preparation of Polymer Demixed Thin Films	124
6.3 Results: Characterisation	125
6.3.1 Wettability: Contact Angle	125
6.3.2 Surface Chemistry: FTIR	126
6.3.3 Surface Chemistry: XPS	130
6.3.4 Surface Topography: AFM.....	137
6.4 Results: Stability in LB Media	143
6.4.1 Wettability: Contact Angle	143
6.4.2 Surface Chemistry: FTIR	144

6.4.3 Topography: AFM.....	146
6.5 Results: Bacterial Response	153
6.5.1 PS/PCL	153
6.5.2 PS/PMMA	154
6.5.3 PCL/PMMA	155
6.6 Discussion	156
6.6.1 Polymer Demixing Process.....	156
6.6.1.1 Immiscibility of Polymers	156
6.6.1.2 Vertical Phase Separation	157
6.6.1.3 Lateral Phase Separation	161
6.6.2 Bacterial Response	165
6.7 Conclusion	168
Chapter 7: Conclusions and Recommendations for Future Studies	169
7.1 Conclusions	169
7.2 Recommendations for Future Studies	171
References.....	173

Nomenclature

AFM	Atomic force microscopy
at. %	Atomic % concentration
BE	Binding energy
BTMOS	Isobutyltrimethoxysilane
CFU	Colony forming unit
d	Day
DET3	N-(3-trimethoxysilylpropyl)diethylenetriamine
ECM	Extracellular matrix
eV	Electron volt
f-PDMS	Flat polydimethylsiloxane
f-PDMSox	Plasma treated flat polydimethylsiloxane
FTIR	Fourier-transform infrared spectroscopy
hr	Hour
IR	Infrared
K _a	Acid dissociation constant
KE	Kinetic energy
LB	Luria-Bertani
LMW	Low molecular weight
min	Minute
MW	Molecular weight
NO	Nitric oxide
PBS	Phosphate buffered saline
PCL	Polycaprolactone
PDMS	Polydimethylsiloxane
PET	Polyethylene terephthalate
PETox	Plasma treated polyethylene terephthalate
PMMA	Poly(methyl methacrylate)
PS	Polystyrene
PTMOS	Trimethoxypropylsilane

PTMSPA	N-(3-trimethoxysilylpropyl)aniline
Ra	Average roughness
RNI	Reactive nitrogen intermediate
ROI	Reactive oxygen intermediate
Rq	Root mean square roughness
RSNO	Nitrosothiol
SE	Silicone elastomer
SEM	Scanning electron microscopy
SEox	Plasma treated silicone elastomer
s-PDMS	Structured polydimethylsiloxane
s-PDMSox	Plasma treated structured polydimethylsiloxane
UV-Vis	Ultraviolet visible spectroscopy
XPS	X-ray photoelectron spectroscopy

Chapter 1: Introduction

Since the revolutionary discovery of penicillin and its antibacterial properties by Alexander Fleming in 1928, antibiotics have been used with great success against bacterial infection.¹ A golden era for the discovery of antibiotics between 1940 and 1980 led to many classes reaching the commercial market.² However, in more recent times the discovery and development of antibiotics has come to a standstill; the last class of antibiotics to be discovered was the diarylquinolines, in 1997. Whilst antibiotics have been undoubtedly paramount to improved longevity and quality of life over the past century, the overuse and misuse of these drugs has led to the emergence of antibiotic resistance by bacteria (Figure 1.1).³ This has become a global concern as multi-drug resistant strains have evolved to render certain antibiotics completely obsolete.

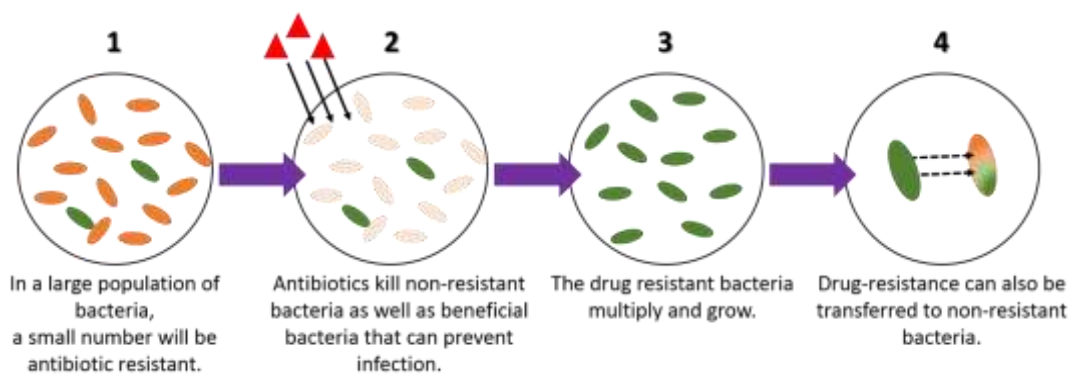


Figure 1.1: General scheme for antibiotic resistance of bacteria. [Adapted from Ref. 3]

When antibiotics are administered, they are intended to kill large amounts of bacteria at the site of infection. However, some bacterial cells may resist the killing and survive the treatment. Antibiotics can also kill beneficial bacteria that contribute to protection from infection. The resistant bacteria now have an environment in which they can grow and multiply without competition.

Along with antibiotic resistance, there is an increasing prevalence of health-care associated infections (HAIs) with levels rising by 6.4 % and over 1 000 000 cases

reported each year in England.⁴ These infections lead to increased morbidity and mortality rates in patients and result in large financial burdens on healthcare services.

As medicine and technology develops so does life expectancy and the prevalence of age-related diseases. Due to this, implantable medical devices, such as: pacemakers, catheters and orthopaedic prostheses have become paramount in modern healthcare and are necessary for prolonging and improving the life of critically ill patients. The increased use of such devices is not without significant problems; one being their susceptibility to bacterial adhesion and subsequent biofilm formation.⁵

A biofilm is a species-specific or multi-species community of bacteria embedded within an extracellular matrix of polymers and polysaccharides (ECM). This protective matrix, amongst a whole host of other resistance mechanisms can significantly reduce the efficacy of antibiotics. Species such as *Pseudomonas aeruginosa*, *Staphylococcus aureus* and *Staphylococcus epidermis* have shown strong forces of adhesion to foreign bodies which is the first step in the formation of a biofilm. It is estimated that over 80 % of microbial infections within the human body are the result of biofilm formation.⁶

Of particular concern is *P. aeruginosa*, a Gram-negative species of bacteria commonly found in soil, water and plants. It is an opportunistic pathogen that can cause both acute and chronic infection in humans, plants and animals. The ubiquitous presence of *P. aeruginosa* at infection sites, its tendency to form biofilms and the increasing occurrence of multi-drug resistant strains have led to the World Health Organisation (WHO) classifying it as one of the top three pathogens in critical need of new antibiotic treatments.⁷

As we enter what is termed the 'resistance era' by many in the field, the urgency for developing new alternatives to antibiotics with improved antibacterial performance and less susceptibility to antibiotic resistance and biofilm formation is an ever growing necessity. In this body of work, the specific focus is in designing and engineering synthetic polymers with antibacterial surfaces for their potential use in medical implant applications.

1.1 Aims and Objectives

When designing antibacterial surfaces there are three mechanisms to take into consideration: biocide leaching, contact killing and adhesion resistance.⁸ The strategies employed here will focus on developing surfaces that can resist adhesion and leach biocides, using both physical and chemical surface modifications. The approach taken to modify surfaces chemically will involve tethering molecules onto the surface that can release nitric oxide (NO), a potent antibacterial agent; whilst the approach taken to modify materials physically, will involve using techniques that allow the formation of micro-/nanotopographical surface features.

The key objectives of the study are as follows:

1. Review the key principles of antibacterial surface design and apply them to modify medically relevant synthetic polymers.
2. Adopt a chemical approach to fabricate synthetic polymers that release NO.
3. Adopt a physical approach to fabricate synthetic polymers with micro-/nanotopographical surface features.
4. Combine the two approaches to develop materials with micro-/nanotopographical surface features that release NO.
5. Quantify NO release and payload from NO-releasing surfaces and explore synthetic and parametric changes that can impact them.
6. Assess the antibacterial performance of the synthetic polymer materials in terms of anti-adhesion (biofilm prevention) and bactericidal ability.
7. Determine how NO release concentration effects the antibacterial mechanism of the surface.
8. Investigate bacterial cell-surface interactions and determine how micro-/nanotopographical surface features control cell adhesion.

The structure of this thesis follows the progression of the development of synthetic polymers with antibacterial surfaces, utilising a diverse range of fabrication techniques, with the aim of delivering all the objectives outlined above. As such the subsequent chapters are ordered as follows:

- **Chapter 2:** Literature Review
- **Chapter 3:** Materials and Methods
- **Chapter 4:** Covalently bound *N*-diazoniumdiolates to Polymeric Substrates for the Prevention of Biofilm Formation
- **Chapter 5:** Nitric Oxide-releasing Xerogels as Antibacterial Coatings
- **Chapter 6:** Polymer Demixed Films with Micro-/nanopatterned Surface Topographies to Control Bacterial Response
- **Chapter 7:** Conclusions and Recommendations for Future Studies

1.2 Publications

Some of the results of the research presented in Chapter 4 have been published in the following peer-reviewed paper:

- G. Fleming, J. Aveyard, J. L. Fothergill, F. McBride, R. Raval and R. A. D'Sa, *Polymers*, 2017, **9**, 601.

A copy of this paper has been enclosed at the end of this thesis.

Chapter 2: Literature Review

2.1 Implantable Medical Devices

Medical devices can be defined as *implantable* if they are incorporated into the human body to act as part or whole of a biological structure.^{9,10} As the population grows and the average life span increases so does the occurrence of age-related disease and the need to develop new technologies with prolonged life spans. From bone cements and hormonal implants, to motion preservation devices and intraocular lenses; applications of implantable medical devices stretch across the whole human body.¹⁰ Some of the more common examples of their uses are presented in Figure 2.1.

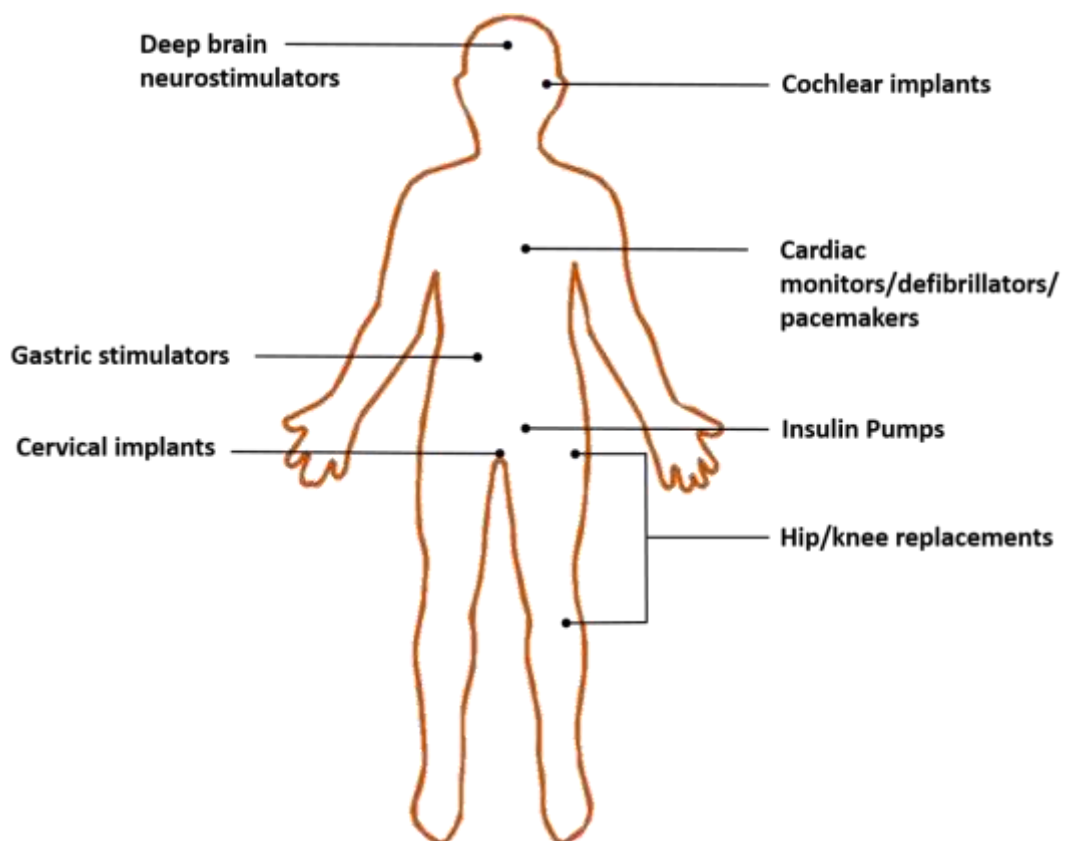


Figure 2.1: Applications of implantable medical devices within the human body.

Materials used for implantable medical devices can generally be divided into three categories: metals, ceramics and polymers. Metallic implantable devices are extensively used as total joint replacements for hips, knees, elbows, shoulders etc; they also find use as fracture plates and dentistry castings.¹¹ Whilst metals are most commonly used for load-bearing implants, ceramics do not have a sufficient fracture

toughness for such applications. Due to their similar properties to bone, the most common use of ceramics is to replace/fix hard connective tissue. Ceramics are often used in restorative dentistry, such as crowns and dentures.¹² The use of polymeric implants will be discussed in Section 2.1.1.

2.1.1 Polymeric Implants

The versatility of polymers has led to their favourability over materials like metals and ceramics for use as biomaterials. Polymers are generally classified into two groups: naturally occurring and synthetic polymers. Natural polymers, such as: collagen, dextran, gelatin and chitosan are innately biocompatible but can suffer disadvantages due to the possibility of microbial contamination.¹³ Batch-to-batch variation can also occur due to the variation of naturally derived sources (organisms).

Synthetic polymers are more commonly employed as implants due to their ease and reproducibility in production, their availability and their versatility. The applications of some common synthetic polymers have been outlined in Table 2.1.

Table 2.1: Summary of the applications of some synthetic polymers as implantable devices.

Polymer	Applications	References
Polyurethanes	Catheters, drug delivery systems, prosthesis, vascular grafts.	14-16
Poly(vinyl chloride)	Blood bags, tubing.	10
Poly(methyl methacrylate)	Dental implants, bone cements, intraocular lenses.	17-19
Polycaprolactone	Orthopaedic coatings, sutures, drug delivery systems.	20-22
Poly(ethylene terephthalate)	Surgical mesh, sutures, vascular grafts/prosthesis.	21, 23, 24
Polydimethylsiloxane/ Silicone elastomers	Shunts, plastic surgery implants, pacemakers, catheters, orthopaedics.	25-27

2.2 Implant-associated Biofilm Infections

Both Gram-positive and Gram-negative bacteria have been shown to inhabit and infect an implant site through biofilm formation.²⁸ The most common causative Gram-positive species include *Staphylococcus epidermis* and *Staphylococcus aureus*; whilst multi-drug resistant *Pseudomonas aeruginosa* and *Escherichia coli* are amongst the Gram-negative strains that have also been implicated.²⁸ Some of the more common implants sites prone to biofilm infection and the causative bacterial species are outlined in Table 2.2.

Table 2.2: Common bacteria involved in biofilm formation at implant sites.

Medical Implant	Biofilm-forming Bacteria	Reference
Central venous catheters	<i>P. aeruginosa</i> , <i>S. epidermis</i> , <i>S. aureus</i> , <i>Klebsiella pneumoniae</i> , <i>Enterococcus faecalis</i> .	29, 30
Urinary catheters	<i>P. aeruginosa</i> , <i>S. epidermis</i> , <i>K. pneumoniae</i> , <i>E. faecalis</i> , <i>P. mirabilis</i>	31
Cardiac pace makers	<i>S. aureus</i> , <i>S. epidermis</i> .	32
Endotracheal tubes	<i>P. aeruginosa</i> , <i>S. aureus</i> , <i>E. faecalis</i>	33
Contact lenses	<i>P. aeruginosa</i>	34
Orthopaedic implants	<i>P. aeruginosa</i> , <i>S. epidermis</i> , <i>S. aureus</i> , <i>P. mirabilis</i> , <i>E. coli</i> , <i>Streptococci</i> , <i>Enterococci</i>	35, 36

As seen from the table above biofilm infections are found ubiquitously at medical implant sites. The major issue with biofilm infections is their ability to tolerate antibacterial agents compared to their planktonic (free-moving) counterparts. Anwar *et al.* reported that a dose of tobramycin able to reduce *P. aeruginosa* planktonic cell counts by > 8-log, only reduced biofilm cell counts by 2-log.³⁷ It was estimated that complete eradication of mature biofilms (\approx 7 days old), would require around 5000 times the minimal bactericidal concentration (MBC).^{37, 38} The sections

below outline the life-cycle of a biofilm and the mechanisms that cause them to resist antibacterial agents so effectively.

2.2.1 Biofilm Formation

When a device is implanted into the body there is a risk of bacterial infection. It is believed that contamination occurs with a small cohort of external micro-organisms transferring onto the medical device during implantation.³⁹ These are often transferred from the skin of the patient/clinical staff, surgical equipment or contaminated disinfectants.^{6, 39} The inoculated bacteria irreversibly attach to the surface of the device by secreting an extracellular matrix of polymers and polysaccharides (ECM). The ECM encases the cells to form a bacterial mass known as a biofilm, which continues to grow and mature. After time, detachment occurs in which planktonic bacteria are released which can further recolonise and repeat the process again. This can lead to a spread of infection throughout the body, which had originated at one initial site. The five main stages of biofilm formation are outlined in Figure 2.2.⁴⁰

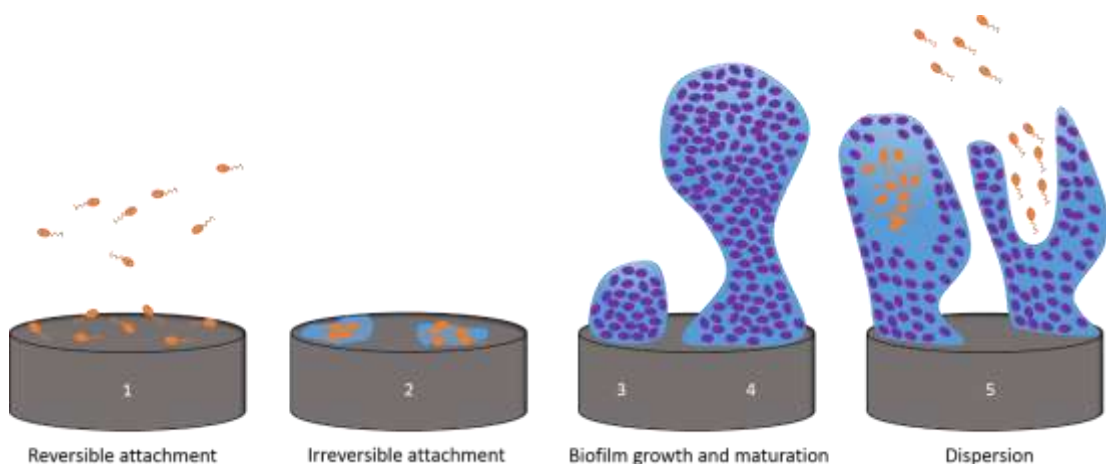


Figure 2.2: The five stages of biofilm formation: (1) Reversible attachment of planktonic bacterial cells. (2) Secretion of ECM results in irreversible attachment. (3) Early development of biofilm architecture. (4) Maturation of biofilm. (5) Motile planktonic cells dispersed from biofilm to repeat process. (Planktonic cells are orange and biofilm-associated cells purple). [Image adapted from Ref. 40]

2.2.2 Mechanisms of Antibiotic Resistance in Biofilms

The behaviour of biofilm-associated cells is very different to that of planktonic cells. Cells within a biofilm community are less susceptible to antimicrobial agents, like antibiotics and antibodies, than planktonic cells. There are a number of proposed mechanisms for the resistance exhibited by biofilms, which have been outlined in Figure 2.3

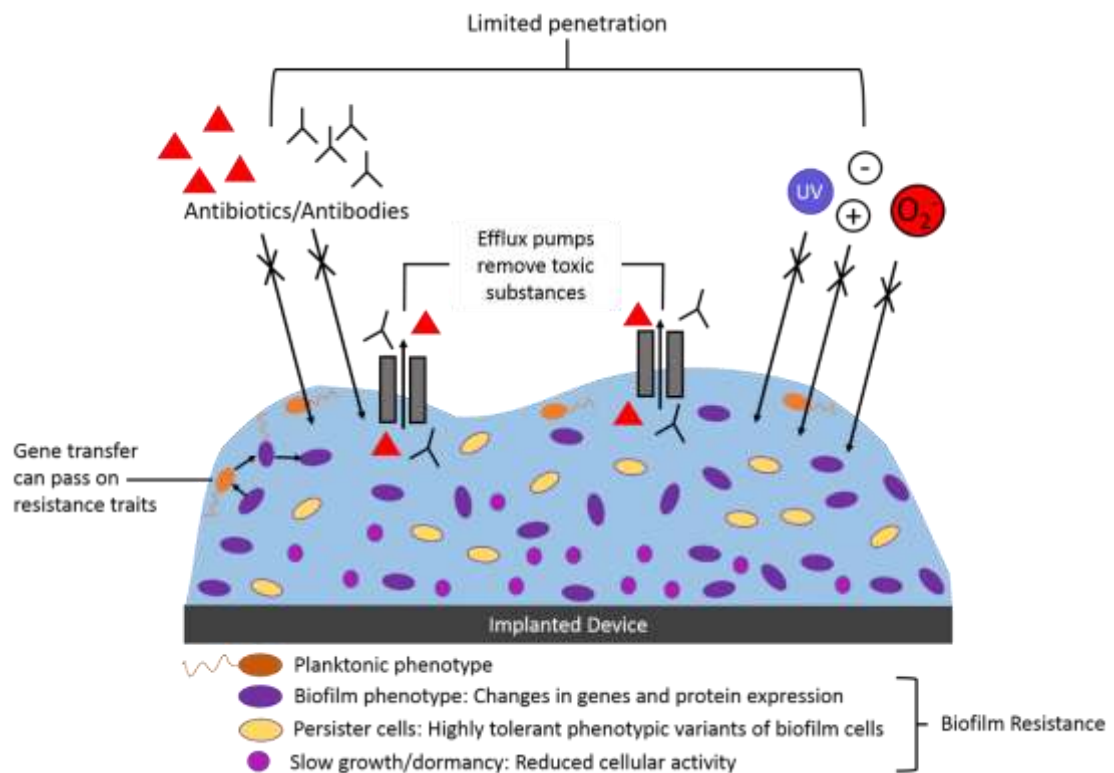


Figure 2.3: An overview of biofilm resistance mechanisms

The first is the ‘barrier’ mechanism which is due to the physical presence of the ECM leading to slow or incomplete penetration of antibiotics and other antimicrobial substances into the biofilm.⁴¹ The ECM may also bind to antimicrobials like superoxides, charged metals or bleach, neutralising or diluting them to sub-lethal concentrations before penetration.⁵ It is thought that other potentially detrimental, external stimuli such as UV light and dehydration may also be unable to affect cells due to the matrix.⁵

There are many antibiotics that are able to penetrate the ECM, yet even when this is the case biofilm cells can remain unaffected. One particular example of ‘non-barrier’ mechanisms of resistance has been demonstrated using *Klebsiella pneumoniae*.⁴²

Stewart *et al.* demonstrated the ability of two antibiotics, ampicillin and ciprofloxacin, to penetrate into *K. pneumoniae* biofilms.^{43,44} It was shown that slow-growing stationary phase bacteria with limited access to nutrients within the biofilm were less susceptible to these antibiotics than planktonic bacteria growing at quicker rates. All antibiotics require some degree of cellular activity. For instance β -lactams effectively kill rapidly dividing Gram-positive bacteria by interrupting cell-wall synthesis. It is hypothesised therefore that dormant cells starved of nutrients in a stationary phase within the biofilm may be less susceptible to antibiotics due to reduced cellular activity.

Another theory to antibiotic resistance in biofilms is the presence of 'persister' cells (not mutants). These are randomly formed phenotypic variants within a microbial population. Lewis *et al.* showed that both *Pseudomonas aeruginosa* biofilm and stationary-phase planktonic cells actually had similar resistance to antibiotics, largely dependent on the presence of persister cells.⁴⁵ Leibler *et al.* later determined that the inherent heterogeneity of bacterial populations led to the phenotypic switching of normally growing cells to dormant persister cells with reduced growth rates and increased resistance to antibiotics.⁴⁶

Other mechanisms include the prevalence of efflux pumps in the biofilm, which regulate the internal cell environment by removing toxic substances, like antibiotics.⁴⁷ These are particularly apparent in Gram-negative species. In addition to this gene transfer between conjugated cells may lead to the acquisition of resistance traits in diverse biofilm populations.⁴⁸

2.3 Strategies for Antibacterial Surface Design

When considering the design of antibacterial surfaces, the complex behaviour of bacterial populations and the broad range of surface properties can be overwhelming. Through years of research the development of three main design strategies has progressed (Figure 2.4).⁸

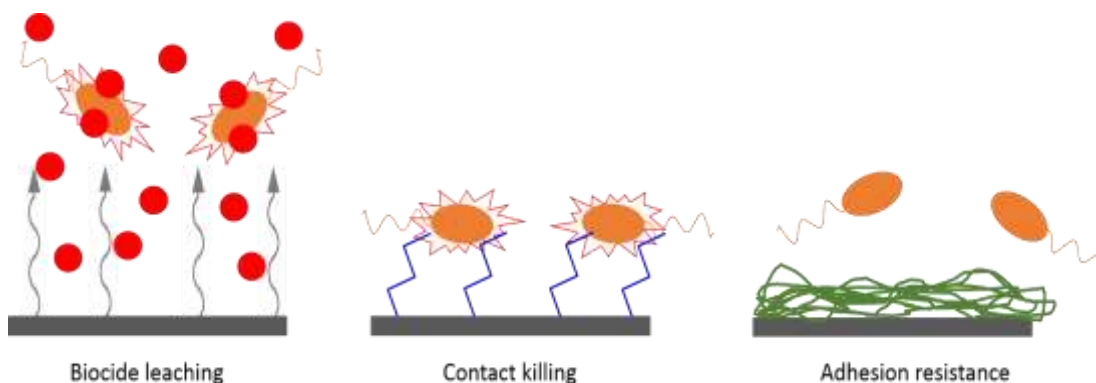


Figure 2.4: Three main strategies for antibacterial surface design: Contact killing, biocide leaching and adhesion resistance.

The first strategy is the use of biocide leaching. This approach involves the release/diffusion of cytotoxic compounds from the surface of a material that can cause cell death to adhered or nearby bacteria. This method of design originates back to ancient times when silver was used in the fabrication of drinking vessels. Biocide leaching can be advantageous due to the controlled release of antibacterials or antibiotics but care should be taken to ensure the leaching compounds do not have adverse effects towards mammalian tissue.

The second approach is to design surfaces that can kill bacteria through contact. This method primarily focusses on designing a surface conjugated with antibiotic functional groups that cause the death of adhered bacterial cells. Examples of these include: positively charged phosphonium salts,⁴⁹ guanidine polymers⁵⁰ and quaternary ammonium salts⁵¹ which are thought to be able penetrate/disrupt the cell membrane and induce cell death. The discovery of bactericidal nanopillars of the cicada wing,⁵² has also led to a non-classical, non-chemical design of nanopatterned surfaces that are inspired by nature with contact killing ability.⁵³

The final design approach involves fabricating surfaces that are resistant to adhesion. The fabrication of superhydrophobic materials has been one way to achieve this by preventing aqueous suspensions of bacteria coming into contact with the surface.⁵⁴ Minimising the area available for cell-surface interactions through topographical modifications is another way to minimise cell adhesion.^{52, 55}

2.4 Nitric Oxide

Nitric oxide (NO) first came to the attention of the biomedical community in the late 1980s when Furchgott,⁵⁶ Ignarro⁵⁷ and Murad⁵⁸ independently determined it to be the endothelium-derived relaxing factor (EDRF); a chemical responsible for vasodilation and regulation of blood pressure. This finding led to the inception of much focussed research into NO and its ubiquitous physiological presence. A summary of the roles NO plays in various physiological systems has been outlined in Table 2.3.

Table 2.3: Summary of the role of nitric oxide in different physiological systems.

Physiological System	Roles of Nitric Oxide	Reference
Immune system	<ul style="list-style-type: none"> • Antimicrobial activity. • Anti-tumour activity. • Anti-inflammatory effect. • Immunoregulation. • Modulates production and function of cytokines and growth hormones. 	59-67
Respiratory system	<ul style="list-style-type: none"> • Modulates airway smooth muscle relaxation (bronchodilation). • Mediates fetal lung development. • Transcriptional regulation in the lung. • Stimulates airway submucosal gland secretion. 	68-76
Cardiovascular system	<ul style="list-style-type: none"> • Regulates vascular tone. • Regulates cardiac contractility. • Anti-thrombotic effect. • Regulates leukocyte adhesion. 	77-84
Central nervous system	<ul style="list-style-type: none"> • Neurotransmission • Regulates cell signalling events • Neuroprotection • Neurosecretion 	85-89
Reproductive System	<ul style="list-style-type: none"> • Regulates penile erection • Regulates ovarian function 	90-93

2.4.1 Endogenous NO Formation

Endogenous NO is primarily biosynthesised through the oxidation of L-arginine to citrulline, catalysed by nitric oxide synthase (NOS) proteins.⁹⁴ The NOS enzymes facilitate a complex two-step reaction, as displayed in Figure 2.5, which utilises NADPH and molecular oxygen as co-factors.

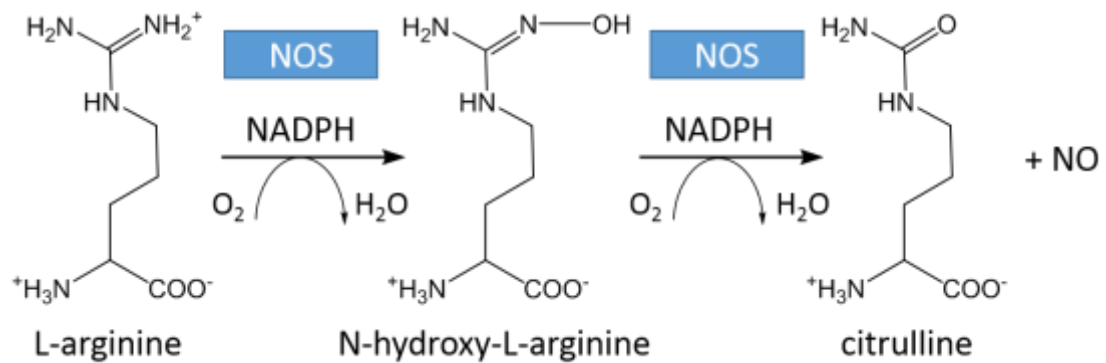


Figure 2.5: Simplified reaction scheme of the endogenous production of NO through NOS-catalysed oxidation of L-arginine [Figure adapted from Ref. 94].

There are three distinct isoforms of NOS produced by different genes, with different catalytic properties, found at different physiological sites: neuronal (nNOS), inducible (iNOS) and endothelial (eNOS).⁹⁵ nNOS and eNOS are considered constitutive and NO production is activated and regulated by the concentration of calcium bound to calmodulin.⁹⁶ iNOS proteins are induced by inflammatory mediators to produce higher concentrations of NO for a prolonged time.⁹⁶ Whilst constitutively expressed NOS proteins primarily produce NO for signalling purposes, the NO produced by iNOS is predominantly focussed on immune defense, in roles such as: mediation of inflammation,⁹⁷ tumourcidal activity⁹⁸ and control of intracellular bacteria (eg. *Mycobacterium tuberculosis*).⁹⁹

2.4.2 Antibacterial Behaviour of NO

NO displays antimicrobial properties against a wide range of microbes, such as: bacteria,¹⁰⁰⁻¹⁰⁴ fungi,¹⁰⁵⁻¹⁰⁸ parasites¹⁰⁹⁻¹¹³ and viruses.¹¹⁴⁻¹¹⁶ There are a number of plausible mechanisms for the antibacterial behaviour of NO. The reaction of NO with reactive oxygen intermediates (ROIs), such as superoxide ($O_2^{\cdot-}$) and molecular oxygen (O_2), leads to formation of antimicrobial agents, as displayed in Figure 2.6.

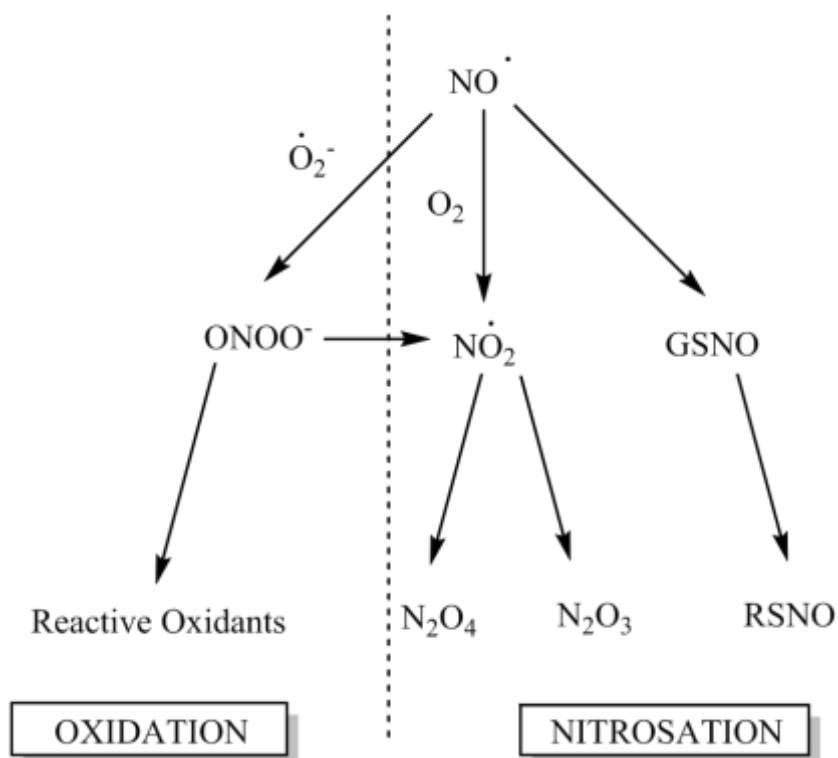


Figure 2.6: Formation of NO-derived reactive oxygen intermediates (ROIs) and reactive nitrogen intermediates (RNIs). $ONOO^-$ - peroxynitrite, NO_2^{\cdot} - nitrogen dioxide, GSNO – S-nitrosoglutathione, N_2O_4 – dinitrogen tetroxide, N_2O_3 – dinitrogen trioxide, RSNO – S-nitrosothiol.

The formation of these ROIs and reactive nitrogen intermediates (RNIs) such as peroxynitrite ($OONO^-$), nitrogen dioxide (NO_2^{\cdot}), dinitrogen tetroxide (N_2O_4), dinitrogen trioxide (N_2O_3), S-nitrosothiol (RSNO), a whole host of reactive oxidants and NO itself primarily target DNA, leading to deamination, strand breaks and oxidative damage.¹¹⁷ Furthermore, through nitrosation of important amino acids by $OONO^-$ and oxidation by $OONO^-$ and NO_2^{\cdot} , certain proteins can become inactivated.¹¹⁸ The inactivation of metabolic enzymes through the NO-induced nitrosylation of free thiol groups has also been shown to occur.¹¹⁹ Other mechanisms

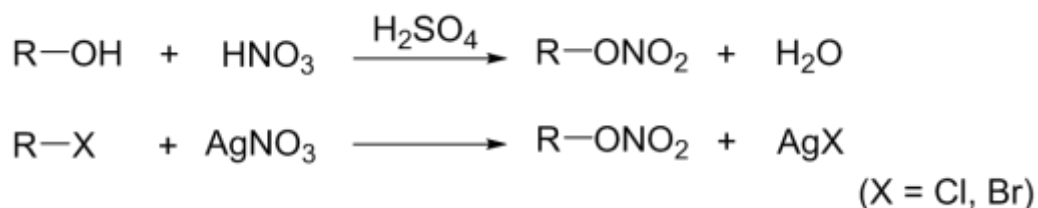
concerning specific bacteria have been reported: De Groote and Fang¹²⁰ found various protein targets of RNIs in *Salmonella typhimurium*, whilst Morris and Hansen observed an *S*-nitrosothiol-mediated bacteriostatic effect on outgrowing spores of *Bacillus cereus*.¹⁰⁰

2.5 Nitric Oxide Donors

Compounds that have the ability to generate NO through decomposition, oxidation or reduction are known as NO-donors. The variation in properties seen between classes of NO donors is vast and structural variations lead to large differences in the NO release kinetics. Some NO donors can decompose spontaneously in the presence of light or heat, whilst other more stable donors need a metal ion catalyst or oxidant to release NO. NO release from some donors is pH dependent, whilst from others it is dependent on the addition of a certain chemical, such as a thiol. The sections below aim to summarise an extensive catalogue of literature regarding the many classes of NO-donor.¹²¹

2.5.1 Organic Nitrates

Organic nitrates (RONO₂) can be synthesised simply by esterification of alcohols or nucleophilic substitution between alkyl halides and silver nitrate (AgNO₃), as shown in Scheme 2.1.^{121, 122}



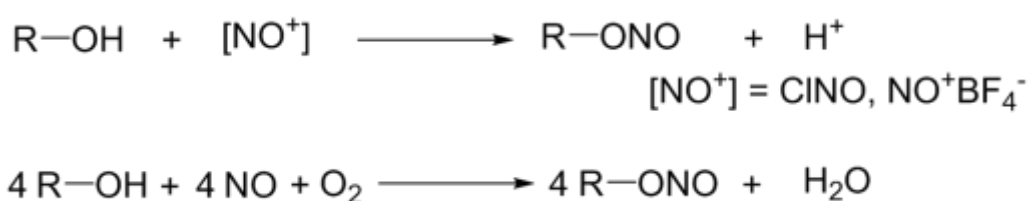
Scheme 2.1: Formation of organic nitrates can occur through esterification of alcohols or nucleophilic substitution of silver nitrate with alkyl halides.

One particularly desirable property of the organic nitrates is their longevity. Due to their low solubility in water, these compounds are stable for years in weakly acidic and neutral aqueous solution. There are also less desirable properties: when used therapeutically, prolonged exposure to organic nitrates causes the build-up of a nitrate tolerance in patients, leading to undesirable increased dosage quantities.¹²¹ Furthermore, although no studies have yet to fully define the mechanism of

endogenous NO release from organic nitrates, either an enzymatic or non-enzymatic (cellular thiol-involving) mechanism, both involving a three-electron reduction is thought most likely to be involved.¹²³ This leads to a further disadvantage when assessing organic nitrates *in vitro*, as the need for specific enzymes and/or thiol groups can lead to unpredictable NO release rates.

2.5.2 Organic Nitrites

RONOs are synthesised by reacting alcohol with nitrosating agents,¹²⁴ such as nitrosyl chloride (ClNO) or nitrosonium salts (NO^+BF_4^-) or gaseous NO (in air),¹²⁵ as shown in Scheme 2.2.



Scheme 2.2: Formation of organic nitrites can occur through reactions between alcohols and nitrosating agents or between alcohols and gaseous NO in the presence of air.^{124, 125}

The release of NO from organic nitrites requires a one-electron reduction. There are many studies that have shown the endogenous NO release mechanism to be enzyme-catalysed: The metabolism of alkyl nitrites with glutathione (GSH) is catalysed by glutathione-S-transferase (GST) enzymes in cell membranes,¹²⁶ whilst Doel *et al.* proved that under anaerobic conditions xanthine oxidase (XO) enzymes can act as catalysts in the reduction of organic nitrites.¹²⁷ Unlike the organic nitrates mentioned previously, when used therapeutically no patient tolerance is observed towards organic nitrites.^{128, 129}

2.5.3 Metal-nitrosyl Complexes

NO as a ligand, has a strong affinity for metal ion centres; in many endogenous processes primary targets for NO are the metal centres of proteins.¹³⁰ The primary mediator for the vast physiological activity of NO is soluble guanylyl cyclase (sGC), a protein containing a ferrous heme domain. NO binds to the heme to form a 5-coordinate metal-nitrosyl (M-NO) complex.^{131, 132}

Whilst the formation of these compounds is a necessary process in human physiology, the M-NO complexes can also act as NO donors. The NO release of metal-nitrosyl complexes is most commonly through photochemical reactions.¹³³ One of the most common metal-nitrosyl complexes is sodium nitroprusside (SNP) (Figure 2.7).

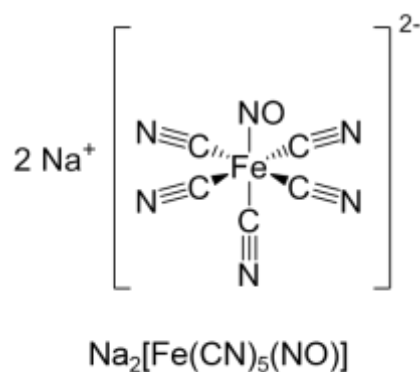


Figure 2.7: Sodium nitroprusside (SNP)

2.5.4 Nitrosothiols (RSNOs)

Long before the benefits of NO as a therapeutic agent were realised, nitrosothiols (RSNOs) were first synthesised by Tasker *et al.* in 1909.¹³⁴ The nitrosothiol class can be identified by a consecutive S-N=O bonding system: examples of more common RSNOs are displayed in Figure 2.8.

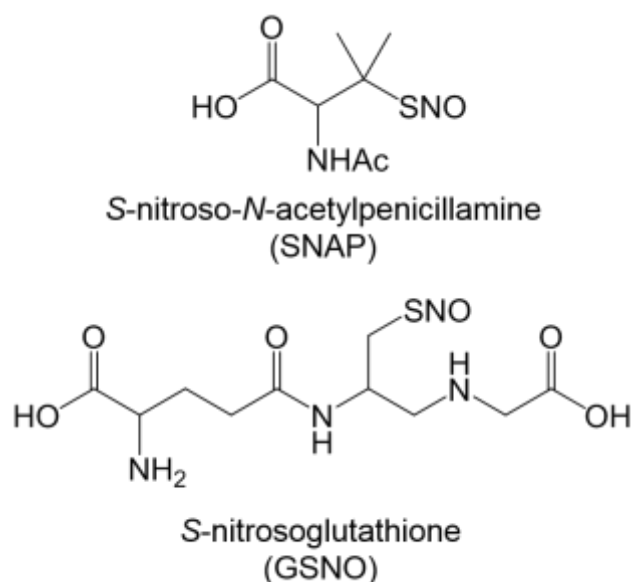
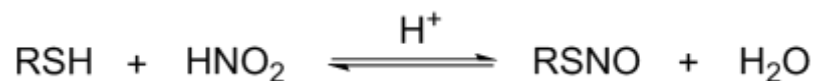


Figure 2.8: Some examples of nitrosothiols.

The simplest, most convenient route to the formation of RSNOs is through the nitrosation of thiols (RSH) by nitrous acid (HNO₂) in aqueous solvents,¹³⁵ shown in the equation below.



Whilst HNO₂ is most commonly used, any carrier of NO⁺ could theoretically be used in the synthetic process. Reaction of RSH with NO can also take place to form RSNOs in the presence of trace O₂.¹³⁶

The decomposition of RSNOs to release NO can occur through a whole host of mechanisms. The first is thermal decomposition: a homolytic cleavage of the S-N bonds leads to the formation of disulfide (RSSR) compounds and an NO radical. The ease of this reaction owes to the fact that RSNOs only require low temperatures (sometimes room temperature) to decompose thermally.¹³⁶ The second way in which RSNOs can decompose is photochemically. The same homolytic cleaving reaction occurs as in the thermal decomposition, but the initiating step is the irradiation of the nitrosothiol at either $\lambda_{\text{max}} = 340$ or 545 nm. Nitrosothiols can also decompose through a metal-ion (Cu⁺, Fe²⁺, Hg²⁺, Ag⁺) catalysed mechanism.^{137, 138}

One major drawback of RSNOs is their thermal instability. As mentioned previously thermal decomposition of some compounds can occur spontaneously at room temperature. Whilst tertiary RSNOs like *S*-nitroso-*N*-acetylpenicillamine (SNAP) are much more stable than their primary alkyl and aryl counterparts, premature decomposition before reaching the target site is still a concern. The current focus is on developing novel therapeutics with desirable pharmacokinetic properties for NO storage and delivery.

2.5.5 *N*-Diazeniumdiolates

When primary or secondary amines are treated with NO gas, the NO adduct of the precursor amine, known as an *N*-diazeniumdiolate is formed (Figure 2.9). The first such compound was prepared in 1960 by Drago and co-workers, which has today led to this class of compounds sometimes being referred to as Drago complexes.¹³⁹ Although *N*-diazeniumdiolates can be formed effectively on primary amines, the

most reported synthesis of these molecules has been by treating a secondary amine-containing compound with high pressures of NO gas.^{139, 140} The NO release mechanism of these compounds is initiated by protonation of the amine nitrogen to release 2 mol of NO per molecule of *N*-diazoniumdiolate. An external base is most often employed during synthesis to keep the product stable by preventing protonation, however inter- and intramolecular bonding can also play this role.¹⁴¹ The general formation and decomposition cycle of the *N*-diazoniumdiolates is shown in Figure 2.9.

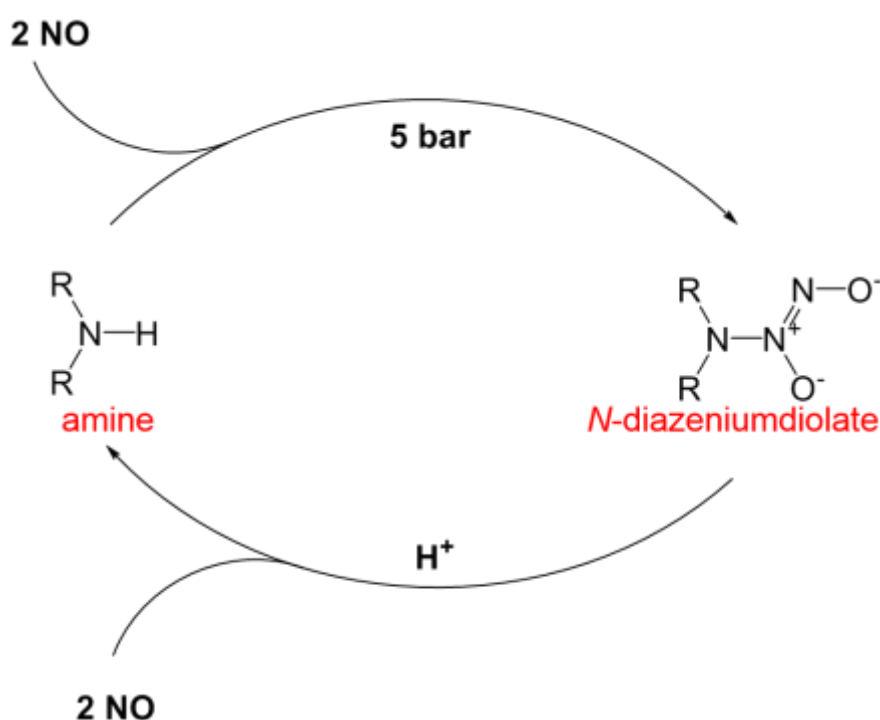


Figure 2.9: Formation and decomposition of *N*-diazoniumdiolates.

The NO-release rates of *N*-diazoniumdiolates can vary greatly, depending on the pKa of the amine precursor, the pH of the reaction medium and the temperature; reported half-lives range from 2 s to 20 hrs.¹⁴² As such this class of NO donors is the most versatile, therapeutically, as they allow for controlled NO rates and concentration that can be tuned depending on the desired biological target.

2.5.6 Comparison of NO Donors as Antibacterial Agents

Whilst the previous sections gave a small insight into the most common NO donors, their different NO-release mechanisms and some of their advantages and disadvantages as therapeutic agents, the primary concern of this thesis is to use NO

donors to antibacterial materials for use in medical implant applications. This section discusses the NO donors mentioned previously and compares them to one another for use as antibacterials.

Organic nitrates and nitrites probably exhibit the least potential as antibacterial agents. The NO-release mechanism is primarily initiated by enzymes that are not present in bacteria. However endogenous enzymes however are found in the surrounding tissue of an infection and so premature NO release can occur.¹⁴³ The metal nitrosyl complexes are extremely light-sensitive which poses a number of problems. In a clinical environment this is an issue as exposure to light is almost guaranteed before administration, potentially leading to premature NO-release before arriving at the infected site. Furthermore, if the infection is internal, incorporating an external light source to initiate release of NO that can penetrate tissue during the clinical process would be difficult. The RSNOs show more promise as antibacterials. They spontaneously release in physiological conditions and as well as releasing NO they also generate thiyl radicals; due to this RSNOs can adversely *trans*-nitrosylate thiolated proteins in bacteria.¹⁴⁴ The versatility and tuneability of the *N*-diazoniumdiolates make them the most promising candidates for antibacterial agents. The NO-release occurs spontaneously under physiological conditions, and the dependency on temperature and a proton initiated mechanism means these compounds can be stored relatively simply at low temperatures.

2.6 *N*-diazoniumdiolated NO Storage and Delivery vehicles

N-Diazoniumdiolates were historically synthesised as small molecule donors.¹⁴⁵ Their utility as antibacterial coatings has been greatly expanded through their incorporation into macromolecular coatings and scaffolds. Whilst there are a number of vehicles that can incorporate *N*-diazoniumdiolates, the main focus within this thesis is on polymers and xerogels, due to their potential as materials/coatings for implant applications and more detailed discussions of these are found in the following subsections. *N*-diazoniumdiolates have, however, been incorporated into other storage and delivery vehicles and an overview of their release abilities have been outlined in Table 2.4.

Table 2.4: An overview of some *N*-diazoniumdiolated NO storage and delivery vehicles and their NO release capabilities.

Storage and Delivery Vehicle	Category	Total NO release	NO release Duration	Ref.
Serum albumin	Protein	40 mol per mol	≈6 months	146
Fumed silica	Silica particles	0.6 μmol per mg	7 hrs	147
Sol-gel synthesised silica particles	Silica particles	11.26 μmol per mg	101 hrs	148
Gold monolayer protected clusters	Metal nanoparticles	0.39 μmol per mg	16 hrs	149
poly(amidoamine)	Dendrimer	5.60 μmol per mg	> 16 hrs	150

2.6.1 Polymer-based Strategies

In an attempt to facilitate localised NO-delivery, small molecule *N*-diazoniumdiolates can be incorporated into polymeric materials. *N*-diazoniumdiolate-incorporated polymeric scaffolds can be categorised based on their interaction with the small molecule *N*-diazoniumdiolate: physical dispersal throughout the polymer matrix or covalent attachment of *N*-diazoniumdiolated precursor or *N*-diazoniumdiolate to the polymer backbone. Representative structures are displayed in Figure 2.10.

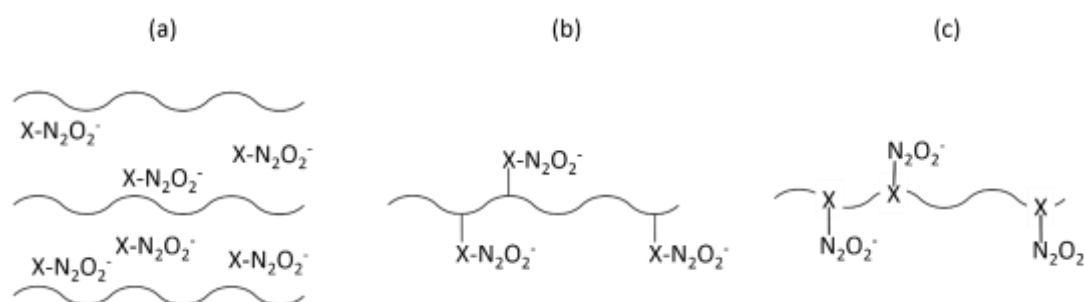


Figure 2.10: *N*-diazoniumdiolates are incorporated into polymers through (a) non-covalent dispersal (b) covalent attachment of *N*-diazoniumdiolate precursor or (c) covalent attachment of *N*-diazoniumdiolate. Wavy lines represent polymer backbone.

2.6.1.1 Physically Dispersed LMW NO Donors

The first report of non-covalent dispersion of small molecule *N*-diazoniumdiolates into polymeric matrices was by Smith *et al.* in 1996, incorporating an *N*-diazoniumdiolated triamine species into poly(caprolactone).¹⁵¹ NO detection by chemiluminescence showed NO release for a full week with a release of 56 nmol NO per mg of polymer for the duration. It was also calculated that 93 % of stored NO was recovered. Later work by Mowery *et al.* showed that non-covalent doping of small molecule *N*-diazoniumdiolates can lead to leaching.¹⁵² *N*-Diazoniumdiolated *N,N*-dimethyl-1,6-hexanediamine was dispersed through poly(vinyl chloride) (PVC) or polyurethane (PU). High-performance liquid chromatography (HPLC) analysis showed the formation of a potentially toxic nitrosamines; a class of compound known for their carcinogenic properties. It was hypothesised that decomposed free amine was most likely leaching out of the polymer and reacting with intermediates of NO oxidation to form the nitrosamine. In 2003, Batchelor *et al.* developed more

lipophilic *N*-diazoniumdiolates by altering the alkyl chain length of precursor diamines, after recognising the water-solubility of non-covalently dispersed *N*-diazoniumdiolates through the hydrophobic polymer was the cause of leaching.¹⁵³

2.6.1.2 Covalently Bound LMW NO Donors

The leaching of non-covalently doped small molecule *N*-diazoniumdiolates can be attenuated by covalently binding *N*-diazoniumdiolated precursor/*N*-diazoniumdiolates to the polymer backbone. Smith *et al.* first demonstrated the simplicity in covalently binding *N*-diazoniumdiolates to polymers.¹⁵¹ In this work two different approaches were used: the first to modify polymers with precursor amines to form *N*-diazoniumdiolate side chains, perpendicular to the polymer backbone. NO-releasing materials were synthesised by using the precursor dipropylenetriamine and the polymer dextran. Two slightly different protocols were employed: a pre-diazoniumdiolated treatment in which the precursor amine was *N*-diazoniumdiolated and then grafted to dextran; and a post-diazoniumdiolated treatment where the precursor amine was first grafted to dextran and then the whole material treated with NO. Whilst both techniques led to NO release, a pre-diazoniumdiolated synthetic process led to greater NO release over longer periods of time. The second approach was through the treatment of amine-containing polymer backbones with NO to incorporate *N*-diazoniumdiolates directly. Insoluble poly(ethylenimine) (PEI) was treated with 5 bar of NO gas to and the secondary amines in the polymer backbone were *N*-diazoniumdiolated (PEI/NO). Vascular grafts were coated with PEI/NO and constant NO release was measured for a duration of 5 weeks.

Meyerhoff and co-workers furthered the work by Smith and covalently attached *N*-diazoniumdiolates to other polymers, such as: silicone rubbers (SRs),¹⁵⁴ polymethacrylates,¹⁵⁵ polyurethanes¹⁵⁶ and poly(vinyl chlorides).¹⁵² Zhang *et al.* covalently attached di- and triamines to cured SR and then treated with 5 bar of NO to form *N*-diazoniumdiolated SRs. The most promising material, DACA-6/N₂O₂-SR, a *N*-diazoniumdiolated silicone rubber with a diamine precursor, showed NO release profiles lasting approximately 20 d, through a thermally driven dissociation of the *N*-diazoniumdiolate moiety. When coated on intravascular sensors, reduced platelet activation and clotting was observed.¹⁵⁷ Boc-protected secondary amine containing-

methacrylate monomers were co-polymerised with methyl methacrylate by Parzuchowski *et al.*¹⁵⁵ The ratios of the two monomers were varied to give 20, 40 and 100 mol. % of amine-containing monomer. As this concentration increased, NO release increased proportionally but interestingly the percentage of *N*-diazoniumdiolated amine sites decreased. This was hypothesised to be caused by the increased solubility of the amine monomer during diazeniumdiolation. Reynolds *et al.* employed two synthetic methods to generate *N*-diazoniumdiolate containing PU, either by first incorporating a precursor diamine into the polymer backbone or as a linked pendant chain.¹⁵⁶ When the amines were present in the polymer backbone an additional counter cation and a base were necessary to stabilise the *N*-diazoniumdiolate. This was not necessary for the PU modified with *N*-diazoniumdiolate pendant chains due to less rigidity allowing amine sites to act as the stabilising base. *N*-diazoniumdiolates incorporated into the backbone released 21 nmol NO per mg of PU over 24 hrs, whilst *N*-diazoniumdiolates as pendant chains released 17 nmol NO per mg of PU over 6 days.

2.6.2 Xerogel Coatings

Over the past decade the sol-gel process has been used extensively to develop NO releasing coatings due to the mild conditions needed for synthesis and the flexibility of the technique to give such vastly different products. In particular, the incorporation of *N*-diazoniumdiolates into xerogels has been used to synthesise coatings for polymeric materials for a range of biomedical applications.

In 2001, Schoenfisch and co-workers first co-condensed an alkylsilane, (isobutyltrimethoxysilane (BTMOS)) and an aminosilane, (N-(3-trimethoxysilylpropyl)diethylenetriamine (DET3)) and allowed gelation and solvent evaporation to form amine-containing xerogel networks.¹⁵⁸ 3 days under 5 bar of NO allowed *N*-diazoniumdiolate formation at the amine sites. NO release was observed for 24 hrs and the level of release was proportional to the concentration of DET3. These materials were tested for their antibacterial efficacy against *P. aeruginosa*. The NO-releasing xerogels exhibited up to 44 % reduction of cell coverage when compared to the non-releasing controls.

In 2003, Robbins and Schoenfisch synthesised NO-releasing methyltrimethoxysilane (MTMOS)/aminoethylaminomethyl)phenethyltrimethoxysilane (AEMP3) xerogels using the same method described above, for incorporation into patterned microarrays.¹⁵⁹ The surface flux of NO ($\approx 6 \text{ pmol cm}^{-2} \text{ s}^{-1}$) was comparable to that produced endogenously by stimulated epithelial cells and release was observed for a period of up to 7 d. The NO-releasing materials were shown to reduce platelet adhesion relative to their controls.

In a subsequent study, combinations of aminosilane: DET3, AEMP3 or (6-aminohexyl)aminopropyltrimethoxysilane (AHAP3) and alkylsilane, BTMOS were co-condensed to form smooth stable xerogel coatings.¹⁶⁰ A pre-hydrolysis of BTMOS was incorporated into the protocol due to the increased rate at which aminosilanes hydrolyse compared to alkylsilanes. A xerogel is formed when a sol-gel solution is allowed to dry and a temperature of 70 °C speeds up this process. Schoenfisch demonstrated that aminosilane concentrations greater than 45 % or drying temperatures above 70 °C, produced coatings that were nonhomogeneous, brittle or opaque. This study again showed the ability to control the NO flux through changes in the structure and concentration of the aminosilane precursor: 40 % DET3/BTMOS gave initial NO fluxes of $60 \text{ pmol cm}^{-2} \text{ s}^{-1}$ in PBS, whilst 5 % AEMP3/BTMOS gave $< 1 \text{ pmol cm}^{-2} \text{ s}^{-1}$; 40 % AHAP3/BTMOS xerogels showed release durations of up to 20 d. Aminosilane to *N*-diazoniumdiolate conversion studies were also carried out and DET3 showed the greatest efficiency. This can be attributed to the additional amine groups that stabilise the *N*-diazoniumdiolates through hydrogen bonding. NO-releasing 40 % AHAP3/BTMOS coatings showed reduced platelet and bacterial adhesion.

This study also corroborated the results from previous reports that NO release from *N*-diazoniumdiolates is temperature dependent, with the flux of 40 % AEMP3/BTMOS xerogels nearly doubling when the temperature was increased from 25 °C to 37 °C.¹⁴⁰ Further, this report confirmed preservation of *N*-diazoniumdiolates when storing at temperatures below freezing, by showing that NO release at 0 °C was negligible.

In a subsequent study the antibacterial properties of NO-releasing AHAP3/BTMOS xerogel coatings were explored for use on orthopaedic implants.¹⁶¹ The bacterial

adhesion of *Pseudomonas aeruginosa*, *Staphylococcus aureus* and *Staphylococcus epidermis* at 25 °C and 37 °C on NO-releasing AHAP3/BTMOS-coated stainless steel was significantly reduced compared to bare and control xerogel-coated steel.

Nablo *et al.* employed a protective PVC polymer coating for the xerogels.¹⁶² This increased the stability of the xerogels whilst only a small reduction in NO flux was observed. The controlled surface chemistry of the PVC-protected xerogels allowed a correlation between bacterial adhesion and NO flux to be determined. It was seen that the reduction in *P. aeruginosa* cell adhesion was proportional to NO flux. *N*-diazoniumdiolated AHAP3/BTMOS xerogels were later shown to also kill adhered *P. aeruginosa* cells when total NO release was increased from 25 to 750 nmol cm⁻² over 15 hrs; a 96 % decrease in adhered cell viability was observed.¹⁶³

In the protocols of all the literature described above a 'post-diazoniumdiolation' was employed in which the aminosilane xerogels were formed first before treatment with NO gas to form the *N*-diazoniumdiolates. In 2013, Storm and Schoenfisch employed a 'pre-diazoniumdiolate' technique, where the aminosilanes were first functionalised with *N*-diazoniumdiolate groups before incorporation into the xerogel.¹⁴¹ Indeed pre-diazoniumdiolated xerogels showed an NO release of more than 10 times their post-diazoniumdiolated counterparts. This work also highlighted the importance of comparable reaction kinetics between alkylsilane and aminosilane. A one-step hydrolysis and co-condensation was initially carried out but due to the increased rate of hydrolysis by *N*-diazoniumdiolated aminosilanes compared with alkylsilanes the two silanes were not stable in their connection. A pre-hydrolysis of the alkylsilane was employed to solve this issue. When MTMOS and BTMOS were used as the alkylsilane, the resulting xerogels of the former displayed cracking and of the latter remained viscous and tacky even after drying. A third alkylsilane, trimethoxypropylsilane (PTMOS), was employed to give stable, non-tacky xerogels by changing the water to silane ratios, depending on the aminosilane.

2.7 Topographical Control of Bacterial Response

Most research to date has focussed on using a chemical approach to control bacterial response. Recently, bioinspired physical approaches to fabricating antibacterial surfaces without the use of chemicals have been developed. These physical strategies hold significant promise as they do not involve the use of chemical antibiotics and bacteria will therefore have a lower tendency to developing antibacterial resistance. Another advantage of this approach is the reduced risk of cytotoxicity to mammalian cells. This section discusses the effect physical changes in the surface topography has on the antibacterial performance of materials.

2.7.1 Natural Antibacterial Topographies.

The natural world that exists today is a result of millions of years of evolution; it exists because it has adapted to survive. The field of biomimetics takes inspiration from nature's tried and tested blueprints when considering design. There are many natural materials that display antibacterial behaviour due to their surface structure as shown in Figure 2.11.

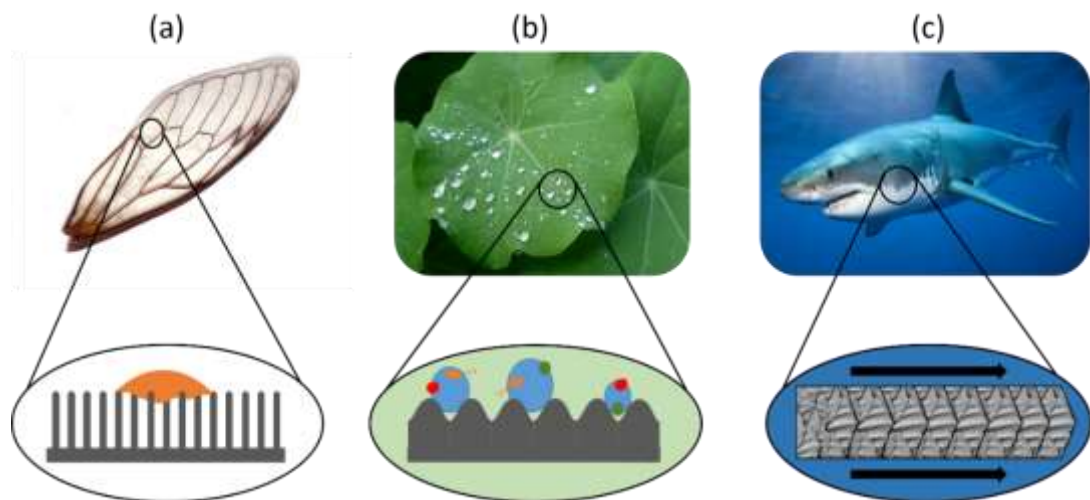


Figure 2.11: Examples of naturally occurring antibacterial topographies: (a) Bactericidal nanopillars of the cicada wing pierce the bacterial membrane. (b) Superhydrophobic topography of the lotus leaf enables a self-cleaning surface. (c) Shark skin has microscale structures which run parallel to the flow of water, promoting low drag and inhibiting microorganisms to adhere.

The cicada wing (Figure 2.11 a) is an example of a natural material that owes its bactericidal ability to its topography. In 2013, Ivanova *et al.* explored the antifouling properties of the wing of one species of cicada (*Psaltoda claripennis*) against *P. aeruginosa* when it became apparent that the wings' were lethal towards the cells.⁵² The surface of the cicada wing is comprised of nanopillars. The nanopillars were measured as 200 nm tall, 100 nm diameter at base, 60 nm diameter at the top, with 170 nm spacing between each pillar. Viability tests showed the effect to be very fast with kill of all adhered bacterial cells occurring in ≈ 5 mins. The lethal effect was seen to be due to penetration of the bacterial cells by the nanopillars. To assess whether the surface chemistry played a significant role in the observed behaviour, the wing was sputter-coated with gold and again tested for bactericidal behaviour. The bactericidal effect of the wing was left unchanged, indicating the primary factor is the physical surface structure.

Many natural surfaces show antifouling properties, preventing bacterial adhesion and eventually biofilm formation. Barthlott and Neinhuis carried out experiments on an array of plant leaves to assess their antifouling and self-cleaning properties and found the lotus leaf performed best (Figure 2.11 b).¹⁶⁴ SEM images showed microstructures on the surface of the lotus leaf; small cone-like protuberances. These cause the surface to have increased roughness which leads to superhydrophobicity ($\approx 160^\circ\text{C}$). This property creates surfaces that do not wet, with water droplets remaining spherical and rolling off picking up contaminants and particulates, including bacteria along the way. The skin of certain shark species (Figure 2.11 c) is another example of a naturally occurring antifouling material.¹⁶⁵ The surface of the skin is made up of tooth like micro-scales with riblet structures parallel to the flow of water. These promote low drag and do not allow micro-fouling organisms to attach to the surface.

2.7.2 Synthetic Materials with Micro-/Nanopatterned Topographies.

The field of taking inspiration from nature is called biomimetics.¹⁶⁶ Of particular interest to this thesis, is the development of materials with distinct topographies on the micro- and nanometer length scales for their antibacterial behaviour.

2.7.2.1 Patterning at the Micro-/Nanometre Scale

When fabricating materials with distinct patterns at the micro- and nanometer scale, the approach can either be top-down or bottom-up.¹⁶⁷ Top-down techniques start with a large 'block' and material is eroded/etched away until the desired pattern is formed. These techniques include electron beam lithography which can give very high resolution patterns but can be expensive and time consuming. Bottom-up techniques use atoms, molecules or polymers as building blocks to build up to achieve the desired structure. A summary of some of the advantages and disadvantages of some common patterning techniques are displayed in Table 2.5.¹⁶⁷

Table 2.5: Advantages and disadvantages of some common patterning techniques.

Technique	Lateral resolution	Advantages	Disadvantages	Ref
Photolithography	40 nm	No shape limitations.	Expensive.	167, 168
Electron beam lithography	15 nm	Very good resolution.	Very slow. Expensive.	169
Colloidal lithography	50 nm	Even spacing. Colloids readily available. Do not require specialised techniques.	Only hexagonal structures possible.	170
Nanoimprint lithography	< 100 nm	Topographical only. (No chemistry). Controllable spatial distribution.	Uneven swelling. Low resolution.	171
Polymer demixing	Sub-micrometre	Very easy fabrication technique. Quick. Cheap. Flexibility in material choice.	Little variation in patterns. Hard to fabricate ordered topographies with uniform feature size.	172, 173
Electrospinning	Fibre size-dependent.	Flexibility in material choice.	Little flexibility in final pattern (bed of fibres).	174
Surface roughening	Hard to control.	Uniform throughout sample. Controlled chemistry	No control in surface structures.	175, 176
Metallic oxidation	15 nm	Size of pattern features easily controllable.	No flexibility in material choice (metals only).	177

2.7.2.2 Antibacterial Behaviour of Micro-/Nanopatterned Materials

The effect of surface topography on the response of mammalian cells has been explored in great detail in comparison to its effect on bacterial cell attachment. Micro-/nanotopographical control of bacterial cell response is an emerging research area and this section discusses some recent studies exploring bacterial response when the topography of a material is altered at comparable length scales to the bacteria.

In 2006, Diaz *et al.* assessed the initial stages of *Pseudomonas fluorescens* cell attachment on nanopatterned copper and gold.¹⁷⁸ The nanostructures were in the form of channels 90 nm in height and 900 nm in width. SEM images showed that on smooth surfaces bacterial adhesion was uneven, whilst on nanostructured Au substrates, in particular, cells underwent orientation to align themselves in the trenches and crevices.

Hochbaum and Aizenberg explored this phenomenon in more depth (Fig. 2.12) and saw that when the pitch between nanoposts was greater than the length of *Pseudomonas aeruginosa* cells, they aligned randomly within the trenches (Fig. 2.12 a), however the cells showed a slight preference to adhere at the points where nanoposts and the substrate met.⁵⁵ When the spacing between nanoposts was comparable to the length of *P. aeruginosa* (1.2-1.5 μm), cells positioned themselves parallel to the substrate and perpendicular to one another, contacting multiple neighbouring posts (Fig. 2.12 b and 2.12 c). As the pitch between posts decreased further to approximately 0.8 μm , cells positioned themselves perpendicular to the substrate aligning along the vertical lengths of the posts (Fig. 2.12 d).

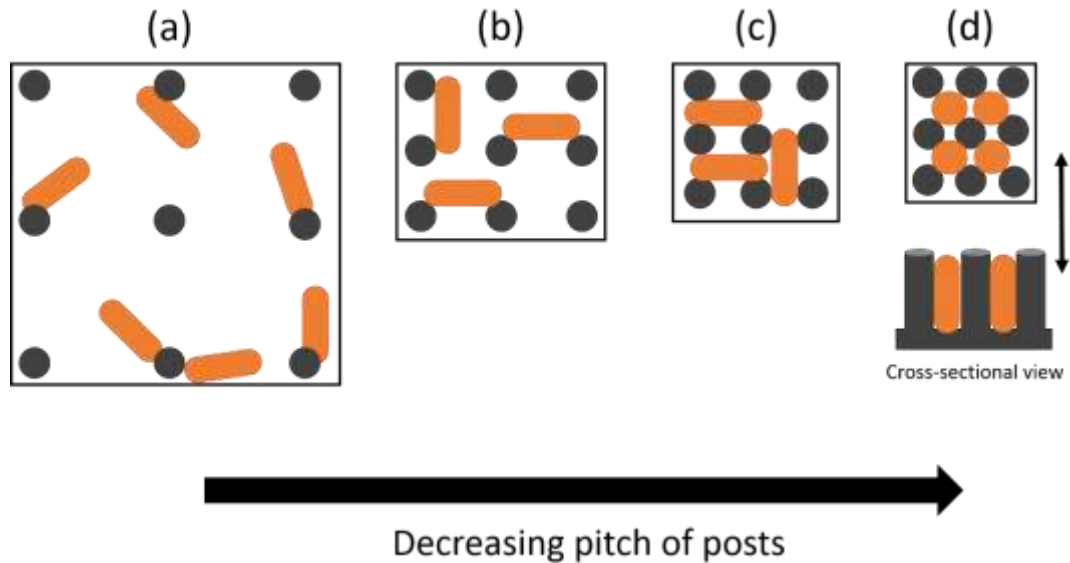


Figure 2.12: Schematic showing the change in orientation by bacterial cells to maximise cell-surface contact area when spacing between surface features is decreased. [Image adapted from Ref. 55]

Hochbaum and Aizenberg have effectively shown that there is a definite response of bacterial cells to ordered topographical features and that bacteria organise themselves to maximise contact area with the surface. A study conducted by Moraru and co-workers corroborated these results with three other species of bacteria (*P. fluorescens*, *Escherichia coli*, *Listeria innocua*).¹⁷⁹ Here they have shown that cell size and morphology was a factor in the response of bacterial cells to topography.

The feature size-dependent anti-adhesion effects of micro-/nanopatterned materials has been the specific focus of many studies. Lu *et al.* fabricated PDMS films with micropatterned surface topographies with feature sizes ranging from 0.5 – 4 μm .¹⁸⁰ Three species of bacteria (*Staphylococcus aureus*, *E. coli*, *P. aeruginosa*) with different size properties were studied to assess the relationship between cell size, feature size and the anti-adhesion properties of the films. For all three species of bacteria the same trend was observed: when the feature sizes were smaller than the size of the cells, bacterial cell adhesion was significantly reduced. For example, *S. aureus* is $\approx 0.66 \mu\text{m}$ length and when inoculated onto patterned surfaces with feature diameters of 0.5 μm , the surfaces demonstrated anti-adhesion properties, with a 43 % reduction in cell attachment compared to controls. Conversely, on surfaces where

the *S. aureus* length was less than the pattern size, there was no reduction in bacterial cell adhesion. In the case of *P. aeruginosa* ($\approx 1.34 \mu\text{m}$ length), patterns with feature diameters of 2 – 4 μm showed an increase in bacterial adhesion compared to non-patterned controls. In the same study,¹⁸⁰ SEM images also showed that *P. aeruginosa* cells preferred to adhere in the grooves between patterns rather than on top of them. Hou *et al.* observed a similar phenomenon and investigated whether gravitational forces played a role.¹⁸¹ *E. coli* was inoculated onto patterned surfaces and turned upside down before incubation and it was found that cells still preferred to adhere in the grooves rather than on the top of the protruding patterns. This experiment indicated that gravity was not the reason and bacterial cells actively chose the attachment site.

Whilst the current literature finds difficulty in defining a conclusive set of factors to explain bacterial attachment and its site specificity, a theoretical thermodynamic approach¹⁸² can offer some reasoning on the phenomena discussed above.^{55, 178-180} This model indicates that bacteria will prefer to bind to a substrate when the energy of the cell-substrate interface is lower than that of the cell-medium interface. The system energy can be lowered with increased contact area between the cell and the surface and so bacteria arrange themselves, according to the surface topography, to maximise surface contact and minimise the energy required to adhere.

In 2018, Michalska *et al.* fabricated black silicon with varied nanopillar morphologies that exhibited bactericidal efficiency against multiple species.¹⁸³ Sharp and blunt nanopillars were fabricated and the mechanism of cell death observed was different for both. SEM images showed that long, sharp nanopillars pierced the cell membrane and caused cytoplasm leakage; whilst when cells adhered to short, blunt nanopillars the membrane became stretched, enhanced by increased attractive strength between cell and surface. The rate of killing seemed to be affected by properties of the bacterial cell such as: abundance of flagella, nature of cell wall and outer membrane, and the nature and extent of polysaccharide secretion.

2.7.2.3 Commercial Applications: Sharklet AF™

One particular success story of the design of synthetic materials with antibacterial topographies is the research carried out to mimic the antifouling effect displayed by

shark skin topographies. Brennan and co-workers designed a technology known commercially as Sharklet AF™.¹⁸⁴ The process uses photolithographic techniques to create silicon wafers with shark-skin like riblets. The Sharklet AF™ topography is patterned by curing poly(dimethyl siloxane) (PDMS) over these wafers. Sharklet AF™ and smooth PDMS were tested against *S. aureus* to assess any inhibition of cell adhesion and biofilm formation on the structured material.¹⁸⁵ After 14 d the percentage coverage was 54 % on the smooth surfaces compared to 7 % on the Sharklet AF™ PDMS. Biofilm colonisation was not observed until 21 d after colonisation. In a more recent study, the Sharklet AF™ micropattern was incorporated into polyurethane materials to assess its potential in improving biocompatibility for central venous catheters.¹⁸⁶ After 18 hrs *S. aureus* and *S. epidermis* colonisation were reduced by 70 % and 71 %, respectively, and platelet adhesion reduced by 86 % compared with non-patterned controls.

2.8 Summary

The review of the literature considered here provides a detailed background for the study and design of antibacterial surfaces for use as medical implants. This review has focussed on both chemical and physical antibacterial approaches. Specifically, the antibacterial properties of NO, its release from NO donor molecules (particularly *N*-diazoniumdiolates) and the maximising of NO release capabilities using NO storage and delivery vehicles has been reviewed. The literature reviewed concerning a physical antibacterial approach, has focussed on natural antibacterial materials with distinct topographies, and the design and fabrication of synthetic micro-/nanopatterned surfaces and their ability to adversely affect bacteria. The work in this thesis has used the literature reviewed in this chapter as a guideline to design NO releasing surfaces and also surfaces with discrete micro-/nanotopographical features for use as antibacterials, and help to gain a mechanistic understanding of their antibacterial behaviour. Nitric oxide is a diverse biomolecule that has shown great therapeutic potential, namely in antibacterial applications. With its extremely short half-life the use of an NO-donor is paramount to prevent premature NO release. From reviewing the literature it is also clear to see that certain NO-mediated processes are a function of NO release concentrations. Therefore this study will

explore the control of NO release through different methods and the effect changes in this have on antibacterial mechanisms.

Chapter 3 - Materials and Methods

3.1 Introduction

This chapter details medically relevant polymers that have been modified for antibacterial implant applications, the chemicals used to functionalise them and the techniques and protocols required for modification. In order to confirm chemistry and topography, an array of analytical techniques were employed. The efficacy of the antibacterial surfaces was evaluated by several methodologies listed here.

3.2 Polymer Substrates

The polymers selected for this study were chosen for their medical relevance and their current use in medical implant applications. Silicone elastomer (SE) and poly(ethylene terephthalate) (PET) have been modified, as they are materials commonly used in making medical devices, such as catheters and sutures, which can be prone to bacterial infection.¹⁸⁷ Polystyrene (PS), poly(methyl methacrylate) (PMMA) and polycaprolactone (PCL) have also been used throughout this study due to their medical relevance. In Figure 3.1 the structures of the monomer repeating units of the polymers used are shown.

From Goodfellow, UK:

- SE
- PET

From Sigma-Aldrich:

- PS (M_w :280000)
- PMMA (M_w :350000)
- PCL (M_w :48000-90000)

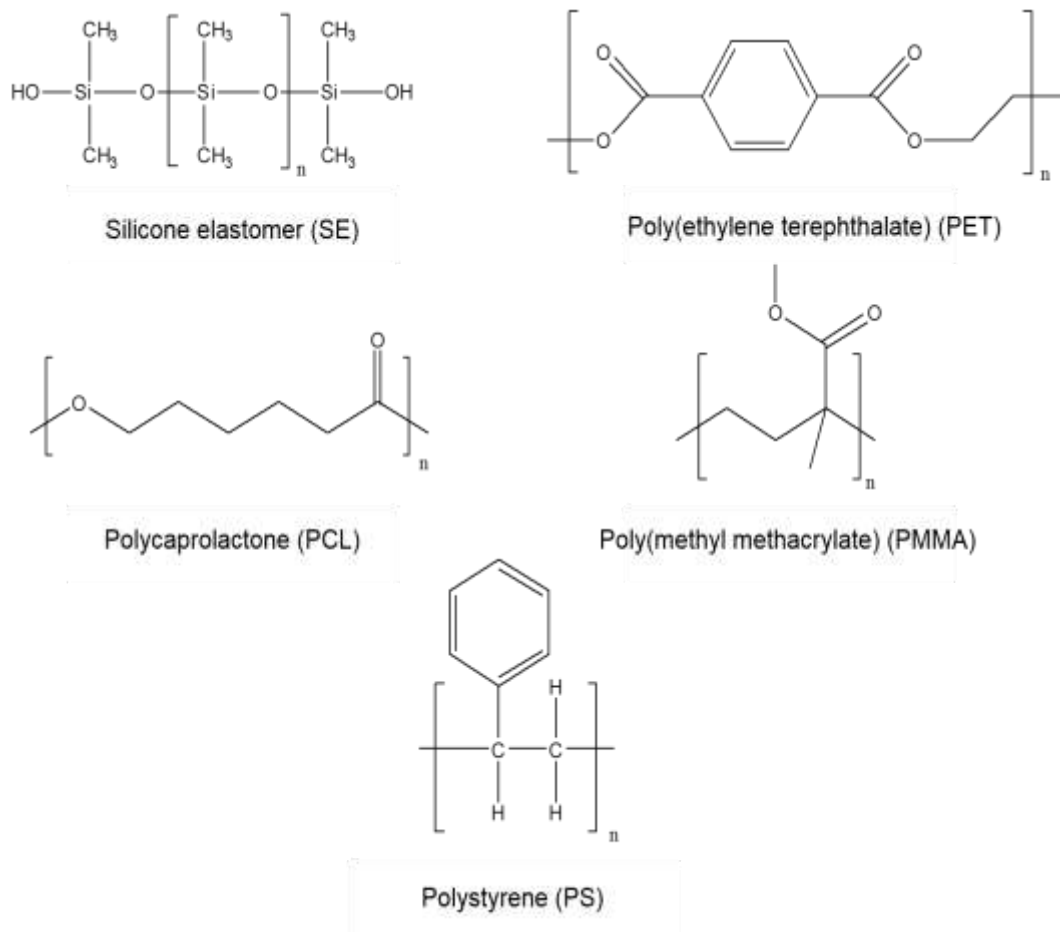
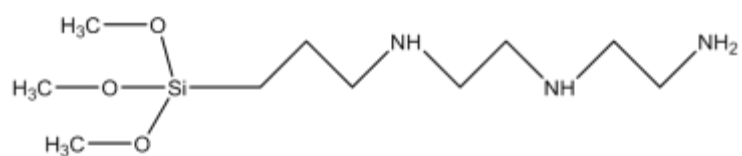


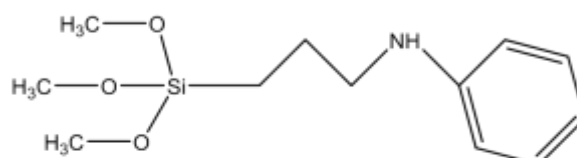
Figure 3.1: Chemical structures of the repeating units of the polymers.

3.3 Silanes

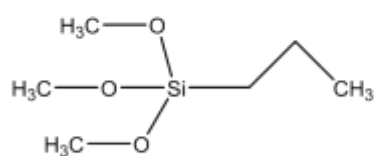
Aminosilanes were used to modify the surface with amine functionality which were then utilised as anchor points for diazeniumdiolate synthesis. Two secondary amine-containing aminosilanes: N-(3-Trimethoxysilylpropyl)diethylenetriamine (DET3) and N-(3-trimethoxysilylpropyl)aniline (PTMSPA) have been used. Alkylsilanes were also used in the synthesis of xerogels (Chapter 5). Two alkylsilanes: trimethoxy(propyl)silane (PTMOS) and isobutyl(trimethoxy)silane (BTMOS) were investigated. Structures of all silanes are as displayed in Figure 3.2.



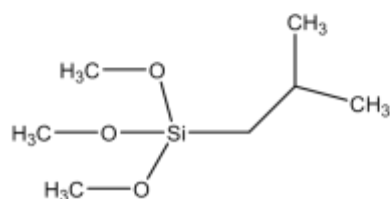
N-(3-trimethoxysilylpropyl)diethylenetriamine (DET3)



N-(3-trimethoxysilylpropyl)aniline (PTMSPA)



Trimethoxy(propyl)silane (PTMOS)



Isobutyl(trimethoxy)silane (BTMOS)

Figure 3.2: Chemical structures of silanes.

3.4 Synthesis

In this work different materials, with varying properties, have been fabricated: *N*-diazoniumdiolate-tethered polymers, *N*-diazoniumdiolated xerogels, polymer demixed films and micropatterned PDMS. The scientific protocol for the fabrication of each material mentioned has its own unique reaction scheme and so for clarity an experimental section at the start of each chapter has been provided. Common protocols used throughout the thesis have been outlined below.

3.4.1 Preparation of Substrates for Analysis

Sheets of PET, 0.175 mm thick and SE, 1 mm thick (Goodfellow, Cambridge, UK) were cut into disks, 6 mm in diameter for NO release quantification experiments and bacterial assays. For all other analyses, substrates were cut into 15 x 15 mm squares. The disks were washed in 70 % EtOH for 3 x 5 mins, rinsed with DI water and dried in air before use.

3.4.2 Plasma treatment of Substrates

Pristine substrates were subjected to oxygen (BOC, Guildford, U.K.) plasma treatment at a gas flow rate of 14 standard cubic centimetres per minute (sccm) and a pressure of 0.75 mbar using a HPF100 plasma treatment system (Henniker Plasma, Warrington, U.K.).

3.5 Analytical Techniques

The surface chemistry and topography throughout each step of each fabrication process were characterised through a number of techniques. Static water contact angle measurements were carried out to assess the changes in surface wettability; X-ray photoelectron spectroscopy (XPS) and Fourier-transform Infrared Spectroscopy (FTIR) were employed to determine chemical changes on the surface; NO detection *via* chemiluminescence was carried out to understand the kinetics of NO-release from *N*-diazoniumdiolate-functionalised materials; atomic force microscopy (AFM) enabled the acquisition of surface roughness values and the imaging of surfaces at the micro-/nanoscale.

3.5.1 Contact Angle Analysis

Static contact angles of water were used to determine changes in surface wettability using an Attension ThetaLite optical tensiometer (Biolin Scientific, Västra Frölunda,

Sweden). The sessile drop method was used and contact angles were taken at 17 frames per second for 10 s. Data was collected using OneAttension software (Biolin Scientific, Västra Frölunda, Sweden). At least three readings were performed per sample type and samples were produced in triplicate. The results recorded as mean average \pm standard deviation.

3.5.2 Fourier-transform Infrared Spectroscopy

The infrared (IR) region of the light spectrum is split into three sub-regions and ranges in wavelength from approximately 0.78 – 1000 μm , however wavelengths between 2.5 – 15 μm are most useful for IR spectroscopy (Table 3.1).

Table 3.1: IR spectral sub-regions

Region	Wavelength (μm)	Wavenumber (cm^{-1})
Near	0.78-2.5	12800-4000
Mid	2.5-50	4000-200
Far	50-1000	200-10
Most Used (spectroscopically)	2.5-15	4000-670

Higher energy radiation types such as x-ray, ultraviolet and near-infrared deal with electronic transitions, whilst the lower energy of IR radiation is only concerned with rotational and vibrational energy transitions. An absolute necessity in IR active compounds is that the molecules exert net change in the dipole moment as they vibrate or rotate. This arises when the elemental components are different in electronegativity making the charge unevenly dispersed. When such molecules vibrate and rotate the fluctuation in dipole moment is observed. The electrical field of the IR radiation interacts with these fluctuations. When the frequency of the radiation and vibrational frequency of the molecule match, the radiation can be absorbed, which leads to a change in the amplitude of molecular vibration.

In these studies FTIR spectra were obtained at room temperature in the spectral range between 3200 cm^{-1} and 1400 cm^{-1} , using a PerkinElmer Frontier FTIR Spectrometer (Perkin Elmer, UK). The spectra were obtained with 64 scans at

resolution of 4 cm^{-1} and data was collected using PerkinElmer Spectrum v10.4 software.

3.5.3 X-ray Photoelectron Spectroscopy

Like FTIR analysis, X-ray photoelectron spectroscopy (XPS) is a method of analysis to determine chemical composition of a surface. In XPS, the surface of a sample is irradiated by soft x-rays ($\text{Mg K}\alpha$ or $\text{Al K}\alpha$) with the energy of $h\nu$. This process allows mono-energetic photons to approach the surface atoms, after which one of three events can occur:

1. The photon can pass through the atom without any interaction.
2. Scattering of the photon by an atomic orbital electron can lead to partial energy loss.
3. The photon energy is totally transferred to an atomic orbital electron resulting in electron emission from the atom.

This third event (photoemission) is what provides an essential basis for the XPS technique and is outlined in Figure 3.3.

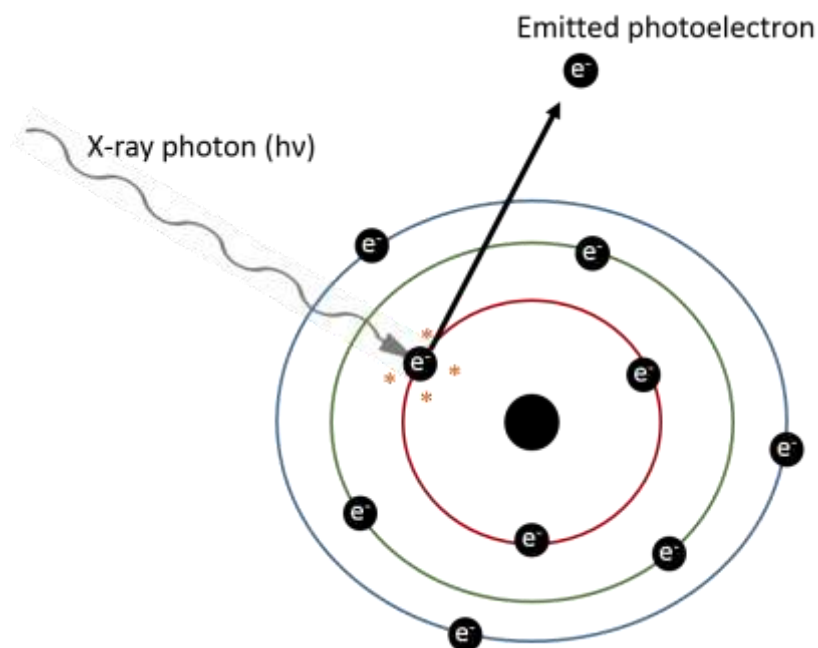


Figure 3.3: A photon source of efficiently high energy will transfer its energy to a core-level electron enabling it to be emitted as a photoelectron able for detection by XPS.

The sampling depth of XPS is related to the inelastic mean free path of the electrons. This is the ability to travel much further through solids than electrons. 1 keV (typical energy of x-rays used in XPS) can penetrate the surface to a depth of 1 μm , where an electron of the same energy can only penetrate ≈ 10 nm. Photoelectrons emitted due to x-ray excitation, below the uppermost surface will penetrate 1 μm into the surface however, electrons are only ejected from the top 10 nm. This is because electrons that are ejected below 10 nm in depth will undergo inelastic scattering with other atoms and lose energy before they can escape. It is for these reasons that XPS can be considered highly surface sensitive (top 10 nm).

The x-ray photoelectron spectrometer measures the kinetic energy of emitted electrons that have reached the detector with no energy loss. By using the Einstein equation:

$$\text{KE} = h\nu - \text{BE} - \phi \quad (3.1)$$

where KE, represents kinetic energy of photoelectron, $h\nu$ is the energy of the excitation photon, BE is the binding energy of the electron in the atom and ϕ is the spectrometer's work function, some valuable information can be obtained. The binding energy deduced from Equation 3.1 can provide great detail about where its corresponding electron originated.

The chemical information of ionic and covalent bonds can be gathered from the calculated binding energies. The binding energy of an electron is a measure of how well a negatively charged electron is bound to a positively charged nucleus. Each atom has a different nuclear charge and so the binding energy of each element is different. When other atoms are bound to the atom of interest the electron distribution is altered which also affects the binding energy. More specifically, the more electronegative the species bonded to the atom of interest is, the greater the binding energy of the electron. As a result of this XPS can be used to identify chemical composition and surface elemental concentrations.

The advantages of XPS are that it is a non-destructive surface sensitive technique that can identify all elements except hydrogen and helium. The interpretation and theory behind XPS is relatively straightforward and high information content on chemical bonding can be retrieved, quantitatively. The disadvantages of XPS include its relatively large analysis area ($\approx 10 \mu\text{m}$), the cost of the instrument, as well as the running and maintaining of it, and the use of a high vacuum which samples must be compatible with.

In these studies XPS analysis was carried out on an Axis-Supra instrument (Kratos Analytical, Manchester, UK) using a monochromated Al K α x-ray source operating at a power of 225 W. Charge compensation was performed using a low-energy electron flood source. Survey and narrow region scans were carried out at pass energies of 160 and 20 eV and step sizes of 1 and 0.1 eV, respectively. Hybrid lens mode was used in both cases. Data was converted to vamas (*.vms) format and analysed using CASAXPS 2.3 software (Casa Software, Devon, UK). Spectra were calibrated to 284.6 eV for SE samples and 285 eV for all other polymers, corrected with linear background removal and fitted using Gaussian-Lorentzian line curves. Three separate areas on each sample were recorded and the average results are reported as atomic % concentrations (at. %) \pm standard deviation

3.5.4 Atomic Force Microscopy

Atomic force microscopy (AFM) is a scanning probe microscopy technique, which involves the use of an atomically sharp tip that interacts with the surface. The tip is at the end of a cantilever that is placed parallel to the sample surface. The tip, which is typically made of silicon or silicon nitride, is brought into contact with the surface, which leads to an interaction force between the tip and the surface. As this force varies, deflections are produced in the cantilever. Before operation, a laser spot is positioned on top of the cantilever at an angle allowing it to be reflected into the photodetector. The deflections of the cantilever are measured by these reflections into the photodiode, to produce a three dimensional topographical image at the micro-/nanoscale. A schematic representation of AFM system is displayed in Figure 3.4.

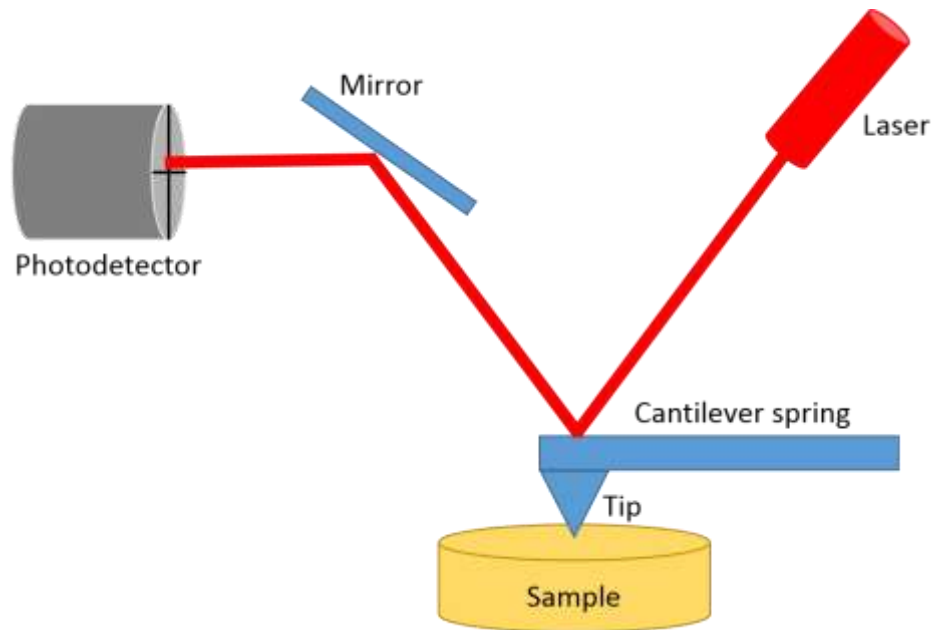


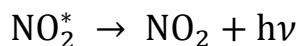
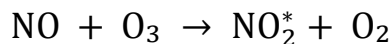
Figure 3.4: Schematic representation of an operating AFM system

There are three modes of operation for AFM: tapping, contact and non-contact. In this research tapping mode was used. In this mode the tip oscillates over the surface, and only touches it for a very small amount of time, reducing the issue of lateral force damage and drag across the surface. The topography is imaged by adding the short-range repulsive and long-range attractive forces together to get an average force response curve.

In this study AFM was used to image the topography of sample surfaces, measure the dimensions of surface micro-/nanofeatures, and determine surface roughness values. A Bruker Multimode 8 (Bruker, Billerica, MA, USA) system fitted with a NanoScope V controller was used and samples were imaged in air in ScanAsyst mode using a silicon RTESPA-150A tip, operating at a scan rate of 0.9 Hz. Third order flattening was used to correct any errors in piezo linearities whilst processing the image. Samples were analysed over a $5 \times 5 \mu\text{m}^2$ sample area and average roughness (Ra) and root mean square roughness (Rq) were calculated from at least three replicates of each sample type using NanoScope Analysis 1.7 software. Ra is the arithmetic average of the absolute values of the peaks and valleys over the whole length of the sample. Rq is the root mean square average of the profile height deviations from the mean over the whole length of the sample.

3.5.5 Nitric Oxide Detection by Chemiluminescence

This method of detection utilises the chemiluminescence signal of the reaction between nitric oxide and ozone:



NO first reacts with ozone to form a molecule of nitrogen dioxide (NO_2) in an excited state (NO_2^*). Decomposition of NO_2^* to its ground state emits a photon, which is what the detection of NO depends on. This method of detection requires a carrier gas to push the NO through the reaction cell. This carrier gas (N_2 in this work) plays an essential role in the overall process. NO_2^* returns to its ground state by quenching and this quenching occurs through collisions of NO_2^* with the carrier gas.

In these studies a Sievers Nitric Oxide Analyser NOA 280i (GE Analytical, Boulder, CO, USA) system was used. The system was calibrated with air passed through a zero air cylinder (0 ppm NO) and NO standard gas (89.2 ppm NO). A three-necked round bottom flask containing 5 ml acetate buffer or phosphate-buffered saline (PBS) were used for pH 4 and pH 7.4 experiments, respectively. The sample was dropped into the buffered solution once the baseline was stable.

A vacuum pump is employed to continuously draw the carrier gas (N_2) and any NO produced into the analyser at a constant flow rate. A standard frit restrictor keeps the flow rate at 200 ml/min. Ozone is generated from an external O_2 supply into an electrostatic ozone generator. The rate of gas flow into the ozone generator is ≈ 30 ml/min, controlled using a regulator (adjusted to 6 psi) and small diameter tubing restrictors. The ozone generator works alongside a high voltage transformer to generate ozone at a concentration of $\approx 2\%$ v/v (balance O_2). This is sufficient concentration for NO measurements up to 500 ppm. The reaction between NO and ozone takes place in a reaction cell with small volumetric capacity (20 ml). The small volume allows measurement of low concentration of NO at low flow rates. Three other compounds give chemiluminescence products when reacted with ozone: sulphur compounds, ethylenic compounds and carbonyls. The light from these is emitted at shorter wavelengths and so the system is fitted with an optical filter

installed between the reaction cell and photomultiplier tube that only transmits red wavelengths (> 600 nm). The photomultiplier tube is where the photon emission is measured and to increase sensitivity is cooled to -12°C . Data was collected using the Plot program of the NOAnalysis 3.21 software (GE Analytical, Boulder, CO, USA). Three replicates of each sample were used to acquire NO release data. Average maximum NO release is reported in $\mu\text{M s}^{-1} (\text{cm}^{-2}) \pm$ standard deviation. Average total NO release is reported in $\mu\text{mol} (\text{cm}^{-2}) \pm$ standard deviation

3.5.6 Scanning Electron Microscopy

Scanning electron microscopy (SEM) images a sample by scanning the surface with a focussed beam of electrons. These electrons interact with surface atoms, producing secondary electrons which are collected by a detector to form images. Due to the much shorter wavelengths of electrons, compared to light, electron microscopes allow for much better resolution compared to light microscopes. Typically, SEMs can give resolutions between 1 and 20 nm. If samples are non-conductive, they must be metal sputter coated. Analysis is carried out under vacuum and so samples must be able to handle moderate vacuum pressures.

In this study, samples were sputter coated with 15 nm coatings of chrome using a Quorum QT150T turbomolecular pumped coater (Quorum Technologies, Lewes, UK). Samples were imaged using a JSM-6610LV SEM system (JEOL USA, Peabody, MA, USA), at a working distance of 14 mm and using an accelerating voltage of 10 keV.

3.6 Biological Assessment

3.6.1 Preparation of Bacterial Solutions

Antibacterial tests were carried out against the *P. aeruginosa* laboratory reference strain PA14. Overnight cultures of *P. aeruginosa* were diluted from frozen stock (-80°C) to McFarland Standard 0.5 in Luria-Bertani (LB) broth or phosphate buffered saline (PBS) buffer (pH 7.4).

3.6.2 Planktonic Cell CFU Assay

Substrate disks were placed in 24-well plates and 2 mL of the bacterial solution added before incubating at 37°C for 1, 4 or 24 hrs. Substrate disks were then transferred to sterile well plates and washed with PBS to remove any non-adhered planktonic bacteria. Substrates were then placed in fresh wells and repeatedly washed and

agitated vigorously to remove and re-suspend the attached cells. A serial dilution was performed on LB agar using the Miles and Misra method in order to enumerate the bacteria. Non-treated substrates were used as positive control and % reduction in adhered cells was calculated as a function of cells attached to controls. All samples were studied in triplicate and repeated at least three times. Graphs are displayed as bar charts in which bars represent average CFU/ml \pm standard error.

3.6.3 Adhered Cell CFU Assay

Substrate disks were placed in 24-well plates and 2 mL of the bacterial solution added before incubating at 37 °C for 1, 4 or 24 hrs. A serial dilution was performed on LB agar using the Miles and Misra method in order to enumerate the bacteria. Non-treated substrates and bacterial solutions without substrates were used as positive controls. The % reduction of cell counts in wells containing treated substrates, compared to positive controls can be considered directly proportionate to kill rate. All samples were studied in triplicate and repeated at least three times. Graphs are displayed as bar charts in which bars represent average CFU/ml \pm standard error.

3.6.4 Fixation of Bacteria

The size of the bacteria was determined by SEM analysis. In order to image the bacteria the cells needed to be fixed. Clean glass coverslips were inoculated with 2 ml of a 1:100 bacterial solution, prepared from an overnight culture. The bacteria were then fixed with 2.5 % glutaraldehyde solution in sterile PBS for 4 hrs. The bacteria were then dehydrated in increasing concentrations of ethanol (30, 50, 75, 90, 95 and 100 v/v %) by soaking for 5 mins in each ethanol concentration. The coverslips were dried in air and stored at 4 °C before SEM imaging.

3.7 Statistical Analysis

Where appropriate, statistical analysis was performed using the data analysis package, SigmaPlot 13.0 (Systat Software, San Jose, CA, USA). One-way analysis of variance (ANOVA) was used to establish differences between group means and thus variance between treatment types. Significance between treatment types was determined using the Student–Newman–Keuls (SNK) method. A value of $p < 0.05$ was taken as statistically significant.

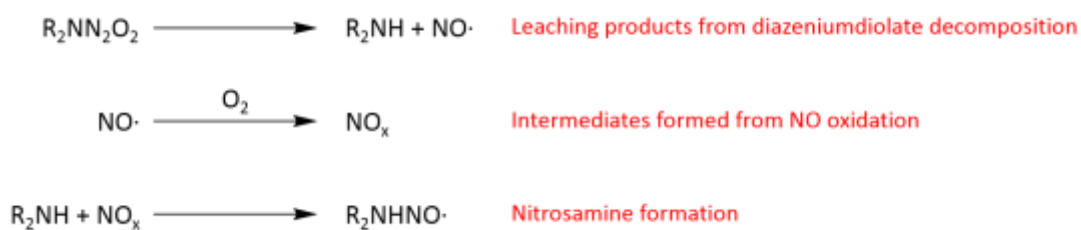
Chapter 4: Covalently bound *N*-diazoniumdiolates to Polymer Surfaces for Prevention of Biofilm Formation

4.1 Introduction

Nitric oxide (NO) is an endogenously produced diatomic free radical messenger molecule that, as well as playing fundamental roles in wound healing,¹⁸⁸ neurotransmission⁸⁸ and vasodilation,⁸⁴ has displayed antibacterial behaviour against multiple species.¹⁰⁰⁻¹⁰⁴ With NO involved in such a vast array of physiological processes, it has become a heavily studied area to modify material surfaces with NO-donor groups that can release the molecule at appropriate concentrations. *N*-diazoniumdiolate NO donors are advantageous due to the tuneable NO release kinetics, through changes in pH, temperature and precursor structure.¹⁴² The incorporation of these donors into polymeric matrices has been carried out previously, in one of three ways:¹⁵¹

1. Non-covalent dispersal throughout the polymer matrix.
2. Covalently bound aminosilane precursors to the polymer backbone to form donor pendant groups.
3. Covalently bound *N*-diazoniumdiolates directly incorporated into *N*-sites of a polymer backbone.

Whilst all three protocols have been found to improve NO storage and delivery potential compared to small molecule *N*-diazoniumdiolates, reactions between leaching free amines and oxidative intermediates of NO, leading to the formation of potentially carcinogenic nitrosamines, has been observed when non-covalently dispersed (Scheme 4.1).¹⁵²



Scheme 4.1: Free amines (R_2NH) and $\text{NO}\cdot$ can leach from a polymer matrix when *N*-diazeniumdiolates ($\text{R}_2\text{NN}_2\text{O}_2$) are non-covalently dispersed throughout. Oxidative intermediates of NO (NO_x) then react with leaching R_2NH to form nitrosamine ($\text{R}_2\text{NHNO}\cdot$).

N-diazeniumdiolates have been covalently tethered to many biomedically relevant polymers previously, including: silicone rubbers (SRs),¹⁵⁴ polyurethanes (PUs),¹⁵⁶ poly(vinyl chlorides) (PVCs)¹⁵² and polymethacrylates¹⁵⁵ to form NO storage and delivery vehicles for a controlled and sustained release. Herein, *N*-diazeniumdiolates, formed by functionalising aminosilane precursors, have been covalently tethered to two biomedically-relevant polymers, used for medical implant applications (poly(ethylene terephthalate) (PET) and silicone elastomer (SE)). The reaction scheme is outlined in Figure 4.1 and the full experimental protocol is described in Section 4.2.

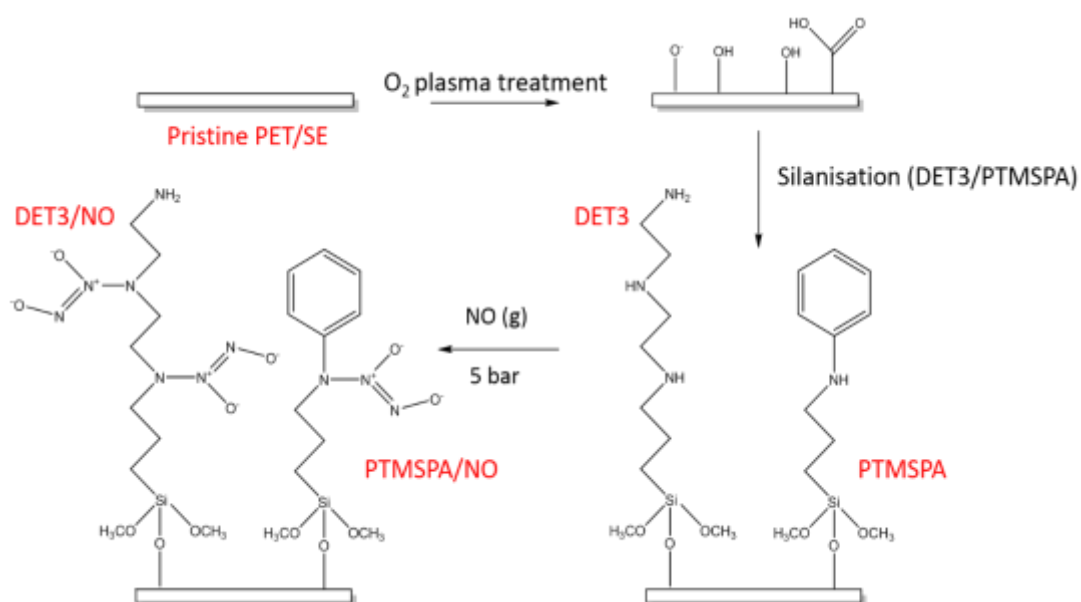


Figure 4.1: Reaction scheme for the covalent tethering of *N*-diazeniumdiolates onto PET and SE.

In order to assess the effect aminosilane precursor structure has on tuneable NO release kinetics of the *N*-diazoniumdiolates an aliphatic aminosilane with two 2° amines and one 1° amine, N-(3-(trimethoxysilyl)propyl)diethylenetriamine (DET3) and an aromatic aminosilane with one 2° amine, N-(3-(trimethoxysilyl)propyl)aniline (PTMSPA) have been used separately as precursors. The pH dependence on NO release will also be discussed.

This chapter introduces the use of NO as an antibacterial agent and particularly its ability in preventing bacterial cell adhesion and biofilm formation. The prevention of biofilm on the surface of a medical implant is highly important because when bacterial cells are in this state the ability to resist antibacterial treatment is greatly increased.¹⁸⁹ The biofilm prevention assays have been carried out against a lab strain of *Pseudomonas aeruginosa* (PA14). This particular isolate is a well-characterised, medically-relevant opportunistic biofilm former. By inoculating the samples for 24 hrs at pH 7.4, this study aims to provide insight in to the potential of covalently binding *N*-diazoniumdiolates to synthetic polymers for use in preventing bacterial cell adhesion, leading to biofilm formation on the surfaces of medical implants.

4.2 Experimental

4.2.1 Aminosilanisation

Pristine PET and SE were subjected to oxygen (BOC, Guildford, U.K.) plasma for optimum treatment times of 7 and 2 mins, respectively, as determined from preliminary experiments. Substrates were then aminosilanised using DET3 and PTMSPA (Sigma-Aldrich, St. Louis, MO, USA). Immediately following plasma treatment the polymers were immersed in 10 % solutions of either DET3 or PTMSPA in EtOH for 2 hrs. Substrates were rinsed in anhydrous EtOH, dried in air and cured for 4 hrs at 80 °C.

4.2.2 *N*-diazoniumdiolate tethering

N-Diazoniumdiolate tethering was carried out using a stainless steel reactor built in-house. Aminosilanised substrates were placed into the reactor and purged with 6 bar of argon (BOC, Guildford, UK) for 3 x 5 mins and 3 x 10 mins. The reactor was then filled with 5 bar of NO (BOC, Guildford, UK) for 96 hrs. Upon release of NO from

the system, the system was again purged with 6 bar of argon for 2 x 5 mins and 2 x 10 mins. Substrates were removed from the reactor and stored at -20 °C prior to use.

4.3 Results

4.3.1 Ageing Test: Contact Angle

Contact angles were recorded immediately after plasma treatment, then at 15 min intervals for 1 hr. Measurements were also taken 1 d and 10 d after treatment. Figures 4.2 and Figure 4.3 show the relationship between contact angle and ageing time, after different plasma treatment times, for PET and SE, respectively.

PET

In the case of the PET samples, all treatment times resulted in reduced contact angles, in comparison to the untreated control. The contact angle of surfaces after 7 mins treatment time had the lowest rate of recovery. After an immediate reduction to 5°, these surfaces retained low contact angles for up to 60 mins after treatment with values of 10°, 12° and 8°, for 15, 30 and 60 mins, respectively. Hydrophobic recovery was observed after 10 d (30°) but contact angle did not return to values of pristine non-treated PET ($\approx 80^\circ$).

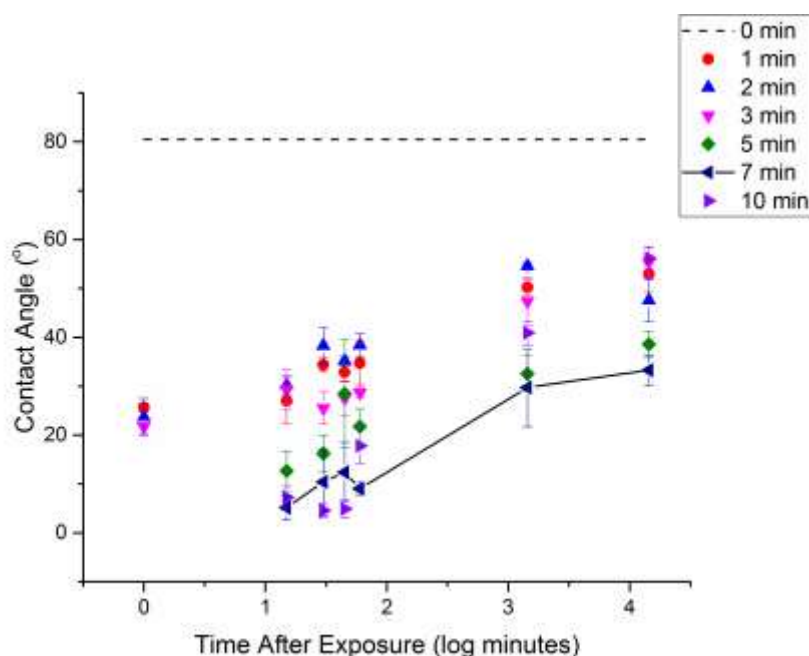


Figure 4.2: Ageing profile of static water contact angle on PET as a function of time after oxygen plasma treatment for different oxygen plasma treatment times.

SE

All SE samples subject to plasma treatment showed a reduction in contact angles compared with the pristine state. The contact angle of surfaces after 2 mins treatment time had the lowest rate of recovery. After an immediate reduction to 13° , these surfaces started recover up to 60 mins after treatment with values of 30° , 37° and 61° , for 15, 30 and 60 mins, respectively. Complete hydrophobic recovery was observed after 1 d.

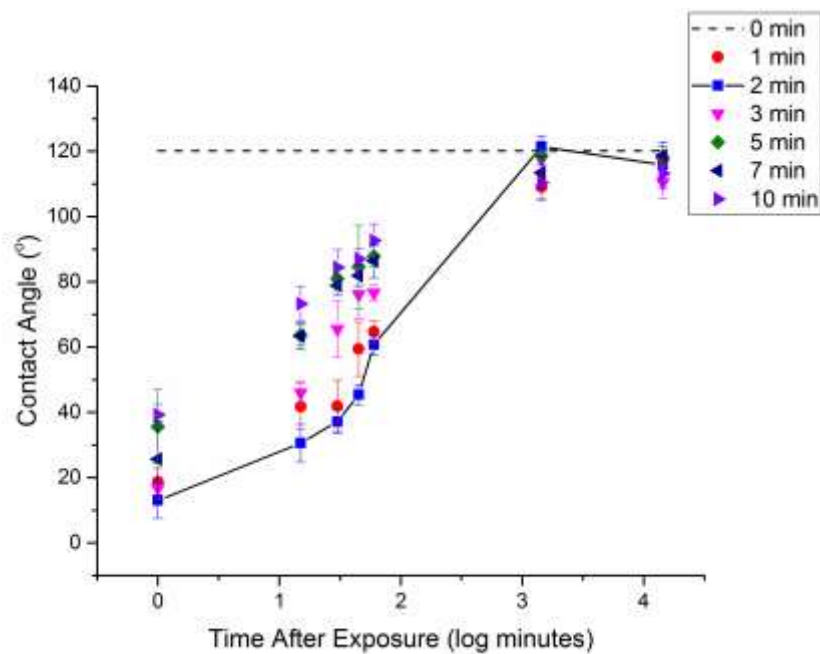


Figure 4.3: Ageing profile of static water contact angle on SE as a function of time after oxygen plasma treatment for different oxygen plasma treatment times.

4.3.2 Wettability: Contact Angle

The average contact angle values after each synthesis step are recorded in Table 4.1. A reduction in contact angle was observed on both substrates following plasma treatment, confirming an increase in wettability as result of surface functionalisation. Upon aminosilanisation, all substrates showed an increase in contact angle: PET-DET3 (90.2°), PET-PTMSPA (88.5°), SE-DET3 (116.6°) and SE-PTMSPA (119.2°). A decrease in contact angles was observed after diazeniumdiolate formation: PET-DET3/NO (79.0°), PET-PTMSPA/NO (81.7°), SE-DET3/NO (108.8°) and SE-PTMSPA/NO (108.6°). This increased wettability may be due to an increased polarity of the $[N(O)NO]^-$ *N*-diazeniumdiolate moiety, as well as decomposition products (NO_2^- and NO_3^-) produced upon the water droplet contacting the surface.

Table 4.1: Static water contact angle measurements of aminosilanised and diazeniumdiolate-tethered PET and SE substrates

	Contact Angle (°)	
	PET	SE
Pristine	88.1±1.0	113.0±2.3
Plasma treated	19.7±1.8	11.0±1.2
DET3	90.2±0.9	116.6±1.8
DET3/NO	79.0±0.4	108.8±2.0
PTMSPA	88.5±0.3	119.2±1.5
PTMSPA/NO	81.7±1.9	108.6±2.8

4.3.3 Surface Chemistry: XPS

The functionalisation of the surface with *N*-diazoniumdiolate groups was followed after each synthesis step by XPS.

PET

The XPS spectra for PET substrates are displayed in Figures 4.4 - 4.6 and the resulting quantitative data recorded in Tables 4.2 and 4.3. The repeat unit of PET is C₁₀H₈O₄. An O/C ratio of 4:10, gives a theoretical at. % of 28.6 for oxygen and 71.4 for carbon.

Curve fitting of the C 1s envelope of PET gave three components: C-C/C-H at 285.0 eV, C-O at 286.5 eV and O-C=O at 288.9 eV. A fourth peak was fitted in the C 1s envelope of PETox at 288.0 eV due to C=O. The peak displayed in the O 1s region was resolved into two components at 532.0 eV and 533.5 eV, due to the carbonyl (O=C) and ether (O-C) constituents of the ester groups, respectively. PET is comprised of two ester groups and so as expected the ratio of the two O 1s components was approximately 1:1. An increase in O=C and decrease in O-C of 12.6 % after oxygen plasma treatment was observed.

Successful immobilisation of aminosilane molecules onto PETox was confirmed by the appearance of peaks in the N 1s and Si 2p envelopes. The peak in the N 1s envelope of PET-DET3 and PET-PTMSPA was curve fitted to give two components, centred at 399.9 eV and 401.1 eV the former due to free amine nitrogen (N-H) and the latter due to positively charged amine nitrogen (N⁺). Two peaks were also resolved when curve fitting the Si 2p envelope. The first at 102.1 eV is assigned to Si-O-Si polymer bridges, the second at 102.7 eV is due to Si-O-C. Tethering of the *N*-diazoniumdiolate was confirmed with the appearance of a third component in the N 1s spectra of PET-DET3/NO and PET-PTMSPA/NO at 402.5 eV.

Table 4.2: XPS-derived at. % of C 1s, O 1s, N 1s and Si 2p regions for PET surfaces.

	at. %			
	C 1s	O 1s	N 1s	Si 2p
PET	73.0±0.4	27.0±0.4	-	-
PETox	66.0±0.2	34.0±0.2	-	-
PET-DET3	56.0±1.1	22.5±0.2	4.7±0.3	16.8±1.3
PET-DET3/NO	57.2±0.3	26.9±0.1	5.7±0.7	10.2±0.4
PET-PTMSPA	61.7±1.1	25.4±0.2	3.3±0.3	9.6±0.6
PET-PTMSPA/NO	59.6±0.6	25.5±0.6	4.5±0.9	10.4±1.4

Table 4.3: XPS-derived at. % of curve-fitted C 1s, O 1s, N 1s and Si 2p components for PETsurfaces.

	at. % (Binding Energy, eV)									
	C 1s					N 1s				
	C-C/C-H (285.0)	β -shifted C (285.7)	C-O (286.6)	C=O (288.0)	O-C=O (289.1)	N-H (399.9)	N+	N-O (402.5)		
PET	59.0±1.0	-	24.4±1.0	-	16.6±0.2	-	-	-	-	-
PETox	41.9±1.1	-	29.6±1.6	6.9±1.2	21.6±0.4	-	-	-	-	-
PET-DET3	59.5±2.0	19.4±1.5	14.4±1.1	2.4±0.4	4.3±0.0	52.0±0.9	48.1±0.9	-	-	-
PET- DET3/NO	15.9±3.8	43.5±1.7	26.6±0.6	3.9±0.6	10.1±1.2	31.6±5.0	34.6±3.1	33.8±1.9	-	-
PET-PTMSPA	22.8±4.2	42.9±4.0	20.5±0.7	2.9±0.4	10.8±1.0	68.7±1.1	31.3±1.2	-	-	-
PET- PTMSPA/NO	30.8±6.8	35.5±4.4	22.0±2.1	3.8±0.3	8.3±0.6	28.1±3.1	36.0±1.5	36.0±1.5	-	-
	O 1s					Si 2p				
	O=C (532.0)			O-C (533.5)		Si-O-Si (102.1)		Si-O-C (102.7)		
PET	46.4±1.3			53.6±1.3		-		-		
PETox	33.8±4.2			66.2±4.2		-		-		
PET-DET3	90.3±1.1			9.7±1.1		33.9±5.2		66.1±5.2		
PET- DET3/NO	69.2±2.6			30.8±2.6		45.8±7.8		54.2±7.8		
PET-PTMSPA	66.9±3.4			29.9±2.6		47.3±0.3		52.7±0.3		
PET- PTMSPA/NO	70.2±2.2			29.8±2.2		48.2±2.7		51.8±2.7		

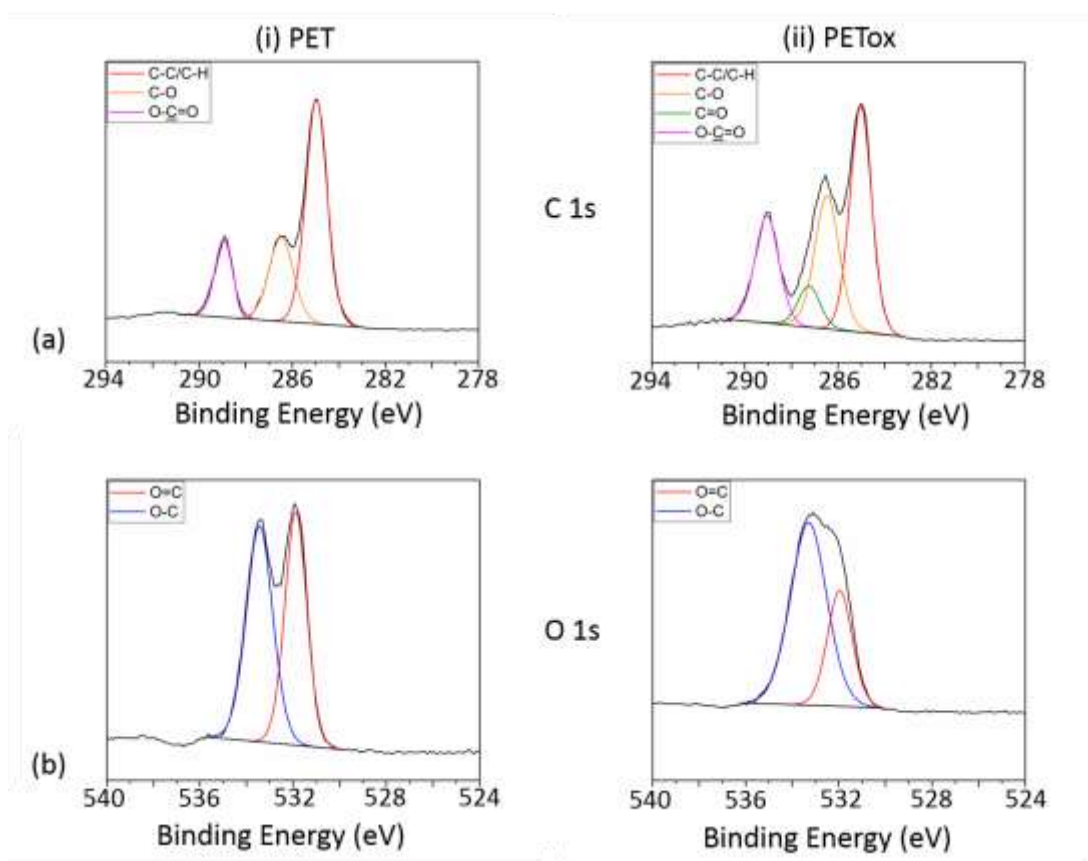


Figure 4.4: Curve fitted (a) C 1s and (b) O 1s XPS spectra for (i) PET and (ii) PETox.

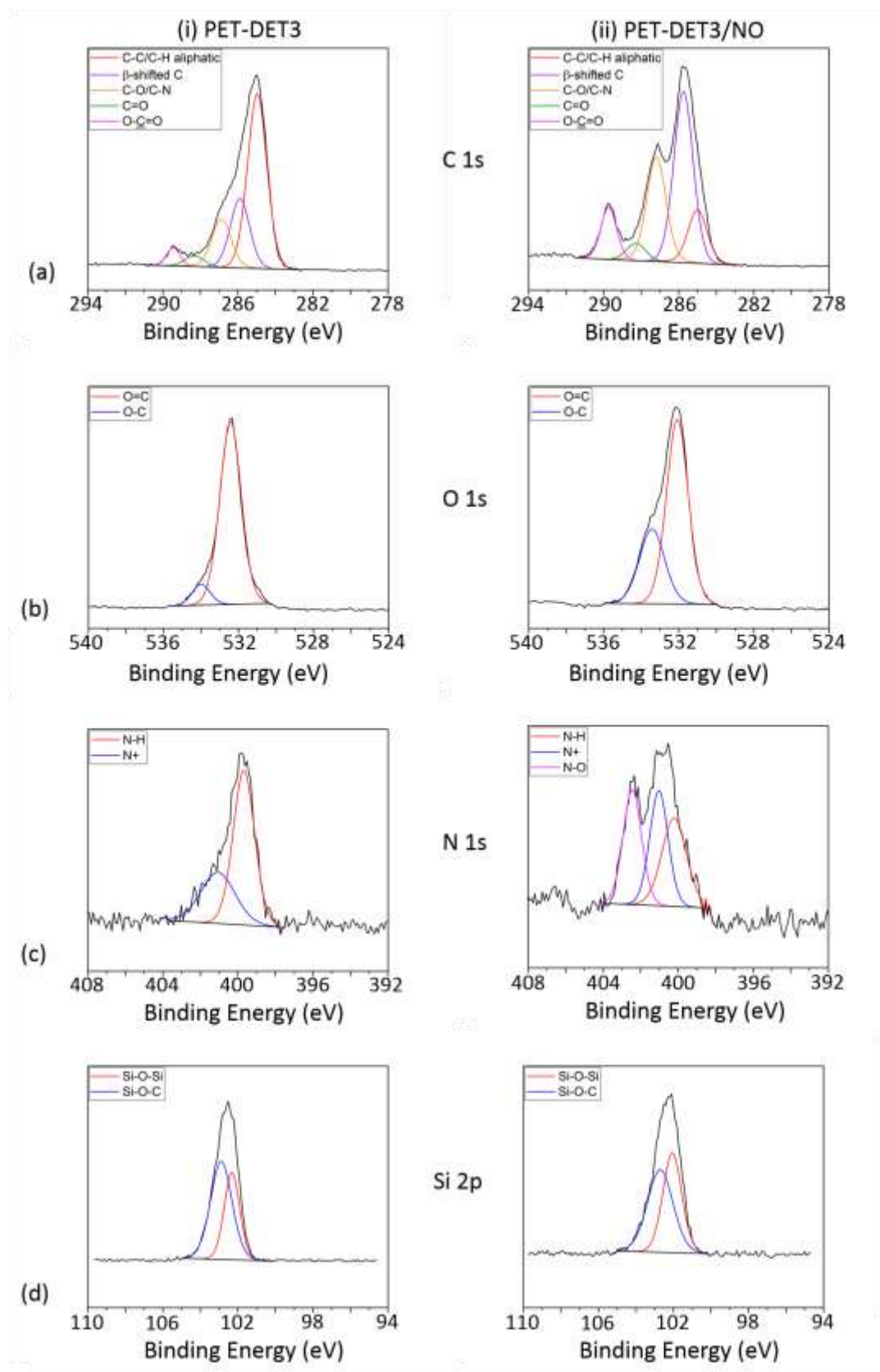


Figure 4.5: Curve fitted (a) C 1s (b) O 1s (c) N 1s and (d) Si 2p XPS spectra for (i) PET-DET3 and (ii) PET-DET3/NO.

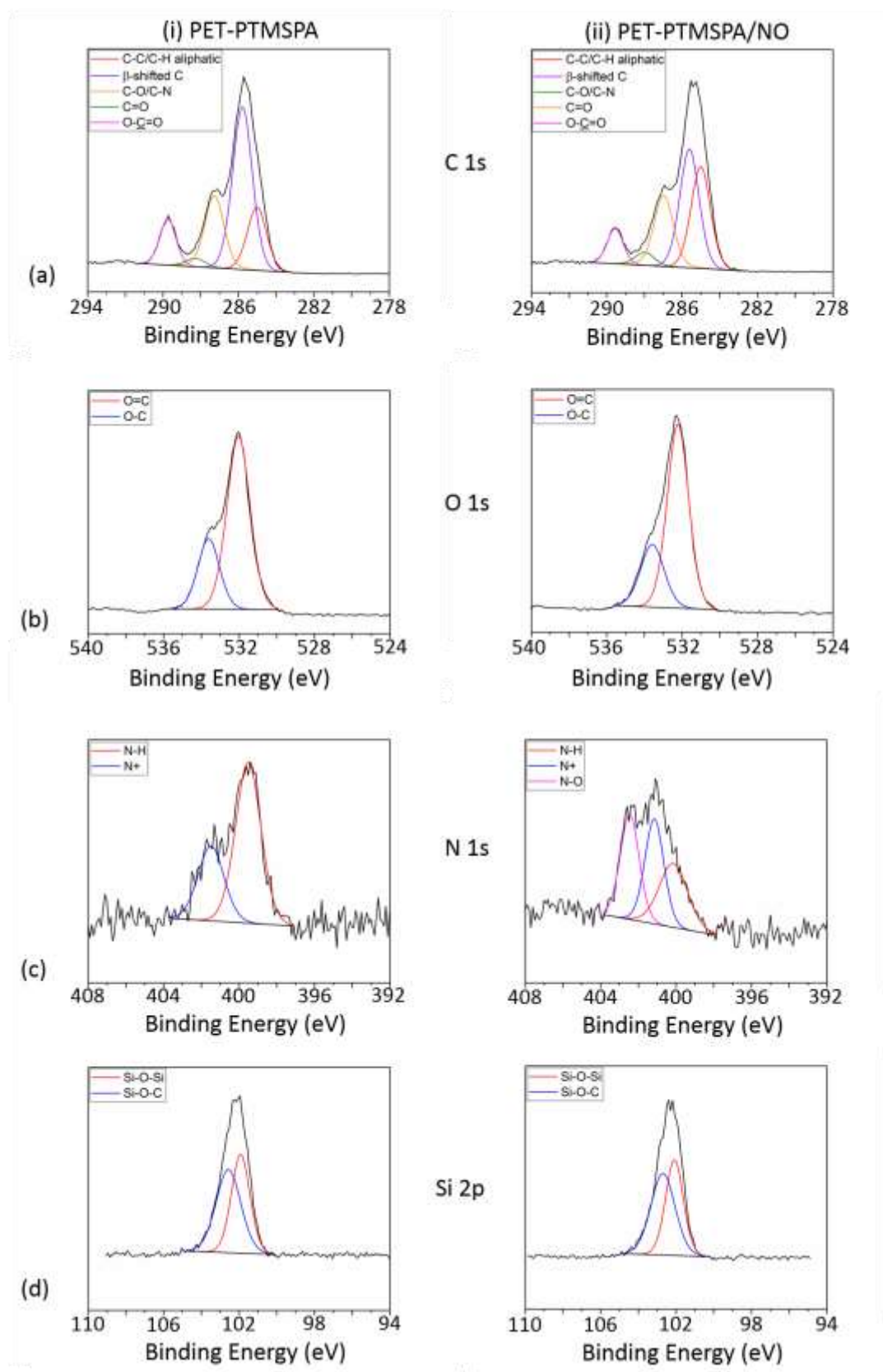


Figure 4.6: Curve fitted (a) C 1s (b) O 1s (c) N 1s and (d) Si 2p XPS spectra for (i) PET-PTMSPA and (ii) PET-PTMSPA/NO.

SE

The XPS spectra for SE substrates are displayed in Figures 4.7 - 4.9 and the resulting quantitative data recorded in Tables 4.4 and 4.5. The C 1s envelope of SE was curve fitted to give one component at binding energy 284.6 eV, characteristic of C-C/C-Si/C-H. The high resolution O 1s spectra was curve fitted to give two peaks: Si-O-Si at 532.2 eV and O-Si-O at 533.1 eV.¹⁹⁰ Four peaks were found after curve fitting the Si 2p envelope: At 102.1 eV, the first peak is attributed to Si-O-Si bridges. The next peak, at 102.7 eV, is characteristic of R₂-Si(O)₂. The third peak is seen at 103.5 eV and is assigned to R-Si(O)₃, and the final peak at 104.1 eV due to Si(O)₄.

After plasma treatment, changes in the XPS spectra indicated the step was successful. There is an increase in the overall at. % of oxygen from 32.3 % to 35.1 %. Peak fitting of the C 1s envelope of SEox showed the presence of four components: C-C/C-Si/C-H at 284.6 eV as present in SE, C-C-O at 285.7 eV, C-O at 286.6 eV and C=O at 288.8 eV. In the Si 2p envelope, a decrease of 19.1 % in the concentration of the Si-O-Si was observed, whilst the other components, where Si is bound to more oxygen atoms, increased.

Similarly to PET, immobilisation of the two aminosilane molecules was confirmed by the introduction of a peak in the N 1s envelope, curve fitted to give N-H and N⁺ peaks. The diazeniumdiolate formation on the surface was confirmed by a third peak in the N 1s envelope fitted at 402.5 eV due to N-O.

Table 4.4: XPS-derived at. % of C 1s, O 1s, N 1s and Si 2p regions for SE surfaces.

	at. %			
	C 1s	O 1s	N 1s	Si 2p
SE	38.2±1.5	32.2±1.2	-	29.6±0.3
SEox	35.4±1.5	35.1±1.6	-	29.6±0.5
SE-DET3	41.3±1.2	28.4±1.0	3.7±0.5	26.6±0.7
SE-DET3/NO	33.8±0.9	35.1±0.7	2.4±0.2	29.4±0.7
SE-PTMSPA	40.5±1.5	30.0±1.3	1.8±0.0	27.7±0.3
SE-PTMSPA/NO	37.1±0.4	33.4±0.4	1.6±0.1	28.0±0.0

Table 4.5: XPS-derived at. % of curve-fitted C 1s, O 1s, N 1s and Si 2p components for SE surfaces.

	at. % (Binding Energy, eV)						
	C 1s				N 1s		
	C-C/C-Si (284.6)	β -shifted C C-C-O ^a (285.7)	C-O (286.6)	C=O (288.0)	N-H (399.9)	N+ (401.1)	N-O (402.5)
SE	100±0.0	-	-	-	-	-	-
SEox	68.8±5.3	20.9±5.8 ^a	5.4±2.2	4.9±0.4	-	-	-
SE-DET3	67.4±1.1	21.1±1.1	11.5±0.8	-	54.8±3.2	45.2±3.2	-
SE-DET3/NO	71.9±0.9	16.7±1.1	11.4±0.9	-	39.3±0.2	30.4±0.1	30.4±0.1
SE-PTMSPA	76.9±0.8	15.5±1.5	7.6±0.8	-	58.0±4.6	42.0±4.6	-
SE- PTMSPA/NO	75.8±3.4	16.2±3.4	8.0±0.4	-	43.8±4.5	28.1±2.2	28.1±2.2
	Si 2p				O 1s		
	Si-O-Si (102.1)	R ₂ -Si(O) ₂ (102.7)	R-Si(O) ₃ (103.5)	Si(O) ₄ (104.1)	Si-O-Si (532.2)		O-Si-O (533.1)
SE	45.4±6.7	19.7±4.3	18.1±3.2	16.9±3.3	52.0±4.5		48.0±4.5
SEox	26.3±4.0	28.2±2.9	21.8±2.8	23.7±3.9	38.2±2.5		61.8±2.5
SE-DET3	38.5±9.4	32.7±10.3	21.0±8.1	8.0±5.0	93.2±2.3		6.8±2.3
SE-DET3/NO	30.2±3.4	30.2±1.0	24.4±0.9	15.2±4.1	67.5±2.9		32.6±2.9
SE-PTMSPA	42.5±1.7	27.4±4.9	20.7±5.3	11.4±2.0	60.6±9.0		39.4±9.0
SE- PTMSPA/NO	33.2±3.8	30.5±0.5	22.3±1.8	14.1±5.8	61.6±4.2		38.4±4.2

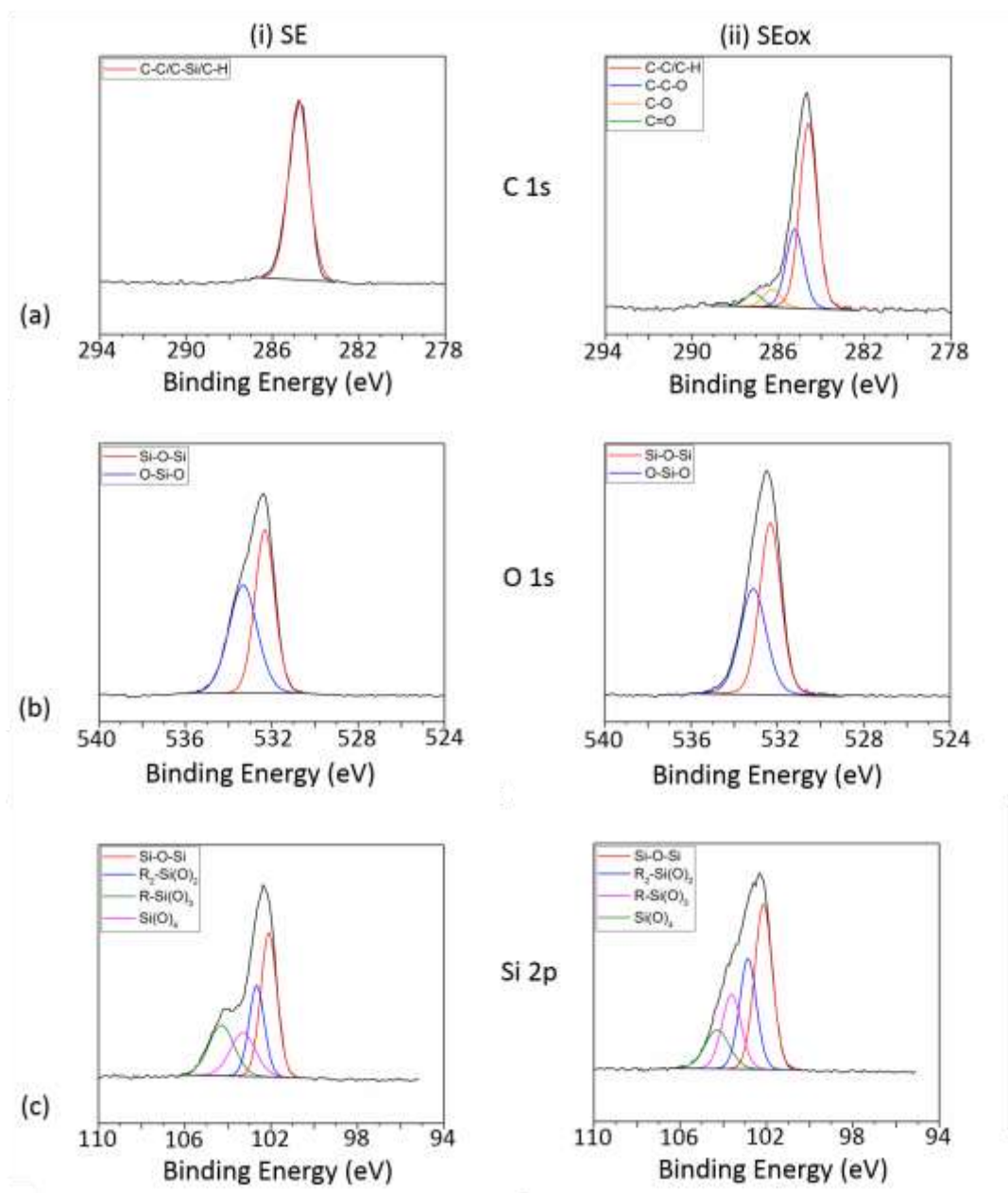


Figure 4.7: Curve fitted (a) C 1s (b) O 1s and (c) Si 2p XPS spectra for (i) SE and (ii) SEox.

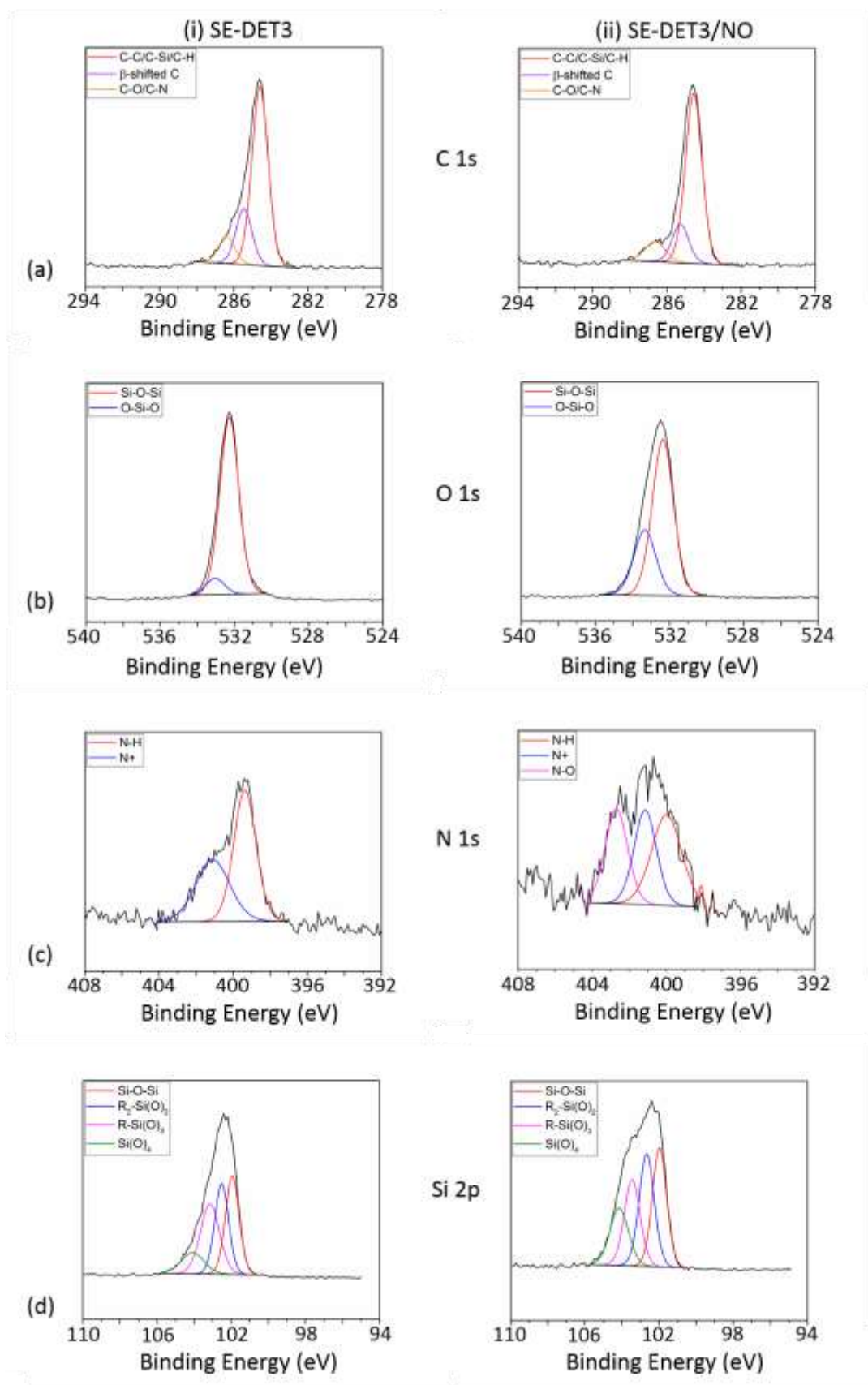


Figure 4.8: Curve fitted (a) C 1s (b) O 1s (c) N 1s (d) Si 2p XPS spectra for (i) SE-DET3 and (ii) SE-DET3/NO.

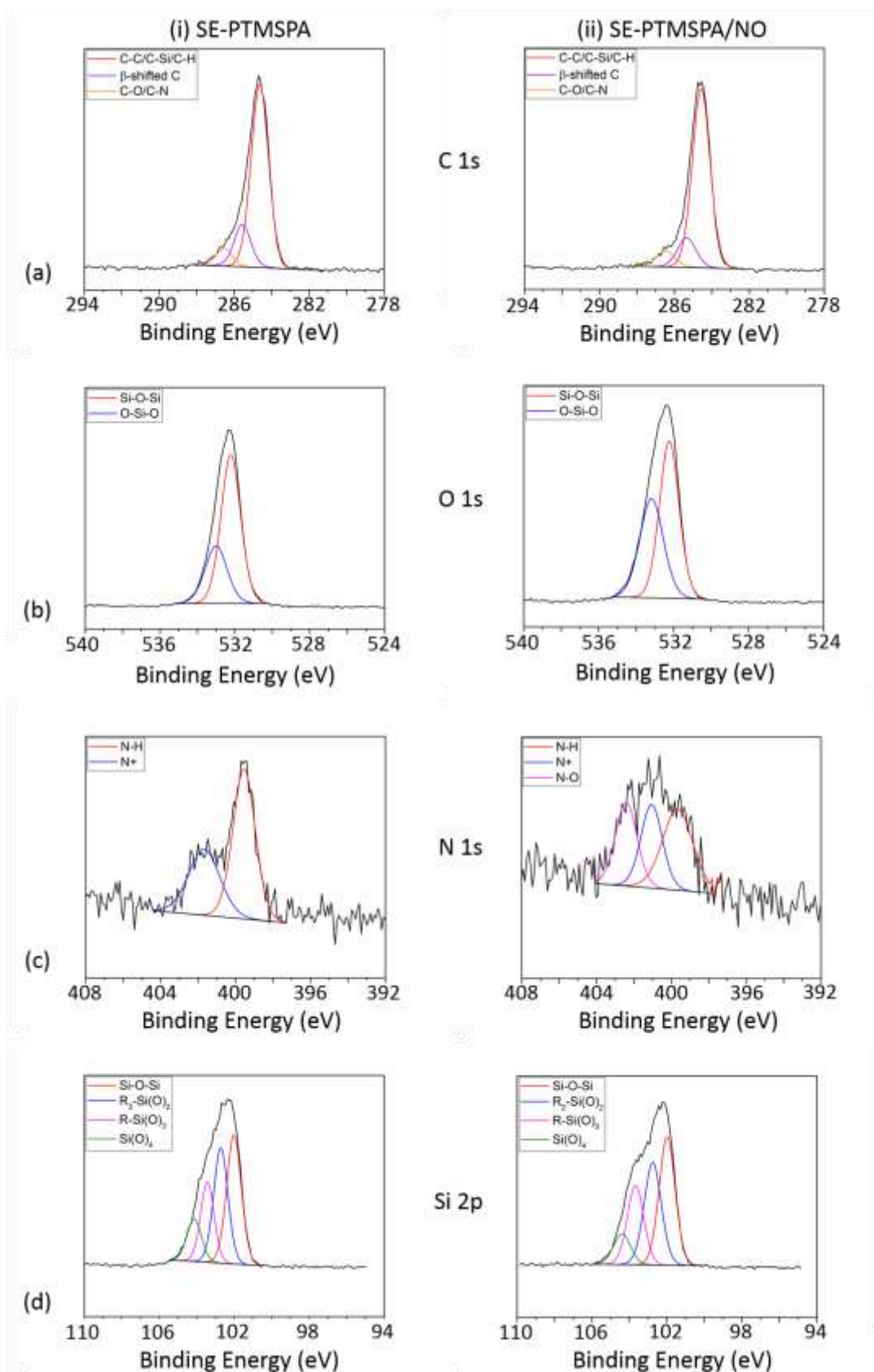


Figure 4.9: Curve fitted (a) C 1s (b) O 1s (c) N 1s (d) Si 2p XPS spectra for (i) SE-PTMSPA and (ii) SE-PTMSPA/NO.

4.3.4 Surface Topography: AFM

PET

The surface topography and roughness of PET, PETox, PET-DET3, PET-DET3/NO, PET-PTMSPA and PET-PTMSPA/NO surfaces were assessed using AFM. Representative images and corresponding root mean square roughness (Rq) and average roughness (Ra) values are displayed in Figure 4.10. The roughness values of pristine PET (Rq = 5.0 nm and, Ra = 3.2 nm) indicate a fairly smooth topography. After plasma treatment, an increase in roughness was observed for PETox (Rq = 14.3 nm, Ra = 8.0 nm), indicating that the surface underwent plasma-induced etching. After aminosilanisation, a decrease in roughness was seen for PET-DET3 (Rq = 4.5 nm, Ra = 3.2 nm) in comparison to PETox. A large variation in roughness values across samples was observed for PET-PTMSPA. This is thought to be due to the ease in which aminosilanes form inhomogeneous layers when silanisation is carried out through solution phase deposition.¹⁹¹ A decrease in roughness was seen for PET-DET3/NO (Rq = 2.9 nm, Ra = 2.0 nm) and PET-PTMSPA/NO (Rq = 2.6 nm, Ra = 1.6 nm) in comparison to aminosilanised surfaces.

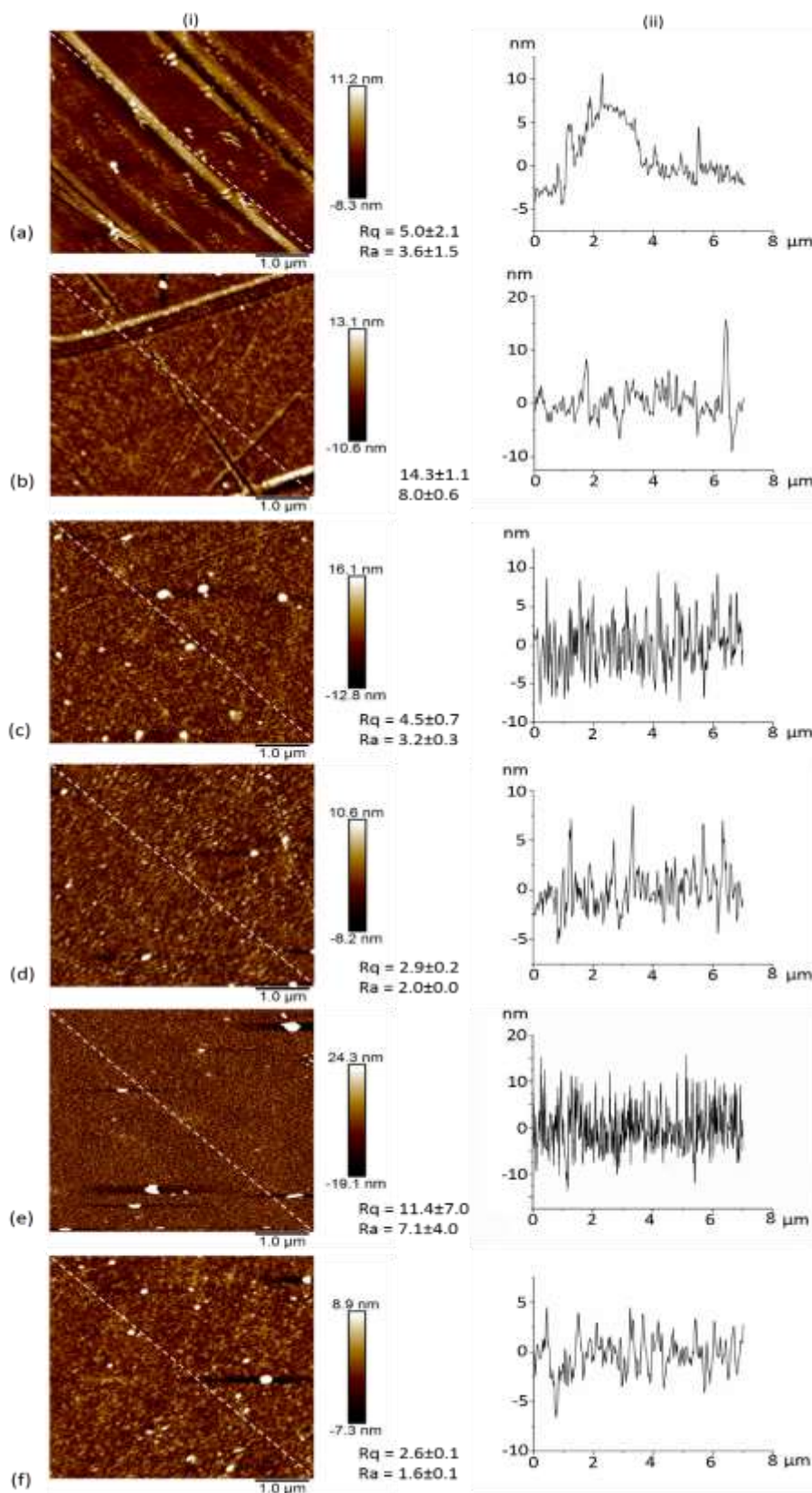


Figure 4.10: AFM 3D images ($5 \times 5 \mu\text{m}^2$) and corresponding depth profiles of (a) PET (b) PETox (c) PET-DET3 (d) PET-DET3/NO (e) PET-PTMSPA and (f) PET-PTMSPA/NO. Rq and Ra values are given in nm.

SE

The surface topography and roughness of SE, SEox, SE-DET3, SE-DET3/NO, SE-PTMSPA and SE-PTMSPA/NO surfaces were assessed using AFM. Representative images and corresponding root mean square roughness (Rq) and average roughness (Ra) values are displayed in Figure 4.11. Pristine SE has roughness values of Rq = 29.3 nm, Ra = 23.0 nm. After plasma treatment, large cracks in the polymer could be seen (Figure 4.11 b). This is consistent with the literature in which SE forms a brittle, inorganic silica outer layer, susceptible to cracking after oxygen plasma treatment.¹⁹²⁻¹⁹⁷ No significant difference ($p < 0.05$) in surface roughness was observed after aminosilanisation and diazeniumdiolate formation, however a less uniform array of peaks and troughs can be seen when compared to pristine SE. This is due to agglomerates of aminosilane which have self-assembled on the surface.¹⁹⁸

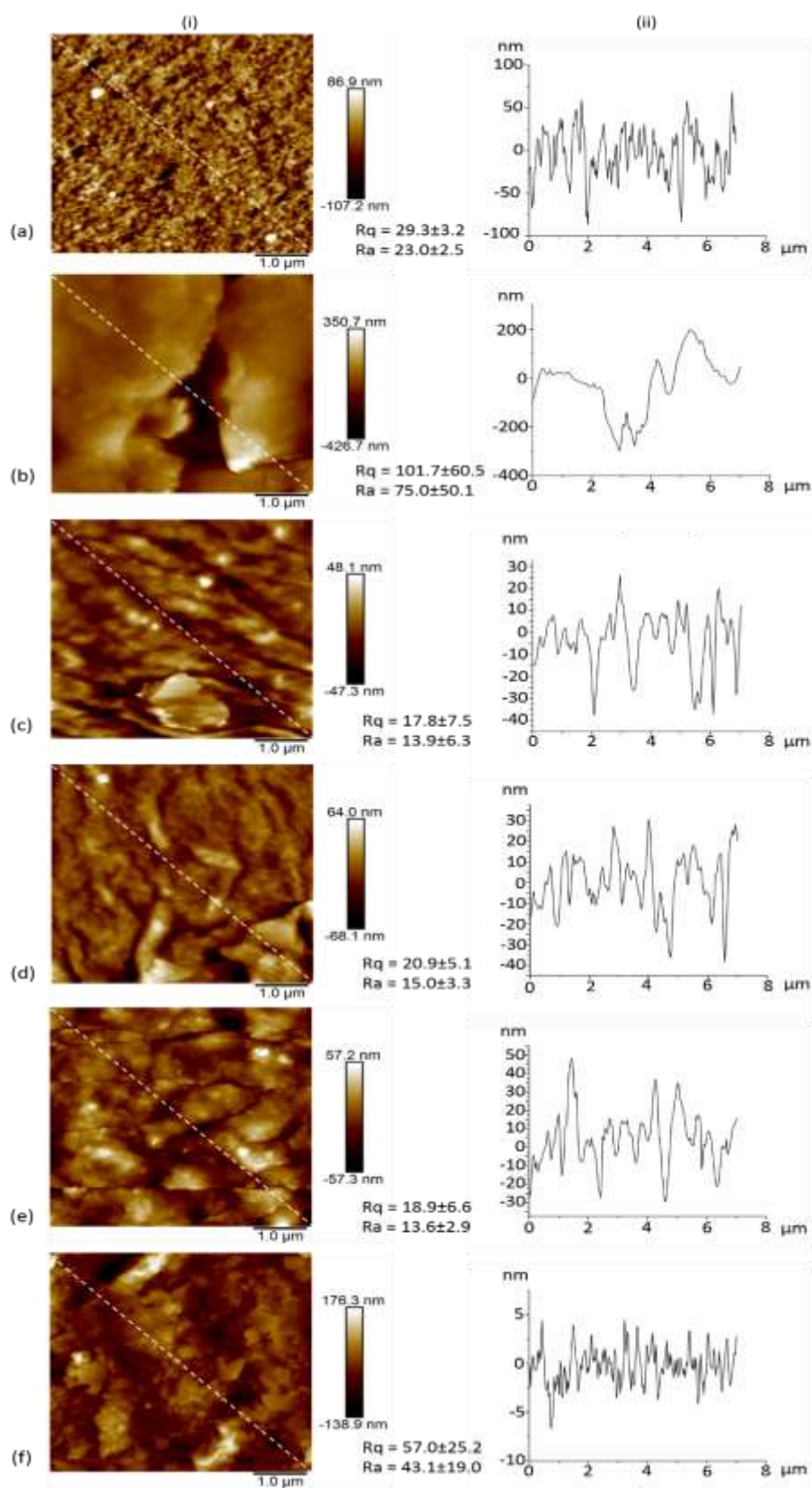


Figure 4.11: AFM 3D images ($5 \times 5 \mu\text{m}^2$) and corresponding depth profiles of (a) SE (b) SEox (c) SE-DET3 (d) SE-DET3/NO (e) SE-PTMSPA and (f) SE-PTMSPA/NO. Rq and Ra values are given in nm.

4.3.5 NO Release: Chemiluminescent Detection

PET

NO release was monitored for PET-DET3/NO and PET-PTMSPA/NO at ambient temperature (25 °C) in real time *via* chemiluminescence at pH 4 and pH 7.4 shown in Figures 4.12 and 4.13, respectively, and NO release data is presented in Table 4.6. At pH 4, PET-DET3/NO exhibited an average maximum release of $0.42 \mu\text{M s}^{-1}$ of NO after 2.5 hrs. After this the rate of NO release decreased. A total release of 453 μmol was observed after 17 hrs. At pH 7.4, the NO release of PET-DET3/NO reached an average peak of between $0.17 \mu\text{M s}^{-1}$ in just under 3 hours. This remained constant for approximately 5 hrs, before a descent back to base levels of NO. The total NO released was 177 μmol after 12 hrs.

At pH 4, PET-PTMSPA/NO exhibited an initial NO release peaking at $0.31 \mu\text{M s}^{-1}$ after 5 hrs and a total release of 289 μmol after 22 hrs. At pH 7.4, PET-PTMSPA/NO released a maximum of $0.07 \mu\text{M s}^{-1}$ and a total of 44 μmol after 10 hrs.

Table 4.6: NO release data for PET-DET3/NO and PET-PTMSPA/NO at pH 4 and 7.4

	Max NO release ($\mu\text{M s}^{-1}$)	Max NO Release ($\mu\text{M s}^{-1} \text{cm}^{-2}$)	Total NO release (μmol)	Total NO release ($\mu\text{mol cm}^{-2}$)
PET-DET3/NO (pH 4)	0.42 ± 0.18	0.19 ± 0.08	453 ± 95	201 ± 42
PET-DET3/NO (pH 7.4)	0.17 ± 0.05	0.08 ± 0.02	177 ± 5	79 ± 2
PET-PTMSPA/NO (pH 4)	0.31 ± 0.13	0.14 ± 0.16	289 ± 49	129 ± 22
PET-PTMSPA/NO (pH7.4)	0.07 ± 0.03	0.03 ± 0.01	44 ± 2	20 ± 1

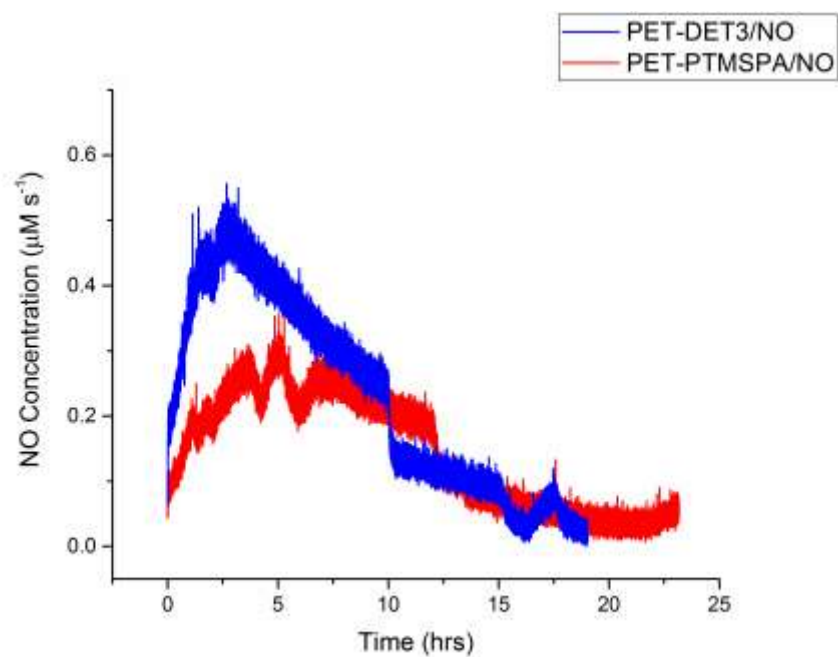


Figure 4.12: NO release profiles for *N*-diazeniumdiolate-tethered PET at pH 4 determined by chemiluminescence detection.

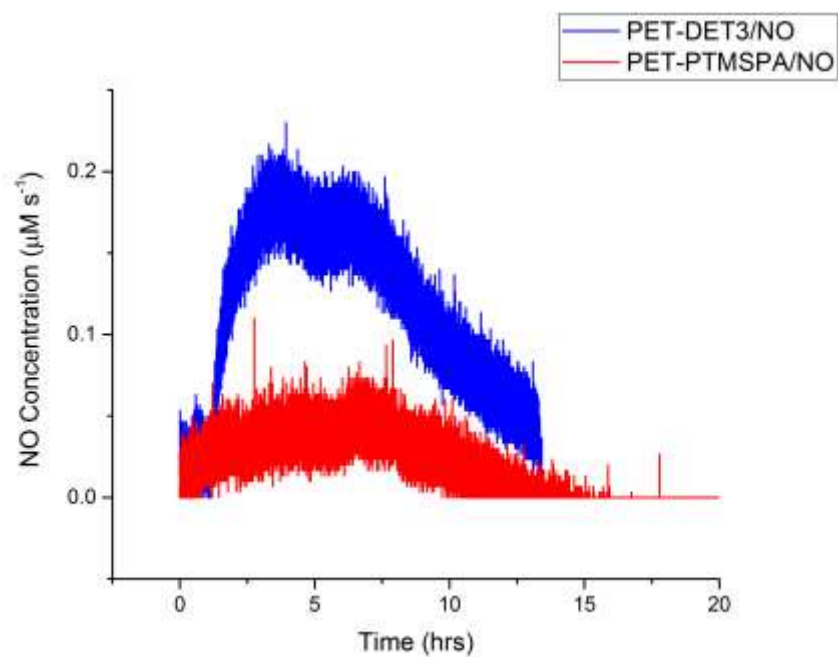


Figure 4.13: NO release profiles for *N*-diazeniumdiolate-tethered PET at pH 7.4 determined by chemiluminescence detection.

SE

NO release was monitored for SE-DET3/NO and SE-PTMSPA/NO at ambient temperature (25 °C) in real time *via* chemiluminescence detection at pH 4, and pH 7.4 shown in Figures 4.14 and 4.15, respectively and NO release data is presented in Table 4.7. At pH 4, a burst release of NO to a maximum of $3.37 \mu\text{M s}^{-1}$ after 18 mins was observed for SE-DET3/NO with 536 μmol released after 7 hrs. At pH 7.4 a more prolonged release was observed. A maximum NO release of $0.31 \mu\text{M s}^{-1}$ and total release of 184 μmol after 14 hrs was observed.

At pH 4 burst release was also seen for SE-PTMSPA/NO in which a maximum NO concentration of $0.49 \mu\text{M s}^{-1}$ was released after 6 mins and a total of 212 μmol NO after 8 hrs. At pH 7.4, steady releases of NO were observed reaching a maximum of $0.36 \mu\text{M s}^{-1}$ and releasing 115 μmol over 11 hrs.

Table 4.7: NO release data for SE-DET3/NO and SE-PTMSPA/NO at pH 4 and 7.4.

	Max NO release ($\mu\text{M s}^{-1}$)	Max NO Release ($\mu\text{M s}^{-1} \text{cm}^{-2}$)	Total NO release (μmol)	Total NO release ($\mu\text{mol cm}^{-2}$)
SE-DET3/NO (pH 4)	3.37±0.80	1.50±0.36	536±38	238±17
SE-DET3/NO (pH 7.4)	0.31±0.07	0.14±0.03	184±7	82±3
SE-PTMSPA/NO (pH 4)	0.49±0.04	0.22±0.02	212±4	94±2
SE-PTMSPA/NO (pH 7.4)	0.36±0.15	0.17±0.07	115±29	51±13

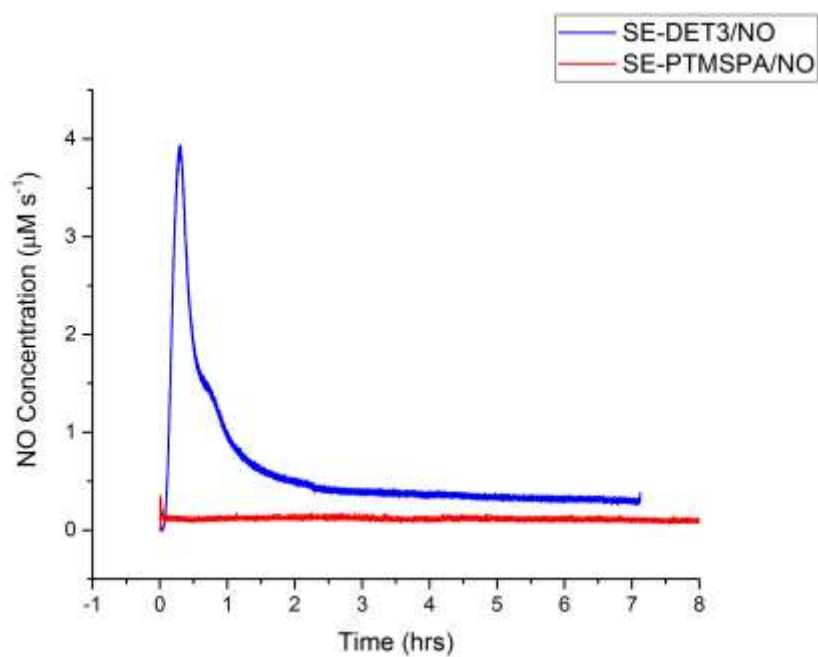


Figure 4.14: NO release profiles for *N*-diazeniumdiolate-tethered SE at pH 4 determined by chemiluminescence detection.

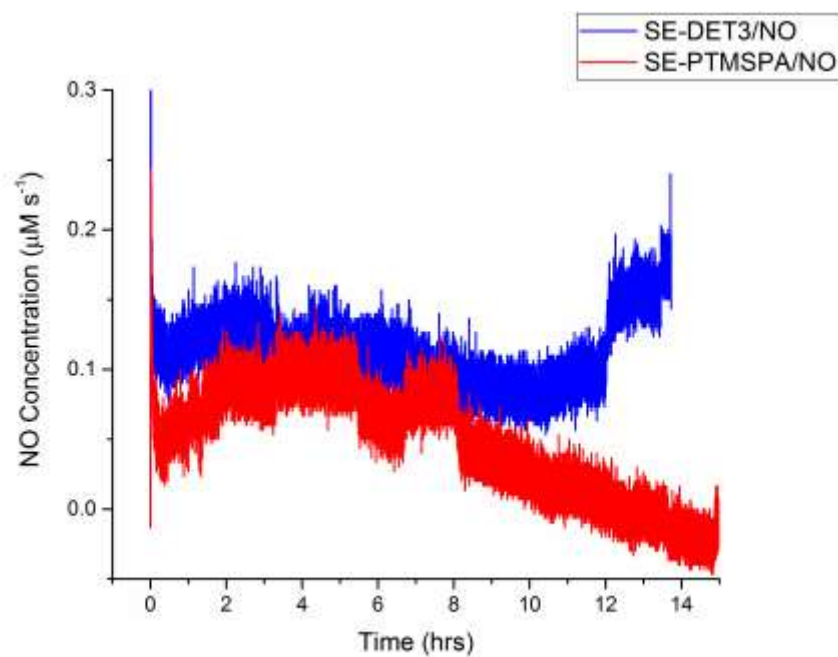


Figure 4.15: NO release profiles for *N*-diazeniumdiolate-tethered SE at pH 7.4 determined by chemiluminescence detection.

4.3.6 Bacterial Response

Antibacterial activity was investigated by carrying out an adhered cell colony forming unit (CFU) assay against *P. aeruginosa*, lab strain PA14. Surfaces were inoculated with bacterial solution for 24 hrs to allow cell adhesion and biofilm formation. Planktonic bacteria was washed away and remaining viable bacteria on the surface were counted to test the efficacy of the NO-releasing surfaces against cell adhesion and in biofilm prevention. The results are given in Figures 4.16 and 4.17 for PET and SE, respectively. For all NO-releasing materials, a statistically significant ($p < 0.05$) reduction in CFU count, compared to pristine, plasma and corresponding silane-tethered control substrates demonstrated that all NO-releasing polymers are capable of preventing formation of *P. aeruginosa* biofilms. No significant difference was observed between any control groups ($p > 0.05$). Specifically, in the case of PET-DET3/NO and PET-PTMSPA/NO, 83 % and 62 % reductions in viable adhered cells were observed, respectively, compared to pristine, plasma-treated and corresponding silane-tethered control surfaces. Likewise, for SE-DET3/NO and SE-PTMSPA/NO, 92 % reduction was observed for both, compared to pristine, plasma-treated and corresponding silane-tethered control surfaces.

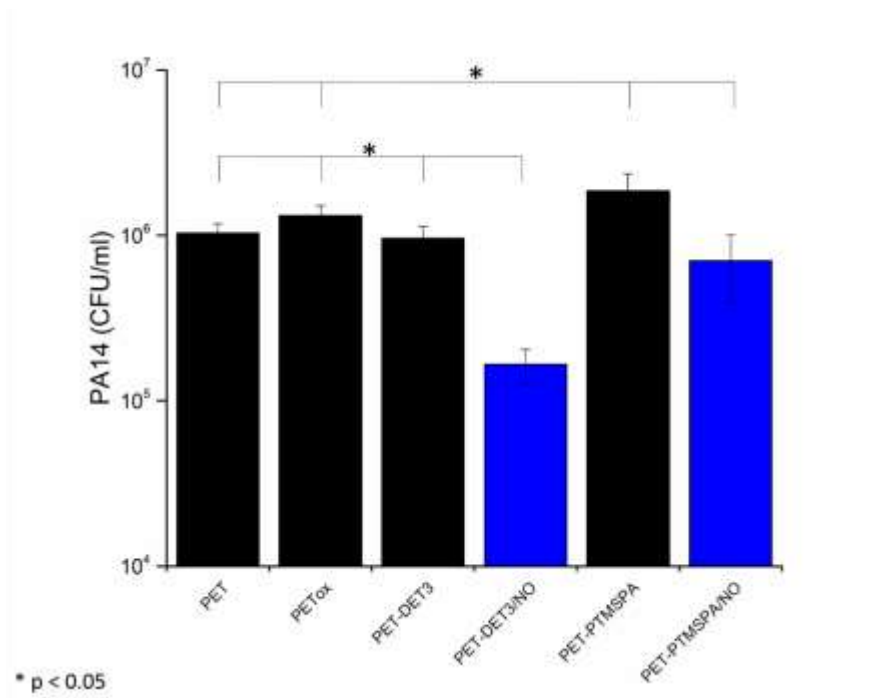


Figure 4.16: Viable adhered PA14 cell counts (CFU/ml) after 24 hrs on PET substrates. Black bars indicate control surfaces; blue bars indicate NO-releasing surfaces.

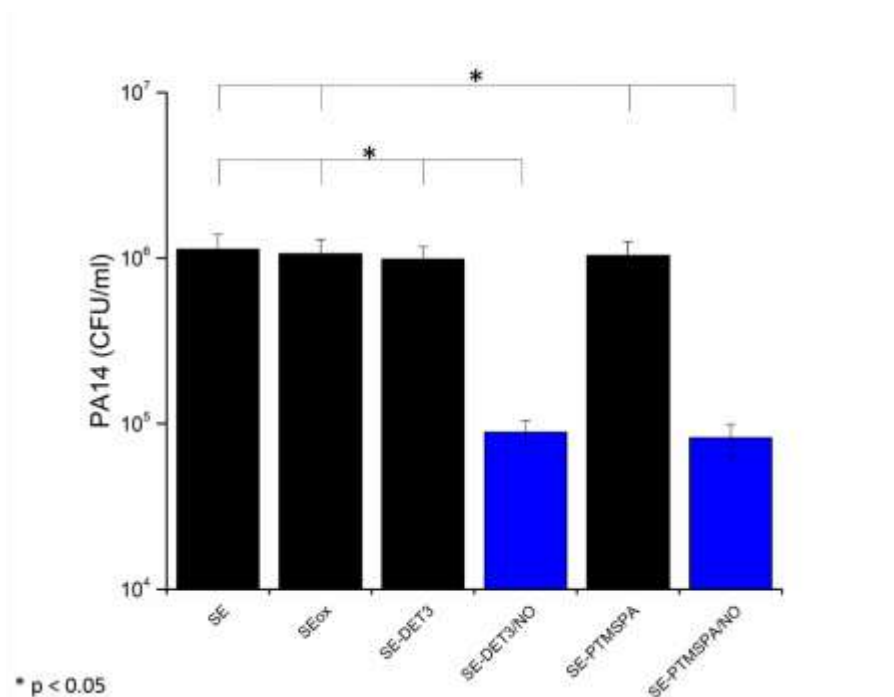


Figure 4.17: Viable adhered PA14 cell counts (CFU/ml) after 24 hrs on SE substrates. Black bars indicate control surfaces; blue bars indicate NO-releasing surfaces.

4.4 Discussion

4.4.1 Oxygen Plasma Treatment of Polymeric Surfaces

Plasma treatment is a useful tool in activating hydrophobic and inert polymers to allow for addition of oxidative functional groups which can then be used to conjugate molecules of interest. After optimum plasma treatment times, contact angles were measured to be 19.7° and 11.0° for PET and SE, respectively. A reduction in contact angle is the cause of an increased wettability of the surface due to the presence of oxygen functionalities. By using XPS data combined with studies found within the literature two feasible mechanisms for oxidation of the polymers have been described below.

PET

Alteration in the surface chemistry of PET after plasma treatment was confirmed by a reduction in the contact angle from 88.1° before treatment to 19.7°. In the XPS C 1s spectra, the contribution of aromatic C-C/C-H decreased, whilst the O- $\underline{\text{C}}\text{H}_2\text{CH}_2$ (C-O) and O= $\underline{\text{C}}\text{-O}$ (C=O) contributions increased. This corroborated the mechanism outlined by Gonzalez *et al.*¹⁹⁹ in which oxygen functionality is induced on the phenyl ring.

SE

An alteration in the surface chemistry of SE after plasma treatment was first confirmed through contact angle. A change from 113.0° to 11.0° indicated an increase in the hydrophilicity post treatment. Smith and Owen outlined a mechanism for plasma treatment of polydimethylsiloxane (PDMS) surfaces in which the methyl carbons become oxidised; however, were unable to distinguish between C-OH and CH₃ in the C 1s envelope from their XPS data.¹⁹⁴ In this work a distinction could be made with the C 1s envelope being resolved into two peaks with a shoulder at a greater binding energy showing oxidation of carbon.

Morra *et al.*¹⁹³ reported the preference of plasma species to interact with silicon atoms; the Si 2p envelope of the untreated polydimethylsiloxane (PDMS) could be fitted into two peaks, with the small shoulder at a higher binding energy corresponding to Si bound to 3 O atoms. After plasma treatment the peak shape

changed so that the relative intensity was reversed with the more oxidised silicon displaying a greater relative contribution to the envelope.

In this present work, although the Si 2p peak shapes were not analogous to those seen by Morra¹⁹³, the same conclusion could be drawn. The reason behind the differences observed is most likely due to the difference in the degree of polymerisation of the materials used. The work carried out by Morra employed native PDMS polymers, whilst in this work elastomers were used as the substrate. Elastomers are the product of largely cross-linked PDMS chains with a greater degree of polymerisation and this explains why it is possible to resolve the Si 2p envelope of untreated SE into four. After plasma treatment the relative contribution of the peaks at the higher binding energies, corresponding to Si atoms bound to multiple oxygens all increased at the expense of the Si-O-Si contribution. Furthermore, the relative contribution of the O-Si-O group in the O 1s spectra increases as Si-O-Si decreases, further supporting the notion that Si atoms are the preferred choice of plasma attack. The ageing profile of SE in Figure 4.3, supports the highly reported phenomenon that the polymer recovers back to its native hydrophobicity after plasma treatment.¹⁹²⁻¹⁹⁷ Complete hydrophobic recovery of SE is seen 1 day after treatment.

There are several possible explanations for hydrophobic recovery. Owen and Smith hypothesised that plasma-induced hydrophilic surface groups reorient towards the bulk. They also stated that migration of treated polymer chains into the bulk and untreated chains to the surface are other possible mechanisms for hydrophobic recovery.^{194, 196} Lee and Homan reported that condensation of the surface silanol groups eliminated hydroxyl species.²⁰⁰

Additionally, the formation of a thin, brittle, inorganic silica-like surface layer prone to cracking is also a factor in the recovery mechanism.^{194, 196, 197, 201} These cracks allow a pathway from the bulk to the surface, in which untreated low molecular weight (LMW) chains can migrate to the surface. Toth *et al.*²⁰² concluded that this mechanism accounts for roughly two thirds of the recovery, whilst reorientation of polar groups plays a less extensive role. A schematic diagram of the different regions in plasma treated silicone elastomer has been displayed in Figure 4.18.

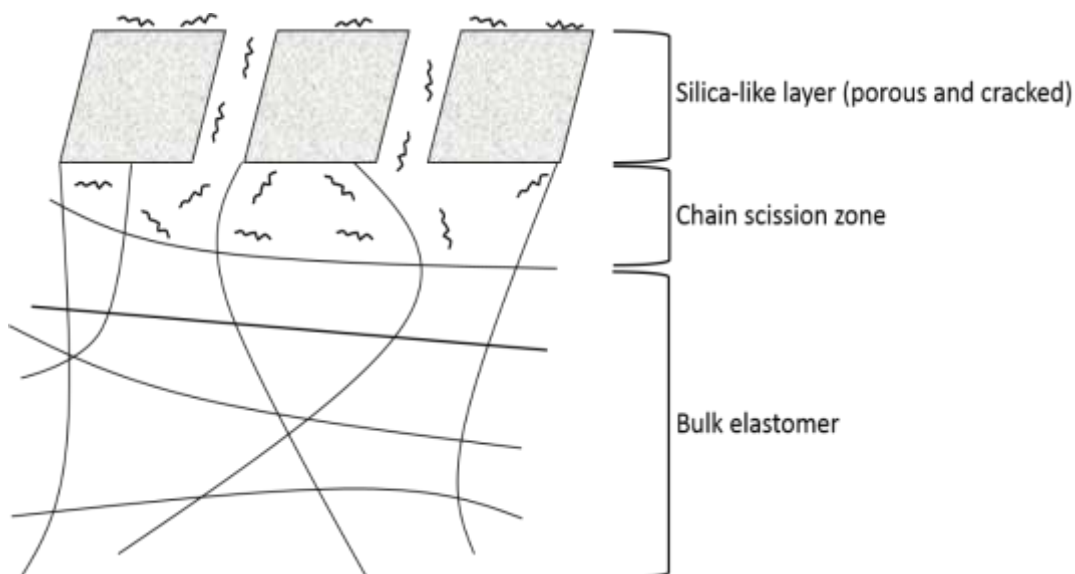


Figure 4.18: A schematic representation of the different regions in plasma treated SE. The pores and cracks in a silica-like top layer allows LMW untreated components to migrate to the surface, whilst treated polymer chains can migrate to the bulk.

4.4.2 *N*-Diazeniumdiolate Formation and NO Release

In this chapter, the aim was to determine whether aminosilane linkers could be used to facilitate *N*-diazeniumdiolate formation on the surface and the NO release profile could be controlled by the nature of this aminosilane precursor.

In these experiments, it was clear that the structure of the aminosilane used had an effect on the flux and payload of NO released. DET3 is an aminosilane that contains three amines (2 secondary, 1 primary), which can all act as an anchor point for *N*-diazeniumdiolate formation. The PTMSPA molecules contain only one secondary amine (in aniline form) that can act as a potential site for *N*-diazeniumdiolate formation. At pH 4, the initial burst release for SE-DET3/NO is 7 times more concentrated than SE-PTMSPA/NO and total NO release approximately 4.5 times greater. For PET-DET3/NO, the maximum NO release is comparable to PET-PTMSPA/NO but the total NO release is approximately 1.5 times greater. At pH 7.4, PET-DET3/NO and SE-DET3/NO released more NO over a longer period of time than PET-PTMSPA/NO and SE-PTMSPA/NO, respectively. These results highlight the pH-dependency for NO release of the *N*-diazeniumdiolates, depending on the aminosilane precursor used.

The acid dissociation constant (K_a) is a quantitative measure in determining the strength of an acid (HA) through its ability to dissociate into a proton (H^+) and conjugate base (A^-), as shown in Equation 4.1.

$$K_a = \frac{[H^+][A^-]}{[HA]} \quad (4.1)$$

The Henderson-Hasselbach equation can be derived from the acid dissociation equation (Eq. 4.2) as:

$$pH = pK_a + \log_{10} \frac{[A^-]}{[HA]} \quad (4.2)$$

which can be rearranged to give:

$$10^{pH-pK_a} = \frac{[A^-]}{[HA]} \quad (4.3)$$

From Equation 4.3 it can be seen that when $pH = pK_a$, $[A^-] = [HA]$. Therefore when $pH > pK_a$, the concentration of deprotonated species is greater than protonated species. Vice versa, when $pH < pK_a$, a larger concentration of the compound would be in its protonated form than deprotonated form.

McIntyre and co-workers²⁰³ reported the pK_a values of diethylenetriamine (the precursor molecule to DET3) to be 9.7, 8.6 and 3.6 at 30 °C. The PTMSPA precursor is an aniline-containing compound, in which the amine nitrogen has a pK_a of 4.6.²⁰⁴ In DET3, two of the three acid dissociation constants are larger than both pH values (pH 4 and 7.4) used in these experiments. This would suggest that a larger concentration of the amines in the *N*-diazoniumdiolate undergo protonation leading to quicker decomposition and NO release. The lower pK_a of PTMSPA indicates that the aniline nitrogen is less basic than two of the three amines in DET3, which would suggest protonation is relatively more difficult. Prolonged NO release by DET3/NO can be attributed to intramolecular amine molecules acting as counter ions and stabilising the *N*-diazoniumdiolate moieties. The increased NO payload of DET3/NO surfaces is due to increased number of amines in these molecules.

4.4.3 Bacterial Response

One estimation by the National Institutes of Health (NIH) is that 80 % of all chronic infections are biofilm associated and that 65 % of all microbial infections are, in some way, due to biofilm growth. There are a multitude of effective antibacterial strategies against planktonic cells that often do not translate in terms of their efficacy when tested against biofilms.²⁰⁵ In this chapter the bacterial response of the NO-releasing *N*-diazoniumdiolate-tethered polymeric substrates was tested against persistent cultures of a lab strain of *P.aeruginosa* (PA14) grown over the surfaces for a 24 hr incubation period.

A number of studies have reported on NO-mediated biofilm formation and dispersal of *P. aeruginosa*.^{104, 206-208} Barraud *et al.* utilised sodium nitroprusside (SNP) NO donors to exogenously produce low-level, non-toxic concentrations of NO.¹⁰⁴ Pre-established 1-day old biofilms were treated with 0.5 nM NO for 24 hrs and cell detachment and dispersal from the surface was observed, resulting in an 80 % reduction in biofilm surface coverage. Darling *et al.* showed that the adherence of *P. aeruginosa* cells was reduced up to 72 % in cystic fibrosis (CF) epithelial cells when the cells were transfected with iNOS;²⁰⁷ an endogenously produced enzyme that facilitates NO production from L-arginine.

All four *N*-diazoniumdiolated surfaces, PET-DET3/NO, PET-PTMSPA/NO, SE-DET3/NO and SE-PTMSPA/NO showed a reduction in cell counts after 24 hrs. The surfaces were washed in PBS to remove any planktonic bacteria floating on the surface, making the cell count specific to surface-adhered cells. SE-DET3/NO and SE-PTMSPA/NO showed > 1 log reduction in cell counts of PA14 after 24 hrs, whilst PET-DET3/NO and PET-PTMSPA/NO exhibited 83 % and 62 % reduction in cell counts, respectively. SE-DET3/NO released comparable amounts of NO over the period of analysis compared with SE-PTMSPA/NO, which would explain the equal reductions in cell counts for both surfaces. The increased performance of PET-DET3/NO compared to PET-PTMSPA/NO was most likely due to the difference in total NO release with PET-DET3/NO releasing 133 μmol NO more over the period of analysis.

The reduction in cell counts of NO-releasing PET surfaces were not as great as their corresponding NO-releasing SE surfaces. One reason for this could be due to the

difference in wettabilities of the PET and SE surfaces. It is generally accepted that bacteria with more hydrophilic characteristics prefer hydrophilic surfaces, whilst hydrophobic bacteria prefer hydrophobic surfaces.^{209, 210} In one study by Das *et al*²¹¹ contact angles of wildtype PA14 were measured at 49.9°, indicating the strain to be hydrophilic in nature. The PET surfaces are more hydrophilic than the SE surfaces and this may be a more desirable environment for cell adhesion for this hydrophilic *P. aeruginosa* strain.

4.5 Conclusion

In this chapter the fabrication of covalently bound *N*-diazoniumdiolates to PET and SE substrates has been successfully characterised. XPS analysis confirmed that plasma treatment did induce oxygen functionality on the surface of the substrates. The subsequent aminosilane and *N*-diazoniumdiolate modifications were confirmed through the occurrence of peaks in the N 1s envelope of the XPS spectra. The NO payload and release were controlled by the nature of the aminosilane precursor, in terms of number of NO tethering sites and pK_a of the amine groups. All NO-releasing coatings in this study were shown to significantly reduce *P. aeruginosa* (PA14) adhesion over 24 hrs with the efficacy being a function of the aminosilane modification and the underlying substrate. These NO-releasing polymers demonstrate the potential and utility of this facile coating technique for preventing biofilms on medical implant devices.

Chapter 5: Nitric Oxide-releasing Xerogels as Antibacterial Coatings

5.1 Introduction

The concentration of NO has been shown to have a varying effect on bacteria, from being a biofilm dispersal agent at low concentrations to bactericidal at higher concentrations.^{104, 212} In Chapter 4, aminosilane molecules were tethered to polymers to allow the formation of *N*-diazoniumdiolate surface molecules and the resulting low payload of NO led to the prevention of biofilm formation. The aim of this chapter was to tune the payload of NO released in order to generate the concentrations necessary to have a bactericidal effect.

The first way to facilitate an increase in NO payload is to increase the surface area of the coatings allowing for an increased density of *N*-diazoniumdiolate groups on the surface. This can be achieved through the fabrication of NO-releasing xerogels using the sol-gel process to generate coatings with large surface areas as shown in Figure 5.1.

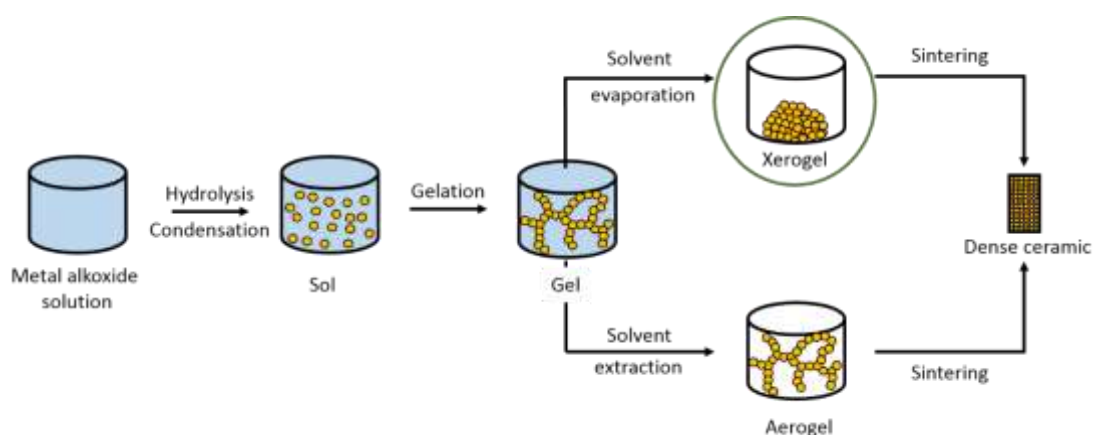


Figure 5.1: Xerogels are fabricated using the sol-gel process by evaporating the solvent from a gel.

Xerogels are particularly attractive coatings for use in biomaterial applications because of the mild synthetic parameters required for their formation and modification. By incorporating preformed *N*-diazoniumdiolates into the initial alkoxy silane solution, NO-releasing xerogels with large surface areas (allowing for increased density of *N*-diazoniumdiolates) are formed (Fig. 5.1). These types of coatings will be described as *N*-diazoniumdiolated xerogel coatings and the experimental method is described in section 5.2

The *N*-diazoniumdiolated xerogels to be discussed in this chapter have been synthesised using a preformed *N*-diazoniumdiolate, which allows for an increase in the NO payload. There are two ways to form tethered *N*-diazoniumdiolates as shown in Figure 5.2

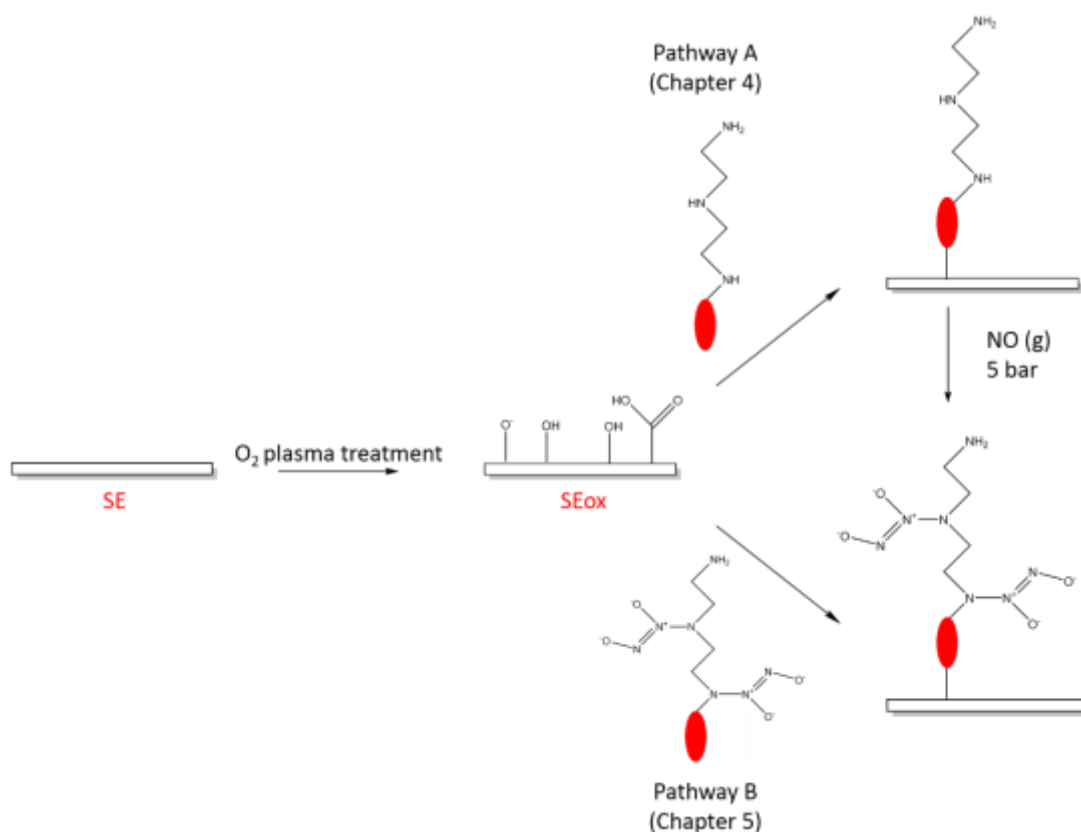


Figure 5.2: The two pathways to tether *N*-diazoniumdiolates to the substrate surface. (For clarity only DET3 has been included but the same reaction steps were carried out for PTMSPA).

In Pathway A, a substrate is first functionalised with aminosilanes before being exposed to high pressures of NO to allow *N*-diazoniumdiolate formation to occur *in*

situ on the surface (Chapter 4). In Pathway B, an aminosilane solution is first exposed to high pressures of NO to afford a preformed *N*-diazoniumdiolate solution before being tethered to the substrate (Chapter 5). The rationale behind using a preformed *N*-diazoniumdiolate is based on work by Schoenfisch *et al.* which has demonstrated that preformed *N*-diazoniumdiolates have the potential to increase NO payload 10-fold when compared with diazeniumdiolates formed *in situ*.^{141, 213, 214}

The aim of this chapter is to use both of these strategies (forming xerogels for increased surface area and preforming the *N*-diazoniumdiolate) in order to investigate the effect that increasing the payload of NO has on the bactericidal efficacy of the material.

5.2 Experimental

5.2.1 Preparation of Preformed *N*-Diazoniumdiolate Solutions

In this chapter the *N*-diazoniumdiolate was preformed in solution before being placed onto the polymer substrate. The reaction scheme is outlined in Figure 5.3.

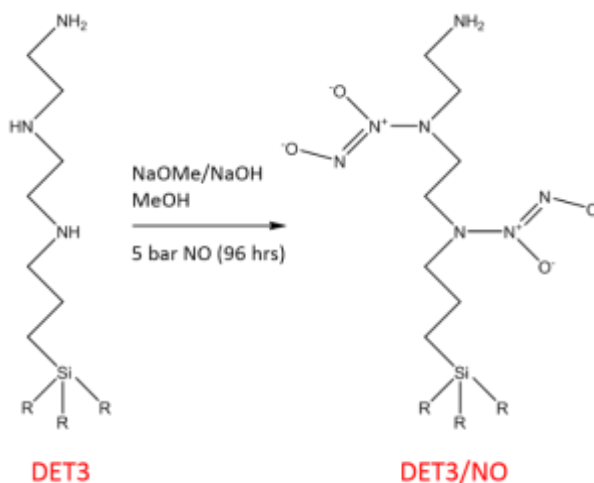


Figure 5.3: Synthesis of preformed *N*-diazoniumdiolate solution. (For clarity only DET3 has been included but the same reaction steps were carried out for PTMSPA).

A 10 % aminosilane solution (DET3 or PTMSPA) was prepared in methanol containing either 0.5 M methanolic sodium methoxide (NaOMe) or 0.1 M sodium hydroxide (NaOH) so that the solution contained 1 molar equivalent of base for every secondary amine. Aminosilane solutions were purged with 6 bar of argon (BOC, Guildford, UK) for 3 x 5 mins and 3 x 10 mins in an in-house built NO reactor. Following purging, the

reactor was filled with 5 bar of NO (BOC, Guildford, UK) for 96 hrs. At the end of this time, NO was released and the reactor was purged with 6 bar of argon for 2 x 5 mins and 2 x 10 mins. Solutions were then stored at -20 °C until use.

5.2.2 Preparation of *N*-diazoniumdiolated Xerogel Coatings

The preformed *N*-diazoniumdiolates were next incorporated into xerogel coatings and tethered to SE substrates, as in the reaction scheme displayed in Figure 5.4.

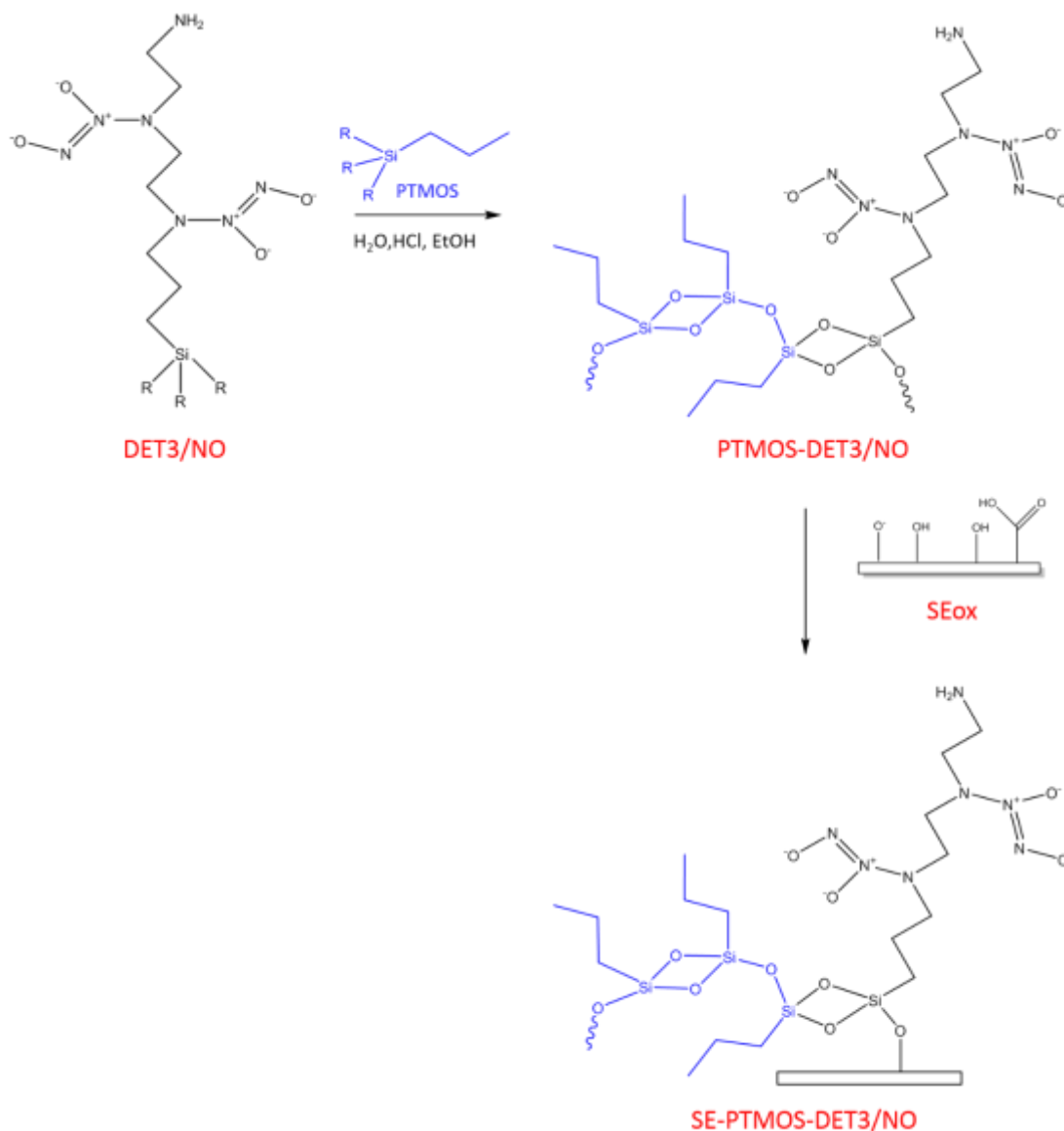


Figure 5.4: Preformed *N*-diazoniumdiolate solutions are incorporated into alkylsilane (PTMOS) sol-gel solutions before being coated onto plasma-treated SE (SEox), and allowed to dry to form *N*-diazoniumdiolated xerogel coatings on SE (For clarity only DET3 has been included but the same reaction steps were carried out for PTMSPA).

Briefly, EtOH (983 μ l), H₂O (190 μ l) and 0.5 M HCL (31.5 μ l) were premixed and added to either trimethoxypropylsilane (PTMOS) (353 μ l) or isobutyltrimethoxysilane (BTMOS) (378 μ l), to maintain a 1:3.2 molar ratio of silane to H₂O (Section 5.2.3). This mixture was stirred for 1 hr to pre-hydrolyse the alkylsilane. Preformed DET3/NO (2564 μ l) or PTMSPA/NO (2439 μ l) solution was then added to the solution to give a 2:1 molar ratio of alkylsilane to aminosilane. This solution was mixed for 3 hrs. SE substrates were treated with oxygen plasma for 2 min. The alkylsilane/*N*-diazoniumdiolated aminosilane sols (15 μ l) were dropped onto the surface of the substrate. The xerogel coated SE substrates were then pre-dried for 10 mins in air before drying in a vacuum desiccator for 3 d at 60 °C. Materials were stored at -20 °C until use.

5.2.3 Optimisation of Sol-gel Process

Depending on aminosilane and backbone of the alkylsilane, the silane to water ratio must be varied to produce stable, non-tacky coatings.¹⁴¹ In much of the work by Schoenfisch, isobutyltrimethoxysilane (BTMOS) was the alkylsilane used to prepare xerogel materials.^{161, 215, 216} As a result, to optimise the sol-gel process in this work, BTMOS was also used. Sol-gels with varying silane to water ratios (1:0, 1:0.5, 1:1, 1:3.2, 1:10) were prepared. Photographic images of BTMOS-DET3 and BTMOS-PTMSPA xerogels with varying silane to water ratios are displayed in Figures 5.5 and 5.6.

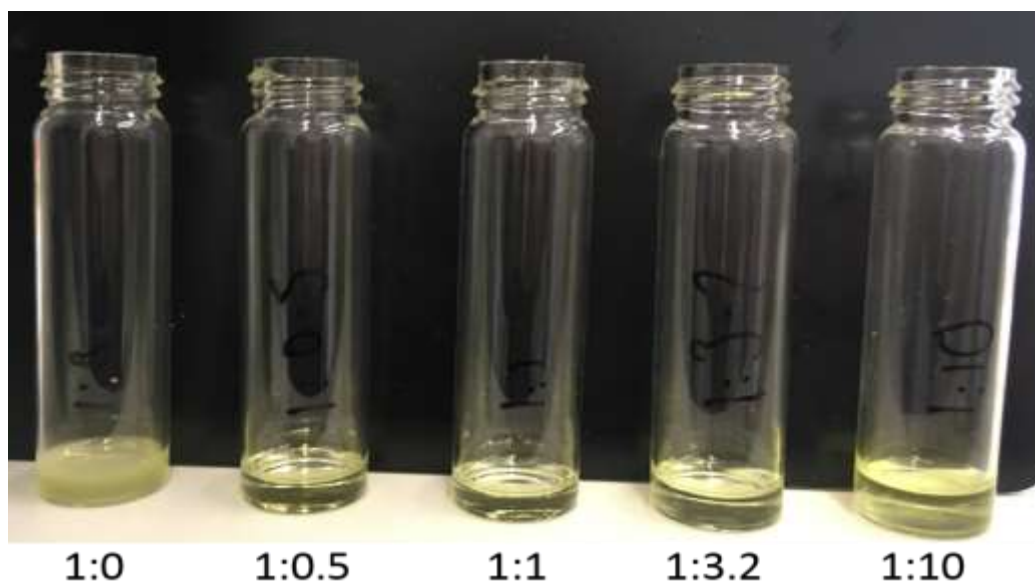


Figure 5.5: BTMOS-DET3 processed gels with varying silane to water ratios.

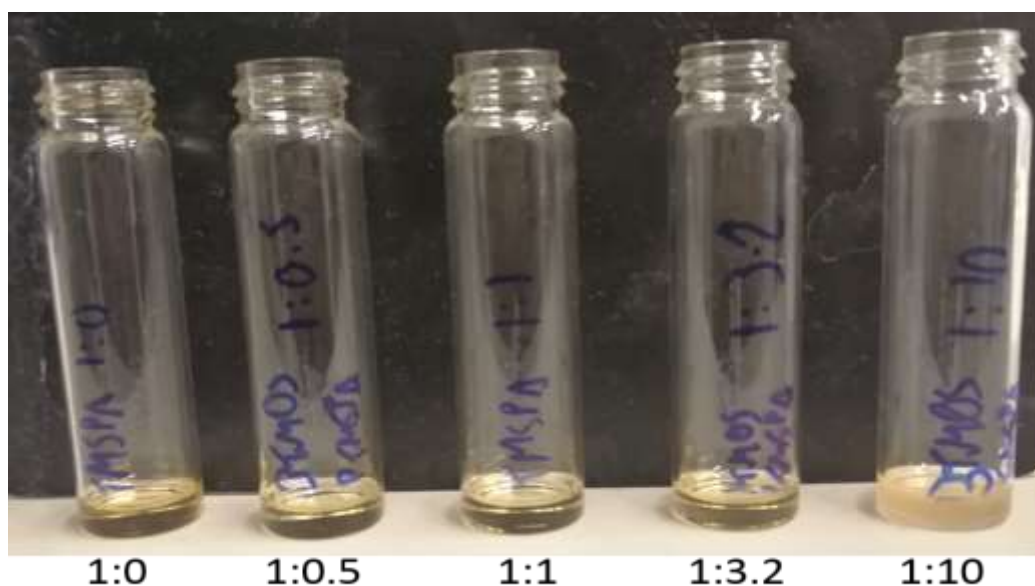


Figure 5.6: BTMOS-PTMSPA processed gels with varying silane to water ratios.

BTMOS-DET3 (1:1) and BTMOS-DET3 (1:3.2) displayed the most transparency, however all xerogels were tacky and unsuitable for use as coatings. The same was true for BTMOS-PTMSPA xerogels. As a result, an alternative alkylsilane was employed.

BTMOS was replaced with trimethoxypropylsilane (PTMOS) and the experiment described above was repeated. The photographic images of PTMOS-DET3 and

PTMOS-PTMSPA with varying silane to water ratios (1:0, 1:0.5, 1:1, 1:3.2, 1:10) are displayed in Figures 5.7 and 5.8, respectively.

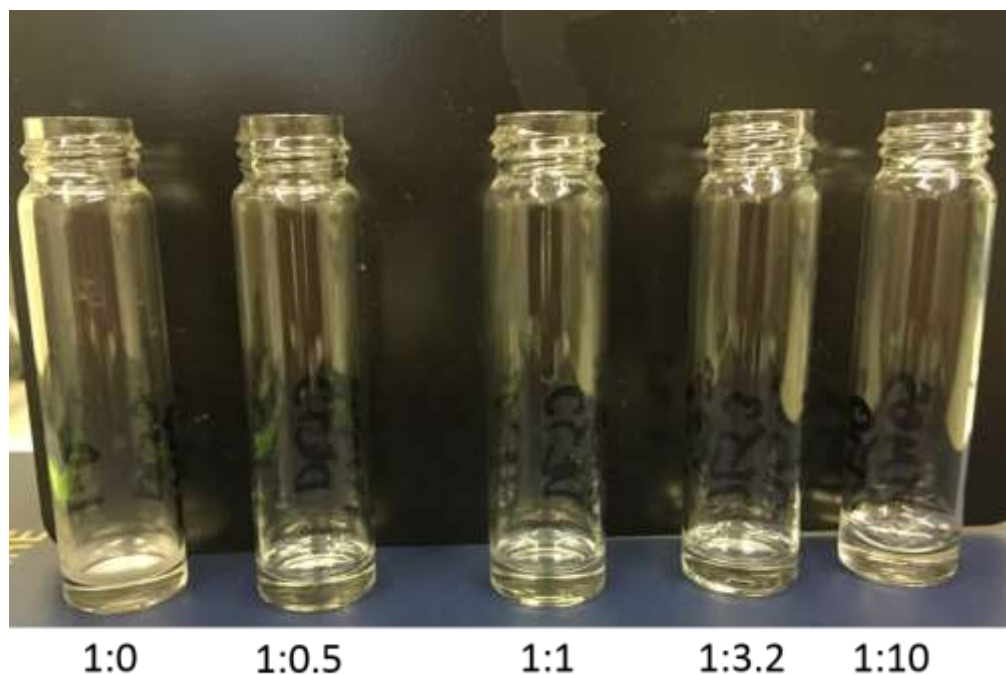


Figure 5.7: PTMOS-DET3 processed gels with varying silane to water ratios.

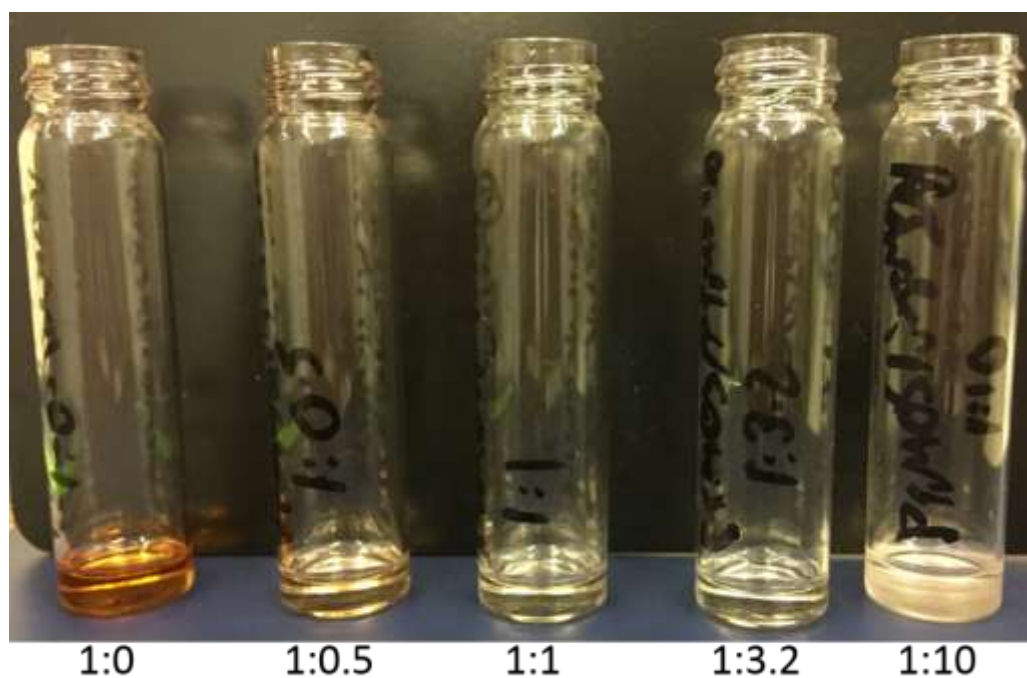


Figure 5.8: PTMOS-PTMSPA processed gels with varying silane to water ratios.

PTMOS-DET3 xerogels were transparent apart from PTMOS-DET3 (1:0) which was opaque. The xerogel formation process was slow and gelation was not observed.

PTMOS-DET3 (1:10) formed a tacky xerogel. PTMOS-DET3 (1:1) and PTMOS-DET3 (1:3.2) both formed nontacky xerogels. PTMOS-PTMSPA (1:0) formed a solution that did not gel, whilst PTMOS-PTMSPA (1:10) gave an opaque xerogel. PTMOS-PTMSPA (1:3.2) gave the most desirable non-tacky xerogel. As a result silane to water ratios of 1:3.2 for both PTMOS-DET3 and PTMOS-PTMSPA were used for all experiments.

5.3 Results: Preformed *N*-diazoniumdiolate Solutions

This chapter explores an increased NO payload onto the surfaces of SE, by forming *N*-diazoniumdiolated xerogels on the surface (Fig. 5.4) and performing the *N*-diazoniumdiolate before tethering it onto the surface (Fig. 5.3). The results in Section 5.3, characterise the preformed *N*-diazoniumdiolate solution before incorporation into the xerogel. Chemical characterisation of these solutions was achieved using UV-Vis spectroscopy. A preliminary experiment, in which NO release was quantified by chemiluminescence detection, was also carried out to ascertain the importance of base in stabilising the preformed *N*-diazoniumdiolate and prolonging NO release before incorporation into the xerogel.

5.3.1 UV-Vis Spectroscopy

The *N*-diazoniumdiolate solutions were characterised by UV-Vis spectroscopy (Figure 5.9). Absorbance maxima of 251 nm and 244 nm for DET3/NO and PTMSPA/NO, respectively, are indicative of *N*-diazoniumdiolate formation as previously reported.^{140, 141, 217}

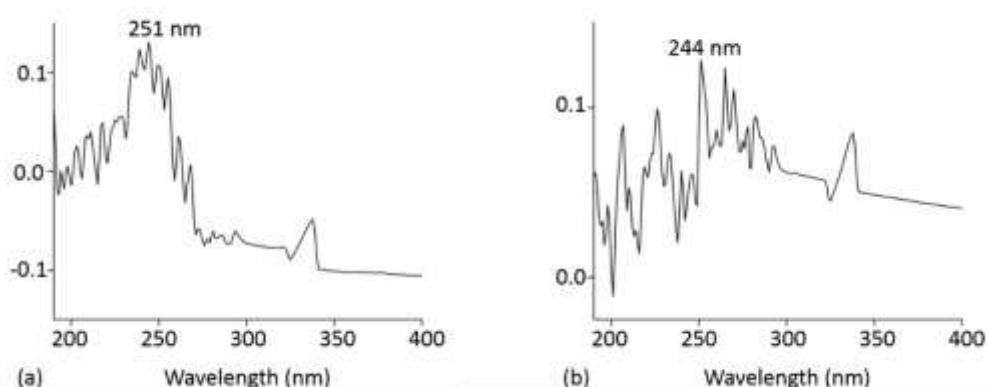


Figure 5.9: UV-Vis spectra of (a) DET3/NO and (b) PTMSPA/NO in 1 M NaOH solution, using DET3 and PTMSPA solutions to deduce respective baselines.

5.3.2 NO Release: Chemiluminescence Detection

A preliminary experiment was carried out to evaluate whether the presence of a base had an effect on NO release of the preformed *N*-diazoniumdiolate solutions, DET3/NO and PTMSPA/NO, before incorporation into the xerogel coating as shown in Figures 5.10 and 5.11, respectively (NO release data in Table 5.1 and 5.2). The rationale to using a base (NaOMe/NaOH) was to promote formation and stabilisation of the *N*-diazoniumdiolate (Fig 5.4).¹⁴¹ DET3/NO (NaOMe), DET3/NO (NaOH) and DET3/NO (no base) exhibited maximum NO releases of $626.5 \mu\text{M s}^{-1}$, $347.0 \mu\text{M s}^{-1}$ and $42.0 \mu\text{M s}^{-1}$, respectively, after 2 mins. The total NO payloads of DET3/NO (NaOMe), DET3/NO (NaOH) and DET3/NO (no base) were 25434 μmol , 26728 μmol and 8647 μmol , respectively.

Table 5.1: Nitric oxide release data for preformed DET3/NO solutions.

	Maximum NO release ($\mu\text{M s}^{-1}$)	Maximum NO release ($\mu\text{M s}^{-1} \mu\text{l}^{-1}$)	Total NO (μmol)	Total NO ($\mu\text{mol} \mu\text{l}^{-1}$)
DET3/NO (NaOMe)	626.5±99.7	52.2±8.3	25434±5726	2120±477
DET3/NO (NaOH)	347.0±67.9	28.9±5.7	26728±1225	2227±102
DET3/NO (no base)	42.0±5.7	3.5±0.5	8647±1328	721±111

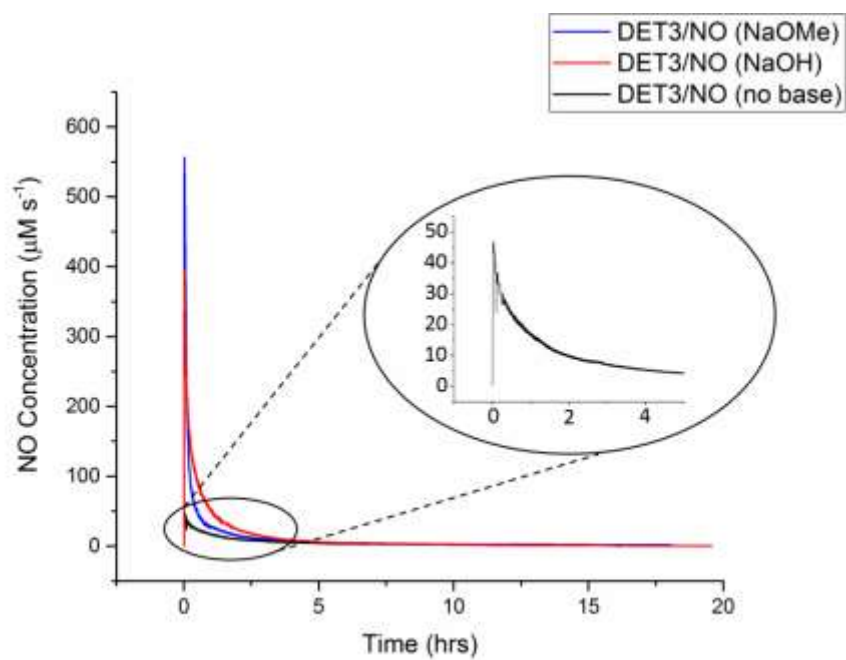


Figure 5.10: NO-release profiles for preformed DET3/NO solution using NaOMe (blue line), NaOH (red line) or no base (black line) at pH 4, determined by chemiluminescence detection.

PTMSPA/NO (NaOMe) solution exhibited a maximum release of $178.7 \mu\text{M s}^{-1}$ after 1 min, and PTMSPA/NO (NaOH) released $14.5 \mu\text{M s}^{-1}$ after 0.5 min; PTMSPA/NO (no base) gave a maximum NO release of $4.6 \mu\text{M s}^{-1}$ instantaneously. The total NO payloads for PTMSPA/NO (NaOMe), PTMSPA/NO (NaOH) and PTMSPA/NO (no base) were $592 \mu\text{mol}$, $137 \mu\text{mol}$ and $7 \mu\text{mol}$, respectively.

Table 5.2: Nitric oxide release data for preformed PTMSPA/NO solutions.

	Maximum NO release ($\mu\text{M s}^{-1}$)	Maximum NO release ($\mu\text{M s}^{-1} \mu\text{l}^{-1}$)	Total NO (μmol)	Total NO ($\mu\text{mol} \mu\text{l}^{-1}$)
PTMSPA/NO (NaOMe)	178.7 ± 15.3	14.9 ± 1.3	592 ± 83	49 ± 7
PTMSPA/NO (NaOH)	14.5 ± 0.5	1.2 ± 0.0	137 ± 106	11 ± 9
PTMSPA/NO (no base)	4.6 ± 0.6	0.4 ± 0.1	7 ± 1	< 1

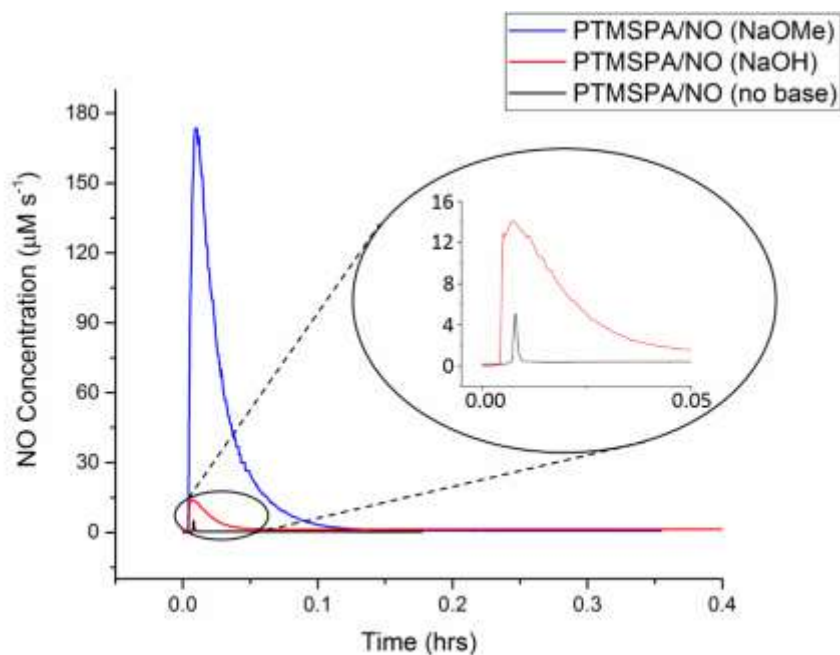


Figure 5.11: NO-release profiles for preformed PTMSPA/NO solution using NaOMe (blue line), NaOH (red line) or no base (black line) at pH 4, determined by chemiluminescence detection.

5.4 Results: *N*-diazoniumdiolated Xerogel Coatings

The results presented below detail the modification of SE substrates using NO-releasing *N*-diazoniumdiolated xerogels consisting of an alkylsilane and a preformed *N*-diazoniumdiolate. The results presented below are of *N*-diazoniumdiolated xerogels with PTMOS as the alkylsilane (optimisation of the sol-gel process has been described previously in Section 5.2.3).

5.4.1 Wettability: Contact Angle

The average contact angle values after each fabrication step are recorded in Table 5.3. A reduced contact angle after plasma treatment confirmed an increased wettability of the SE substrates, due to oxygen functionalisation. An increase in contact angle was observed after applying all xerogel coatings onto the substrates. There was no difference in the contact angles of SE-PTMOS-DET3 (115.2°) and SE-PTMOS-DET3/NO (115.7°) surfaces. SE-PTMOS-PTMSPA displayed a contact angle of 88.0° and an increased contact angle of 108.1° was observed for SE-PTMOS-PTMSPA/NO.

Table 5.3: Static water contact angle measurements of xerogel coated SE substrates.

	Contact Angle (°)
SE	113.0±2.3
SEox	11.0±1.2
SE-PTMOS-DET3	115.2±1.9
SE-PTMOS-DET3/NO	115.7±2.1
SE-PTMOS-PTMSPA	88.0±4.5
SE-PTMOS-PTMSPA/NO	108.1±5.4

5.4.2 Surface Chemistry: XPS

The XPS spectra for SE substrates are displayed in Figures 5.12 - 5.14 and corresponding at. % are given in Tables 5.4 and 5.5. The C 1s envelope of SE was curve fitted to give one component at binding energy 284.6 eV, characteristic of C-C/C-Si/C-H bond. The high resolution O 1s spectra was curve fitted to give two peaks: Si-O-Si at 532.2 eV and O-Si-O at 533.1 eV.¹⁹⁰ The high resolution Si 2p envelope was curve fitted into four components at 102.1 eV (Si-O-Si bridges), 102.7 eV ($R_2\text{-Si(O)}_2$), 103.5 eV ($R\text{-Si(O)}_3$) and 104.1 eV (Si(O)_4).

After plasma treatment, there was a small increase in the overall at. % of oxygen from 32.3 % to 35.1 %. Peak fitting of the C 1s envelope of SEox showed the presence of four components: C-C/C-Si/C-H at 284.6 eV as present in SE, C-C-O at 285.7 eV, C-O at 286.6 eV and C=O at 288.8 eV. In the Si 2p envelope, a decrease of 19.1 % in the concentration of the Si-O-Si was observed, whilst the other components, where Si is bound to more oxygen atoms, increased ($R_2\text{-Si(O)}_2$, $R\text{-Si(O)}_3$, Si(O)_4).

After attachment of the xerogels onto SE, the C 1s spectra was curve fitted into four peaks: 284.6 eV (C-C/C-Si/C-H), 285.7 eV (β -shifted C), 286.4 eV (C-O/C-N) and 288.8 eV (C=O). The presence of C=O components can be attributed to amide formation by reaction with CO_2 when storing in air.²¹⁸ The presence of N-H (399.3 eV) and N+ (400.4 eV) peaks in N 1s spectra for SE-PTMOS-DET3 and SE-PTMOS-PTMSPA confirmed the presence of aminosilane groups and a third at 402.5 eV due to N-O in the N 1s envelopes of SE-PTMOS-DET3/NO and SE-PTMOS-PTMSPA/NO confirmed the presence of the *N*-diazoniumdiolates.

Table 5.4: XPS-derived at. % of C 1s, O 1s, N 1s and Si 2p regions of xerogel coated SE substrates.

	at. %			
	C 1s	O 1s	N 1s	Si 2p
SE	38.2±1.5	32.2±1.2	-	29.6±0.3
SEox	35.4±1.5	35.1±1.6	-	29.6±0.5
SE-PTMOS-DET3	48.9±2.6	27.3±1.4	6.0±0.4	17.7±1.6
SE-PTMOS-DET3/NO	46.9±0.3	33.6±3.4	6.7±0.6	12.7±3.5
SE-PTMOS-PTMSPA	49.2±1.2	28.1±1.3	0.9±0.8	21.9±2.4
SE-PTMOS-PTMSPA/NO	53.0±3.9	25.9±2.5	1.4±0.8	19.7±6.6

Table 5.5: XPS-derived at. % of curve-fitted C 1s, O 1s, N 1s and Si 2p components for xerogel coated SE substrates.

		at. % (Binding Energy, eV)										
		C 1s					N 1s					
		C-C/C-H (284.6)	β -shifted C C-C-O ^a (285.7)	C-O/C-N (286.4)	C=O (288.8)	N-H (399.3)	N+ (400.4)	N-O (402.5)				
SE		100.0±0.0	-	-	-	-	-	-	-	-	-	
SEox		68.8±5.3	20.9±5.8 ^a	5.4±2.2	4.9±0.4	-	-	-	-	-	-	
SE-PTMOS-DET3		51.4±0.6	30.5±0.7	7.6±0.3	10.5±0.3	75.5±7.5	24.5±7.5	-	-	-	-	
SE-PTMOS-DET3/NO		56.6±0.7	25.1±1.0	6.0±1.5	12.3±1.3	47.3±5.4	33.4±2.3	19.3±4.8	-	-	-	
SE-PTMOS-PTMSPA		66.3±4.6	16.7±0.7	7.0±1.8	9.9±2.48	100.0±0.0	-	-	-	-	-	
SE-PTMOS-PTMSPA/NO		53.5±0.4	27.7±0.7	10.2±2.7	8.5±2.2	74.3±0.2	14.4±5.6	7.0±0.2	-	-	-	
		O 1s					Si 2p					
		O-Na (530.8)	O-C/O-Si (532.2)	O-Si-O (533.1)	O=C (533.9)	Na KLL (535.9)	Si-O-Si (102.1)	R ₂ -Si(O) ₂ (102.7)	R-Si(O) ₃ (103.5)	Si(O) ₄ (104.1)		
SE		-	52.0±4.5	48.0±4.5	-	-	45.4±6.7	19.7±4.3	18.1±3.2	16.9±3.3	-	-
SEox		-	38.2±2.5	61.8±2.5	-	-	26.3±4.0	28.2±2.9	21.8±2.8	23.7±3.9	-	-
SE-PTMOS-DET3		18.7±4.9	72.9±4.0	-	-	8.4±0.9	65.2±3.9	34.8±3.9	-	-	-	-
SE-PTMOS-DET3/NO		15.0±2.5	75.1±2.6	-	-	9.9±0.0	55.4±1.6	44.6±1.6	-	-	-	-
SE-PTMOS-PTMSPA		-	87.2±2.2	-	5.3±1.0	7.6±1.4	62.1±5.5	37.9±5.5	-	-	-	-
SE-PTMOS-PTMSPA/NO		-	90.1±3.6	-	2.5±1.8	7.5±1.8	53.9±2.6	46.1±2.6	-	-	-	-

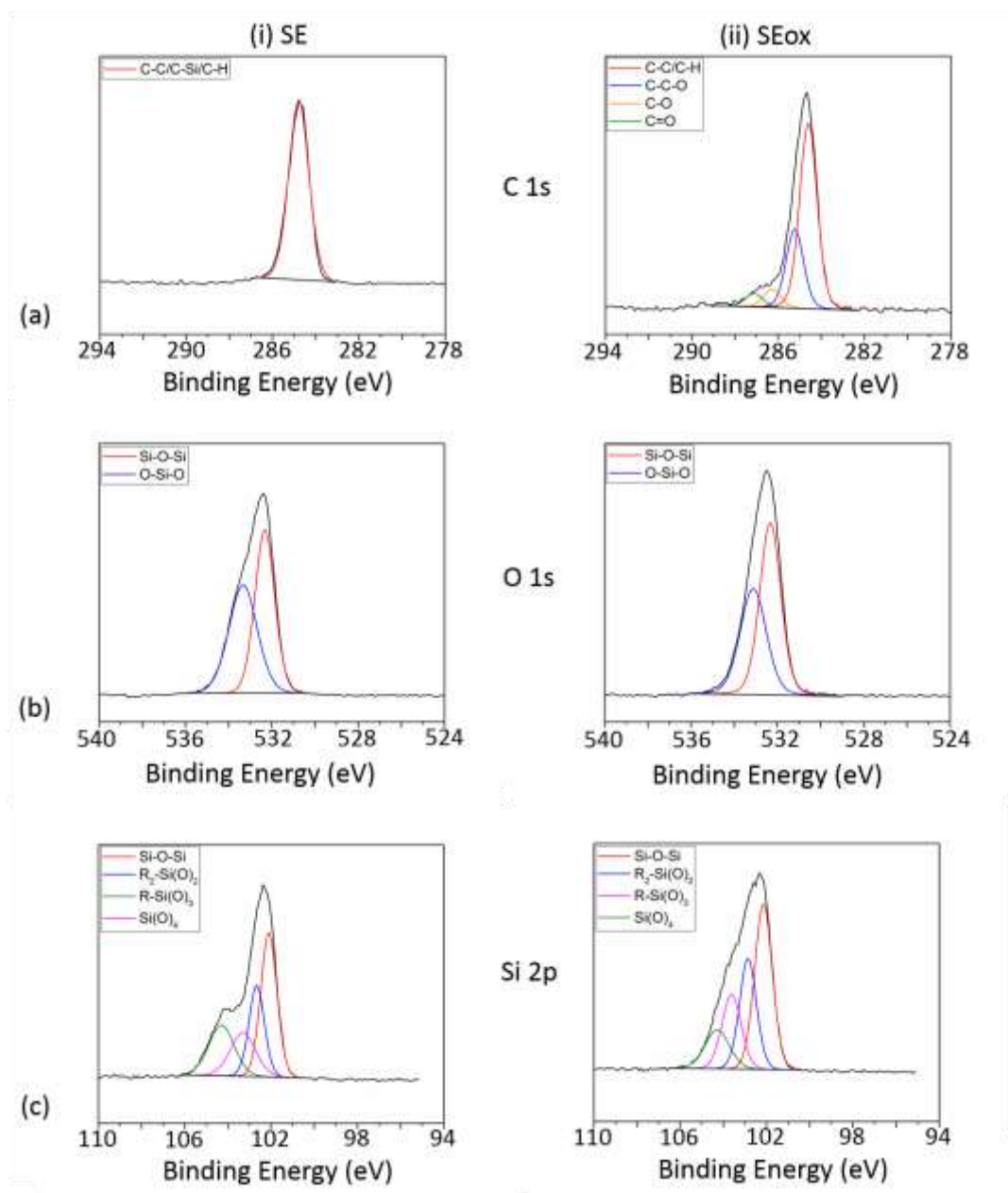


Figure 5.12: Curve fitted (a) C 1s (b) O 1s and (c) Si 2p XPS spectra for (i) SE and (ii) SEox

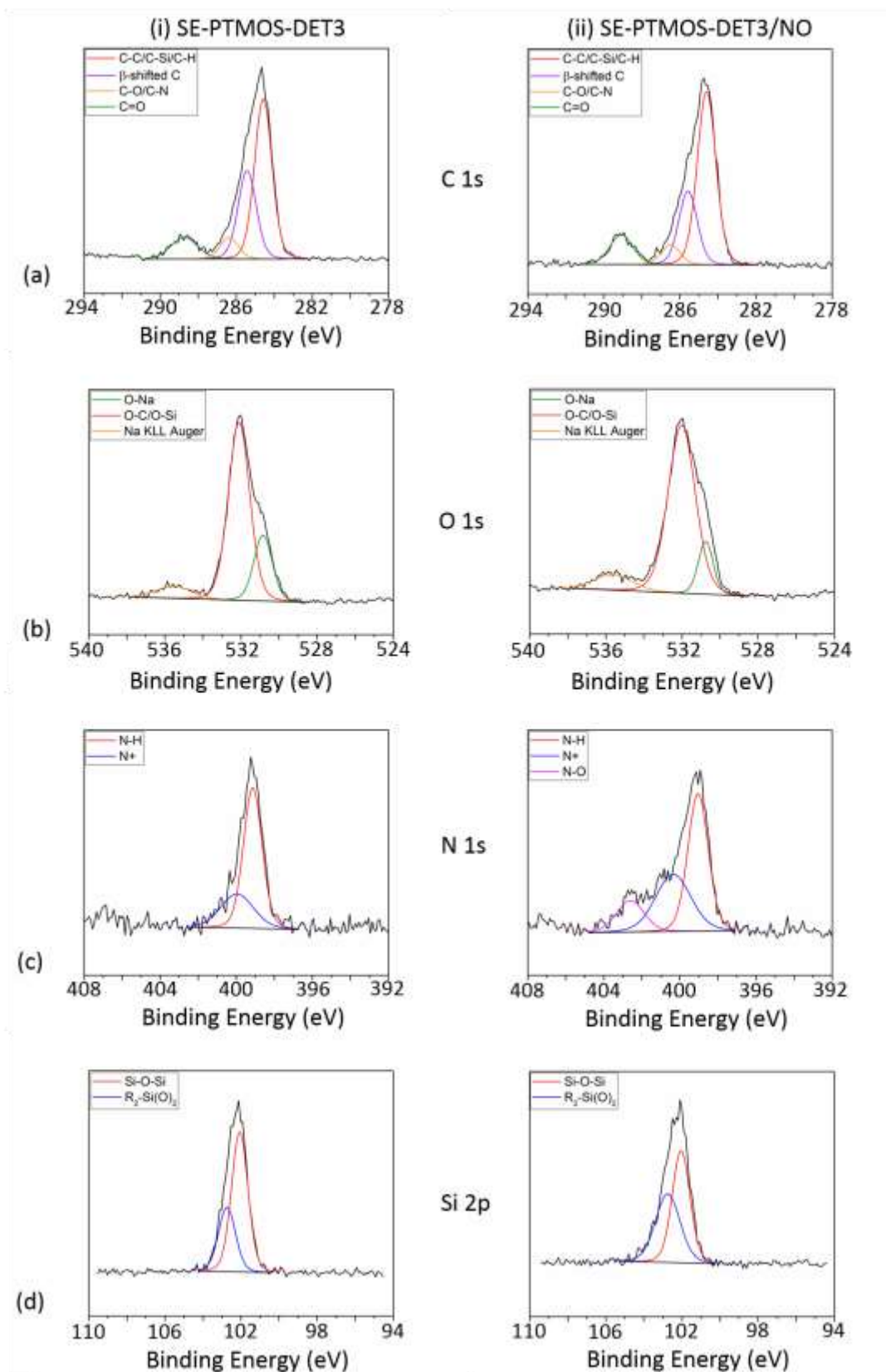


Figure 5.13: Curve fitted (a) C 1s (b) O 1s (c) N 1s (d) Si 2p XPS spectra for (i) SE-PTMOS-DET3 and (ii) SE-PTMOS-DET3/NO.

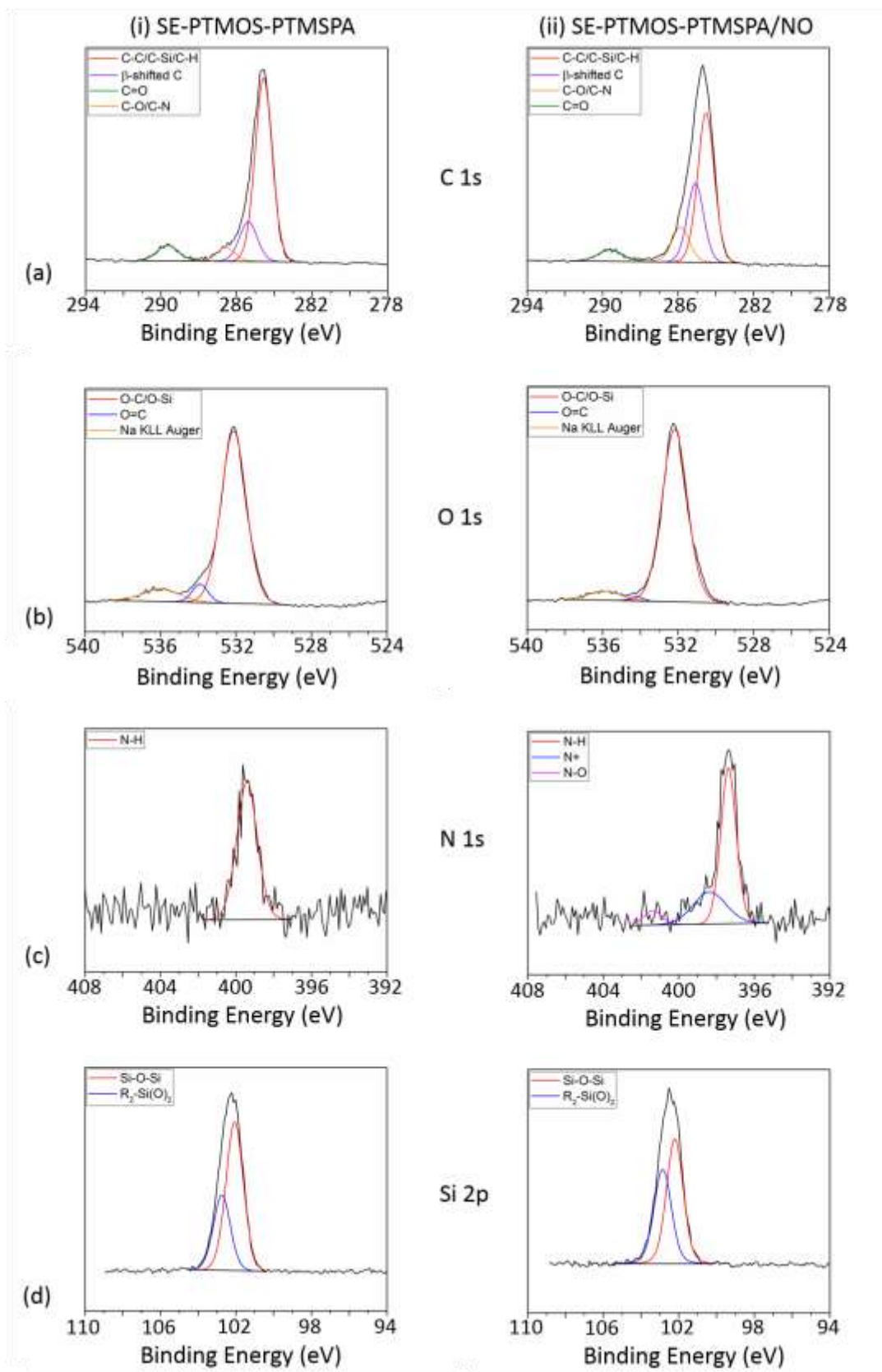


Figure 5.14: Curve fitted (a) C 1s (b) O 1s (c) N 1s (d) Si 2p XPS spectra for (i) SE-PTMOS-PTMSPA and (ii) SE-PTMOS-PTMSPA/NO.

5.4.3 Surface Topography: AFM

The surface topography of SE, SEox, SE-PTMOS-DET3, SE-PTMOS-DET3/NO, SE-PTMOS-PTMSPA and SE-PTMOS-PTMSPA/NO were examined by AFM. In Figure 5.15, representative 3D images, depth profiles and average roughness values of the surfaces are displayed. The roughness value of SE ($R_a = 23.0$ nm) increased after plasma treatment (SEox) to $R_a = 101.7$ nm, due to large cracks forming in the polymer (Figure 5.15 b). In Figures 5.15 c and 5.15 d, although roughness values of SE-PTMOS-DET3 ($R_a = 108.6$ nm) and SE-PTMOS-DET3/NO ($R_a = 141.7$ nm) are not significantly ($p < 0.05$) different to SEox, a change in surface morphology can be observed; topographic surface features of elevated height, indicated that xerogel coatings were present on the substrate. A decrease in roughness was observed for SE-PTMOS-PTMSPA ($R_a = 19.9$ nm) and SE-PTMOS-PTMSPA/NO ($R_a = 55.4$ nm). In both cases discrete topographical surface protrusions were apparent, possibly due to dewetting of the sol-gel on the SE substrate before hardening to form a xerogel.

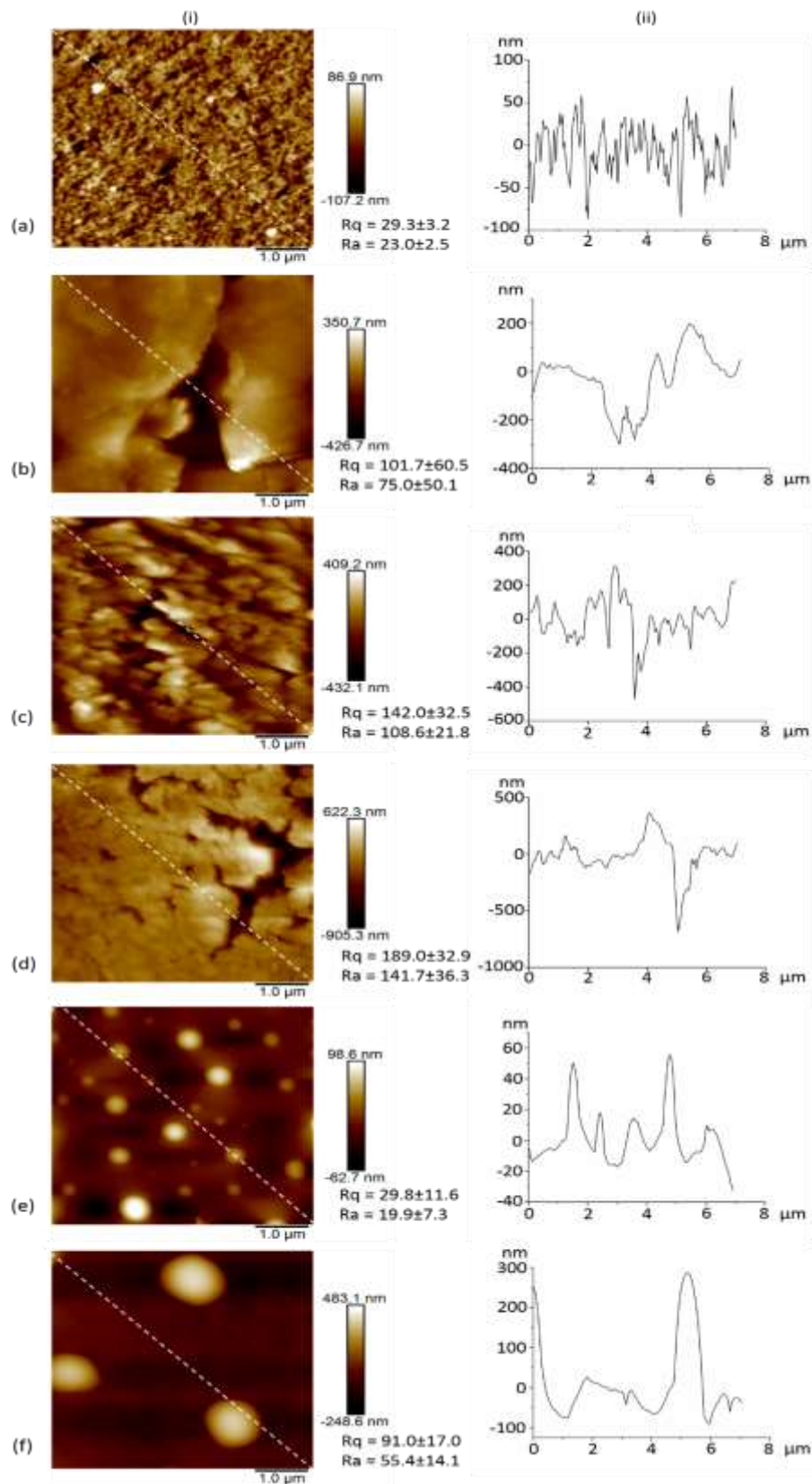


Figure 5.15: AFM (i) 3D images (5 x 5 μm^2) and (ii) depth profiles of (a) SE; (b) SEox; (c) SE-PTMOS-DET3, (d) SE-PTMOS-DET3/NO, (e) SE-PTMOS-PTMSPA and (f) SE-PTMOS-PTMSPA/NO. Rq and Ra values given in nm.

5.4.4 NO release: Chemiluminescence Detection

NO is released from *N*-diazoniumdiolates upon protonation and is controlled by the pKa of the amine nitrogen (Figure 5.16). As the pH of the release medium decreases, the rate of NO release increases. To investigate this, NO release of the *N*-diazoniumdiolated xerogel coatings was assessed in release mediums of differing pH.

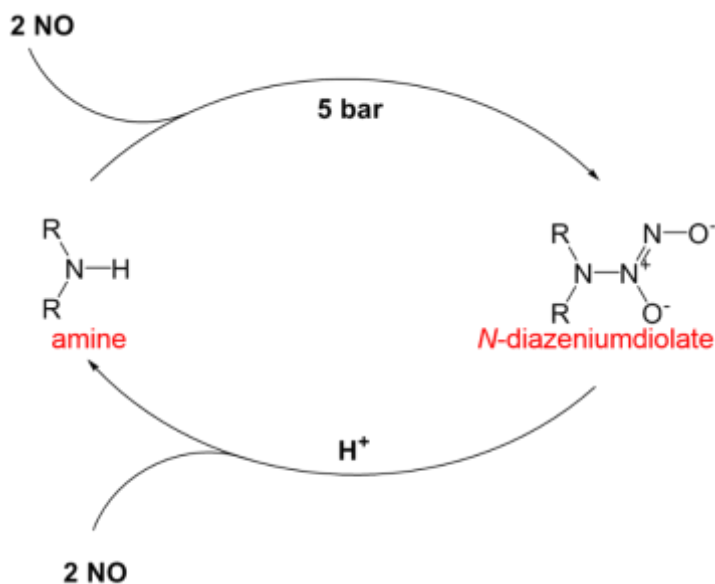


Figure 5.16: NO release rates of *N*-diazoniumdiolates are controlled by protonation of the amine nitrogen. Therefore the pKa of the amine nitrogen and the pH of the reaction medium are important factors for NO release.

Additionally, NO release is also affected by temperature; the rate of NO release increases at physiological temperatures (37 °C) vs ambient temperatures (25 °C).¹⁴⁰ Therefore, the NO release of *N*-diazoniumdiolated xerogel coatings was also compared at physiological and ambient temperatures. Finally the NO release of *N*-diazoniumdiolated xerogel coatings was compared when the preformed *N*-diazoniumdiolate was synthesised using different bases.

5.4.4.1 Effect of pH

Nitric oxide release of SE-PTMOS-DET3/NO and SE-PTMOS-PTMSPA/NO was monitored in real time *via* chemiluminescence detection at pH 4 and 7.4 with the corresponding representative release profiles and concentrations given in Figures 5.17 and 5.18, respectively. NO release data is displayed in Table 5.6. At pH 4, SE-PTMOS-DET3/NO exhibited an initial burst reaching $193.0 \mu\text{M s}^{-1}$ after 5 mins and released a total of 11313 μmol . At pH 7.4, the same surfaces reached a maximum

NO release of $5.4 \mu\text{M s}^{-1}$ after approximately 8 mins and released $3531 \mu\text{mol NO}$ in total over a 25 hr period. At pH 4, SE-PTMOS-PTMSPA/NO released up to $0.7 \mu\text{M s}^{-1}$ as a burst release and released $21 \mu\text{mol}$ in total after 30 mins. At pH 7.4, these surfaces reached a maximum NO release of $0.1 \mu\text{M s}^{-1}$ in a burst release and a total of $6 \mu\text{mol}$ after 1 hr.

Table 5.6: Nitric oxide release data from *N*-diazoniumdiolated xerogel coatings on SE at pH 4 and 7.4.

	Maximum NO release ($\mu\text{M s}^{-1}$)	Maximum NO release ($\mu\text{M s}^{-1} \text{cm}^{-2}$)	Total NO (μmol)	Total NO ($\mu\text{mol cm}^{-2}$)
SE-PTMOS-DET3/NO (pH 4)	193.0 ± 60.8	68.9 ± 21.7	11313 ± 272 6	4040 ± 974
SE-PTMOS-DET3/NO (pH 7.4)	5.4 ± 3.2	1.7 ± 1.1	3531 ± 223	1261 ± 80
SE-PTMOS-PTMSPA/NO (pH 4)	0.7 ± 0.1	0.2 ± 0.0	21 ± 9	7 ± 3
SE-PTMOS-PTMSPA/NO (pH 7.4)	0.1 ± 0.0	< 0.1	6 ± 4	2 ± 1

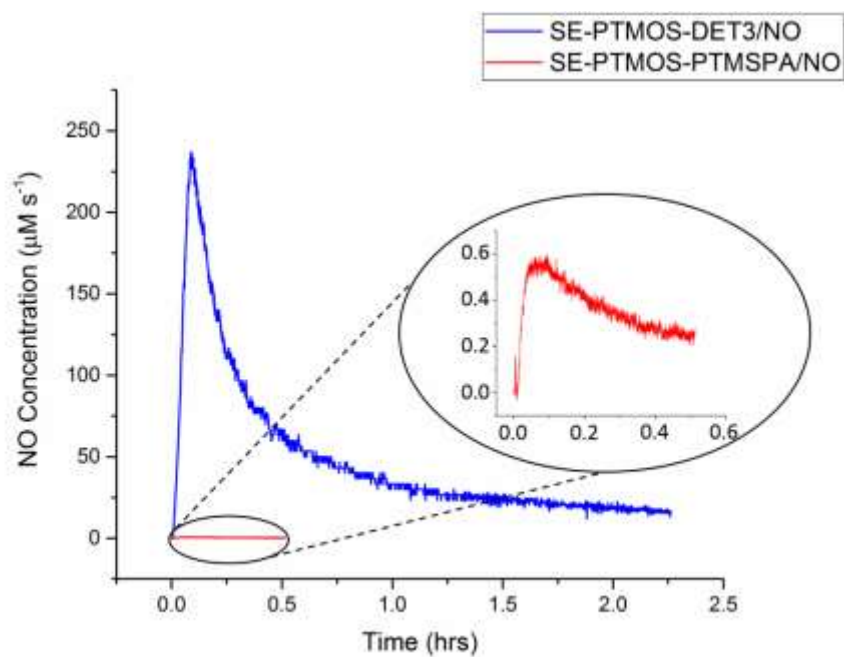


Figure 5.17: NO release profiles for SE-PTMOS-DET3/NO (blue line) and SE-PTMOS-PTMSPA/NO (red line) at pH 4, determined by chemiluminescence detection.

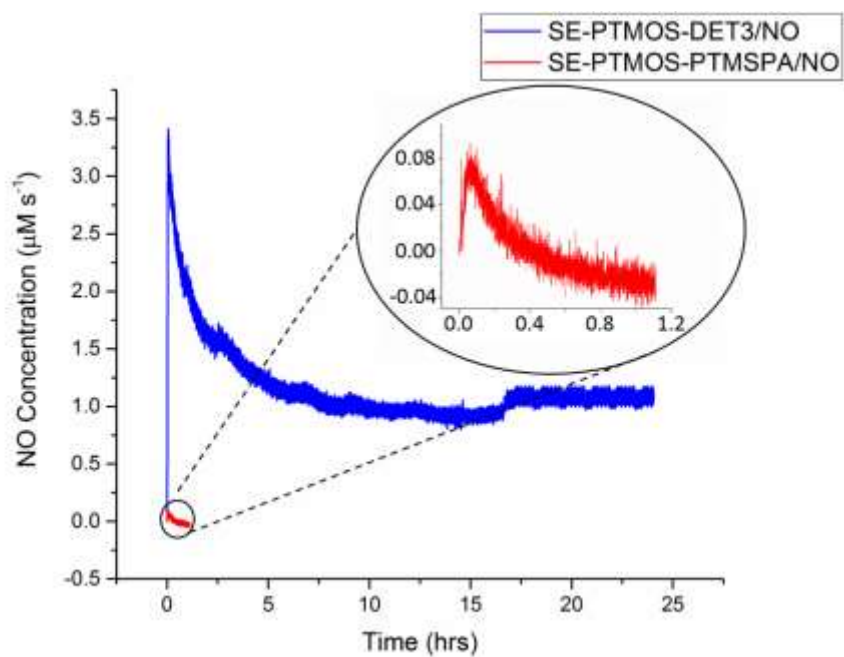


Figure 5.18: NO release profiles for SE-PTMOS-DET3/NO (blue line) and SE-PTMOS-PTMSPA/NO (red line) at pH 7.4, determined by chemiluminescence detection.

5.4.4.2 Effect of Temperature

Nitric oxide release and representative NO release profiles of SE-PTMOS-DET3/NO and SE-PTMOS-PTMSPA/NO are given in Figures 5.19 and 5.20, respectively, at physiological (37 °C) and ambient (25 °C) temperature. All release profiles were recorded at pH 7.4. NO-release data is reported in Table 5.7. At 25 °C, SE-PTMOS-DET3/NO exhibited a maximum NO release of 5.4 $\mu\text{M s}^{-1}$ and a total payload of 3531 μmol . When the temperature was increased to 37 °C a maximum release of 9.1 $\mu\text{M s}^{-1}$ NO and a total payload of 6760 μmol NO was observed. At 25 °C, the maximum NO release for SE-PTMOS-PTMSPA/NO was 0.1 $\mu\text{M s}^{-1}$ and a total of 6 μmol was released after 1 hr. At 37 °C NO release increased; maximum and total NO release of 1.0 $\mu\text{M s}^{-1}$ and 65 μmol were observed, respectively, releasing beyond 3 hrs.

Table 5.7: Nitric oxide release metrics from N-diazeniumdiolate-modified xerogel coatings on SE at different temperatures.

	Maximum NO release ($\mu\text{M s}^{-1}$)	Maximum NO release ($\mu\text{M s}^{-1} \text{cm}^{-2}$)	Total NO (μmol)	Total NO ($\mu\text{mol cm}^{-2}$)
SE-PTMOS-DET3/NO (25 °C)	5.4±3.2	1.7±1.1	3531±223	1261±80
SE-PTMOS-DET3/NO (37 °C)	9.1±1.6	3.2±0.6	6760±78	2414±28
SE-PTMOS-PTMSPA/NO (25 °C)	0.1±0.0	< 0.1	6±4	2±1
SE-PTMOS-PTMSPA/NO (37 °C)	1.0±0.2	0.3±0.1	65±4	24±1

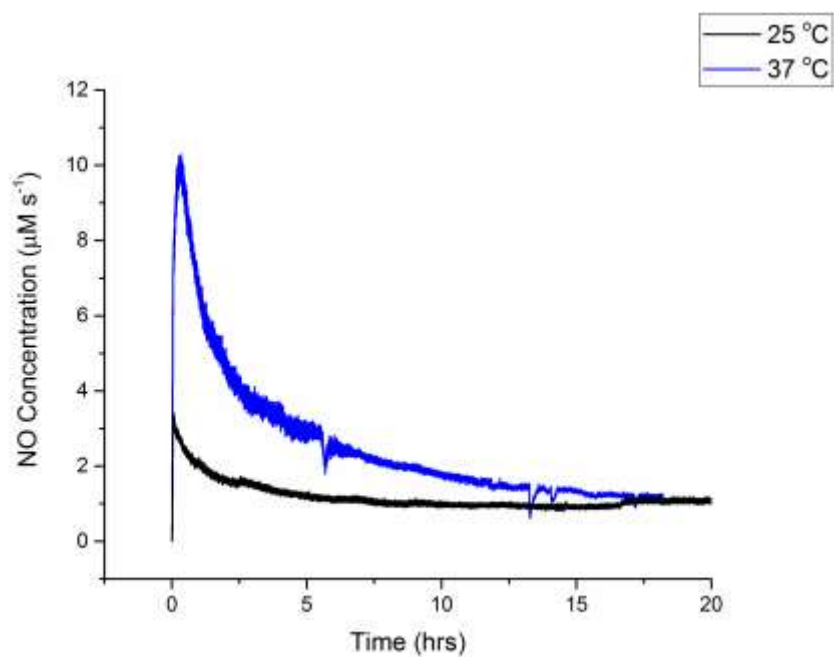


Figure 5.19: NO release profiles for SE-PTMOS-DET3/NO at 25 °C (black line) and 37 °C (blue line) at pH 7.4, determined by chemiluminescence detection.

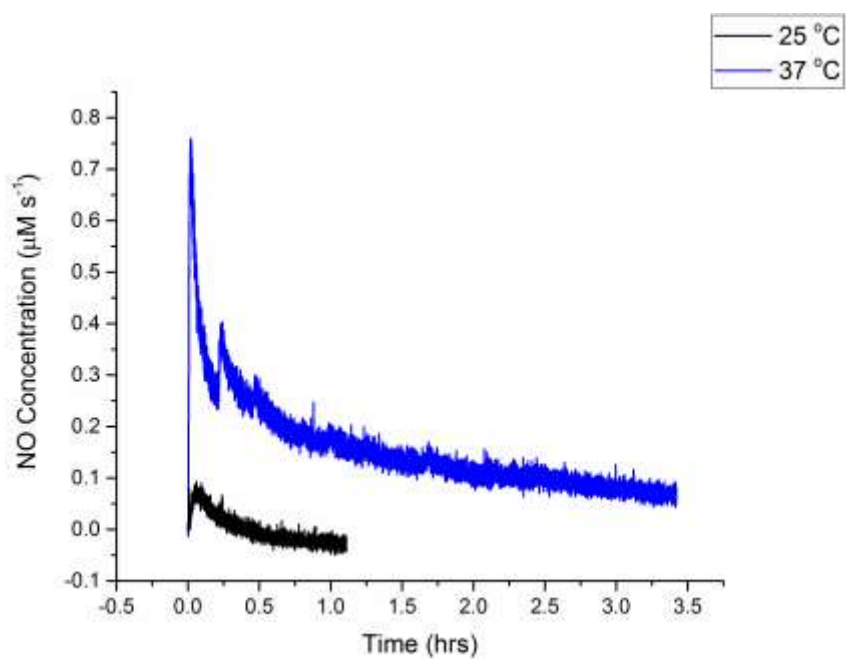


Figure 5.20: NO release profiles for SE-PTMOS-PTMSPA/NO at 25 °C (black line) and 37 °C (blue line) at pH 7.4, determined by chemiluminescence detection.

5.4.4.3 Effect of Bases

In the literature, NaOMe has been used effectively as a base for the formation of the *N*-diazoniumdiolate and was the initial choice when synthesising the preformed *N*-diazoniumdiolate (Figure 5.3). Although effective, the reaction produces methanol which can be bactericidal itself (see Section 5.5 Discussion), thereby complicating the clarity of the source of the antibacterial effect. As such this chapter also explored the NO release of the *N*-diazoniumdiolated xerogel coatings on SE using NaOH when performing the *N*-diazoniumdiolate, where the by-product is water.

To test the effect base has on NO release from *N*-diazoniumdiolated xerogel coatings, preformed DET3/NO was also prepared with NaOH instead of NaOMe. The NO release profiles (pH 7.4) of SE-PTMOS-DET/NO when forming DET3/NO with different bases, are displayed in Figure 5.21 and NO-release data presented in Table 5.8. When NaOMe was used SE-PTMOS-DET3/NO reached a maximum NO release of $5.4 \mu\text{M s}^{-1}$ after approximately 8 minutes and released $3531 \mu\text{mol NO}$ in total over a 25 hr period. When NaOH was used as a base, a maximum release of $3.0 \mu\text{M s}^{-1}$ was reached after approximately 2.5 hrs. After 20 hrs a total release of $3866 \mu\text{mol NO}$ was observed. In the absence of base, the maximum NO release was $0.3 \mu\text{M s}^{-1}$ with a total release of $298 \mu\text{mol NO}$, over 20 hrs.

Table 5.8: Nitric oxide release data from DET3/NO xerogel coatings on SE, when varying the base system employed when performing the diazeniumdiolate solution.

	Maximum NO release ($\mu\text{M s}^{-1}$)	Maximum NO release ($\mu\text{M s}^{-1} \text{cm}^{-2}$)	Total NO (μmol)	Total NO ($\mu\text{mol cm}^{-2}$)
DET3/NO (NaOMe)	5.4 ± 3.2	1.7 ± 1.1	3531 ± 223	1261 ± 80
DET3/NO (NaOH)	3.0 ± 1.3	1.1 ± 0.5	3866 ± 692	1381 ± 249
DET3/NO (no base)	0.3 ± 0.1	0.1 ± 0.0	298 ± 9	106 ± 3

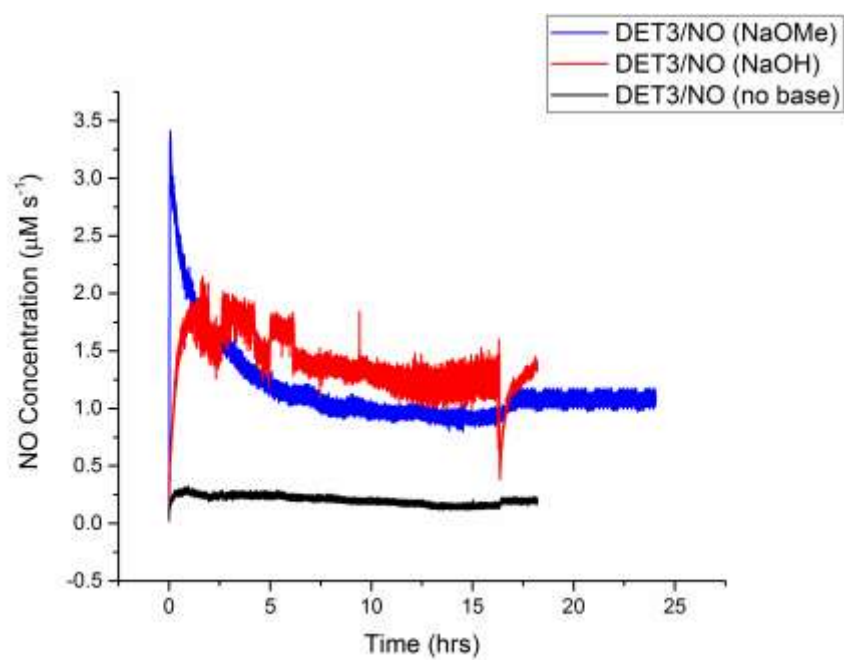


Figure 5.21: NO release profiles for SE-PTMOS-DET3/NO using NaOMe (blue line), NaOH (red line) and no base (black line) to synthesise preformed *N*-diazoniumdiolate solution at pH 7.4, determined by chemiluminescence detection.

5.4.5 Bacterial Response

The bacterial response of the NO-releasing *N*-diazoniumdiolated xerogel coatings on SE substrates was measured in terms of their bactericidal and anti-adhesion ability compared to pristine, plasma-treated and non-releasing xerogel-coated control substrates. Bactericidal efficacy was determined by comparing the viable planktonic cell counts, whilst the anti-adhesion efficacy was tested by counting the viable adhered cell counts, isolated after a PBS wash. Factors including interference from LB media and bactericidal activity from non-releasing xerogel-coated controls meant optimisation of the assays was required to acquire a valid result. This section details the modifications made that enabled a valid conclusion on the bacterial response of the *N*-diazoniumdiolated xerogel coatings to be made.

5.4.5.1 Adhered Cell CFU Assay (LB Media)

The antibacterial efficacy was first tested in terms of anti-adhesion ability against a lab strain of *P. aeruginosa* (PA14) using a CFU assay. The CFU/ml counts are given in Figure 5.22. It can be seen that NO-releasing surfaces tested against PA14 exhibited no significant reduction in cell count when compared to pristine, plasma-treated, or non-releasing xerogel-coated control substrates.

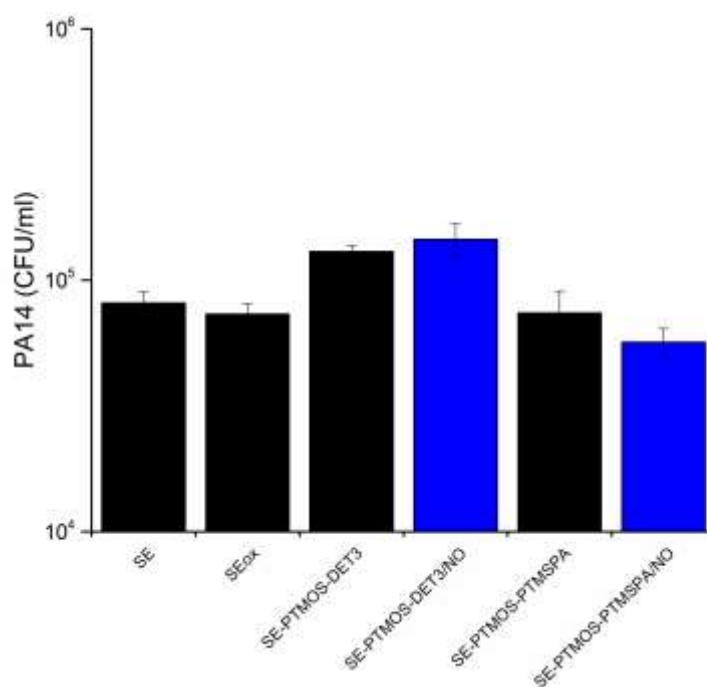


Figure 5.22: Viable *P. aeruginosa* (PA14) adhered cell counts (CFU/ml) after 24 hrs of growth on SE surfaces. Blue bars indicate NO-releasing materials.

5.4.5.2 Planktonic and Adhered Cell CFU Assays (Phosphate Buffered Saline)

The results from Section 5.4.5.1 showed no reduction in cell counts on *N*-diazoniumdiolated xerogel coatings when compared to pristine, plasma-treated and non-releasing xerogel-coated control substrates. As a result planktonic and adhered cell CFU assays were carried out in PBS, against non-growing PA14 cells and assayed at 1, 4 and 24 hr time points. PBS rather than LB broth was used as Brooun *et al.* has previously shown the antibacterial ability of materials is often hindered in fresh rich media due to the ability of the bacteria to recover.²¹⁹ The viable planktonic and adhered cell counts are given in Figures 5.23 and 5.24, respectively.

After 1 hr, on SE-PTMOS-DET3/NO surfaces, a 5-log reduction in planktonic cell count was observed; after 4 hrs the reduction was > 4-log; after 24 hrs the reduction was 5-log. It is important to note that no growth was observed for the non-releasing xerogel-coated control substrate (SE-PTMOS-DET3). SE-PTMOS-PTMSPA/NO surfaces showed no significant reduction in cell count compared to either SE or SE-PTMOS-PTMSPA.

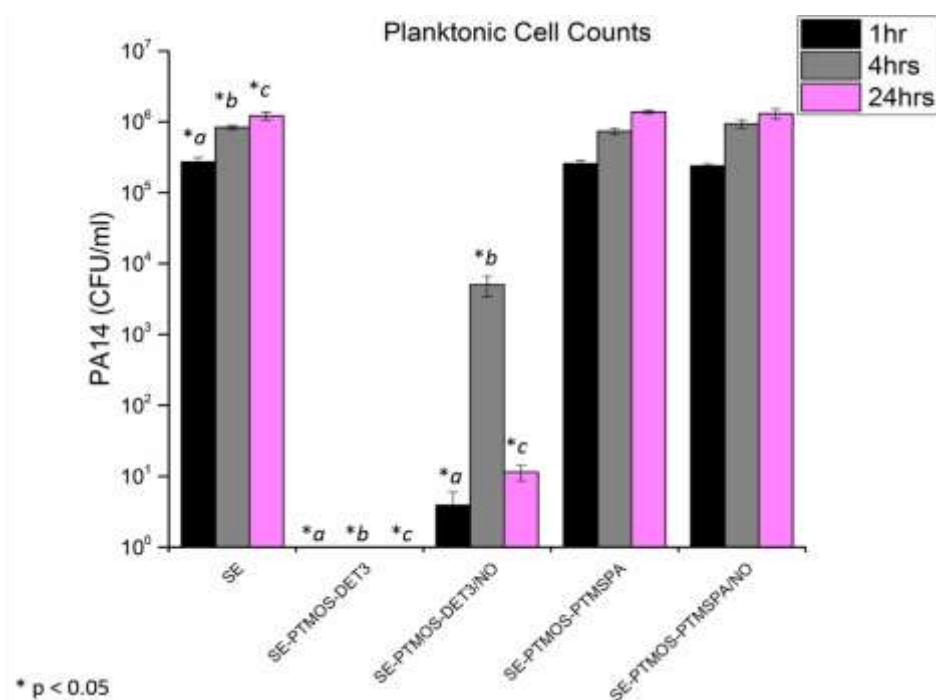


Figure 5.23: Viable *P.aeruginosa* (PA14) planktonic cell counts after 1 hr (black bars), 4 hr (grey bars) and 24 hr (pink bars) inoculation periods. The * symbol indicates the control surfaces that are significantly different to the NO-releasing surfaces at $p < 0.05$.

After 1 hr, on SE-PTMOS-DET3/NO a 2-log reduction in adhered cells was observed compared to pristine SE; after 4 and 24 hrs the reduction was > 4-log. It is important to note that no growth was observed for the non-releasing xerogel-coated control substrate (SE-PTMOS-DET3). SE-PTMOS-PTMSPA/NO surfaces showed no significant reduction in cell count compared to either SE or SE-PTMOS-PTMSPA.

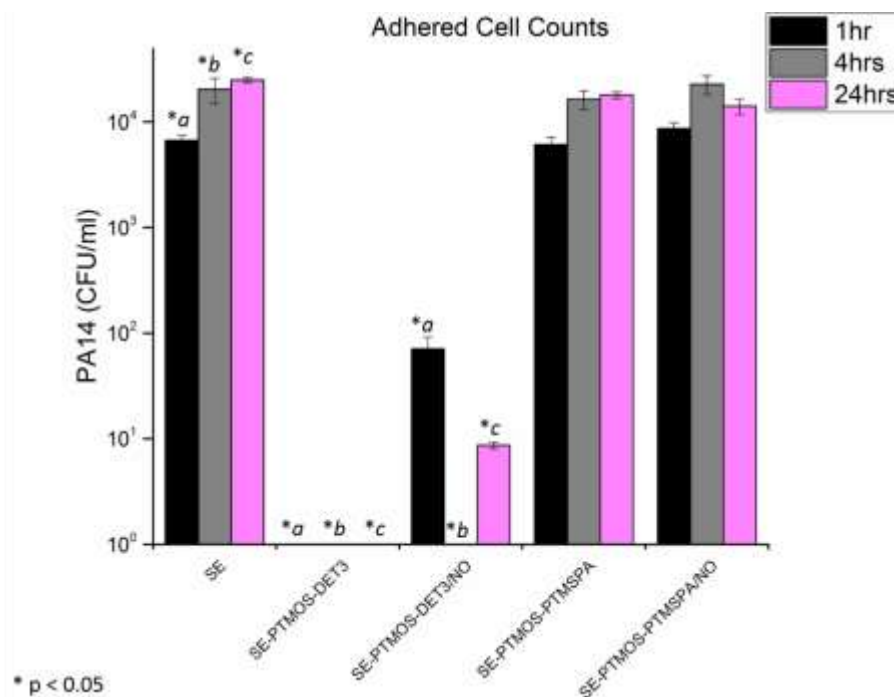


Figure 5.24: Viable *P.aeruginosa* (PA14) adhered cell counts after 1 hr (black bars), 4 hr (grey bars) and 24 hr (pink bars) inoculation periods. The * symbol indicates the control surfaces that are significantly different to the NO-releasing surfaces at $p < 0.05$.

As mentioned above, no bacterial growth was observed in the presence of the silanised control surface, SE-PTMOS-DET3. This was hypothesised to be a bactericidal effect of the residual sodium methoxide base. For this reason, it is not feasible to conclude that the reduction seen on SE-PTMOS-DET3/NO surfaces was solely due to the presence and performance of NO.

5.4.5.3 Effect of Base on Bactericidal Activity

In Section 5.4.5.2, the ability of SE-PTMOS-DET3/NO, and therefore NO, as a bactericidal agent could not be concluded as the non-releasing xerogel-coated control substrate (SE-PTMOS-DET3) showed evidence of bactericidal activity. It was hypothesised that this was most likely due to some bactericidal activity of the sodium methoxide base.

Consequently, a bactericidal assay was carried out in which different bases (NaOH and NaOMe) were employed in performing the *N*-diazoniumdiolate solution (Figure 5.3). The assay was carried out in the same way as in Section 5.4.5.2 with substrates being inoculated for 1, 4 and 24 hrs with a bacterial solution of PA14 in PBS. The viable planktonic cell counts for SE-PTMOS-DET3/NO and corresponding pristine (SE) and non-releasing xerogel-coated control (SE-PTMOS-DET3) substrates are displayed in Figures 5.25-5.27.

(To note: SE-PTMOS-PTMSPA/NO showed no significant reduction in viable planktonic or adhered cell counts compared to pristine (SE) or non-releasing xerogel-coated control (SE-PTMOS-PTMSPA) substrates and so have not been included in the experiments concerning the results in Section 5.4.5.3)

At 1 hr when base was absent, the planktonic cell count in the presence of SE-PTMOS-DET3/NO surfaces was 50 % higher than for SE and 34 % higher compared to the corresponding non-releasing xerogel-coated control substrate (SE-PTMOS-DET3). At 4 hrs and 24 hrs, no significant difference was observed (Fig. 5.25).

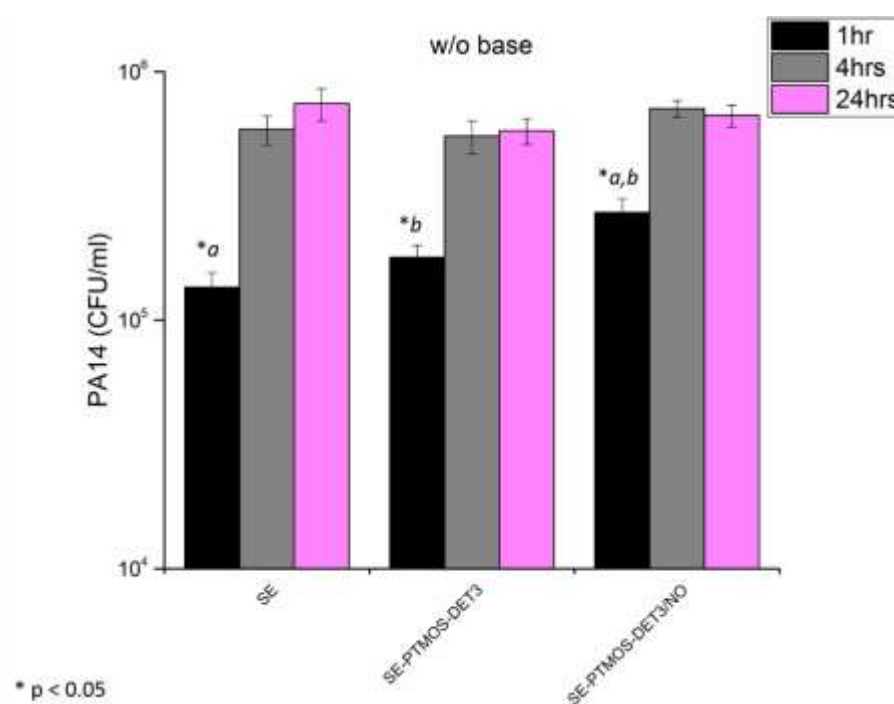


Figure 5.25: Viable *P. aeruginosa* (PA14) planktonic cell counts (CFU/ml) after 1 hr (black bars), 4 hr (grey bars) and 24 hr (pink bars) inoculation periods. The preformed *N*-diazoniumdiolate incorporated into SE-PTMOS-DET3/NO was formed without the use of a base. The * symbol indicates the control surfaces that are significantly different to the NO-releasing surfaces at $p < 0.05$.

When 0.5 M NaOMe was used to synthesise the preformed *N*-diazoniumdiolate solution (Fig. 5.3) before incorporation into SE-PTMOS-DET3/NO, a 5-log reduction in viable planktonic cell counts compared to pristine SE was observed after 24 hrs (Fig. 5.26). It is important to note that no growth was observed for the non-releasing xerogel-coated control substrate (SE-PTMOS-DET3). The results in this section are repeated from those in Section 5.4.5.2 for clarity.

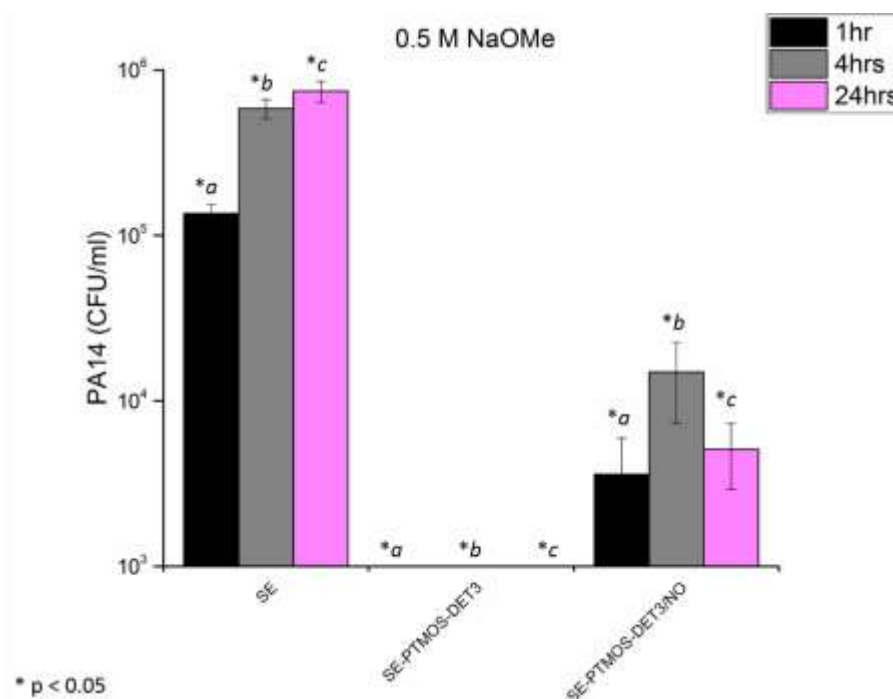


Figure 5.26: Viable *P. aeruginosa* (PA14) planktonic cell counts (CFU/ml) after 1 hr (black bars), 4 hr (grey bars) and 24 hr (pink bars) inoculation periods. The preformed *N*-diazoniumdiolate incorporated into SE-PTMOS-DET3/NO was formed using 0.5 M NaOMe. The * symbol indicates the control surfaces that are significantly different to the NO-releasing surfaces at $p < 0.05$.

When 0.1 M NaOH was used as a base to synthesise the preformed *N*-diazoniumdiolate (Fig 5.3) the viable planktonic cell counts in the presence of the non-releasing xerogel-coated control substrate (SE-PTMOS-DET3) were not significantly different to pristine SE (Fig. 2.7). At 1 hr the cell counts for SE-PTMOS-DET3/NO (NaOH) were 69 % less than SE-PTMOS-DET3 (NaOH). A reduction of 93 % remained consistent after 4 hrs and 24 hrs.

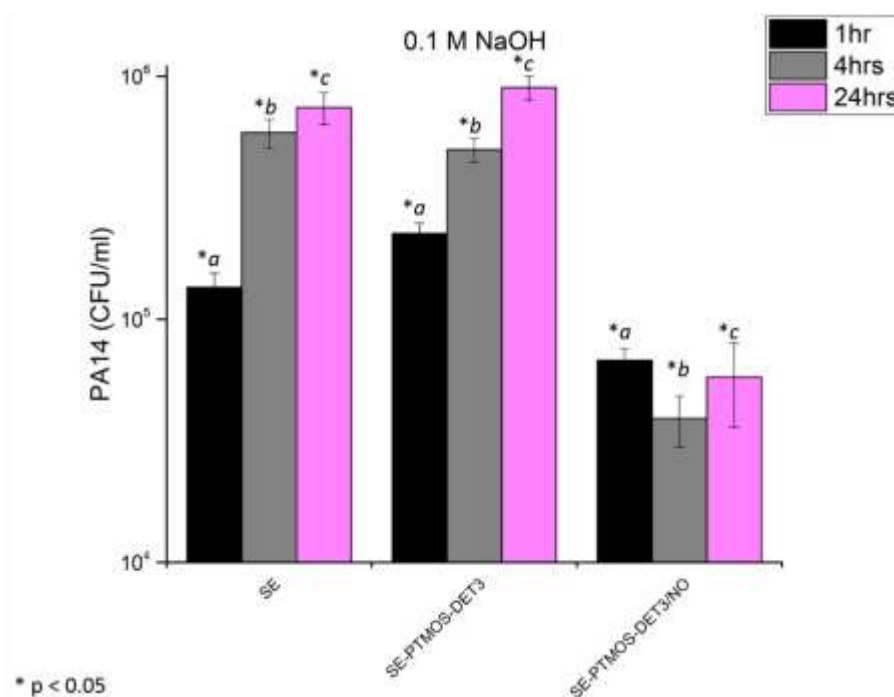


Figure 5.27: Viable *P. aeruginosa* (PA14) planktonic cell counts (CFU/ml) after 1 hr (black bars), 4 hr (grey bars) and 24 hr (pink bars) inoculation periods. The preformed *N*-diazoniumdiolate incorporated into SE-PTMOS-DET3/NO was formed using 0.1 M NaOH. The * symbol indicates the control surfaces that are significantly different to the NO-releasing surfaces at $p < 0.05$.

These results confirmed that NaOMe was responsible for the bactericidal effect observed in the non-releasing xerogel-coated control substrate, SE-PTMOS-DET3 and suggests that NaOH is the most suitable base in preforming the *N*-diazoniumdiolate.

5.5 Discussion

This chapter investigated two different approaches to increase the payload of NO. This was achieved by:

1. Investigating the effects of performing the *N*-diazoniumdiolate in the presence of a base before incorporation into the xerogel coating.
2. Formation of *N*-diazoniumdiolated xerogel coatings on the substrate surface to increase the surface area, thereby increasing the density of *N*-diazoniumdiolate groups on the surface.

5.5.1 Preformed *N*-Diazoniumdiolate Solutions

Performing the *N*-diazoniumdiolate with or without a base was investigated to see the effect it has on stabilising the *N*-diazoniumdiolate and therefore their NO release ability. The solutions were prepared with NaOMe, NaOH or in the absence of base and release profiles recorded at pH 4.

DET3/NO

The total NO payloads of DET3/NO when prepared with NaOMe, NaOH or in the absence of base were 25434 μmol , 26728 μmol and 8647 μmol , respectively. Whilst there was significant difference in maximum NO release between DET3/NO solutions with and without base, there was little difference in the shape of the NO release profiles. NO release returned to base levels after approximately the same length of time (11 hrs). Inter- and intramolecular amines can act as bases to facilitate *N*-diazoniumdiolate formation and stabilisation.¹⁴¹ DET3 contains two secondary amines and one primary, which can stabilise DET3/NO to some extent. Whilst the total payload of NO was significantly reduced with no base present the comparable release duration is most probably due to some intramolecular stabilisation. More importantly, it is clearly apparent that in the absence of base, NO storage and release capabilities are greatly hindered.

PTMSPA/NO

The total NO payloads of PTMSPA/NO when prepared with NaOMe, NaOH or in the absence of base were 592 μmol , 137 μmol and 7 μmol , respectively. When PTMSPA/NO was formed with NaOMe and NaOH the NO release was steady over 40 mins and 120 mins, respectively; whilst with no base the release was in the form of

a rapid and immediate burst. PTMSPA contains one secondary amine, which if *N*-diazoniumdiolated is unable to stabilise other *N*-diazoniumdiolate moieties intermolecularly, resulting in NO storage and release capabilities being greatly hindered.

5.5.2 *N*-diazoniumdiolated Xerogel Coatings

In this chapter, xerogel materials were fabricated with an alkylsilane/preformed *N*-diazoniumdiolated aminosilane solution using the sol-gel process. Schoenfisch has previously used this procedure to produce NO-releasing xerogel coatings for use in a wide range of applications such as: microarrays,²²⁰ orthopaedic implants¹⁶¹ and antibacterials.^{216, 221}

In Chapter 4, *N*-diazoniumdiolate-tethered surfaces were fabricated by aminosilanising polymer substrates then exposing them to NO gas *in situ*. In this chapter, a method of fabrication in which a preformed *N*-diazoniumdiolate is incorporated into a xerogel before being coated onto the substrate surface was employed. Reports show that forming the *N*-diazoniumdiolate as a preliminary step before coating them on to the substrate yielded 10x more NO upon release.¹⁴¹

5.5.2.1 Formation

The ease in material adaptation and modification and the mild synthesis conditions, such as low temperatures and use of aqueous solvents, make xerogels attractive as potential biomaterials.²²² Functionalised xerogels can be prepared using more than one precursor silane. By hydrolysing and co-condensing an alkylsilane and a pre-modified aminosilane (preformed *N*-diazoniumdiolates), xerogel coatings with tuneable NO storage and release potential were fabricated.

Schoenfisch *et al.* previously reported that a one-step hydrolysis and co-condensation of both silanes led to instabilities arising from poor connectivity between the alkylsilane and the preformed *N*-diazoniumdiolate.¹⁴¹ This was most likely due to the hydrolysis rates and thus gelation times of aminosilanes being considerably faster than alkylsilanes.²²³ In this work, a two-step, one-pot reaction in which the alkylsilane (PTMOS) was pre-hydrolysed before adding the preformed *N*-diazoniumdiolate allowed for better matched reaction kinetics between the two silanes during co-condensation.

The preformed *N*-diazoniumdiolate concentration and the total silane to water concentration are two factors that have to be controlled. Xerogels were fabricated with 4 % mol preformed *N*-diazoniumdiolate concentrations; it was reported previously that larger concentrations led to unstable xerogels regardless of parameters changed in the synthetic process.¹⁴¹ In order to optimise the total silane to water concentration ratio, preliminary tests were carried out by synthesising PTMOS-DET3 and PTMOS-PTMSPA sol-gels with varying water content (Section 5.2.3). Schoenfisch *et al.* showed that this ratio was dependent on the nature of the two silanes undergoing co-condensation and the compatibility of their reaction kinetics;¹⁴¹ cracking was observed when using methyltrimethoxysilane (MTMOS), whilst isobutyltrimethoxysilane (BTMOS) remained viscous and tacky.¹⁴¹ The latter was observed to be true in this work at a range of different silane to water ratios. A silane to water ratio of 1:3.2 for both PTMOS-DET3 and PTMOS-PTMSPA gave transparent sols with short gelation times. The subsequently formed xerogels were transparent and non-tacky.

In order to produce xerogels, sol-gels are aged and dehydrated.²²² The environment in which the sol-gels are dried is of paramount importance in producing xerogels with desirable biomaterial properties. Cracking of the xerogels is one of the most common problems observed during the drying phase, due to the pressure gradient caused as a result of solvent evaporation.^{224, 225} The evaporation rate was controlled by drying the sol-gels mildly at 60 °C under vacuum for 3 days and the resulting xerogels were not cracked.

5.5.2.3 NO Release

The *N*-diazoniumdiolated xerogel coatings were tested under a number of different experimental conditions. In Chapter 4 the enhanced NO-release capabilities of SE-DET3/NO compared to SE-PTMSPA/NO was apparent. The same relationship was seen between xerogels made using DET3/NO and PTMSPA/NO: Due to increased number of amine sites and additional inter-/intramolecular stabilisation, SE-PTMOS-DET3/NO released more NO over a more prolonged period than SE-PTMOS-PTMSPA/NO, at both pH 4 and pH 7.4.

The temperature dependency on *N*-diazoniumdiolate decomposition and NO release was also assessed. For SE-PTMOS-DET3/NO approximately 2-fold increase for maximum and total NO release was observed when increasing the temperature from 25 °C to 37 °C; for SE-PTMOS-PTMSPA/NO, the increase was around 10-fold. Hrabie *et al.* observed a temperature dependence of *N*-diazoniumdiolate decomposition and NO release, with increases of up to 9-fold when temperatures were raised from 22 °C to 37 °C.¹⁴⁰ This observation is most likely due to the small increases in pH when temperature is increased.

The NO release capabilities of SE-PTMOS-DET3/NO were also assessed when either 0.5 M NaOMe, 0.1 M NaOH or no base was used in performing the DET3/NO solution. The maximum and total NO release when using NaOMe was comparable to as when using NaOH. It was clearly apparent that xerogels formed when using no base in the preformed *N*-diazoniumdiolate solution greatly hindered the NO release storage and release capabilities of the materials, however low-level steady release was observed, due to inter-/intramolecular catalysis and stabilisation.¹⁴¹

5.5.3 Bacterial Response

In Chapter 4, *N*-diazoniumdiolates were bound to polymeric substrates with low level NO release and showed the ability to prevent bacterial cell adhesion and the biofilm formation on the surface. The aim of this chapter was to assess the bacterial response of materials with increased NO storage and release capabilities. A number of problems arose during assessment of the bacterial response and this section outlines these and the modifications made to the experimental method to ascertain a valid result.

5.5.3.1 Adhered Cell CFU Assay (LB Media)

The high releasing *N*-diazoniumdiolated xerogels were first tested against PA14 in fresh LB media to determine the viable cell count on the surface after 24 hrs. Based on several reports in the literature, it was expected that the enhanced NO flux of the xerogel coatings would lead to a bactericidal effect and improve antibacterial efficacy however in the first assay performed this was not the case.^{226, 227} The experiments carried out here showed no reduction in viable adhered cells. This was in

corroboration with Brooun *et al.* who reported that bacteria are often able to recover when grown in fresh rich media.²¹⁹

5.5.3.2 Planktonic and Adhered Cell CFU Assays (Phosphate Buffered Saline)

Due to the prior result, the assay was modified by changing the inoculating medium from LB broth to phosphate buffered saline (PBS). Both planktonic and adhered cells were counted, to determine bactericidal and anti-adhesion efficacy of the surfaces, respectively. Indeed, the bacteria did not appear to recover and statistically significant reductions in both planktonic and adhered cell counts compared to pristine SE were apparent. A new problem did however arise upon transition to PBS as the inoculating medium: the non-releasing xerogel-coated control substrate (SE-PTMOS-DET3) exhibited a complete bactericidal effect when comparing counts to pristine SE. Whilst SE-PTMOS-DET3/NO surfaces exhibited at least 99 % reduction in planktonic and adhered cell counts at all time points compared to pristine SE, the involvement of NO could not be conclusively determined. One possible explanation is that the decomposition of the coating caused leaching of the NaOMe which exhibited a bactericidal effect, due to the methanol by-product formed. The same bactericidal effect was not observed by the other non-releasing xerogel-coated control substrate (SE-PTMOS-PTMSPA) and no significant reduction in cell counts for the *N*-diazoniumdiolated xerogel-coated substrates (SE-PTMOS-PTMSPA/NO) was observed; most likely due to the short NO release durations (≈ 2 hrs).

When performing the *N*-diazoniumdiolate, 1 mol equivalent of NaOMe was used for every secondary amine in the aminosilane precursor.¹⁴¹ This was to ensure all *N*-diazoniumdiolate moieties would be stabilised through the equimolar availability of Na⁺ counter cations. The lower concentration of NaOMe used in the synthesis process, due to PTMSPA only containing one secondary amine and requiring only half the concentration of NaOMe as used when forming DET3/NO solutions, is most likely the reason that no bactericidal activity was observed by SE-PTMOS-PTMSPA, but was by SE-PTMOS-DET3.

5.5.3.3 Effect of Base on Bactericidal Activity.

The results from the assays carried out in PBS led to a study in which *N*-diazoniumdiolated xerogel coatings were made with preformed DET3/NO solutions

using NaOH instead of NaOMe and tested against planktonic *P. aeruginosa* (PA14). Xerogels prepared when the preformed *N*-diazoniumdiolate solution was prepared in the absence of base (control) showed no significant reduction in viable cell count after 24 hrs. This can be attributed to the reduced NO release rates observed when no counter cation is present to stabilise the *N*-diazoniumdiolate.

When NaOH was used, the cell counts exhibited in the presence of the non-releasing xerogel-coated substrate (SE-PTMOS-DET3) showed no difference, statistically, to pristine SE, meaning the results acquired from the NO-releasing surfaces could be directly attributed to the presence of NO. A reduction in viable planktonic cells was observed at all time points and by 24 hrs this was > 1-log. These surfaces released total payloads of 3866 μmol after 22 hrs and so were above the minimum bactericidal concentration previously seen in other reports.¹⁶³ These xerogels did however become completely delaminated from the surface of the SE substrate, possibly due to NaOH causing silanol cleavage at the substrate surface; it was therefore not possible to carry out adhered cell CFU assays and the xerogels were considered unsuitable as coatings for medical implant devices.

5.6 Conclusion

The aim of this chapter was to create xerogel coatings that had greater NO storage and release potential than the *N*-diazoniumdiolate-tethered polymer substrates fabricated in Chapter 4 and assess the antibacterial advantages these may possess. The sol-gel process was optimised through various parametric alterations to give non-tacky, transparent, NO-releasing *N*-diazoniumdiolated xerogel coatings immune to cracking. *N*-diazoniumdiolates were formed prior to attaching to the SE substrate using NaOMe/NaOH to stabilise the *N*-diazoniumdiolate moiety and prevent premature decomposition. Xerogels made in this way released micromolar concentrations of NO for prolonged durations, dependent on aminosilane structure, temperature and pH. SE-PTMOS-DET3/NO released concentrations an order of magnitude higher than SE-PTMOS-PTMSPA/NO at physiological conditions.

The xerogel coatings were first tested for their ability to prevent biofilm formation. The surfaces were inoculated with a bacterial suspension in LB media, however due

to bacterial recovery no significant reduction in adhered cells on *N*-diazoniumdiolated xerogel coated SE substrates was seen after 24 hrs. A transition to PBS as the inoculation medium led to observable significant reductions of non-growing planktonic and adhered bacteria on SE-PTMOS-DET3 and SE-PTMOS-DET3/NO compared to pristine SE. Complete eradication of bacteria was seen when tested against SE-PTMOS-DET3 controls, so it was not possible to decisively determine whether the antibacterial behaviour exhibited by SE-PTMOS-DET3/NO was a direct result of NO release. SE-PTMOS-PTMSPA/NO showed no reduction compared to pristine (SE) or non-releasing xerogel-coated (SE-PTMOS-PTMSPA) substrates. Further bactericidal assays were carried out using *N*-diazoniumdiolated xerogels that had used different bases when performing the *N*-diazoniumdiolate. When NaOH was employed instead of NaOMe, the planktonic cell count of SE-PTMOS-DET3 was the same, statistically, as pristine SE, indicating that NaOMe was the cause of bacterial cell death. After 24 hrs, planktonic PA14 cells tested against SE-PTMOS-DET3/NO (NaOH) were reduced by 93 % compared to controls, proving that surfaces releasing high levels of NO have great bactericidal efficacy. Adhered cell CFU assays could not be performed on xerogels made with NaOH, however, due to delamination from the substrate surface.

Whilst the aims of this chapter, in terms of surface modification, were achieved in creating high concentration NO-releasing *N*-diazoniumdiolated xerogels and a definitive conclusion concerning the bactericidal abilities of NO could be drawn; these particular materials could not be considered as coatings for medical implant devices, due to their physical instability.

Chapter 6: Polymer Demixed Films with Micro-/Nanotopographies to Control Bacterial Response

6.1 Introduction

In Chapters 4 and 5 polymer substrates were modified chemically to produce antibacterial NO-releasing surfaces that exhibited bactericidal and anti-adhesion effects. In Chapter 6, medically relevant polymer films have been modified physically, using the polymer demixing process, to assess their ability to prevent biofilm formation.

Polymer demixing is a low cost and efficient method in producing binary polymer films. This process utilises the immiscibility of polymers in a blend to form films with distinct topographies and wettabilities (Figure 6.1).²²⁸

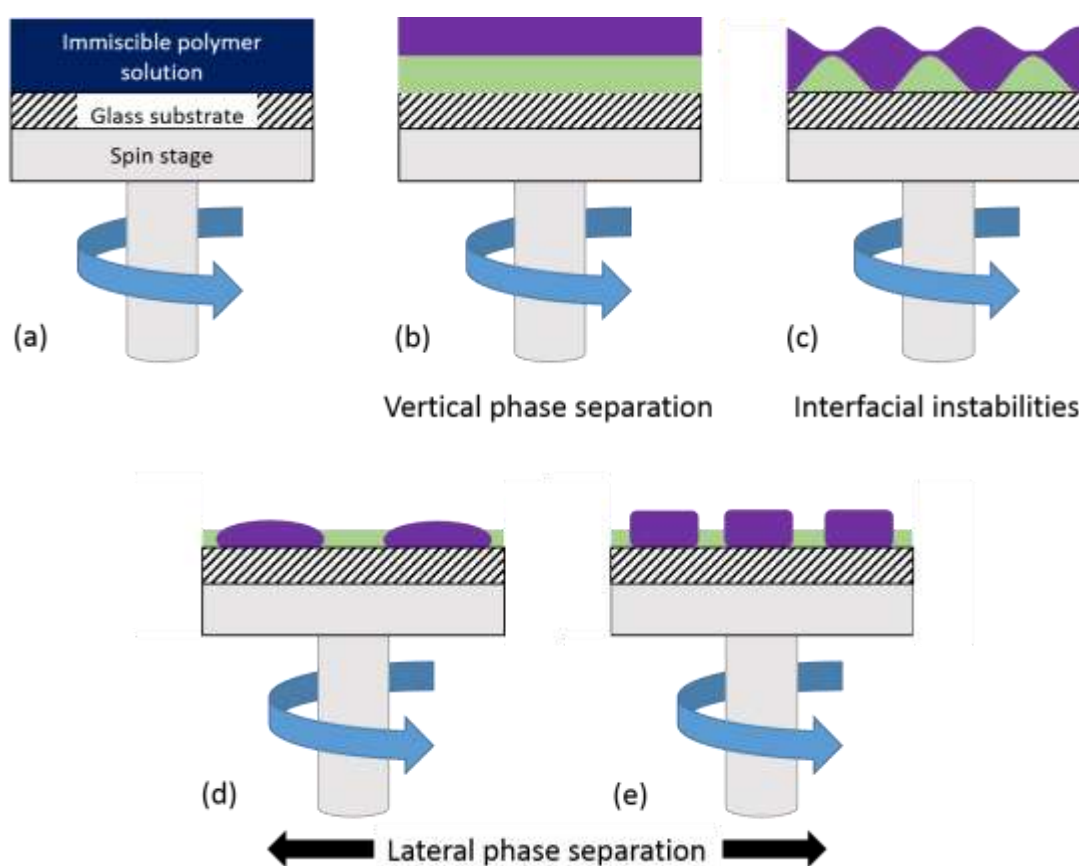


Figure 6.1: The polymer demixing process: a solution of two immiscible polymers is spun down and after an initial spin-off (a) the film splits vertically into two layers (b). Interfacial instabilities then occur between the polymer layers (c) leading to lateral phase separation (d),(e). [Adapted from Ref. 228]

Two or more immiscible polymers are dissolved in a common solvent and spin coated on to a substrate (Fig. 6.1 a). In a binary polymer blend, one polymer will segregate to the air interface and one to the substrate interface (Fig. 6.1 b). The nature of this phase separation and the interfacial instabilities and interactions (Fig. 6.1 c) that occur will determine the resulting surface topography (Fig. 6.1 d), (Fig. 6.1 e). There are a whole host of parameters that can be changed in this process, to give a vast array of surface topographies. These include: solvent type, polymer system, relative polymer concentrations and substrate used.

Before biofilm formation can occur bacteria must first irreversibly adhere to a surface. There are many factors which affect the ability of the bacteria to do this. Cell-surface interactions can be influenced by the surface topography of a material, particularly by micro-/nanotopographical surface structures. Studies by Hochbaum and Aizenberg and Lu *et al.* have shown there is a relationship between the size of bacteria and the size and spacing of the surface structure and bacteria will organise themselves on the surface in order to maximise their cell-surface contact area.^{55, 180}

In this chapter, surfaces with distinct topographies were fabricated by altering the relative polymer concentrations of three different polymers in binary blends: Polystyrene (PS), polycaprolactone (PCL) and poly(methyl methacrylate) (PMMA) to form PS/PCL, PS/PMMA and PCL/PMMA polymer demixed films. The antibacterial performance of these surfaces has been assessed in terms of their anti-adhesion abilities after 24 hrs to see if biofilm formation can be prevented.

6.2 Experimental

6.2.1 Preparation of Polymer Demixed Thin Films

Glass coverslips (13 mm diameter) were cleaned by immersing them in 5 % NaOH for 30 mins, followed by concentrated HNO₃ for 30 mins. Coverslips were then washed in EtOH (4 x 2 min), rinsed in DI water and dried at 80 °C. Coverslips were then treated with oxygen plasma for 1 min.

PS, PCL and PMMA were dissolved in chloroform (CHCl₃) to give 5 % w/v stock solutions. 1 % w/v binary blend solutions of PS/PCL, PS/PMMA and PCL/PMMA were made by diluting and mixing the stock solutions in the following ratios: 0:100, 25:75,

50:50, 75:25 and 100:0. Aliquots of the blend solutions (70 μ l) were spin coated onto freshly cleaned coverslips at 4000 rpm for 2 min, using an SCS 6800 spin coater (Speciality Coating Systems Inc, IN, USA). Spin coated films were dried in a vacuum desiccator at room temperature overnight, to allow evaporation of any remaining CHCl_3 .

6.3 Results: Characterisation

In this chapter, PS/PCL, PS/PMMA and PCL/PMMA polymer demixed films in ratios of 0:100, 25:75, 50:50 and 75:25 were fabricated with micro-/nanotopographical surface features on a comparable length scale to bacteria for which to study bacterial response. In this section, the chemical and topographical surface analysis results of the demixed films have been presented.

6.3.1 Wettability: Contact Angle

The wettability of the surfaces was determined using static contact angle analysis. The contact angles of 100 % polymer films are recorded in Table 6.1 with the corresponding polymer demixed films in Table 6.2. PS100 exhibited the greatest hydrophobicity, with a contact angle of 83.8° . A reduction in contact angle was observed for PCL100 and PMMA100 with values of 76.2° and 68.9° , respectively. For both PS/PCL and PS/PMMA demixed films an increase in contact angle was observed as the concentration of PS was increased. As the concentration of PCL was increased in the PCL/PMMA demixed films the contact angle too increased, showing an expected increase in hydrophobicity.

Table 6.1: Static water contact angle measurements for 100 % polymer films.

	Contact Angle ($^\circ$)
PS100	83.8 ± 1.5
PCL100	76.2 ± 1.2
PMMA100	68.9 ± 1.6

Table 6.2: Static water contact angle measurements of polymer demixed films with varying ratios.

	Contact Angle (°)		
	PS:PCL	PS:PMMA	PCL:PMMA
25:75	71.8±3.6	70.0±1.0	67.2±2.4
50:50	72.9±3.8	68.6±2.4	71.4±1.2
75:25	81.4±2.3	81.1±5.3	72.7±2.8

6.3.2 Surface Chemistry: FTIR

The surface chemistry of 100 % polymer films and polymer demixed films was determined using FTIR and representative spectra are displayed in Figures 6.2-6.4. The resulting spectrum of PS100 (Fig. 6.2 and 6.3) exhibited peaks at 3026 cm^{-1} , due to the aromatic C-H stretching vibration and 2925 cm^{-1} due to the aliphatic C-H stretch. The PCL100 spectrum is displayed in Figures 6.2 and 6.4: Bands at 2948 cm^{-1} and 2865 cm^{-1} are characteristic of asymmetric and symmetric CH_2 stretching, respectively. A strong peak at 1726 cm^{-1} was observed due to the carbonyl stretching mode of PCL. Figures 6.3 and 6.4 display the spectrum of PMMA100. Peaks observed at 2996 cm^{-1} and 2950 cm^{-1} are due to C-H stretching vibrations of CH_3 and CH_2 , respectively. The band at 1732 cm^{-1} confirmed the presence of the acrylate carboxyl group.²²⁹

Figure 6.2 displays FTIR spectra of PS/PCL demixed films in varying ratios (PS25PCL75, PS50PCL50, PS75PCL25). In the PS25PCL75 spectrum a broad peak was seen with its apex at 2948 cm^{-1} , next to a peak at 2864 cm^{-1} , due to symmetric and asymmetric CH_2 stretching of PCL, respectively. As the concentration of PS was increased, the intensity of the band at 1726 cm^{-1} decreased, as PS does not have any carbonyl functional groups in its backbone.

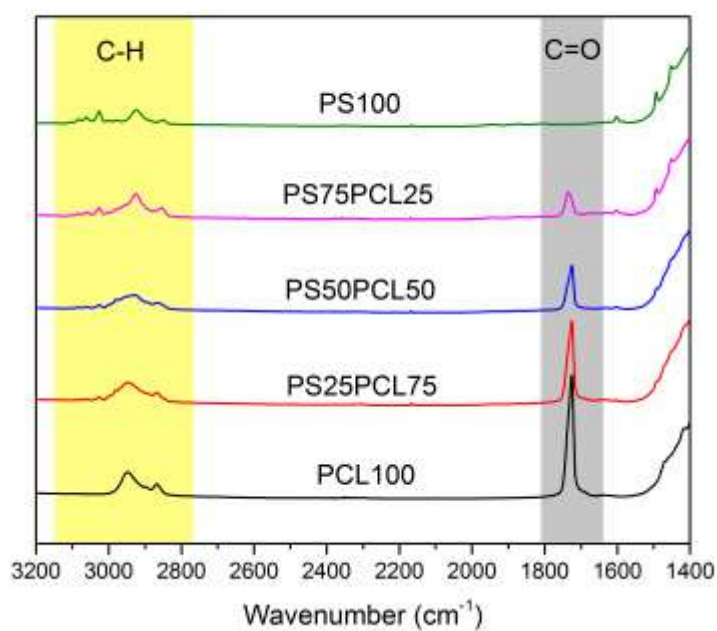


Figure 6.2: FTIR spectra of PS/PCL polymer demixed films.

Figure 6.3 displays FTIR spectra of PS/PMMA demixed films in varying ratios (PS25PMMA75, PS50PMMA50, PS75PMMA25). In PS25PMMA75 peaks were observed at 2997 cm^{-1} and 2950 cm^{-1} , indicative of the C-H stretching vibrations of CH_3 and CH_2 , respectively. As the relative concentration of PS was increased, the emergence of a peak at 3026 cm^{-1} , was attributed to an aromatic C-H stretching. The resulting peak of the PMMA carboxyl stretch at 1732 cm^{-1} was present in all spectra, except PS100.

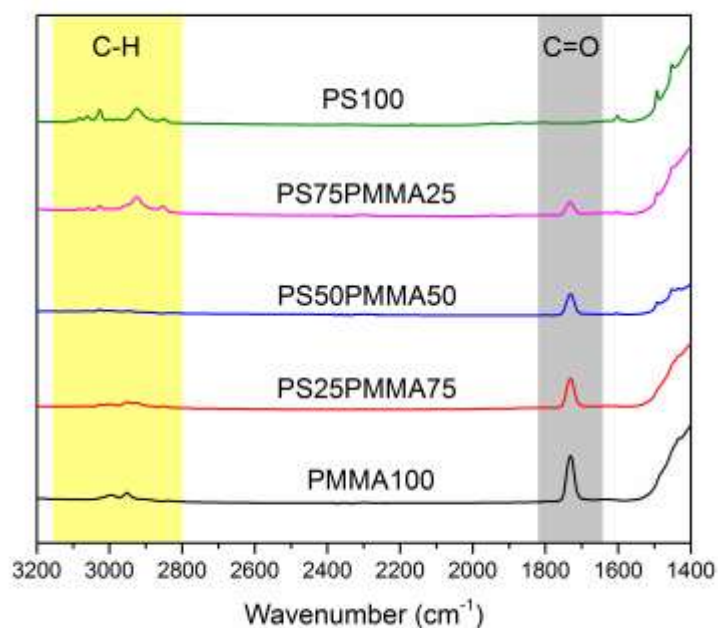


Figure 6.3: FTIR spectra of PS/PMMA polymer demixed films.

Figure 6.4 displays FTIR spectra of PCL/PMMA demixed films in varying ratios (PCL25PMMA75, PCL50PMMA50, PCL75PMMA25). The two CH₂ stretching bands of PCL, at approximately 2950 cm⁻¹ and 2865 cm⁻¹ were seen in the spectra of each film. For PCL25PMMA75, a shoulder was observed on the peak at 2950 cm⁻¹, at 2993 cm⁻¹, due to the increased relative concentration of PMMA, resulting in the presence of the band due to CH₃ stretching. In these spectra, a peak was also seen at 1732-1728 cm⁻¹, with wavenumber depending on the origin of the C=O group. When the concentration of PCL was increased the peak was downshifted from 1732 cm⁻¹ (PCL25PMMA75) to 1728 cm⁻¹ (PCL75PMMA25), as the major C=O contributing polymer shifts from PMMA to PCL.

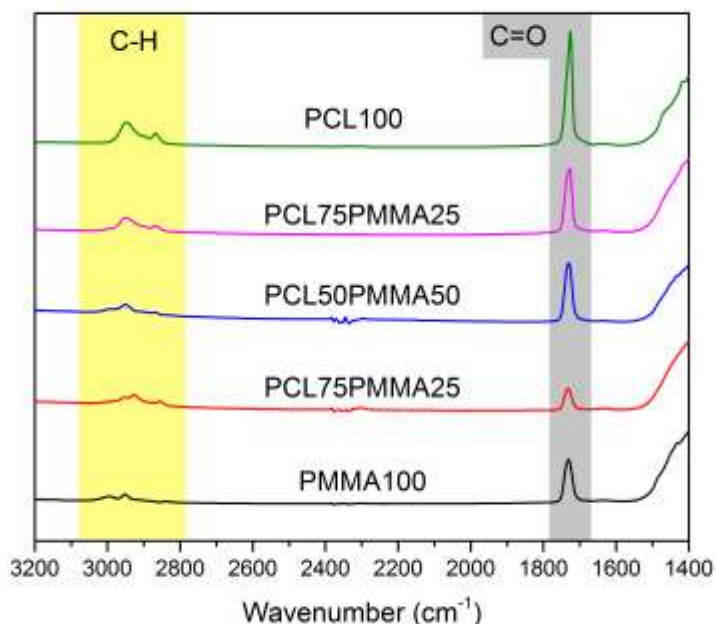


Figure 6.4: FTIR spectra of PCL/PMMA polymer demixed blends.

6.3.3 Surface Chemistry: XPS

The surface compositions of the polymer demixed films were determined by XPS analysis. The spectra of the C 1s and O 1s high resolution scans are given in Figures 6.5 - 6.7.

Curve fitting of the C 1s spectra for PS100 (Fig. 6.5 (e) and 6.6 (e)) gave three components: aromatic C-C/C-H at 285.0 eV, aliphatic C-C/C-H at 285.6 eV and the $\pi - \pi^*$ shakeup at 291.7 eV.²³⁰ For PCL100 (Fig. 6.5 (a) and 6.7 (e)), the C 1s spectra was curve fitted into four components: C-C/C-H at 285.0 eV, β -shifted C at 285.5 eV, C-O at 286.3 eV and C=O at 289.1 eV.²³¹ The C 1s envelope of PMMA100 (Fig. 6.6 (a) and 6.7 (a)) was fitted into four components: C-C/C-H at 285.0 eV, β -shifted C at 285.5 eV, C-O at 286.3 eV and C=O at 289.1 eV.²³² Curve fitting of the O 1s spectra for both PCL100 and PMMA100 gave two components at 532.1 and 533.7, due to the carbonyl (O=C) and ether (O-C) constituents of the ester groups, respectively.

The spectra of the C 1s and O 1s high resolution XPS scans for PS/PCL demixed films are given in Figure 6.5 and the resulting quantitative data is given in Tables 6.3 and 6.4. The peak contribution from aromatic and aliphatic C-C/C-H increased as the PS concentration increased, from 58 % in PCL100 reaching 93.8 % in PS100. The $\pi - \pi^*$ shakeup not observed in PCL100 also increased as PS concentration increased, from 0.7 % in PS25PCL75 up to 6.2 % in PS100. The PCL-specific C-O and C=O component contributions decreased from 8.1 % and 15.7 % to 4.6 % and 1.6 %, respectively, going from PCL100 to PS75PCL25.

Table 6.3: XPS derived at. % of C 1s and O 1s regions for PS/PCL demixed films.

	at. %	
	C 1s	O1s
PCL100	77.4±0.6	22.6±0.6
PS25PCL75	77.6±4.1	22.4±4.1
PS50PCL50	79.8±4.5	20.2±4.5
PS75PCL25	90.1±4.7	9.9±4.7
PS100	100±0.0	-

Table 6.4: XPS-derived at. % of curve-fitted C 1s components for PS/PCL demixed films.

	C 1s Component % (Binding energy, eV)				
	C-C/C-H aliphatic (285.0)	β -shifted C (C-C/C-H aromatic) ^a (285.5)	C-O (286.3)	C=O (289.1)	$\pi - \pi^*$ (291.6)
PCL100	56.0±3.9	15.9±0.7	8.1±2.5	15.7±0.6	-
PS25PCL75	54.4±4.4	21.7±4.7	13.1±0.6	10.2±0.3	0.7±0.2
PS50PCL50	69.3±7.5	15.7±7.5	8.4±0.5	5.6±0.5	1.3±0.4
PS75PCL25	55.9±2.9	34.0±2.9	4.6±0.5	1.6±0.7	3.7±0.7
PS100	69.7±0.6	24.1±0.3 ^a	-	-	6.2±0.3

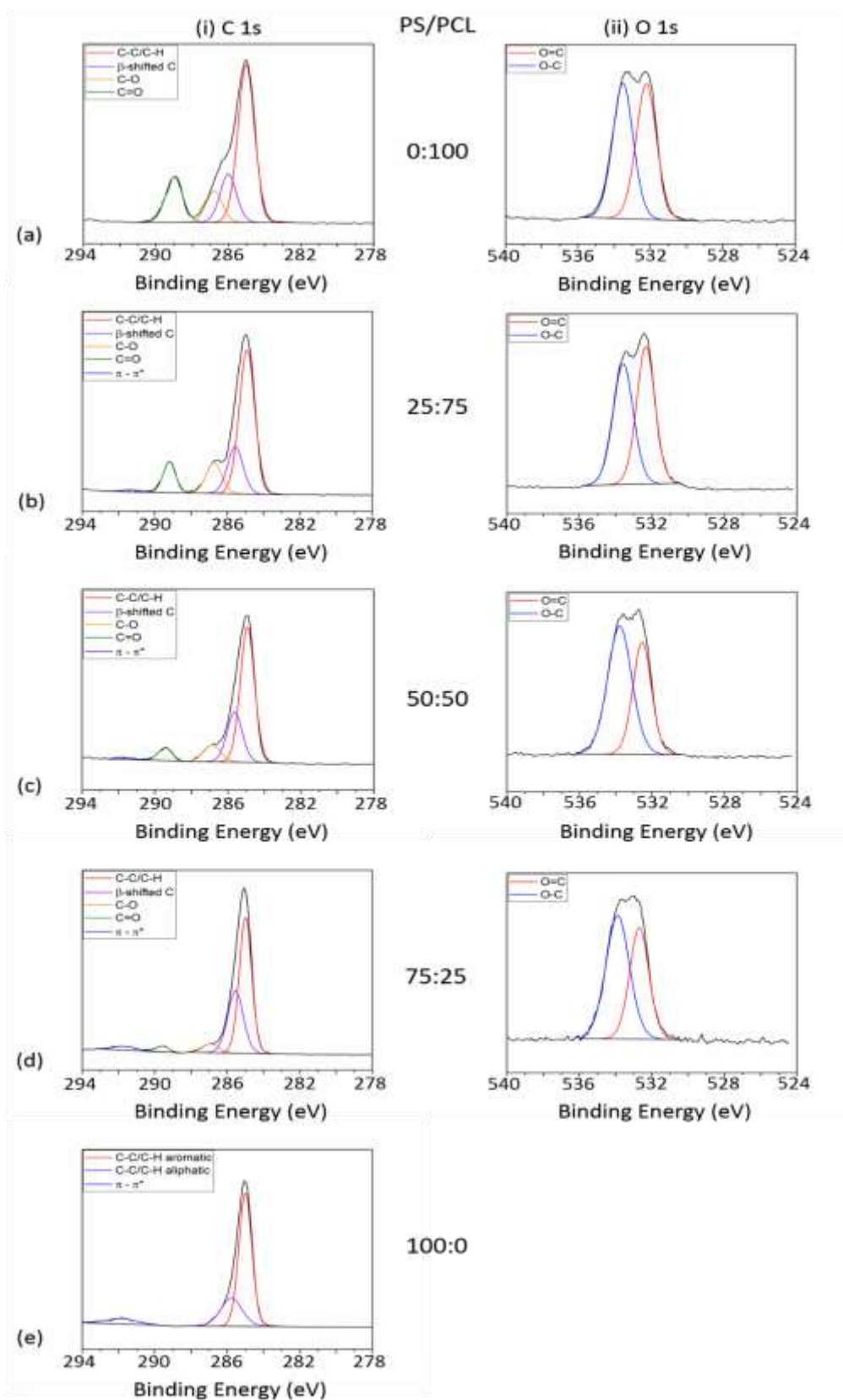


Figure 6.5: Curve-fitted (i) C 1s and (ii) O 1s XPS spectra for PS/PCL polymer demixed films in ratios of (a) 0:100 (b) 25:75 and (c) 50:50 (d) 75:25 and (e) 100:0.

The spectra of the C 1s and O 1s high resolution XPS scans for PS/PMMA demixed films are given in Figure 6.6 and the resulting quantitative data is given in Tables 6.5 and 6.6. The C-C/C-H contribution of the PS/PMMA blends increased as the concentration of PS increased. The three PMMA specific components are β -shifted C, C-O and $\underline{\text{C}}=\text{O}$. There was no significant difference in the contribution of β -shifted C for PS25PMMA75 or PS75PMMA25. The contribution of the $\underline{\text{C}}-\text{O}$ and $\underline{\text{C}}=\text{O}$ decreased by 9.2 % and 8.7 %, respectively. The peak due to $\pi - \pi^*$ shakeup was not observed in PS25PMMA75. The shakeup contributed 1.2 % of the PS50PMMA50 C 1s envelope and 2.0 % of PS75PMMA25.

Table 6.5: XPS derived at. % of C 1s and O 1s regions for PS/PMMA demixed films.

	at. %	
	C 1s	O1s
PMMA100	75.8±1.2	24.2±1.2
PS25PMMA75	77.5±0.5	22.5±0.5
PS50PMMA50	77.7±3.6	22.3±3.6
PS75PMMA25	85.3±2.6	14.7±2.6
PS100	100±0.0	-

Table 6.6: XPS-derived at. % of curve-fitted C 1s components for PS/PMMA demixed films.

	C 1s Component % (Binding energy, eV)				
	C-C/C-H aliphatic (285.0)	β -shifted C (C-C/C-H aromatic) ^a (285.5)	C-O (286.3)	C=O (289.1)	$\pi - \pi^*$ (291.6)
PMMA100	38.0±1.3	21.0±1.8	21.4±2.0	19.6±1.0	-
PS25PMMA75	43.5±3.1	23.0±4.2	18.3±1.0	15.2±1.0	-
PS50PMMA50	54.7±4.5	18.0±5.7	15.1±1.5	10.8±0.6	1.2±0.1
PS75PMMA25	62.2±3.7	20.2±1.3	9.1±3.5	6.5±2.2	2.0±0.6
PS100	69.7±0.6	24.1±0.3 ^a	-	-	6.2±0.3

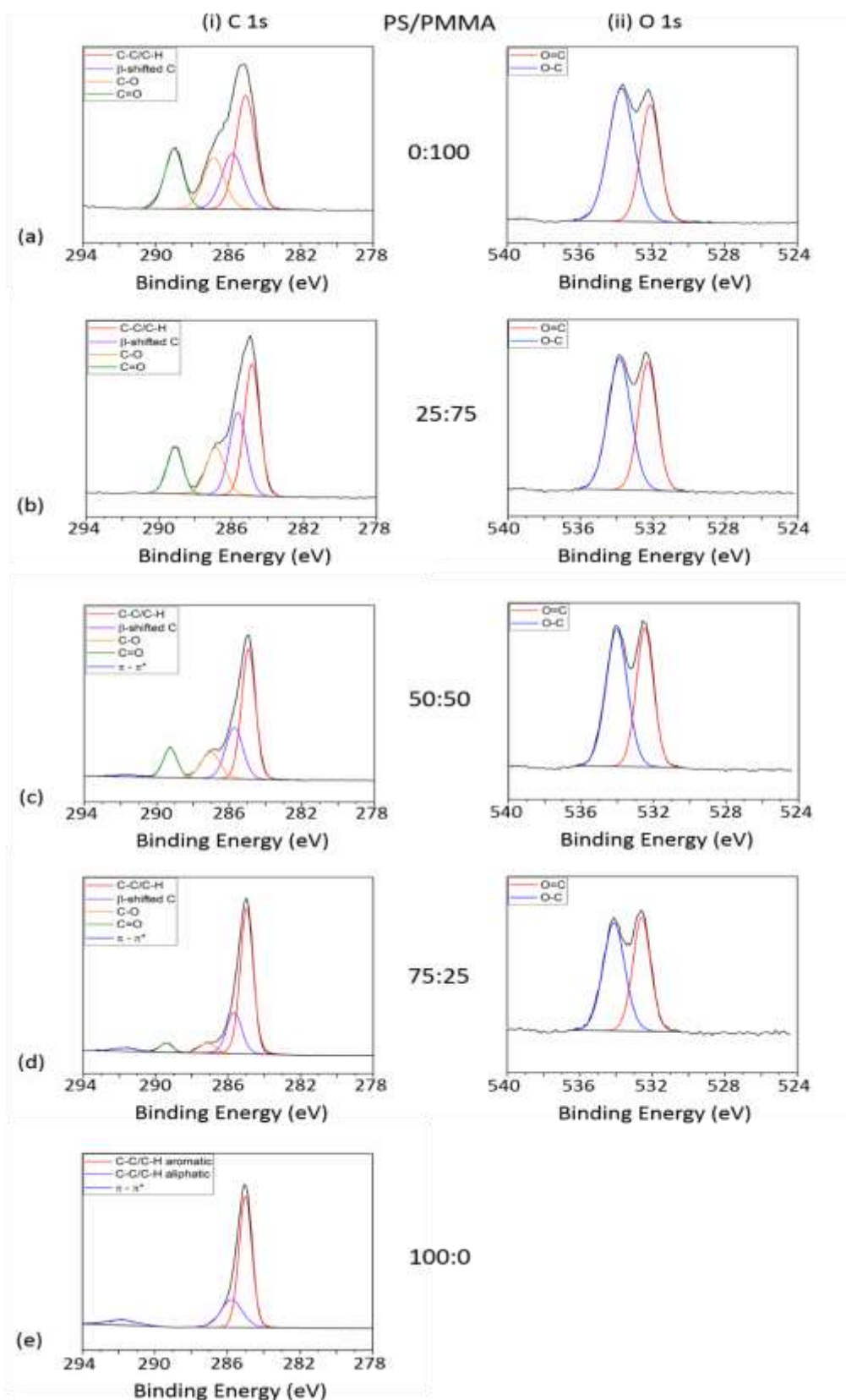


Figure 6.6: Curve-fitted (i) C 1s and (ii) O 1s XPS spectra for PS/PMMA polymer demixed films in ratios of (a) 0:100 (b) 25:75 (c) 50:50 (d) 75:25 and (e) 100:0.

The spectra of the C 1s and O 1s high resolution XPS scans for PCL/PMMA demixed films are given in Figure 6.7 and the resulting quantitative data is given in Tables 6.7 and 6.8. The C 1s spectra for PCL/PMMA demixed films was curve fitted into four components: C-C/C-H, β -shifted C, C-O and C=O. There was no significant difference in the contribution of the C-C/C-H component for any of the blends (44.2 % - 44.5 %), however the contribution was greater than PMMA100 (38.0 %) and less than that from PCL100 (56.0%). There was no significant difference in at. % contribution of the β -shifted C, C-O and C=O peaks

Table 6.7: XPS derived at. % of C 1s and O 1s regions for PCL/PMMA demixed films.

	at. %	
	C 1s	O1s
PMMA100	75.8±1.2	24.2±1.2
PCL25PMMA75	74.3±1.0	25.7±1.0
PCL50PMMA50	75.9±0.8	24.1±0.8
PCL75PMMA25	76.4±0.1	23.6±0.1
PCL100	77.4±0.6	22.3±0.6

Table 6.8: XPS-derived at. % of curve-fitted C 1s components for PCL/PMMA demixed films.

	C 1s Component % (Binding energy, eV)			
	C-C/C-H aliphatic (285.0)	β -shifted C (285.5)	C-O (286.3)	C=O (289.1)
PMMA100	38.0±1.3	21.0±1.8	21.4±2.0	19.6±1.0
PCL25PMMA75	44.5±1.8	18.3±0.6	19.1±0.6	18.4±0.2
PCL50PMMA50	44.5±1.8	17.7±0.8	20.0±3.0	17.8±0.4
PCL75PMMA25	42.2±4.8	21.4±4.2	19.2±0.7	17.3±0.2
PCL100	56.0±3.9	15.9±0.7	8.1±2.5	15.7±0.6

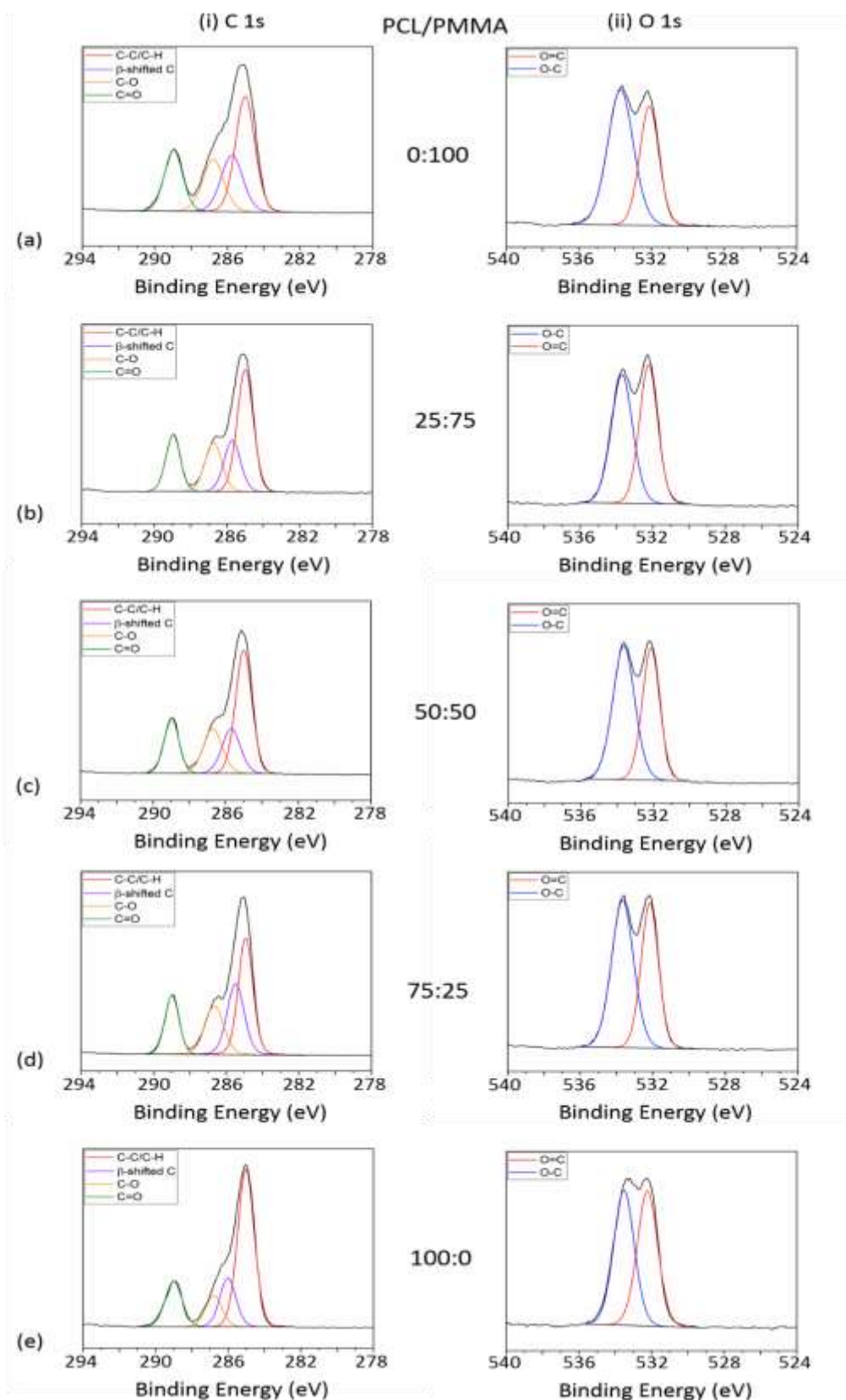


Figure 6.7: Curve-fitted (i) C 1s and (ii) O 1s XPS spectra for PCL/PMMA polymer demixed films in ratios of (a) 0:100 (b) 25:75 (c) 50:50 (d) 75:25 and (e) 100:0.

6.3.4 Surface Topography: AFM

The surface topography of the polymer demixed films was examined by AFM, and representative images and roughness values (R_q , R_a) are displayed in Figures 6.8 – 6.10. AFM derived data, including surface feature dimensions are presented in Tables 6.9 - 6.11. Both PS100 and PMMA100 produced smooth films both with roughness values of $R_q = 0.3$ nm, $R_a = 0.2$ nm. The PCL100 film was rougher in relation ($R_q = 5.2$ nm, $R_a = 3.7$ nm).

Figure 6.8 shows the representative images and corresponding roughness values (R_q , R_a) of PS/PCL polymer demixed films in varying ratios. The roughness values of PS25PCL75 ($R_a = 14.4$ nm), PS50PCL50 ($R_a = 18.7$ nm) and PS75PCL25 ($R_a = 18.9$ nm) were all seen to increase when compared to their corresponding 100 % polymer controls. When PCL was in abundance, island structures were observed with dimensions averaging 48 nm in height and 185 nm in diameter. With PS in abundance a pit-like topography was observed with features averaging 65 nm in height and 711 nm in diameter. When the polymer concentrations were equal, the topography observed was ribbon-like. The height and diameter of these ribbons averaged 72 nm and 609 nm, respectively.

Table 6.9: Topographical data for PS/PCL demixed films determined by AFM

	Topography	Feature height/depth (nm)	Feature diameter (nm)	Feature spacing (nm)
PCL100	flat	-	-	-
PS25PCL75	islands	48±20	185±53	197±69
PS50PCL50	ribbons	65±14	609±185	381±237
PS75PCL25	pits	72±19	711±239	248±152
PS100	flat	-	-	-

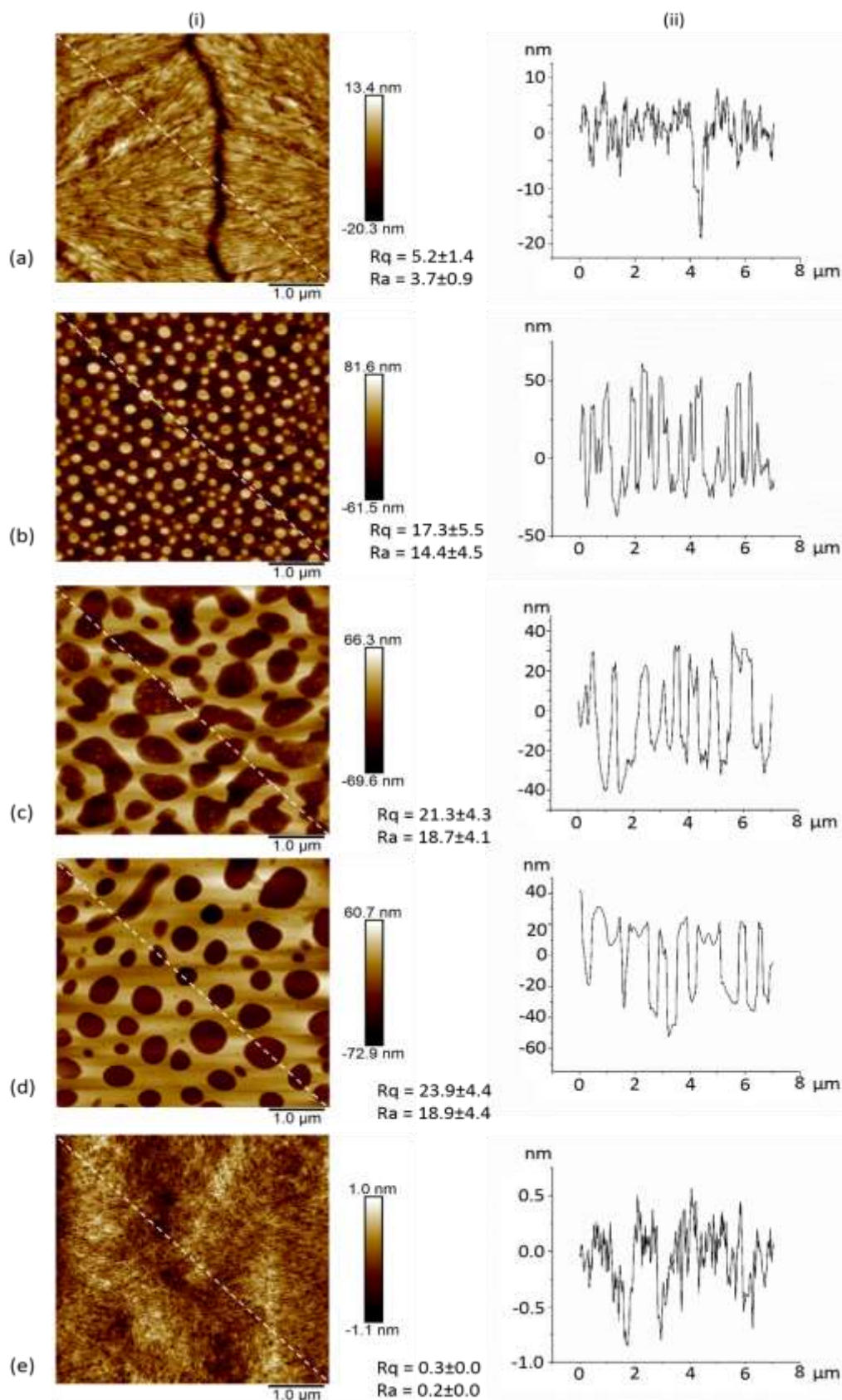


Figure 6.8: AFM (i) 3D images and (ii) depth profiles of PS/PCL polymer demixed films in ratios (a) 0:100 (b) 25:75 (c) 50:50 (d) 75:25 and (e) 100:0.

Figure 6.9 shows the representative images and corresponding roughness values (R_q , R_a) of PS/PMMA polymer demixed films in varying ratios. The roughness values of PS25PMMA75 ($R_a = 2.2$ nm), PS50PMMA50 ($R_a = 2.5$ nm) and PS75PMMA25 ($R_a = 2.7$ nm) were all seen to increase when compared to their corresponding 100 % polymer controls. In this blend system, when PMMA was in a greater concentration, islands were formed averaging 7 nm in height with a diameter of 160 nm. When the polymers were in equal concentration pits were formed, 8 nm in height and 118 nm in diameter. The pit structures were also seen when PS was in abundance with features averaging 11 nm in height and 190 nm in diameter.

Table 6.10: Topographical data for PS/PMMA demixed films determined by AFM.

	Topography	Feature height/depth (nm)	Feature diameter (nm)	Feature spacing (nm)
PMMA100	flat	-	-	-
PS25PMMA75	islands	7±2	160±42	200±69
PS50PMMA50	pits	8±5	118±39	60±33
PS75PMMA25	pits	11±4	190±57	88±28
PS100	flat	-	-	-

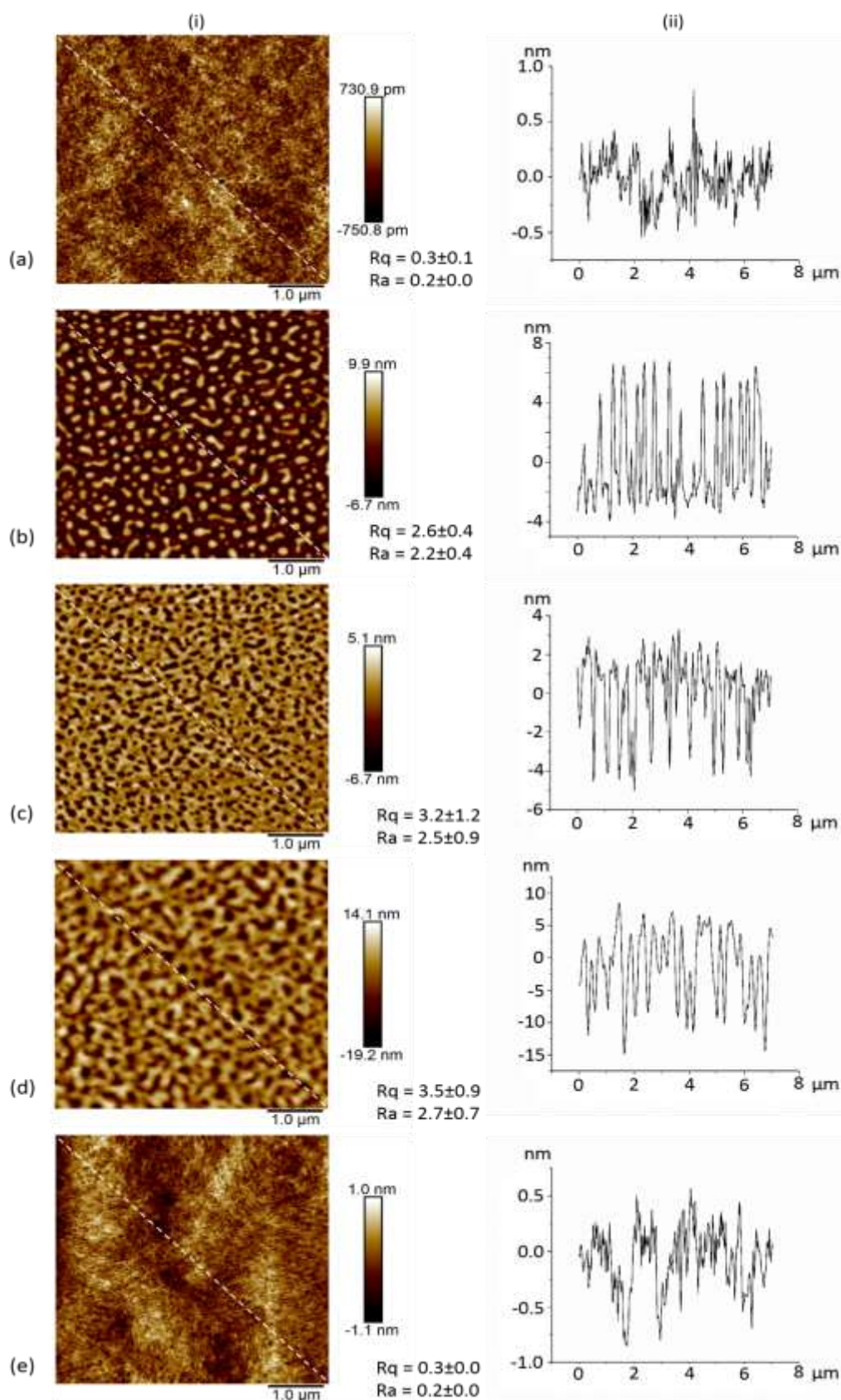


Figure 6.9: AFM (i) 3D images and (ii) depth profiles of PS/PMMA polymer demixed films in ratios (a) 0:100 (b) 25:75 (c) 50:50 (d) 75:25 and (e) 100:0.

Representative images and corresponding roughness values (R_q , R_a) of PCL/PMMA polymer demixed blends in varying ratios are displayed in Figure 6.10. The roughness values of PCL25PMMA75 ($R_a = 8.4$ nm), PCL50PMMA50 ($R_a = 7.9$ nm) and PCL75PMMA25 ($R_a = 2.9$ nm) were all seen to increase when compared to PMMA100; there was no significant difference between the demixed films and PCL100. This blend system produced films with island structures. When PMMA was in abundance these islands were depressed in the apex, with heights of 30 nm and diameters of 232 nm. When polymers were in equal concentration, islands were formed, 30 nm in height and 154 nm in diameter. The islands decreased in height (16 nm) when the PCL concentration was increased to 75 %, but there was no significant difference between the diameter of the structures. Furthermore, there was no depression in the apex of the islands observed for the PCL50PMMA50 and PCL75PMMA25.

Table 6.11: Topographical data for PCL/PMMA demixed films determined by AFM.

	Topography	Feature height/depth (nm)	Feature diameter (nm)	Feature spacing (nm)
PMMA100	flat	-	-	-
PCL25PMMA75	pitted islands	29±12	232±100	145±101
PCL50PMMA50	islands	30±20	154±82	191±113
PCL75PMMA25	islands	16±5	162±57	186±92
PCL100	flat	-	-	-

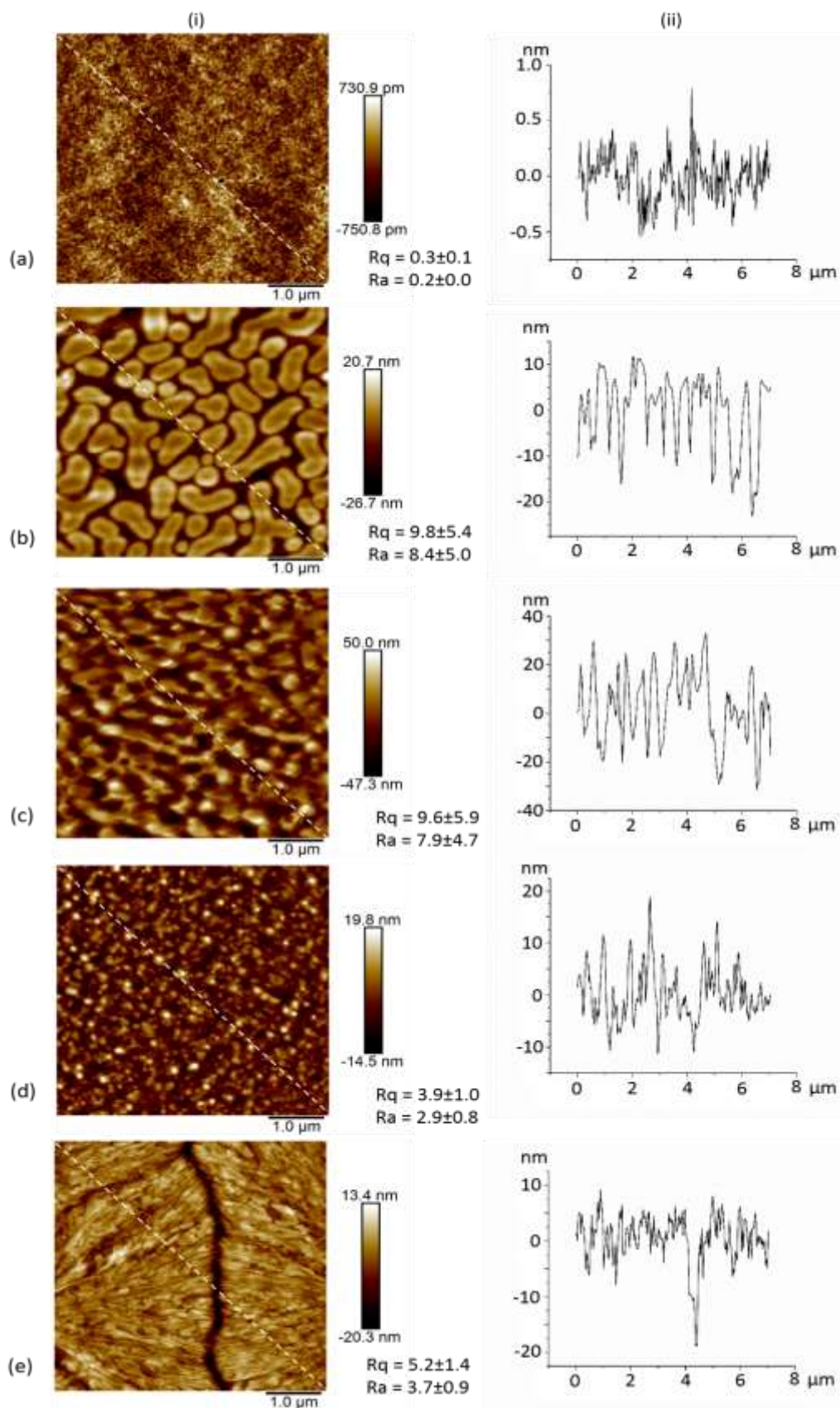


Figure 6.10: AFM (i) 3D images and (ii) depth profiles of PCL/PMMA polymer demixed films in ratios (a) 0:100 (b) 25:75 (c) 50:50 (d) 75:25 and (e) 100:0.

6.4 Results: Stability in LB Media

All the surfaces above were analysed for their stability in LB media before determining the bacterial response. This ensured that the surfaces were stable under the conditions tested. As such all of the characterisation was repeated after soaking the samples in LB for 24 hrs at 37 °C which replicates the conditions for the bacterial assays.

6.4.1 Wettability: Contact Angle

The change in wettability after soaking in LB broth was determined by static water contact angle measurements. Data for 100 % polymer films and polymer demixed films have been recorded in Tables 6.12 and 6.13, respectively.

All polymer demixed films and 100 % polymer control films had noticeably reduced contact angles after soaking. The most hydrophilic 100 % polymer film after soaking was PS100 (32.3°), followed by PCL100 (53.9°) and PMMA100 (58.9°). This trend is the reverse of that seen before soaking, where PS was the most hydrophobic polymer. The observed phenomenon is most probably due to swelling of the polymer in the LB media. Swelling of polymers has been reported to decrease contact angle and increase wettability.²³³

Table 6.12: Static water contact angle measurements of 100 % polymer films after soaking in LB media.

	Contact Angle (°)
PS	32.3±8.0
PCL	53.9±1.5
PMMA	58.9±4.1

Table 6.13: Static water contact angle measurements of polymer demixed films in varying ratios after soaking in LB media.

	Contact Angle (°)		
	PS:PCL	PS:PMMA	PCL:PMMA
25:75	45.2±3.6	49.0±3.9	65.6±3.7
50:50	53.9±2.2	49.9±2.5	60.9±4.22
75:25	37.7±0.7	58.6±1.2	49.2±5.1

6.4.2 Surface Chemistry: FTIR

The polymer demixed films underwent FTIR analysis to determine whether the soaking in media had any effect on the chemical composition of the blends. The spectra are displayed in Figures 6.11 – 6.13.

The characteristic aromatic C-H stretching vibration and aliphatic C-H stretch of PS were seen in the PS100 spectrum (Fig. 6.11 and 6.12) with peaks at 3026 cm^{-1} and 2925 cm^{-1} , respectively. In the PCL100 spectrum (Fig. 6.11 and 6.13) two peaks at 2948 cm^{-1} and 2865 cm^{-1} were due to asymmetric and symmetric CH_2 stretching, respectively. The carbonyl stretching mode was seen at 1726 cm^{-1} . The PMMA100 spectrum (Fig. 6.12 and 6.13) showed three characteristic peaks of PMMA. The first at 2996 cm^{-1} was due to the C-H stretching mode of CH_3 . At 2950 cm^{-1} , due to the C-H stretching mode of CH_2 and at 1732 cm^{-1} , due to the acrylate carboxyl group.²²⁹ All peaks described were observed in the corresponding spectra for the demixed films. The presence of a new peak in all spectra was apparent at 1648 cm^{-1} . This is characteristic of the bending mode of H_2O , which further corroborates the reduced contact angle measurements in indicating that swelling of the polymer may be occurring.

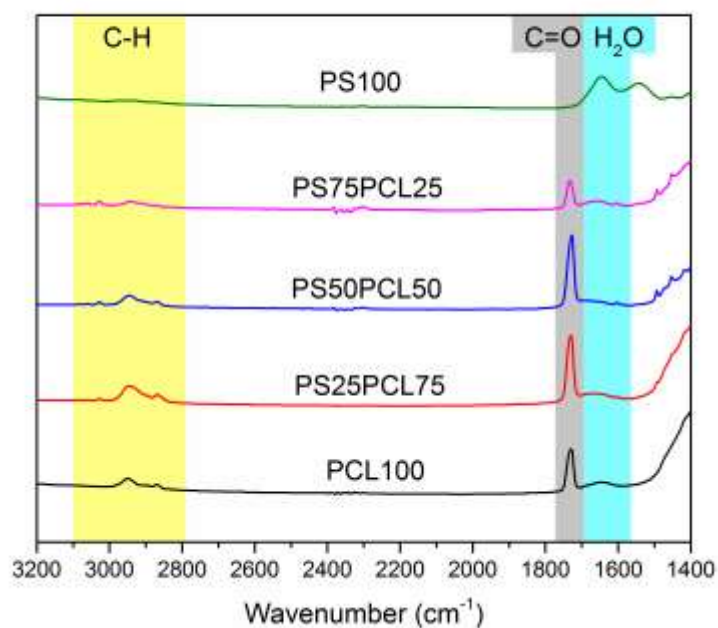


Figure 6.11: FTIR spectra of PS/PCL polymer demixed films after soaking in LB media.

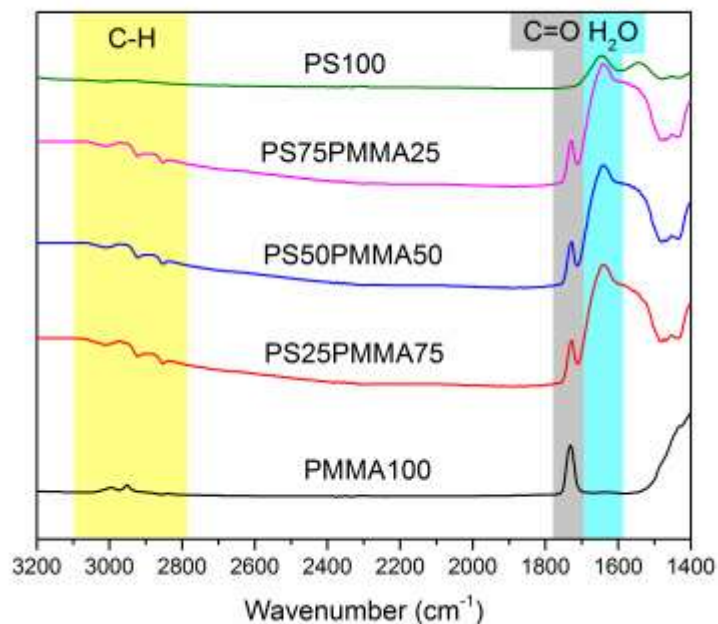


Figure 6.12: FTIR spectra of PS/PMMA polymer demixed films after soaking in LB media.

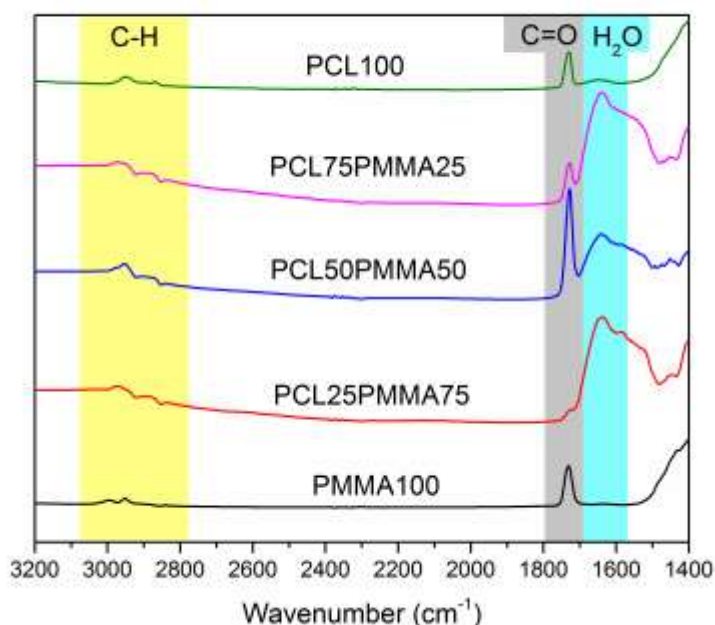


Figure 6.13: FTIR spectra of PCL/PMMA polymer demixed films after soaking in LB media.

6.4.3 Topography: AFM

The surface topography of the polymer demixed films after soaking in LB media was examined by AFM, and representative images and roughness values (R_q , R_a) are displayed in Figures 6.14 – 6.16. AFM derived data, including surface feature dimensions are presented in Tables 6.14 – 6.16. It can be seen that there are changes in the topography of all blends after exposure to the broth attributed to the swelling effect of the polymers.

PS100 (Fig. 6.14 and 6.15) increased in roughness after soaking ($R_q = 12.9$ nm, $R_a = 7.5$ nm). The roughness values of PCL100 (Fig. 6.14 and 6.16) decreased ($R_q = 3.4$ nm, $R_a = 2.5$ nm) and for PMMA100 (Fig. 6.15 and 6.16) values increased slightly after soaking in LB media ($R_q = 1.7$ nm, $R_a = 1.2$ nm).

Figure 6.14 shows the representative images of PS/PCL polymer demixed films in varying ratios. The roughness values of PS25PCL75 ($R_a = 15.1$ nm), PS50PCL50 ($R_a = 9.7$ nm) and PS75PCL25 ($R_a = 7.9$ nm) were all seen to increase when compared to PCL100, whilst only PS25PCL75 was significantly rougher than PS100. When PCL was in abundance, island surface structures 52 nm in height and 252 nm in diameter,

were observed. With PS in abundance, a pit arrangement was observed with features of 32 nm in height and 252 nm in diameter. When the polymer concentrations were equal, a topography with partial character of the two described prior was observed to form a ribbon-like topography. The height and diameter of these features were 38 nm and 226 nm, respectively.

Table 6.14: Topographical data for PS/PCL blends soaked in LB broth determined by AFM

	Topography	Feature Height/Depth (nm)	Feature Diameter (nm)	Feature spacing (nm)
PCL100	flat	-	-	-
PS25PCL75	islands	52±13	252±91	125±62
PS50PCL50	ribbons	38±8	226±79	197±68
PS75PCL25	pits	32±8	252±86	220±57
PS100	flat	-	-	-

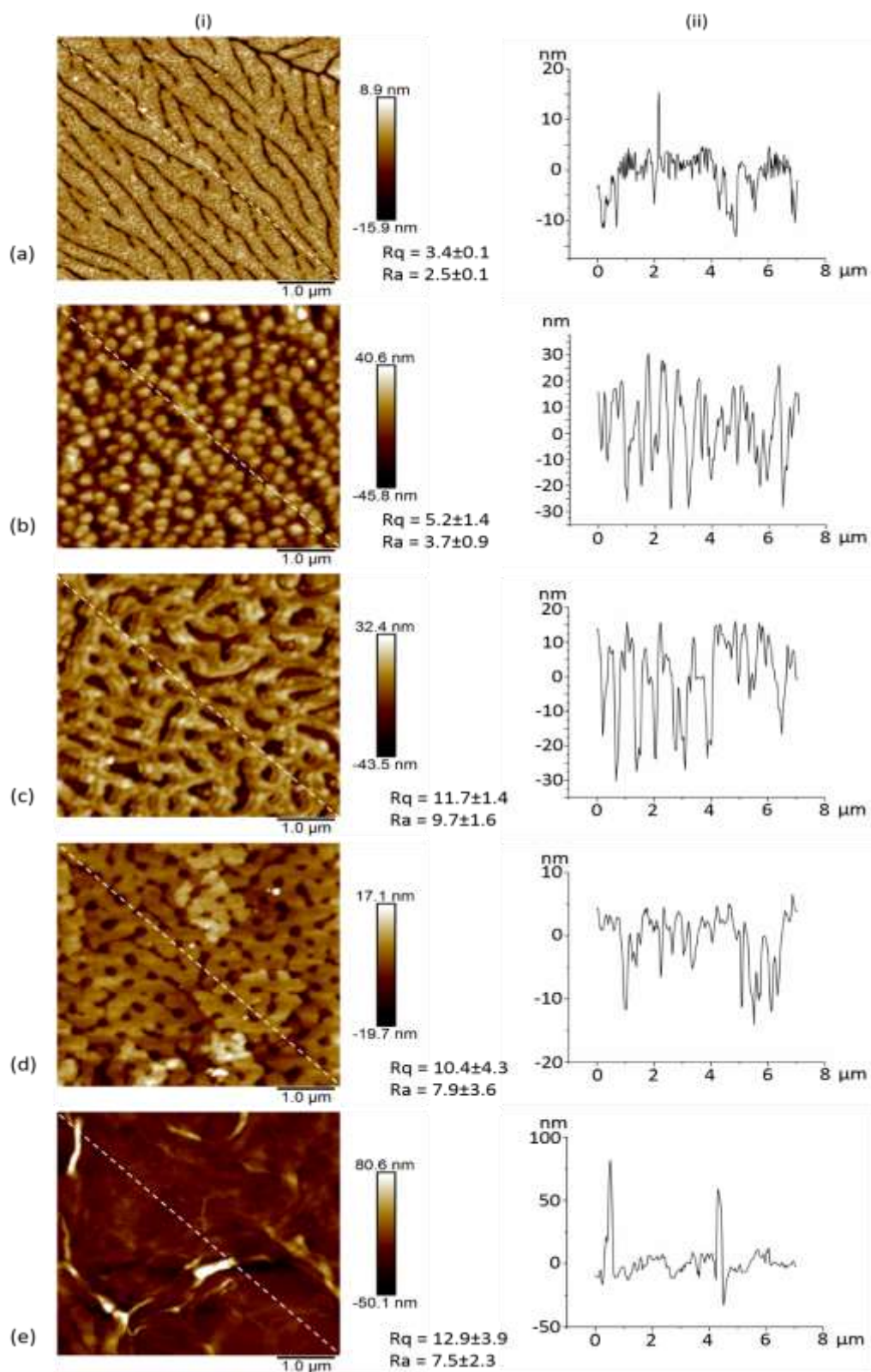


Figure 6.14: AFM (i) 3D images and (ii) depth profiles of PS/PCL polymer demixed films in ratios (a) 0:100 (b) 25:75 (c) 50:50 (d) 75:25 and (e) 100:0 after soaking in LB media.

Figure 6.15 shows the representative images of PS/PMMA polymer demixed films in varying ratios. The roughness values of PS25PMMA75, PS50PMMA50 and PS75PMMA25 were $R_a = 10.3$ nm, 3.1 nm and 22.2 nm, respectively. In this blend system, when PMMA was in a greater concentration islands of 76 nm in height and a diameter of 1530 nm were formed. When the polymers were in equal concentration pits were formed, 16 nm in height and 942 nm in diameter. Islands were also observed when PS was in abundance. Features were 91 nm in height and 1386 nm in diameter.

Table 6.15: Topographical data for PS/PMMA blends soaked in LB broth determined by AFM

	Topography	Feature Height/ Depth (nm)	Feature Diameter (nm)	Feature spacing (nm)
PMMA100	flat	-	-	-
PS25PMMA75	islands	76±12	1530±265	869±512
PS50PMMA50	pits	16±5	942±403	537±226
PS75PMMA25	islands	91±9	1386±444	891±241
PS100	flat	-	-	-

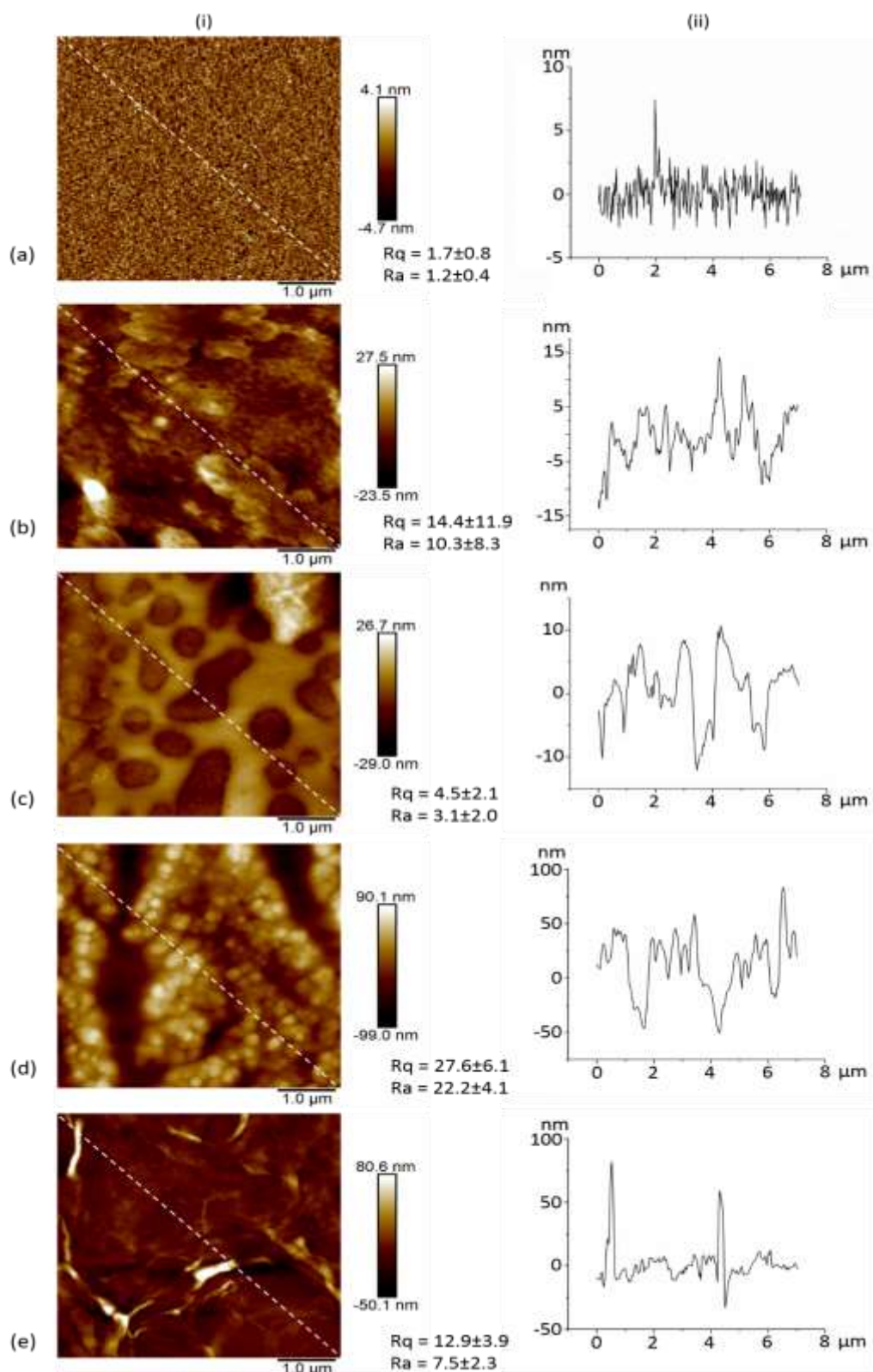


Figure 6.15: AFM (i) 3D images and (ii) depth profiles of PS/PMMA polymer demixed films in ratios (a) 0:100 (b) 25:75 (c) 50:50 (d) 75:25 and (e) 100:0 after soaking in LB media.

Representative images of PCL/PMMA polymer demixed blends in varying ratios are displayed in Figure 6.16. The roughness values of PCL25PMMA75 ($R_a = 22.6$ nm), PCL50PMMA50 ($R_a = 10.2$ nm) and PCL75PMMA25 ($R_a = 21.5$ nm) were all seen to increase when compared to PCL100 and PMMA100. In this blend system all observed topographies were island-like. When PMMA was in abundance these islands had heights of 78 nm and diameters of 418 nm. When polymers were in equal concentration, the islands were 37 nm in height and 176 nm in diameter. Islands of PCL75PMMA25 films were 88 nm high and 512 nm in diameter.

Table 6.16: Topographical data for PCL/PMMA blends soaked in LB broth determined by AFM.

	Topography	Feature Height/Depth (nm)	Feature Diameter (nm)	Feature spacing (nm)
PMMA100	flat	-	-	-
PCL25PMMA75	islands	78±28	418±75	163±38
PCL50PMMA50	islands	37±11	176±45	218±105
PCL75PMMA25	islands	88±19	512±224	412±167
PCL100	flat	-	-	-

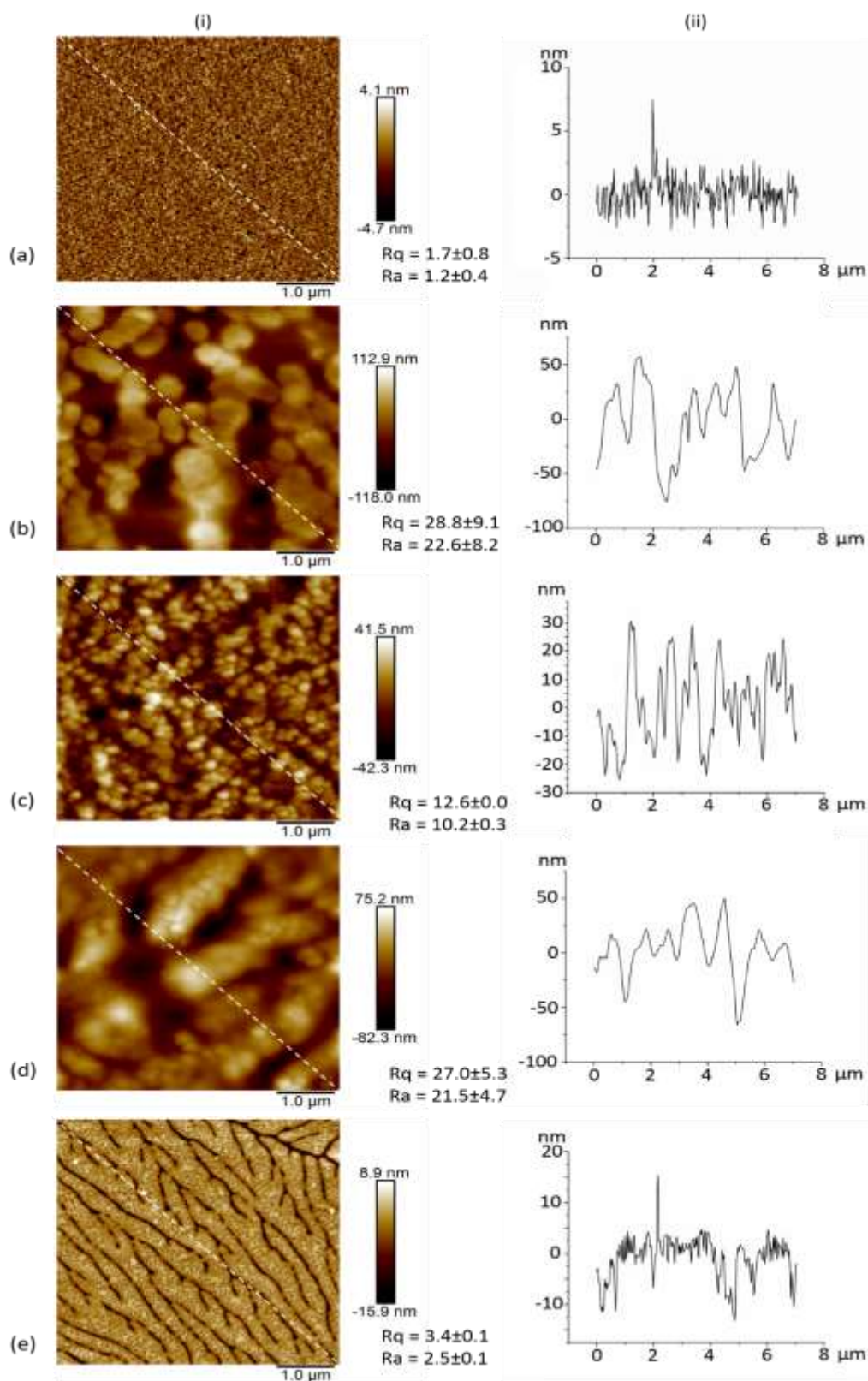


Figure 6.16: AFM (i) 3D images and (ii) depth profiles of PCL/PMMA polymer demixed films in ratios (a) 0:100 (b) 25:75 (c) 50:50 (d) 75:25 and (e) 100:0 after soaking in LB media.

6.5 Results: Bacterial Response

Antibacterial activity was investigated against the lab strain of *P. aeruginosa*, PA14. An adhered cell CFU assay was performed, in which the surfaces were inoculated with bacteria for 24 hrs to allow any potential biofilm formation. After removal of any planktonic bacteria with a PBS wash, remaining viable bacteria from the surface were counted to test the ability of materials with structured surface topographies in preventing adhesion and therefore biofilm formation. The cell counts for the adhered cell CFU assays are given in Figures 6.17 - 6.19 for PS/PCL, PS/PMMA and PCL/PMMA demixed films with 100 % polymer films as control surfaces.

6.5.1 PS/PCL

On PS/PCL demixed films, all bacterial counts were significantly reduced compared to the control surfaces (Fig. 6.17). The PS25PCL75 film reduced the bacterial count by 28 % and 23 % with respect to PCL100 and PS100. For PS50PCL50, reductions of 50 % and 46 % were observed for PCL100 and PS100, respectively. Finally, on the PS75PCL25 films the count was 49 % less than PCL100 and 45 % less than PS100.

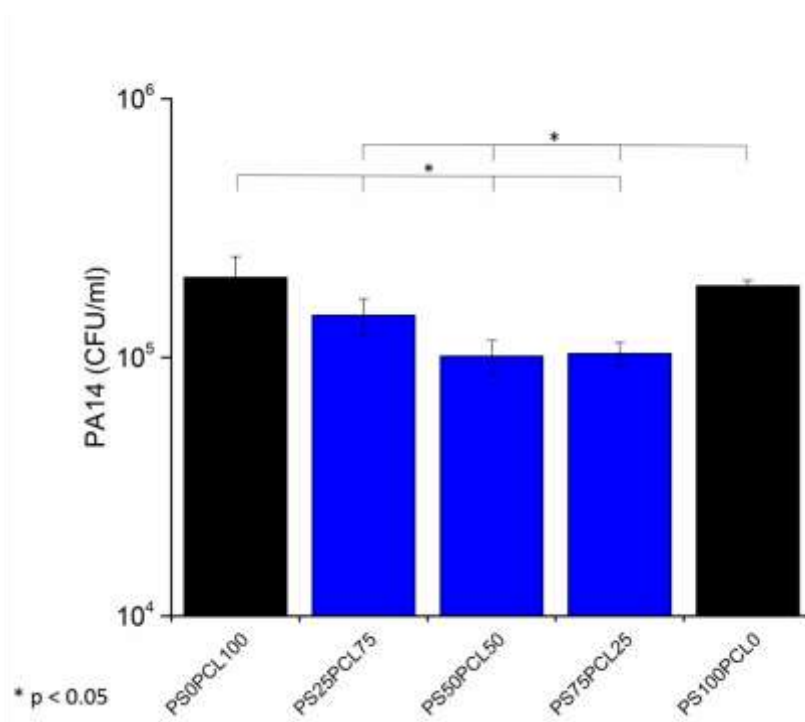


Figure 6.17: Viable adhered PA14 cell counts (CFU/ml) after 24 hr growth on PS/PCL. The symbol '*' and blue bars indicate that all polymer demixed films have a statistically significant reduction in cell counts compared to controls (p < 0.05).

6.5.2 PS/PMMA

In PS/PMMA demixed films, there was no statistically significant reduction for PA14 adhered cell CFU counts, compared to either PS100 or PMMA100 (Fig. 6.18).

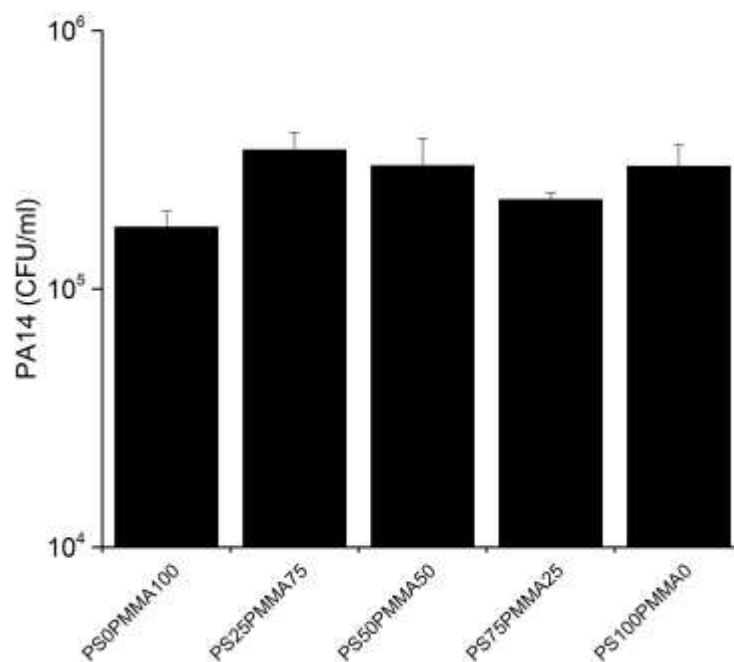


Figure 6.18: Viable adhered PA14 cell counts (CFU/ml) after 24 hr growth on PS/PMMA. Black bars indicate no statistically significant reduction in cell counts between demixed films and controls.

6.5.3 PCL/PMMA

All PCL/PMMA demixed films exhibited statistically significant reductions in CFU counts compared to PCL100 and PMMA100 (Fig. 6.19). The counts on PCL25PMMA75 were reduced by 77 % compared to on PCL100 and 72 % compared to on PMMA100. For PCL50PMMA50, reductions of 78 % and 73 % were observed against PCL100 and PMMA100, respectively. The counts on PCL75PMMA25 were reduced by 76 % and 70 % compared to PCL100 and PMMA100, respectively.

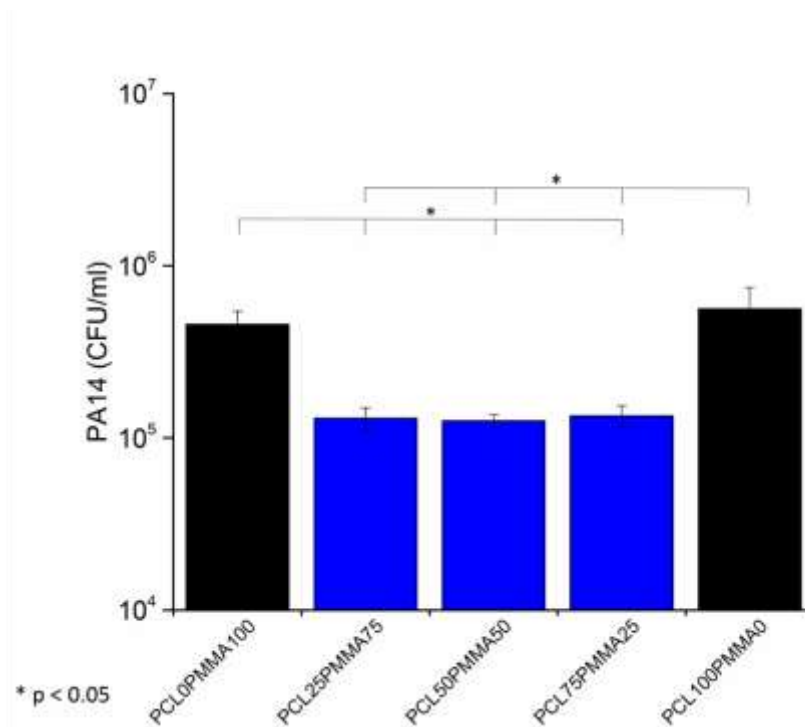


Figure 6.19: Viable PA14 cell counts (CFU/ml) after 24 hr growth on PCL/PMMA demixed films. The symbol '*' and blue bars indicate that all polymer demixed films have a statistically significant reduction in cell counts compared to controls ($p < 0.05$).

6.6 Discussion

6.6.1 Polymer Demixing Process

Polymer demixing provides an economic, efficient alternative in modifying polymer surfaces when compared to the more expensive manufacturing techniques such as electron lithography. A schematic of the steps involved in polymer demixing has been displayed at the beginning of this chapter in Figure 6.1.²²⁸ The sections below will detail the science involved in the formation of surfaces with distinct micro-/nanotopographical features, using the polymer demixing process.

6.6.1.1 Immiscibility of Polymers

The process of polymer demixing utilises the immiscibility of polymers to produce polymer films with varying topographies and wettabilities. Immiscibility between polymers arises as the entropic law that governs the miscibility of low molecular weight (LMW) analogues becomes an almost insignificant contributing factor for high molecular weight materials.²³⁴

The miscibility of two components is governed by:

$$\Delta G_m = \Delta H_m - T\Delta S_m \quad (6.1)$$

where ΔG_m is the free energy of mixing, ΔH_m is the enthalpy of mixing and ΔS_m is the entropy of mixing. As in any Gibbs free energy equation, ΔG_m must be less than 0 for miscibility to occur. When discussing LMW compounds, an increase in temperature tends to lead to an increase in the $T\Delta S_m$ term which will increase the negativity of ΔG_m and thus the miscibility.

In binary polymer mixtures, the Flory-Huggins theory can be applied to account for immiscibility between polymers. In this model the combinatorial entropy of mixing, ΔS_m is:

$$\Delta S_m = -R \left[\frac{\phi_1}{r_1} \ln \phi_1 + \frac{\phi_2}{r_2} \ln \phi_2 \right] \quad (6.2)$$

where, R is the gas constant, ϕ_i is the volume fraction of polymer, i , and r_i is the number of polymer segments. As r_i is proportional to the degree of polymerisation, an increase in molar mass leads to a decrease in ΔS_m values. And so for high molecular weight compounds ΔS_m decreases to such an extent the $T\Delta S_m$ becomes

negligible, regardless of temperature change and immiscibility is the most common outcome.^{235, 236}

6.6.1.2 Vertical Phase Separation

After the initial spin-off stage in which solvent and polymer are removed, an initial bilayer is formed, in which one polymer segregates to the substrate interface and one to the air interface (Fig 6.1 b). Initially, the arrangement is purely kinetic and the relative solubility of the polymers within their common solvent is the dominant factor.^{237, 238} The least soluble polymer will come out of solution first and wet the substrate followed by the more soluble polymer wetting the surface.

With time, thermodynamic factors may also play a role in the interfacial preference of each polymer. The polymer with the lower surface free energy would be expected to segregate to the air interface to maintain the minimum interfacial free energy.^{239, 240} Additionally, the polymer with the higher molecular weight tends to favour the substrate interface so as to avoid potential loss of conformational entropy associated with compression on the film surface.^{240, 241}

In order to determine which polymer segregates to the air interface, analysis of the surface composition was performed by assessing the relative contribution of the ester ($\text{O}-\text{C}=\text{O}$) component to the C 1s envelope in the XPS spectra of the demixed films compared to the 100 % polymer film, as reported previously by Ton-That and D'Sa.^{173, 238} In two of the systems studied (PS/PCL and PS/PMMA), the ester functional group is unique to only one polymer (PCL and PMMA). As such, using Equation 6.3 it is possible to determine the surface composition of each demixed PS/PCL and PS/PMMA film. To determine whether the vertical phase separation was thermodynamically stable, XPS analysis was also carried out on polymer demixed films that had been cured at 80 °C. In the PCL/PMMA demixed films, the ester functional group is present in the backbone of each polymer and therefore this method cannot be used for this blend system.

For both PS/PCL and PS/PMMA blend systems the arbitrary term 'A' can be defined as the fraction of O-C=O peak in the C 1s spectrum:

$$A = \left(\frac{I_{O-C=O}}{I_C} \right) \quad (6.3)$$

In PS/PCL blends the relative contribution of PCL is $6 X_{PCL}$ (six carbon atoms per repeat unit) and in PS/PMMA the relative contribution of PMMA is $5 X_{PMMA}$ (five carbon atoms per repeat unit). The relative contribution of PS in both blend systems is $8(1-X)$ (eight carbon atoms per repeat unit), where X_n is the molar surface concentration of the polymer, to give:

$$A = \frac{X_{PCL}}{6 X_{PCL} + 8(1 - X_{PCL})} \quad (6.4a)$$

for PS/PCL blends and,

$$A = \frac{X_{PMMA}}{5 X_{PMMA} + 8(1 - X_{PMMA})} \quad (6.4b)$$

for PS/PMMA blends. Rearranging 6.4 a and 6.4 b gives 6.5 a and 6.5 b, respectively:

$$X_{PCL} = \frac{8A}{2A+1} \quad (6.5a)$$

$$X_{PMMA} = \frac{8A}{3A+1} \quad (6.5b)$$

In Figures 6.20 and 6.21, the surface fraction of PCL and PMMA in PS/PCL and PS/PMMA demixed films, respectively, deduced from the equation set above, have been compared to the equivalent composition of their corresponding 100 % polymer film.

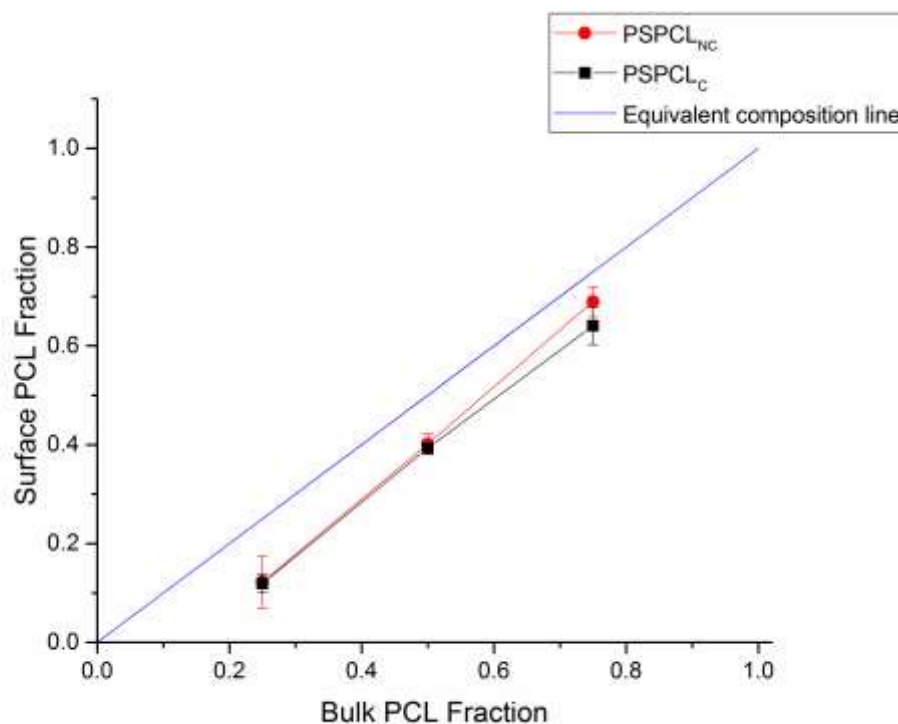


Figure 6.20: Plot of PS/PCL film surface PCL fraction vs bulk PCL fraction. Data obtained using high resolution C 1s XPS measurements and Equation 6.5 a.

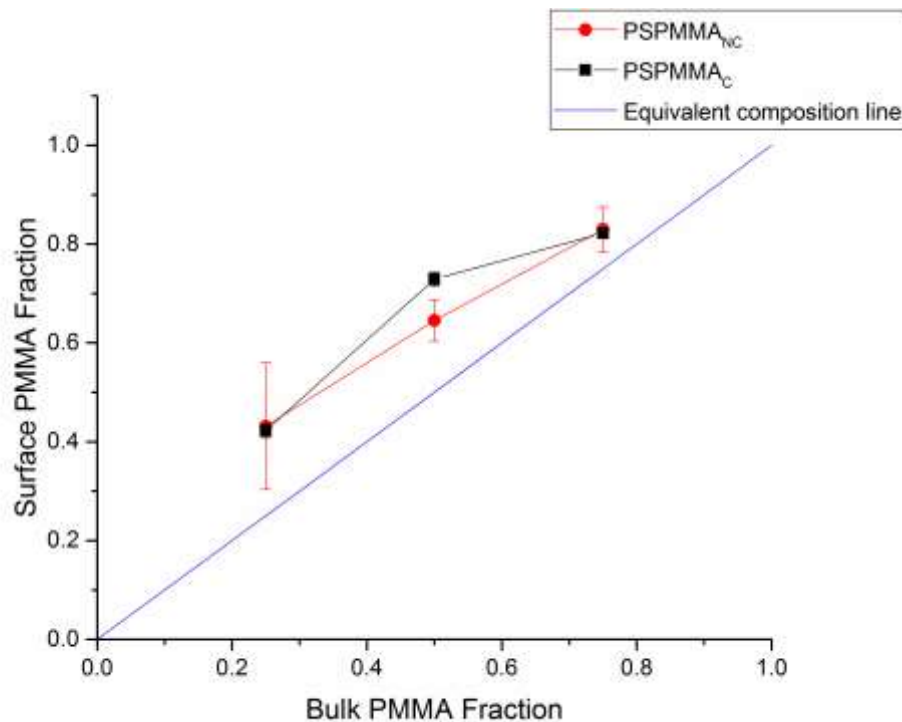


Figure 6.21: Plot of PS/PMMA film surface PMMA fraction vs bulk PMMA fraction. Data obtained using high resolution C 1s XPS measurements and Equation 6.5 b.

In PS/PCL demixed films, it can be seen that the surface fraction of PCL is below the theoretical equivalent composition line, indicating that PS segregates to the air interface. In PS/PMMA demixed films, the PMMA surface fraction is above the equivalent composition line indicating that, in this system, the PMMA wets the substrate-favouring PS. In both figures, red circles show surface composition without curing and black squares show with curing. As there is no movement of the data points across the equivalent composition line, this indicates that the initial kinetic arrangement is also a thermodynamically stable one.

In these experiments, the blend solutions were dissolved in chloroform; a highly volatile compound (BP = 61.2 °C)²⁴². Due to its low boiling point, rapid solvent evaporation occurs, which would be indicative of the demixed films forming under kinetic rather than thermodynamic control.²⁴³ The Hildebrand solubility parameters for chloroform, PS, PCL and PMMA are 9.29, 8.94, 10.35 and 8.80, respectively. The closer the value of a polymer to that of its solvent generally indicates better solubility.

PS/PCL

In PS/PCL blends, PS is the more soluble of the two polymers in chloroform, which corroborates the XPS-derived surface quantification discussed above (Fig. 6.20). PS segregates to the air interface despite having a higher surface energy (PS: 40.7 mN/m, PCL: 30.8 mN/m)^{239, 244, 245} and despite the entropic penalty it incurs being the higher molecular weight component (PS: 280 kDa, PCL: 45 kDa). A possible explanation for this is that the pre-cleaning of the glass substrates renders the surface hydrophilic, thereby having a higher affinity for the more polar PCL.²³⁹

PS/PMMA

Whilst the solubility parameters of PS and PMMA are comparable, it can be assumed that PMMA has better solubility in chloroform from its segregation to the surface of the film (Fig. 6.21). Ton-That *et al.* investigated the effect of curing PS/PMMA demixed films after the spin coating process to allow the system to potentially reassemble under thermodynamic control.²³⁷ Indeed they observed that the initial orientation of the polymers were as a result of kinetics, segregating PMMA to the air interface, but after the addition of heat to the system, PMMA migrated to the substrate interface owing to its lower surface energy. In PS/PMMA demixed films

the XPS analysis shows that PMMA prefers the air interface even after curing, despite having a comparable surface energy to PS (PS: 40.7 mN/m, PMMA: 41.0 mN/m)²⁴⁴ and higher molecular weight (PS: 280 kDa, PMMA: 380 kDa). It is feasible that the curing conditions may have not been adequate to allow the blend system to reach thermodynamic equilibrium.

PCL/PMMA

As the O-C=O component is present in both PCL and PMMA, the XPS-derived relative ester contribution method was unsuitable for PCL/PMMA demixed films. It can however, be hypothesised that due to higher solubility of PMMA in chloroform the PCL deposits first on the substrate, which is in agreement with the work carried out by Khattak *et al.* on PCL/PMMA blends.²⁴⁶ PMMA has a greater surface energy (PCL: 30.8 mN/m, PMMA: 41.0 mN/m)^{244, 245} and higher molecular weight (PCL: 45 kDa, PMMA: 380 kDa) so it is hypothesised that the initial kinetic arrangement is most likely thermodynamically unstable and may result in a rearrangement of PCL to the surface.

There are a host of other parametric changes that can affect initial phase separation, such as solvent and substrate type. These considerations are beyond the scope of this thesis and have been discussed in detail elsewhere.^{172, 247-249}

6.6.1.3 Lateral Phase Separation

The spin coating of polymer demixed blends in varying relative concentrations leads to the formation of films with island-, ribbon- and pit-like micro-/nanotopographical surface structures. This arises through complex dewetting pathways in which one or both polymer in the binary blend dewets the underlying surface, leading to lateral phase separation. The dewetting pathway depends on the relative concentrations of the polymers and the nature of the vertical phase separation.

The two polymers are blended into a single phase system (polymer/polymer/solvent). Once the evaporation process begins the polymer-polymer-solvent system splits into two phases, vertically separated (See Section 6.6.1.2). This gives rise to three interfaces: polymer-air, polymer-polymer and polymer-substrate. The dewetting of the two layers in the system is governed by the dynamics between the deformable polymer-air and polymer-polymer interfaces. An

instability is induced through one of two modes²⁵⁰ depending on which polymer film ruptures first: the bending mode or the squeezing mode. This results in completely different dewetting pathways and potential morphologies. The two modes of instability, bending and squeezing modes, have been schematically shown in Figure 6.22 and 6.23, respectively.

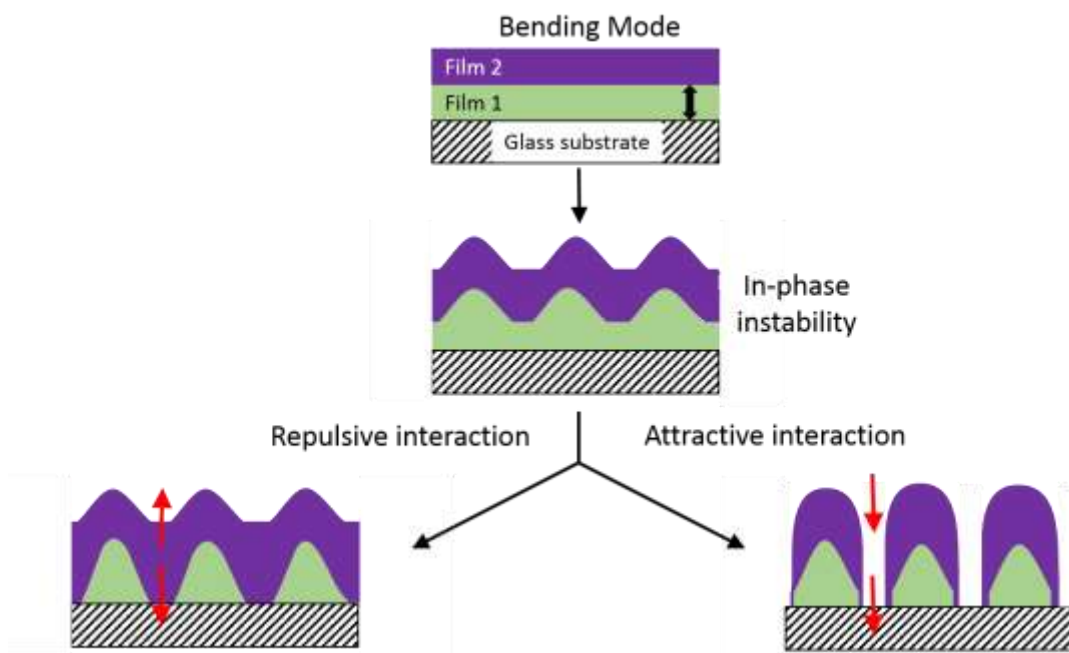


Figure 6.22: Schematic representation of the bending mode of instability in a thin binary polymer blend. Red arrows show the direction of interaction of the polymer-air and polymer-substrate interfaces.

In Figure 6.22, the bending mode of instability is depicted. In this mode, the polymer-polymer interface and polymer-substrate interface have a stronger attractive interaction than the polymer-polymer and polymer-air interfaces, causing Film 1 to dewet first. This deformation leads to an in-phase deformation of Film 2 as it is pulled down towards the substrate. As Film 1 continues to dewet the substrate, holes are formed as the bottom layer ruptures. At the site of these holes the polymer-substrate and polymer-air interfaces can interact; the result of this interaction is the formation of different topographical surface features. If the polymer-substrate and the polymer-air interface have a repulsive interaction, Film 1 dewets forming subsurface islands under an intact top layer. If the interaction is attractive, a deformation over every hole, where the top layer is in contact with the substrate, is

engendered, eventually leading to holes in the top layer. This leads to final surface features that are governed by the structure of the droplets formed in the dewetting of Film 1, encased by Film 2.

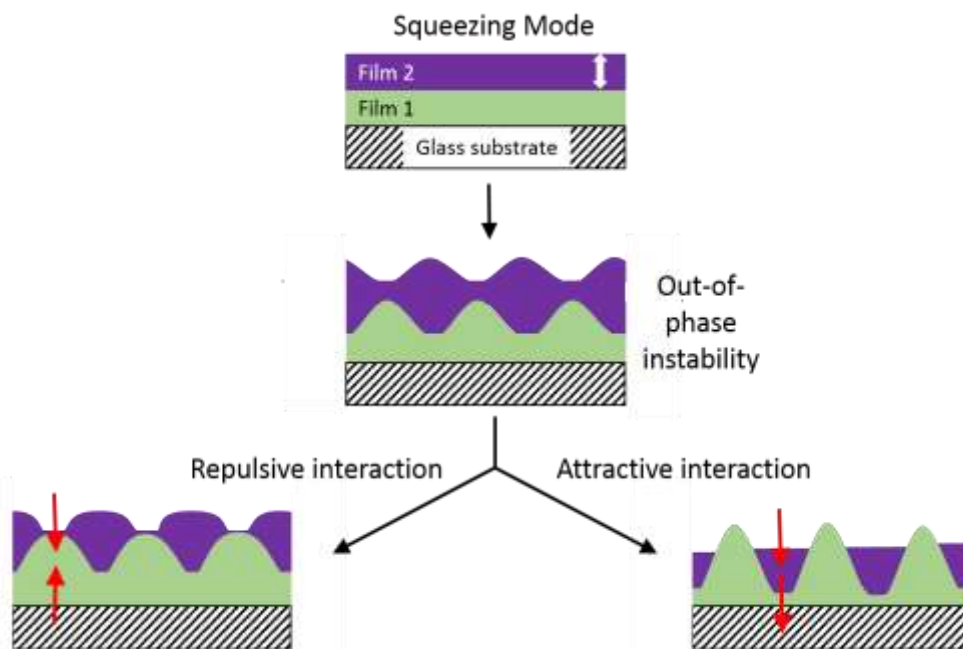


Figure 6.23: Schematic representation of the squeezing mode of instability in a thin binary polymer blend. Red arrows show the direction of interaction of the polymer-air and polymer-substrate interfaces.

In Figure 6.23, the stretching mode of instability is depicted. In this mode, the instability of Film 2, due to attractive interactions between the polymer-polymer and polymer-air-interface initiates the mechanism. Unlike in the bending mode, where the deformation occurs over the rigid substrate, both polymer-polymer and polymer-air interfaces can deform in the squeezing mode and an out-of-phase interaction occurs as the interfaces pull towards one another. As Film 2 dewets Film 1, there are again two pathways the mode can follow, as Film 1 becomes exposed to air. A repulsive interaction between polymer-substrate and polymer-air interface would lead to drops of polymer in Film 2 on a stable Film 1. If the interaction is attractive then Film 1 dewets the substrate. With Film 2 having already dewetted Film 1 this pathway can often lead to complex structural arrangements.

PS/PCL

Ma *et al.* reported on the underlying mechanisms involved in the formation of the surface morphologies seen in PS/PCL demixed films.²³⁹ As in this work, Ma reported that first a vertical phase separation occurs with PS segregating to the air interface. PS/PCL blends with a smaller concentration of PS gave island-like structures. They proposed that the thin upper PS layer leads to interfacial instability, which results in dewetting of the PS layer from the PCL layer, to give PS islands like PS25PCL75 (squeezing mode, Fig. 6.23). When the PS concentration was increased, vertical phase separation led to a liquid-liquid dewetting process, in which both films dewet their underlying surface. The PS chains lose mobility as solvent evaporates, before the dewetting process is complete and result in ribbon like structures, as seen in PS50PCL50. When the concentration of PS was increased further dewetting led to the growth of holes, like the pits formed from PS75PCL25 blend films (bending mode, Fig. 6.22).

PS/PMMA

de Silva *et al.* demonstrated that by varying the concentrations of the polymers in PS/PMMA blends, and as a result, the relative thicknesses of the individual components of the bilayer, the layer instability can be transferred.²⁵¹ It was seen that when the PMMA top layer was thinner than the underlying PS layer the instability was driven by the PMMA layer. Vice versa, when the PMMA concentration was increased (thicker layer) on top of the thinner PS layer a transition to an unstable PS layer was observed. In Figure 6.9, it can be seen that an abundance of PMMA leads to an island-rich morphology, whilst when PS is in excess, pits are formed. de Silva's conclusions²⁵¹ would suggest that the morphology of PS25PMMA75 is due to an initial bending mode of instability (Fig. 6.22), whilst the formation of pits in PS75PMMA25 begins with an instability in the top layer (squeezing mode, Fig 6.23).

PCL/PMMA

Whilst XPS data was unable to confirm the organisation of the vertical phase separation in this blend system (Section 6.6.1.2), the hypothesis that the more soluble PMMA segregates to the air interface corroborates Khattak's work on PCL/PMMA.²⁴⁶ From the reports by both Ma and de Silva, it can be concluded that the initial interfacial instability occurs in the lower concentration (thinner) film.^{239, 251}

In PCL25PMMA75, the pitted island formation is most likely initiated by an instability in the underlying PCL film (bending mode, Fig. 6.22), whilst the island morphology seen for PCL75PMMA25, begins with an instability in the top PMMA layer (squeezing mode, Fig 6.23).

6.6.2 Bacterial Response

In this chapter a low cost, efficient technique was used to fabricate surfaces with micro-/nanotopographical features in order to understand the underlying mechanism of how topography affects bacterial adhesion and prevents biofilm formation. All of the surfaces characterised were assayed for their anti-adhesion efficacy against *P. aeruginosa* (PA14) using an adhered cell CFU assay to see if biofilm formation could be prevented. An inoculating period of 24 hrs was chosen to allow the potential for irreversible adhesion and subsequent biofilm formation.

Bacterial adhesion and biofilm formation can generally be grouped into four stages:

1. Bacteria contacts the surface (Brownian motion, gravitational forces, hydrodynamic forces)
2. Bacterial adhesion to the surface (reversible/irreversible adhesion)
3. Proliferation of adhered bacteria resulting in the synthesis of biofilm matrix.²⁵²
4. Maturation of the biofilm with specific metabolism and physiology.²⁵³

It is generally considered that the second stage of biofilm formation is the one most influenced by the topography of a surface, as physical bacterial cell-surface interactions are involved at this stage. Within the studies reported here, modifying the topography of a material at a comparable length scale to the bacterial cell can prevent adhesion of the *Pseudomonas* strain (PA14) (Figure 6.24).

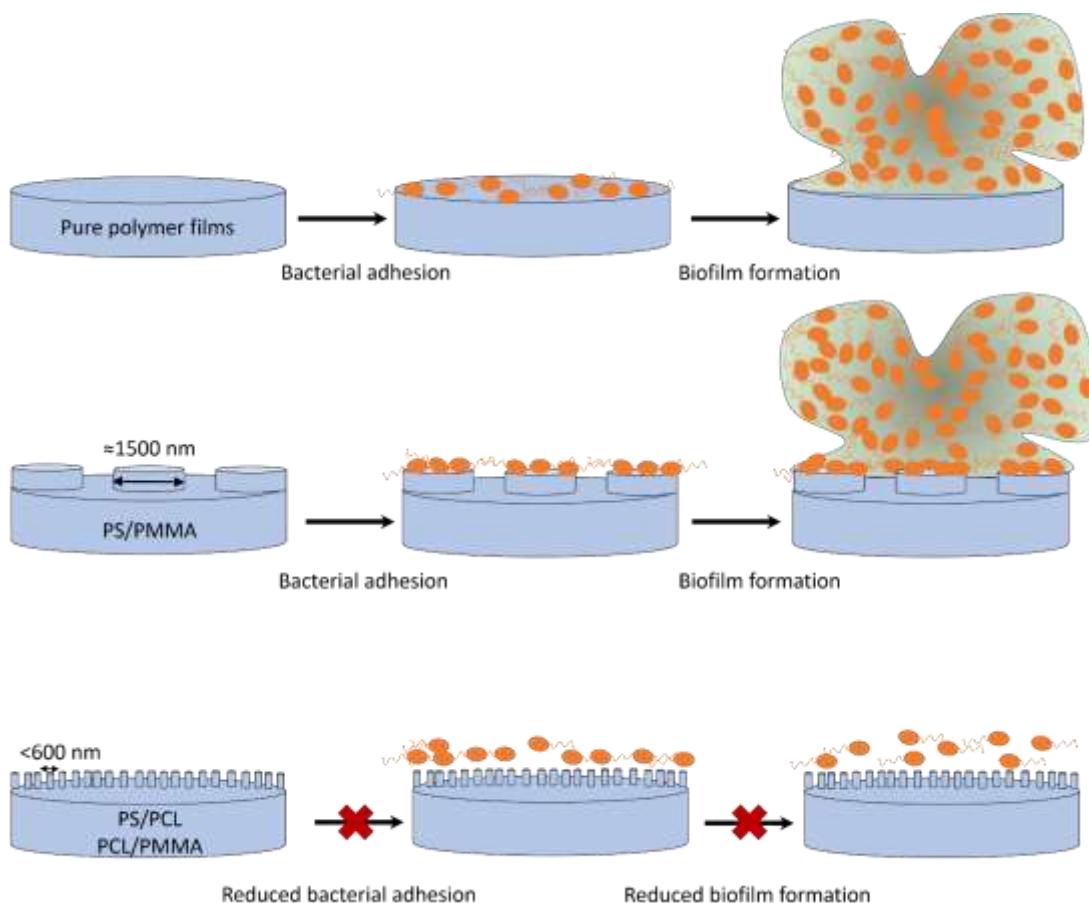


Figure 6.24: Topographical structure diameter and spacing has an effect on bacterial adhesion. If the structures and spacing are comparable in size (PS/PMMA) no anti-adhesion effect is observed. If the structures and spacing are smaller than the cell size (PS/PCL, PCL/PMMA) an anti-adhesion effect is observed.

A study by Lu *et al.* in 2016, reported the anti-adhesive properties of PDMS with micropatterned surfaces.¹⁸⁰ A significant reduction in bacterial adhesion was observed for three different strains of bacteria (*Escherichia coli*, *Staphylococcus aureus* and *Pseudomonas aeruginosa*). When the pattern size was smaller than the bacterial cell diameter an improved anti-adhesion effect was observed; when the pattern size was comparable or larger than the bacterial cell, the anti-adhesion effect was reduced.

The work carried out in this chapter corroborated Lu's findings.¹⁸⁰ PS/PCL and PCL/PMMA demixed films all formed structured films with feature diameters (Tables 6.10, 6.12) significantly smaller than the diameter of PA14 cells ($1.7 \pm 0.3 \mu\text{m}$) and showed significant reduction in bacterial adhesion compared to corresponding 100

% polymer control films. Feature diameters of all PS/PMMA demixed films (Table 6.11) were comparable in size to the diameter of the PA14 cells and showed no reduction in bacterial adhesion compared with their corresponding 100 % polymer control films.

In another study, Hochbaum and Aizenberg demonstrated the ability to affect the spontaneous ordering and arrangement of *P. aeruginosa* cells on nanostructured substrate surfaces by altering the spacing between nanoposts (Figure 6.25).⁵⁵

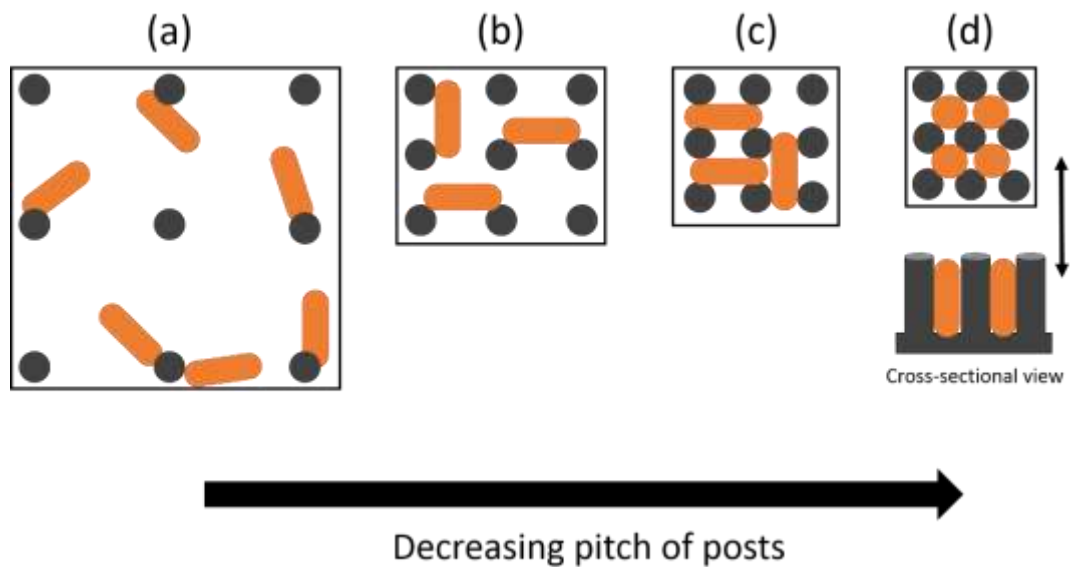


Figure 6.25: Schematic showing the change in orientation by bacterial cells to maximise cell-surface contact area when spacing between surface features is decreased [Adapted from Ref. 55].

It was seen that when spacing is larger than the cell diameter, the adhesion of bacteria on the whole is random, with a slight preference to adhere at sites where the substrate and posts meet (Fig. 6.25 a); as the spacing between features approaches the length of the cell, the bacteria position themselves parallel to the substrate and perpendicular to one another, contacting multiple neighbouring posts, so as to maximise the cell-surface contact area (Fig. 6.25 b, Fig. 6.25 c); when the posts are arranged so densely that bacteria cannot physically arrange parallel to the surface, they orientate perpendicular to the surface and parallel to the posts to maximise their contact area that way (Fig 6.25 d). In this work, the spacing between features in PS/PCL and PCL/PMMA demixed films are again significantly smaller than

the length of the cell. Whilst Hochbaum and Aizenberg concluded that cells adhered vertically, parallel to the posts, when the spacing between posts was smaller than the cell, the posts were 2 μm in height and so adhesion this way allowed for greater contact along the whole length of the cell. The heights of features for PS/PCL and PCL/PMMA were no more than 52 nm and 88 nm, respectively, so vertical orientation, parallel to the height scale of the features would not advantage cells in increasing contact area.

The link between feature size/spacing distance and cell diameter observed is in agreement with the conclusions drawn from the literature.^{55, 167, 180} On the surfaces of PS/PCL and PCL/PMMA demixed films a reduction in adhered cells is due to the reduced diameters and reduced spacing between features. The surface features are also much smaller in height than the cell diameter so adhering perpendicular to the surface would again be an undesirable orientation to maximise contact area. On the surfaces of PS/PMMA demixed films no reduction in adhered cells was observed due to the comparable diameters of both the features and the cells.

6.7 Conclusion

In this chapter, the relationship between surface topography on a length scale comparable to bacterial cell diameters was investigated. Using the polymer demixing process, binary polymer blends were spin coated onto substrates to give polymer demixed films with distinct topographies and wettabilities, as confirmed by AFM and contact angle analysis, respectively. Chemical characterisation of the surface by XPS, enabled determination of the interfacial preferences of the two polymers within the blend during the vertical phase separation. Using this data, as well as the relevant literature,^{239, 246, 250, 251} lateral phase separation through dewetting pathways were hypothesised for the polymer blends. This chapter has shown that, using a low cost and efficient method it is possible to fabricate materials with surface topographies that can control bacterial adhesion and therefore biofilm formation. PS/PCL and PCL/PMMA demixed films were prepared with feature size and spacing between features much smaller than the bacterial cell. As a result of this the surface was less desirable for the bacteria to adhere to due to the inability to maximise cell-surface contact area.

Chapter 7: Conclusions and Recommendations for Future Studies

7.1 Conclusions

The main aim of this thesis was to develop antibacterial alternatives to current antibiotics that kill bacteria and inhibit biofilm formation with a focus on medical implant applications. The current issue with antibiotics is the ever growing threat of them becoming obsolete due to misuse and overuse. The aim of developing novel antibacterial materials is not necessarily to replace antibiotics completely but to provide alternatives that may aid in reducing the dosage and prevalence of antibiotics used in clinical applications. All the antibacterial materials fabricated in this thesis showed greater than 1-log reduction in bacterial counts compared to corresponding controls, showing promising potential as agents in reducing current antibiotic usage.

A diverse range of fabrication and synthesis techniques were employed to develop polymeric materials with varied chemical and physical properties that could adversely affect localised bacteria. XPS and FTIR analysis were used to follow surface specific chemical changes after every synthesis step and AFM analysis was used to observe topographical surface changes at the micro-/nanoscale. The main focus of this thesis involved the incorporation of *N*-diazoniumdiolates onto surfaces with the aim of fabricating NO-releasing synthetic polymer materials; the NO release profiles of such materials were determined *via* chemiluminescence detection. The antibacterial performance of the modified surfaces was assessed in terms of either their bactericidal activity or their anti-adhesion (biofilm preventing) ability. Planktonic cell CFU assays were carried out for bactericidal efficacy and adhered cell CFU assays carried out for anti-adhesion determination, against a lab strain of *P. aeruginosa* (PA14).

In Chapter 4, NO-releasing *N*-diazoniumdiolate-tethered PET and SE substrates were fabricated. The conclusions drawn from this chapter were as follows:

1. NO storage and release is affected by the structure of the aminosilane precursor.

2. Low level NO release from PET and SE significantly reduces cell adhesion on the surface after 24 hrs, preventing biofilm formation.

In Chapter 5, NO-releasing *N*-diazoniumdiolated xerogel coatings on SE substrates were fabricated. The conclusions drawn from this chapter were as follows:

1. Preforming *N*-diazoniumdiolates and incorporating them into xerogel coatings increases NO storage and release compared to tethering *N*-diazoniumdiolates *in situ* (Chapter 4).
2. High level NO release from *N*-diazoniumdiolated xerogel-coated SE kills planktonic bacteria (bactericidal) after 1, 4 and 24 hrs.
3. The materials developed here are physically unstable and not suitable for use in medical implant applications.

In Chapter 6, polymer demixed films with distinct surface micro-/nanotopographies were fabricated. The conclusions drawn from this chapter were as follows:

1. By varying the relative concentration of two polymers in a binary blend, spin coating can result in demixed films with island-, ribbon- and pit-like micro-/nanotopographical features on the surface.
2. Cell adhesion is dependent on surface feature size in comparison to bacterial cell diameter; when the structure size is smaller than the cell, reduction in cell adhesion is observed; when the structure size is comparable to the cell, no reduction in cell adhesion is observed.

Overall, this thesis can be concluded to have achieved the following aims and objectives:

1. A review of the key principles in designing antibacterial surfaces led to the development of a broad range of materials with varying antibacterial abilities. The use of both a chemical approach (NO) and a physical approach (surface topography) allowed the fabrication of materials with bactericidal and/or anti-adhesive properties.
2. NO storage and release capabilities of materials modified with the NO donor class, *N*-diazoniumdiolates were controlled in a number of ways: using aminosilane precursors with varying structures, the pH of the release medium, the temperature at which decomposition is carried out, the preforming of the *N*-diazoniumdiolate compared to *in situ*, and incorporation into xerogels with large surface area.
3. Low level NO-release from *N*-diazoniumdiolate-tethered SE and PET substrates exhibited an anti-adhesion effect after 24 hrs, preventing biofilm formation.
4. High level NO-release from *N*-diazoniumdiolated xerogel coated SE substrates exhibited a bactericidal effect after 24 hrs, but are not suitable for use in medical implant applications due to their physical instability.
5. Polymer demixed binary films are anti-adhesive and prevent biofilm formation after 24 hrs if their surface structures are smaller than the bacterial cell diameter; they exhibit no anti-adhesion effect if the surface structures are comparable in size.

7.2 Recommendations for Future Studies

The research presented here has been directed at developing new antibacterial solutions to combat the ever-growing problem of bacterial and biofilm resistance to the current classes of antibiotics. Modified medically relevant polymeric biomaterials for a range of medical implant applications have been put through the initial stages of antibacterial testing. The extremely promising results, concluded, allow for a number of recommendations for future work with the aim of developing materials suitable for commercial use in medical implant applications.

1. The success of implanted medical devices is dependent on their biocompatibility when integrating into the body. It is important that whilst the material kills bacteria or prevents adhesion, the surrounding tissue remains healthy. It is therefore suggested that cytotoxicity and biocompatibility assays with relevant cells are carried out to ensure these materials would not adversely affect the tissue. A further suggestion is to carry out co-culture experiments in which tissue and bacterial cell viability are assessed when both are present simultaneously.
2. The aim of this thesis was to develop alternatives to current antibiotics used in the clinic today that are becoming ever less effective against certain species of bacteria as resistance grows. The solution to this problem is not necessarily the complete replacement of current antibiotics but the ability to reduce both dosage and clinical prevalence. It is therefore suggested that stewardship studies be carried out in which current antibiotics are complimented with the antibacterial materials developed within this thesis to assess their ability in reducing the required antibacterial dosages for the antibiotics.

References

1. A. Fleming, *British Medical Bulletin*, 1944, **2**, 4-5.
2. R. Aminov, *Frontiers in Microbiology*, 2010, **1**.
3. M. M. M. University of Oxford, <http://modmedmicro.nsms.ox.ac.uk/learn-more-about-antibiotic-resistance/>, (accessed November, 2018).
4. K. Susan Hopkins and L. Simpson, *Health Protection Agency: London*, 2012.
5. L. Hall-Stoodley, J. W. Costerton and P. Stoodley, *Nature Reviews Microbiology*, 2004, **2**, 95.
6. S. Veerachamy, T. Yarlagadda, G. Manivasagam and P. K. Yarlagadda, *Proceedings of the Institution of Mechanical Engineers, Part H: Journal of Engineering in Medicine*, 2014, **228**, 1083-1099.
7. W. H. Organization, *Geneva: World Health Organization*, 2017.
8. J. A. Lichter, K. J. Van Vliet and M. F. Rubner, *Macromolecules*, 2009, **42**, 8573-8586.
9. Y.-H. Joung, *International Neurourology Journal*, 2013, **17**, 98-106.
10. W. Khan, E. Muntimadugu, M. Jaffe and A. J. Domb, in *Focal Controlled Drug Delivery*, eds. A. J. Domb and W. Khan, Springer US, Boston, MA, 2014, DOI: 10.1007/978-1-4614-9434-8_2, pp. 33-59.
11. Q. Chen and G. A. Thouas, *Materials Science and Engineering: R: Reports*, 2015, **87**, 1-57.
12. M. Saini, Y. Singh, P. Arora, V. Arora and K. Jain, *World Journal of Clinical Cases: WJCC*, 2015, **3**, 52.
13. X. Tang, S. K. Thankappan, P. Lee, S. E. Fard, M. D. Harmon, K. Tran and X. Yu, in *Natural and Synthetic Biomedical Polymers*, eds. S. G. Kumbar, C. T. Laurencin and M. Deng, Elsevier, Oxford, 2014, DOI: <https://doi.org/10.1016/B978-0-12-396983-5.00022-3>, pp. 351-371.
14. N. Lamba, K. Woodhouse and S. Cooper, *Boca Raton, FL: CRC*, 2004.
15. R. J. Zdrahala and I. J. Zdrahala, *Journal of biomaterials applications*, 1999, **14**, 67-90.
16. S. H. Ajili, N. G. Ebrahimi and M. Soleimani, *Acta Biomaterialia*, 2009, **5**, 1519-1530.

17. S. B. Kim, Y. J. Kim, T. L. Yoon, S. A. Park, I. H. Cho, E. J. Kim, I. A. Kim and J.-W. Shin, *Biomaterials*, 2004, **25**, 5715-5723.
18. J. J. Klawitter, A. M. Weinstein and L. J. Peterson, *Journal of dental research*, 1977, **56**, 385-393.
19. C. Terrada, K. Julian, N. Cassoux, A.-M. Prieur, M. Debre, P. Quartier, P. LeHoang and B. Bodaghi, *Journal of Cataract & Refractive Surgery*, 2011, **37**, 1977-1983.
20. D. Rohner, D. W. Hutmacher, T. K. Cheng, M. Oberholzer and B. Hammer, *Journal of Biomedical Materials Research Part B: Applied Biomaterials: An Official Journal of The Society for Biomaterials, The Japanese Society for Biomaterials, and The Australian Society for Biomaterials and the Korean Society for Biomaterials*, 2003, **66**, 574-580.
21. C. K. S. Pillai and C. P. Sharma, *Journal of biomaterials applications*, 2010, **25**, 291-366.
22. A. G. A. Coombes, S. C. Rizzi, M. Williamson, J. E. Barralet, S. Downes and W. A. Wallace, *Biomaterials*, 2004, **25**, 315-325.
23. L. Xue and H. P. Greisler, *Journal of Vascular Surgery*, 2003, **37**, 472-480.
24. A. Metzger, *Biomedical Engineering*, 1976, **11**, 301-306.
25. A. Rahimi and A. Mashak, *Plastics, Rubber and Composites*, 2013, **42**, 223-230.
26. A. Colas and J. Curtis, *Biomaterials science: an introduction to materials in medicine*, 2004, **2**, 80-85.
27. A. J. Teo, A. Mishra, I. Park, Y.-J. Kim, W.-T. Park and Y.-J. Yoon, *ACS Biomaterials Science & Engineering*, 2016, **2**, 454-472.
28. M. E. Davey and G. A. O'toole, *Microbiology and molecular biology reviews*, 2000, **64**, 847-867.
29. D. G. Maki, S. M. Stolz, S. Wheeler and L. A. Mermel, *Annals of Internal Medicine*, 1997, **127**, 257-266.
30. T. S. J. Elliott, H. A. Moss, S. E. Tebbs, I. C. Wilson, R. S. Bonser, T. R. Graham, L. P. Burke and M. H. Faroqui, *European Journal of Clinical Microbiology and Infectious Diseases*, 1997, **16**, 210-213.
31. D. Stickler, *Biofouling*, 1996, **9**, 293-305.
32. M. H. Choo, D. R. Holmes, Jr., B. J. Gersh, J. D. Maloney, J. Merideth, J. R. Pluth and J. Trusty, *American Journal of Cardiology*, 1981, **48**, 559-564.

33. C. G. Adair, S. P. Gorman, B. M. Feron, L. M. Byers, D. S. Jones, C. E. Goldsmith, J. E. Moore, J. R. Kerr, M. D. Curran, G. Hogg, C. H. Webb, G. J. McCarthy and K. R. Milligan, *Intensive Care Medicine*, 1999, **25**, 1072-1076.
34. M. D. P. WILLCOX, *Optometry and Vision Science*, 2007, **84**, 273-278.
35. K. L. Garvin and A. D. Hanssen, *JBJS*, 1995, **77**, 1576-1588.
36. P. J. Sanderson, *Journal of Hospital Infection*, 1991, **18**, 367-375.
37. H. Anwar, J. L. Strap, K. Chen and J. W. Costerton, *Antimicrobial Agents and Chemotherapy*, 1992, **36**, 1208.
38. A. E. Khoury, K. Lam, B. Ellis and J. W. Costerton, *ASAIO journal (American Society for Artificial Internal Organs: 1992)*, 1992, **38**, M174-178.
39. C. von Eiff, B. Jansen, W. Kohlen and K. Becker, *Drugs*, 2005, **65**, 179-214.
40. P. Stoodley, K. Sauer, D. G. Davies and J. W. Costerton, *Annual Reviews in Microbiology*, 2002, **56**, 187-209.
41. I. Francolini and G. Donelli, *FEMS Immunology & Medical Microbiology*, 2010, **59**, 227-238.
42. J. N. Anderl, J. Zahller, F. Roe and P. S. Stewart, *Antimicrobial agents and chemotherapy*, 2003, **47**, 1251-1256.
43. J. N. Anderl, M. J. Franklin and P. S. Stewart, *Antimicrobial agents and chemotherapy*, 2000, **44**, 1818-1824.
44. J. Zahller and P. S. Stewart, *Antimicrobial agents and chemotherapy*, 2002, **46**, 2679-2683.
45. A. L. Spoering and K. Lewis, *Journal of bacteriology*, 2001, **183**, 6746-6751.
46. N. Q. Balaban, J. Merrin, R. Chait, L. Kowalik and S. Leibler, *Science*, 2004, **305**, 1622-1625.
47. S. M. Soto, *Virulence*, 2013, **4**, 223-229.
48. M. Hausner and S. Wuertz, *Applied and Environmental Microbiology*, 1999, **65**, 3710-3713.
49. E.-R. Kenawy, S. Worley and R. Broughton, *Biomacromolecules*, 2007, **8**, 1359-1384.
50. L. Bromberg and T. A. Hatton, *Polymer*, 2007, **48**, 7490-7498.
51. K. Lewis and A. M. Klibanov, *TRENDS in Biotechnology*, 2005, **23**, 343-348.

52. E. P. Ivanova, J. Hasan, H. K. Webb, V. K. Truong, G. S. Watson, J. A. Watson, V. A. Baulin, S. Pogodin, J. Y. Wang and M. J. Tobin, *Small*, 2012, **8**, 2489-2494.
53. M. N. Dickson, E. I. Liang, L. A. Rodriguez, N. Vollereaux and A. F. Yee, *Biointerphases*, 2015, **10**, 021010.
54. J. Genzer and K. Efimenko, *Biofouling*, 2006, **22**, 339-360.
55. A. I. Hochbaum and J. Aizenberg, *Nano Letters*, 2010, **10**, 3717-3721.
56. R. F. Furchgott, *Angewandte Chemie International Edition*, 1999, **38**, 1870-1880.
57. L. J. Ignarro, G. M. Buga, K. S. Wood, R. E. Byrns and G. Chaudhuri, *Proceedings of the National Academy of Sciences*, 1987, **84**, 9265-9269.
58. F. Murad, *Angewandte Chemie International Edition*, 1999, **38**, 1856-1868.
59. F. C. Fang, *Nitric oxide and infection*, Springer, 1999.
60. C. Bogdan, in *Nitric Oxide*, Springer, 2000, pp. 443-492.
61. C. Bogdan, *Nature immunology*, 2001, **2**, 907.
62. K. Xie, Z. Dong and I. J. Fidler, *Journal of leukocyte biology*, 1996, **59**, 797-803.
63. S. Pervin, R. Singh and G. Chaudhuri, *Proceedings of the National Academy of Sciences*, 2001, **98**, 3583-3588.
64. C. Bogdan, *Trends in cell biology*, 2001, **11**, 66-75.
65. C. Nathan and M. U. Shiloh, *Proceedings of the National Academy of Sciences*, 2000, **97**, 8841-8848.
66. C. Bogdan, M. Röllinghoff and A. Diefenbach, *Current opinion in immunology*, 2000, **12**, 64-76.
67. D. Berendji, V. Kolb-Bachofen, P. F. Zipfel, C. Skerka and C. Carlberg, *Molecular medicine*, 1999, **5**, 721.
68. M. G. Belvisi, C. D. Stretton, M. Yacoub and P. J. Barnes, *European journal of pharmacology*, 1992, **210**, 221-222.
69. C. G. Li and M. J. Rand, *British journal of pharmacology*, 1991, **102**, 91-94.
70. J. A. Carvajal, A. M. Germain, J. P. Huidobro-Toro and C. P. Weiner, *Journal of cellular physiology*, 2000, **184**, 409-420.
71. A. Halbower, R. M. Tuder, W. A. Franklin, J. S. Pollock, U. Forstermann and S. H. Abman, *American Journal of Physiology-Lung Cellular and Molecular Physiology*, 1994, **267**, L585-L591.

72. A. Hislop, D. Springall, L. Buttery, J. Pollock and S. Haworth, *Archives of Disease in Childhood-Fetal and Neonatal Edition*, 1995, **73**, F17-F21.
73. T. A. Parker, T. D. le Cras, J. P. Kinsella and S. H. Abman, *American Journal of Physiology-Lung Cellular and Molecular Physiology*, 2000, **278**, L202-L208.
74. L. A. Palmer, B. Gaston and R. A. Johns, *Molecular pharmacology*, 2000, **58**, 1197-1203.
75. M. Nagaki, S. Shimura, T. Irokawa, T. Sasaki and K. Shirato, *Respiration physiology*, 1995, **102**, 89-95.
76. F. L. Ricciardolo, P. J. Sterk, B. Gaston and G. Folkerts, *Physiological reviews*, 2004, **84**, 731-765.
77. D. Rees, R. Palmer and S. Moncada, *Proceedings of the National Academy of Sciences*, 1989, **86**, 3375-3378.
78. K. Nozaki, M. A. Moskowitz, K. I. Maynard, N. Koketsu, T. M. Dawson, D. S. Bredt and S. H. Snyder, *Journal of Cerebral Blood Flow & Metabolism*, 1993, **13**, 70-79.
79. N. K. Menon, A. Wolf, M. Zehetgruber and R. J. Bing, *Proceedings of the Society for Experimental Biology and Medicine*, 1989, **191**, 316-319.
80. S. Kourembanas, L. P. McQuillan, G. K. Leung and D. V. Faller, *The Journal of clinical investigation*, 1993, **92**, 99-104.
81. A. Brady, J. B. Warren, P. A. Poole-Wilson, T. J. Williams and S. E. Harding, *American Journal of Physiology-Heart and Circulatory Physiology*, 1993, **265**, H176-H182.
82. M. Radomski, R. Palmer and S. Moncada, *Proceedings of the National Academy of Sciences*, 1990, **87**, 5193-5197.
83. P. Kubes, M. Suzuki and D. Granger, *Proceedings of the National Academy of Sciences*, 1991, **88**, 4651-4655.
84. J. Loscalzo and G. Welch, *Progress in cardiovascular diseases*, 1995, **38**, 87-104.
85. V. Calabrese, C. Mancuso, M. Calvani, E. Rizzarelli, D. A. Butterfield and A. M. G. Stella, *Nature Reviews Neuroscience*, 2007, **8**, 766.
86. J. E. Stern, *Progress in biophysics and molecular biology*, 2004, **84**, 197-215.
87. J. Garthwaite, S. L. Charles and R. Chess-Williams, *Nature*, 1988, **336**, 385.
88. J. Garthwaite and C. Boulton, *Annual review of physiology*, 1995, **57**, 683-706.

89. K. M. Sanders and S. M. Ward, *American Journal of Physiology-Gastrointestinal and Liver Physiology*, 1992, **262**, G379-G392.
90. F. Holmquist, C. G. Stief, U. Jonas and K. E. Andersson, *Acta physiologica scandinavica*, 1991, **143**, 299-304.
91. W. J. Hellstrom, M. Bell, R. Wang and S. C. Sikka, *Fertility and sterility*, 1994, **61**, 1117-1122.
92. M. Rosselli, B. Imthurm, E. Macas, P. Keller and R. Dubey, *Biochemical and biophysical research communications*, 1994, **202**, 1543-1552.
93. M. Rosselli, R. Keller and R. K. Dubey, *Human Reproduction Update*, 1998, **4**, 3-24.
94. R. G. Knowles and S. Moncada, *Biochemical Journal*, 1994, **298**, 249.
95. W. K. Alderton, C. E. Cooper and R. G. Knowles, *Biochemical Journal*, 2001, **357**, 593-615.
96. O. W. Griffith and D. J. Stuehr, *Annual review of physiology*, 1995, **57**, 707-734.
97. J. M. Wong and T. R. Billiar, in *Advances in pharmacology*, Elsevier, 1995, vol. 34, pp. 155-170.
98. C. F. Nathan and J. B. Hibbs Jr, *Current opinion in immunology*, 1991, **3**, 65-70.
99. S. Nicholson, M. da G Bonecini-Almeida, J. L. e Silva, C. Nathan, Q. Xie, R. Mumford, J. R. Weidner, J. Calaycay, J. Geng and N. Boechat, *Journal of Experimental Medicine*, 1996, **183**, 2293-2302.
100. S. L. Morris and J. N. Hansen, *Journal of bacteriology*, 1981, **148**, 465-471.
101. K. Beckerman, H. Rogers, J. Corbett, R. Schreiber, M. McDaniel and E. Unanue, *The Journal of Immunology*, 1993, **150**, 888-895.
102. K. Incze, J. Farkas, V. Mihályi and E. Zúkal, *Applied microbiology*, 1974, **27**, 202-205.
103. S. E. Malawista, R. R. Montgomery and G. Van Blaricom, *The Journal of clinical investigation*, 1992, **90**, 631-636.
104. N. Barraud, D. J. Hasset, S.-H. Hwang, S. A. Rice, S. Kjelleberg and J. S. Webb, *Journal of bacteriology*, 2006, **188**, 7344-7353.
105. E. Cenci, L. Romani, A. Mencacci, R. Spaccapelo, E. Schiaffella, P. Puccetti and F. Bistoni, *European journal of immunology*, 1993, **23**, 1034-1038.

106. J. A. Alspaugh and D. L. Granger, *Infection and Immunity*, 1991, **59**, 2291-2296.
107. T. E. Lane, B. A. Wu-Hsieh and D. H. Howard, *Infection and immunity*, 1994, **62**, 1940-1945.
108. M. Sherman, M. Loro, V. Wong and D. Tashkin, *The Journal of protozoology*, 1991, **38**, 234S-236S.
109. J. Lin and K. Chadee, *The Journal of Immunology*, 1992, **148**, 3999-4005.
110. S. J. Green, M. S. Meltzer, J. Hibbs and C. A. Nacy, *The Journal of Immunology*, 1990, **144**, 278-283.
111. K. Fischer-Stenger and F. Marciano-Cabral, *Infection and immunity*, 1992, **60**, 5126-5131.
112. M. R. Haswell-Elkins, S. Satarug, M. Tsuda, E. Mairiang, H. Esumi, P. Sithithaworn, P. Mairiang, M. Saitoh, P. Yongvanit and D. B. Elkins, *Mutation Research/Fundamental and Molecular Mechanisms of Mutagenesis*, 1994, **305**, 241-252.
113. K. Rockett, M. Awburn, W. Cowden and I. Clark, *Infection and Immunity*, 1991, **59**, 3280-3283.
114. G. Karupiah, Q.-w. Xie, R. Buller, C. Nathan, C. Duarte and J. D. MacMicking, *Science*, 1993, **261**, 1445-1448.
115. J. B. Mannick, K. Asano, K. Izumi, E. Kieff and J. S. Stamler, *Cell*, 1994, **79**, 1137-1146.
116. K. D. Croen, *The Journal of clinical investigation*, 1993, **91**, 2446-2452.
117. M. J. Juedes and G. N. Wogan, *Mutation Research/Fundamental and Molecular Mechanisms of Mutagenesis*, 1996, **349**, 51-61.
118. H. Ischiropoulos and A. B. Al-Mehdi, *FEBS letters*, 1995, **364**, 279-282.
119. F. C. Fang, *The Journal of clinical investigation*, 1997, **99**, 2818-2825.
120. M. A. De Groote and F. C. Fang, *Clinical Infectious Diseases*, 1995, **21**, S162-S165.
121. P. G. Wang, M. Xian, X. Tang, X. Wu, Z. Wen, T. Cai and A. J. Janczuk, *Chemical reviews*, 2002, **102**, 1091-1134.
122. J. Baker and T. Heggs, *Journal*, 1954, 464-464.
123. G. R. Thatcher, *Chemical Society Reviews*, 1998, **27**, 331-337.

124. D. L. H. Williams, *Nitrosation reactions and the chemistry of nitric oxide*, Elsevier, 2004.
125. L. Grossi and S. Strazzari, *The Journal of organic chemistry*, 1999, **64**, 8076-8079.
126. Y. Ji, T. Akerboom and H. Sies, *Biochemical Journal*, 1996, **313**, 377.
127. J. J. Doel, B. L. Godber, T. A. Goult, R. Eisenthal and R. Harrison, *Biochemical and biophysical research communications*, 2000, **270**, 880-885.
128. J. A. Bauer, T. Nolan and H.-L. Fung, *Journal of Pharmacology and Experimental Therapeutics*, 1997, **280**, 326-331.
129. H.-L. Fung and J. A. Bauer, *Journal*, 1996.
130. R. Radi, *Chemical research in toxicology*, 1996, **9**, 828-835.
131. J. R. Stone and M. A. Marletta, *Biochemistry*, 1996, **35**, 1093-1099.
132. W. R. Montfort, J. A. Wales and A. Weichsel, *Antioxidants & redox signaling*, 2017, **26**, 107-121.
133. P. C. Ford, *International Journal of Photoenergy*, 2001, **3**, 161-169.
134. H. S. Tasker and H. O. Jones, *Journal of the Chemical Society, Transactions*, 1909, **95**, 1910-1918.
135. D. L. H. Williams, *Accounts of chemical research*, 1999, **32**, 869-876.
136. V. G. Kharitonov, A. R. Sundquist and V. S. Sharma, *Journal of Biological Chemistry*, 1995, **270**, 28158-28164.
137. D. Williams, *Transition Metal Chemistry*, 1996, **21**, 189-191.
138. H. Swift, *Journal of the Chemical Society, Perkin Transactions 2*, 1997, 1933-1935.
139. R. S. Drago and F. Paulik, *Journal of the American Chemical society*, 1960, **82**, 96-98.
140. J. A. Hrabie, J. R. Klose, D. A. Wink and L. K. Keefer, *The Journal of Organic Chemistry*, 1993, **58**, 1472-1476.
141. W. L. Storm and M. H. Schoenfisch, *ACS Applied Materials & Interfaces*, 2013, **5**, 4904-4912.
142. J. A. Hrabie and L. K. Keefer, *Chemical Reviews*, 2002, **102**, 1135-1154.
143. A. Daiber, P. Wenzel, M. Oelze and T. Münzel, *Clinical Research in Cardiology*, 2008, **97**, 12-20.

144. B. Mordorski, R. Pelgrift, B. Adler, A. Krausz, A. B. da Costa Neto, H. Liang, L. Gunther, A. Clendaniel, S. Harper and J. M. Friedman, *Nanomedicine: Nanotechnology, Biology and Medicine*, 2015, **11**, 283-291.
145. L. K. Keefer, *ACS chemical biology*, 2011, **6**, 1147-1155.
146. J. A. Hrabie, J. E. Saavedra, P. P. Roller, G. J. Southan and L. K. Keefer, *Bioconjugate chemistry*, 1999, **10**, 838-842.
147. H. Zhang, G. M. Annich, J. Miskulin, K. Stankiewicz, K. Osterholzer, S. I. Merz, R. H. Bartlett and M. E. Meyerhoff, *Journal of the American Chemical Society*, 2003, **125**, 5015-5024.
148. J. H. Shin and M. H. Schoenfisch, *Chemistry of Materials*, 2007, **20**, 239-249.
149. M. A. Polizzi, N. A. Stasko and M. H. Schoenfisch, *Langmuir*, 2007, **23**, 4938-4943.
150. N. A. Stasko and M. H. Schoenfisch, *Journal of the American Chemical Society*, 2006, **128**, 8265-8271.
151. D. J. Smith, D. Chakravarthy, S. Pulfer, M. L. Simmons, J. A. Hrabie, M. L. Citro, J. E. Saavedra, K. M. Davies, T. C. Hutsell and D. L. Mooradian, *Journal of Medicinal Chemistry*, 1996, **39**, 1148-1156.
152. K. A. Mowery, M. H. Schoenfisch, J. E. Saavedra, L. K. Keefer and M. E. Meyerhoff, *Biomaterials*, 2000, **21**, 9-21.
153. M. M. Batchelor, S. L. Reoma, P. S. Fleser, V. K. Nuthakki, R. E. Callahan, C. J. Shanley, J. K. Politis, J. Elmore, S. I. Merz and M. E. Meyerhoff, *Journal of Medicinal Chemistry*, 2003, **46**, 5153-5161.
154. H. Zhang, G. M. Annich, J. Miskulin, K. Osterholzer, S. I. Merz, R. H. Bartlett and M. E. Meyerhoff, *Biomaterials*, 2002, **23**, 1485-1494.
155. P. G. Parzuchowski, M. C. Frost and M. E. Meyerhoff, *Journal of the American Chemical Society*, 2002, **124**, 12182-12191.
156. M. M. Reynolds, J. A. Hrabie, B. K. Oh, J. K. Politis, M. L. Citro, L. K. Keefer and M. E. Meyerhoff, *Biomacromolecules*, 2006, **7**, 987-994.
157. M. C. Frost, S. M. Rudich, H. Zhang, M. A. Maraschio and M. E. Meyerhoff, *Analytical chemistry*, 2002, **74**, 5942-5947.
158. B. J. Nablo, T.-Y. Chen and M. H. Schoenfisch, *Journal of the American Chemical Society*, 2001, **123**, 9712-9713.
159. M. E. Robbins and M. H. Schoenfisch, *Journal of the American Chemical Society*, 2003, **125**, 6068-6069.

160. S. M. Marxer, A. R. Rothrock, B. J. Nablo, M. E. Robbins and M. H. Schoenfish, *Chemistry of Materials*, 2003, **15**, 4193-4199.
161. B. J. Nablo, A. R. Rothrock and M. H. Schoenfish, *Biomaterials*, 2005, **26**, 917-924.
162. B. J. Nablo and M. H. Schoenfish, *Biomacromolecules*, 2004, **5**, 2034-2041.
163. E. M. Hetrick and M. H. Schoenfish, *Biomaterials*, 2007, **28**, 1948-1956.
164. W. Barthlott and C. Neinhuis, *Planta*, 1997, **202**, 1-8.
165. G. D. Bixler and B. Bhushan, *Advanced Functional Materials*, 2013, **23**, 4507-4528.
166. B. Bhushan, *Journal*, 2009.
167. K. Anselme, P. Davidson, A. Popa, M. Giazzon, M. Liley and L. Ploux, *Acta biomaterialia*, 2010, **6**, 3824-3846.
168. T. Blättler, C. Huwiler, M. Ochsner, B. Städler, H. Solak, J. Vörös and H. M. Grandin, *Journal of nanoscience and nanotechnology*, 2006, **6**, 2237-2264.
169. A. A. Tseng, C. Kuan, C. D. Chen and K. J. Ma, *IEEE Transactions on Electronics Packaging Manufacturing*, 2003, **26**, 141-149.
170. M. Wood, *Journal of the Royal Society Interface*, 2007, **4**, 1-17.
171. V. N. Truskett and M. P. Watts, *Trends in biotechnology*, 2006, **24**, 312-317.
172. S. Walheim, M. Böltau, J. Mlynek, G. Krausch and U. Steiner, *Macromolecules*, 1997, **30**, 4995-5003.
173. R. A. D'Sa, J. Raj, P. J. Dickinson, F. McCabe and B. J. Meenan, *ACS applied materials & interfaces*, 2015, **8**, 14920-14931.
174. S. Ramakrishna, *An introduction to electrospinning and nanofibers*, World Scientific, 2005.
175. O. Zinger, K. Anselme, A. Denzer, P. Habersetzer, M. Wieland, J. Jeanfils, P. Hardouin and D. Landolt, *Biomaterials*, 2004, **25**, 2695-2711.
176. S. Tajima, J. S. F. Chu, S. Li and K. Komvopoulos, *Journal of Biomedical Materials Research Part A*, 2008, **84A**, 828-836.
177. J. Park, S. Bauer, K. A. Schlegel, F. W. Neukam, K. von der Mark and P. Schmuki, *Small*, 2009, **5**, 666-671.
178. C. Díaz, M. C. Cortizo, P. L. Schilardi, S. G. G. d. Saravia and M. A. F. L. d. Mele, *Materials Research*, 2007, **10**, 11-14.

179. L. C. Hsu, J. Fang, D. A. Borca-Tasciuc, R. W. Worobo and C. I. Moraru, *Applied and Environmental Microbiology*, 2013, **79**, 2703.
180. N. Lu, W. Zhang, Y. Weng, X. Chen, Y. Cheng and P. Zhou, *Food Control*, 2016, **68**, 344-351.
181. S. Hou, H. Gu, C. Smith and D. Ren, *Langmuir*, 2011, **27**, 2686-2691.
182. M. Katsikogianni and Y. Missirlis, *Eur Cell Mater*, 2004, **8**, 37-57.
183. M. Michalska, F. Gambacorta, R. Divan, I. S. Aranson, A. Sokolov, P. Noirot and P. D. Laible, *Nanoscale*, 2018, **10**, 6639-6650.
184. M. L. Carman, T. G. Estes, A. W. Feinberg, J. F. Schumacher, W. Wilkerson, L. H. Wilson, M. E. Callow, J. A. Callow and A. B. Brennan, *Biofouling*, 2006, **22**, 11-21.
185. K. K. Chung, J. F. Schumacher, E. M. Sampson, R. A. Burne, P. J. Antonelli and A. B. Brennan, *Biointerphases*, 2007, **2**, 89-94.
186. R. M. May, C. M. Magin, E. E. Mann, M. C. Drinker, J. C. Fraser, C. A. Siedlecki, A. B. Brennan and S. T. Reddy, *Clinical and translational medicine*, 2015, **4**, 9.
187. M. Maitz, *Biosurface and Biotribology*, 2015, **1**, 161-176.
188. J.-d. Luo and A. F. Chen, *Acta Pharmacologica Sinica*, 2005, **26**, 259.
189. R. M. Donlan, *Emerging Infectious Diseases*, 2001, **7**, 277-281.
190. R. Dahiya, G. Gottardi and N. Laidani, *Microelectronic Engineering*, 2015, **136**, 57-62.
191. M. Zhu, M. Z. Lerum and W. Chen, *Langmuir*, 2012, **28**, 416-423.
192. V. Jokinen, P. Suvanto and S. Franssila, *Biomicrofluidics*, 2012, **6**, 016501.
193. M. Morra, E. Occhiello, R. Marola, F. Garbassi, P. Humphrey and D. Johnson, *Journal of Colloid and Interface Science*, 1990, **137**, 11-24.
194. M. J. Owen and P. J. Smith, *Journal of Adhesion Science and Technology*, 1994, **8**, 1063-1075.
195. J. L. Fritz and M. J. Owen, *The Journal of Adhesion*, 1995, **54**, 33-45.
196. J. Kim, M. K. Chaudhury and M. J. Owen, *Journal of Colloid and Interface Science*, 2000, **226**, 231-236.
197. J. Kim, M. K. Chaudhury and M. J. Owen, *Journal of Colloid and Interface Science*, 2006, **293**, 364-375.

198. Y. Nakamura, N. Yokouchi, Y. Tobita, T. Iida and K. Nagata, *Composite Interfaces*, 2005, **12**, 669-681.
199. E. Gonzalez, M. D. Barankin, P. C. Guschl and R. F. Hicks, *Langmuir*, 2008, **24**, 12636-12643.
200. C. Lee and G. Homan, 1981.
201. H. Hillborg and U. Gedde, *Polymer*, 1998, **39**, 1991-1998.
202. A. Tóth, I. Bertóti, M. Blazsó, G. Bánhegyi, A. Bogнар and P. Szaplóczay, *Journal of applied polymer science*, 1994, **52**, 1293-1307.
203. G. McIntyre Jr, B. Block and W. C. Fernelius, *Journal of the American Chemical Society*, 1959, **81**, 529-535.
204. K. C. Gross, P. G. Seybold and C. M. Hadad, *International Journal of Quantum Chemistry*, 2002, **90**, 445-458.
205. T.-F. C. Mah and G. A. O'toole, *Trends in microbiology*, 2001, **9**, 34-39.
206. N. Barraud, D. Schleheck, J. Klebensberger, J. S. Webb, D. J. Hassett, S. A. Rice and S. Kjelleberg, *Journal of bacteriology*, 2009, **191**, 7333-7342.
207. K. E. Darling and T. J. Evans, *Infection and immunity*, 2003, **71**, 2341-2349.
208. N. E. Van Alst, K. F. Picardo, B. H. Iglewski and C. G. Haidaris, *Infection and immunity*, 2007, **75**, 3780-3790.
209. A. Hogt, J. Dankert and J. Feijen, *Journal of biomedical materials research*, 1986, **20**, 533-545.
210. N. Satou, J. Satou, H. Shintani and K. Okuda, *Microbiology*, 1988, **134**, 1299-1305.
211. T. Das, S. K. Kutty, N. Kumar and M. Manefield, *PLoS One*, 2013, **8**, e58299.
212. A. Ghaffari, C. C. Miller, B. McMullin and A. Ghahary, *Nitric Oxide*, 2006, **14**, 21-29.
213. B. J. Nablo, H. L. Prichard, R. D. Butler, B. Klitzman and M. H. Schoenfisch, *Biomaterials*, 2005, **26**, 6984-6990.
214. S. P. Nichols, W. L. Storm, A. Koh and M. H. Schoenfisch, *Advanced drug delivery reviews*, 2012, **64**, 1177-1188.
215. S. M. Marxer, A. R. Rothrock, B. J. Nablo, M. E. Robbins and M. H. Schoenfisch, *Chemistry of materials*, 2003, **15**, 4193-4199.




216. B. J. Nablo and M. H. Schoenfisch, *Journal of Biomedical Materials Research Part A: An Official Journal of The Society for Biomaterials, The Japanese Society for Biomaterials, and The Australian Society for Biomaterials and the Korean Society for Biomaterials*, 2003, **67**, 1276-1283.
217. A. W. Carpenter, B. V. Worley, D. L. Slomberg and M. H. Schoenfisch, *Biomacromolecules*, 2012, **13**, 3334-3342.
218. N. Graf, E. Yegen, T. Gross, A. Lippitz, W. Weigel, S. Krakert, A. Terfort and W. E. Unger, *Surface Science*, 2009, **603**, 2849-2860.
219. A. Brooun, S. Liu and K. Lewis, *Antimicrobial agents and chemotherapy*, 2000, **44**, 640-646.
220. M. E. Robbins, E. D. Hopper and M. H. Schoenfisch, *Langmuir*, 2004, **20**, 10296-10302.
221. B. J. Nablo and M. H. Schoenfisch, *Biomacromolecules*, 2004, **5**, 2034-2041.
222. C. J. Brinker and G. W. Scherer, *Sol-gel science: the physics and chemistry of sol-gel processing*, Academic press, 2013.
223. F. Rousseau, C. Poinignon, J. Garcia and M. Popall, *Chemistry of materials*, 1995, **7**, 828-839.
224. M. J. Mosquera, M. Desireé, L. Valdez-Castro and L. Esquivias, *Journal of Non-Crystalline Solids*, 2008, **354**, 645-650.
225. G. W. Scherer, *Journal of non-crystalline solids*, 1992, **147**, 363-374.
226. E. M. Hetrick, J. H. Shin, N. A. Stasko, C. B. Johnson, D. A. Wespe, E. Holmuhamedov and M. H. Schoenfisch, *ACS Nano*, 2008, **2**, 235-246.
227. E. M. Hetrick, J. H. Shin, H. S. Paul and M. H. Schoenfisch, *Biomaterials*, 2009, **30**, 2782-2789.
228. S. Y. Heriot and R. A. Jones, *Nature materials*, 2005, **4**, 782.
229. G. Duan, C. Zhang, A. Li, X. Yang, L. Lu and X. Wang, *Nanoscale Research Letters*, 2008, **3**, 118.
230. C. Girardeaux and J.-J. Pireaux, *Surface Science Spectra*, 1996, **4**, 130-133.
231. P. Louette, F. Bodino and J.-J. Pireaux, *Surface Science Spectra*, 2005, **12**, 27-31.
232. P. Louette, F. Bodino and J.-J. Pireaux, *Surface science spectra*, 2005, **12**, 69-73.

233. C. Monteux, A. Tay, T. Narita, Y. De Wilde and F. Lequeux, *Soft Matter*, 2009, **5**, 3713-3717.
234. P. J. Flory, *Principles of polymer chemistry*, Cornell University Press, 1953.
235. P. J. Flory, *The Journal of chemical physics*, 1942, **10**, 51-61.
236. M. L. Huggins, *The Journal of chemical physics*, 1941, **9**, 440-440.
237. C. Ton-That, A. Shard, R. Daley and R. Bradley, *Macromolecules*, 2000, **33**, 8453-8459.
238. C. Ton-That, A. Shard, D. Teare and R. Bradley, *Polymer*, 2001, **42**, 1121-1129.
239. M. Ma, Z. He, J. Yang, Q. Wang, F. Chen, K. Wang, Q. Zhang, H. Deng and Q. Fu, *Langmuir*, 2011, **27**, 1056-1063.
240. K. Tanaka, A. Takahara and T. Kajiyama, *Macromolecules*, 1998, **31**, 863-869.
241. R. P. Wool, *Polymer interfaces: structure and strength*, Hanser, 1995.
242. D. R. Lide, *CRC handbook of chemistry and physics*, CRC Boca Raton, 2012.
243. P. F. Green, T. M. Christensen, T. P. Russell and R. Jerome, *The Journal of chemical physics*, 1990, **92**, 1478-1482.
244. M. Lewin, A. Mey-Marom and R. Frank, *Polymers for advanced technologies*, 2005, **16**, 429-441.
245. L. C. Lins, V. Bugatti, S. Livi and G. Gorrasi, *Polymers*, 2018, **10**, 44.
246. M. Khattak, F. Pu, J. M. Curran, J. A. Hunt and R. A. D'Sa, *Journal of Materials Science: Materials in Medicine*, 2015, **26**, 178.
247. S. Affrossman and M. Stamm, *Macromolecules*, 1998, **31**, 6280-6288.
248. D. Slep, J. Asselta, M. H. Rafailovich, J. Sokolov, D. A. Winesett, A. P. Smith, H. Ade, Y. Strzhemechny, S. A. Schwarz and B. B. Sauer, *Langmuir*, 1998, **14**, 4860-4864.
249. K. Tanaka, A. Takahara and T. Kajiyama, *Macromolecules*, 1996, **29**, 3232-3239.
250. C. Maldarelli, R. K. Jain, I. B. Ivanov and E. Ruckenstein, *Journal of Colloid and Interface Science*, 1980, **78**, 118-143.
251. J. P. de Silva, M. Geoghegan, A. M. Higgins, G. Krausch, M. O. David and G. Reiter, *Physical Review Letters*, 2007, **98**, 267802.
252. S. S. Branda, Å. Vik, L. Friedman and R. Kolter, *Trends in microbiology*, 2005, **13**, 20-26.

253. D. Seyer, P. Cosette, A. Siroy, E. Dé, C. Lenz, H. Vaudry, L. Coquet and T. Jouenne, *Biofilms*, 2005, **2**, 27-36.

Article

Nitric Oxide Releasing Polymeric Coatings for the Prevention of Biofilm Formation

George Fleming¹ , Jenny Aveyard¹ , Joanne L. Fothergill², Fiona McBride³, Rasmita Raval³ and Raechelle A. D'Sa^{1,*} 

¹ Department of Mechanical, Materials and Aerospace Engineering, University of Liverpool, Liverpool L69 3GH, UK; sggflemi@liverpool.ac.uk (G.F.); zippy78@liverpool.ac.uk (J.A.)

² Institute of Infection and Global Health, University of Liverpool, 8 West Derby Street, Liverpool L69 7B3, UK; jofoth@liverpool.ac.uk

³ The Open Innovation Hub for Antimicrobial Surfaces, Surface Science Research Centre, Department of Chemistry, University of Liverpool, Liverpool L69 3BX, UK; fmcbride@liverpool.ac.uk (F.M.); raval@liverpool.ac.uk (R.R.)

* Correspondence: r.dsa@liverpool.ac.uk

Received: 31 August 2017; Accepted: 8 November 2017; Published: 11 November 2017

Abstract: The ability of nitric oxide (NO)-releasing polymer coatings to prevent biofilm formation is described. NO-releasing coatings on (poly(ethylene terephthalate) (PET) and silicone elastomer (SE)) were fabricated using aminosilane precursors. Pristine PET and SE were oxygen plasma treated, followed by immobilisation of two aminosilane molecules: *N*-(3-(trimethoxysilyl)propyl)diethylenetriamine (DET3) and *N*-(3-trimethoxysilyl)propyl)aniline (PTMSPA). *N*-diazoniumdiolate nitric oxide donors were formed at the secondary amine sites on the aminosilane molecules producing NO-releasing polymeric coatings. The NO payload and release were controlled by the aminosilane precursor, as DET3 has two secondary amine sites and PTMSPA only one. The antibacterial efficacy of these coatings was tested using a clinical isolate of *Pseudomonas aeruginosa* (PA14). All NO-releasing coatings in this study were shown to significantly reduce *P. aeruginosa* adhesion over 24 h with the efficacy being a function of the aminosilane modification and the underlying substrate. These NO-releasing polymers demonstrate the potential and utility of this facile coating technique for preventing biofilms for indwelling medical devices.

Keywords: nitric oxide donors; *N*-diazoniumdiolates; drug release; antimicrobial surfaces; biofilm prevention

1. Introduction

Bacterial adhesion followed by biofilm formation at an implantation site can pose a significant health risk for patients with indwelling medical devices. The longevity and viability of these tissue-contacting devices are highly reliant on modifying the material surface properties to impart antimicrobial function. Within the National Health Service (NHS), approximately 300,000 patients acquire healthcare-associated infections (HCAIs) annually, with susceptibility to these increasing when devices are implanted [1]. These HCAIs are of significant economic burden to health services and are linked with increased patient morbidity and mortality [2,3]. The most frequent HCAIs detected were respiratory tract (22.8%), catheter associated-urinary tract (17.2%) and surgical site infections (15.7%) [4]. Owing to the prevalence of these device-related infections, there has been much focus on developing antimicrobial coatings that can eliminate bacterial adhesion and subsequent biofilm formation at the implantation site.

When bacteria first interact with a surface, they are in a planktonic state, which results in a rapid, non-specific, reversible colonization of the surface [5]. If bacteria attach irreversibly, a phenotypic change is triggered as a biofilm is formed. The pattern of gene expression for a planktonic bacterial

cell adhering to the surface is significantly different (up to 70%) to one in a biofilm phenotype. Biofilm bacteria irreversibly anchor to the surface and possess mechanisms that allow them to evade immune responses of the host, thus increasing their virulence [6,7]. This increase in virulence and resistance to antimicrobial therapies makes treating HCAs challenging. *Pseudomonas aeruginosa* is a Gram-negative bacterial pathogen frequently found in water, soil and plants [8,9] that can cause serious infections in hosts such as humans, plants and animals [8,10]. It has been classed by the World Health Organization (WHO) as one of the top three priority pathogens worldwide in urgent need of new antibiotics for treatment [11]. It is the most commonly-isolated organism from patients with hospital stays of one week or more, as well as one of the leading causes of nosocomial infections, worldwide [12,13].

The most commonly-used strategy in terms of infection control for biomaterials and medical devices is to incorporate antimicrobials into coatings in order to kill planktonic cells before a biofilm can be formed at the implant site [14]. Importantly, these coatings must also balance the antimicrobial efficacy against the growing epidemic of antimicrobial resistance. A promising strategy for the next generation of antimicrobial coatings will be to specifically target the bacteria's signalling pathways affecting biofilm formation and detachment. Theoretically, by disrupting bacterial signalling pathways, there should be a lower tendency for the bacteria to develop defence responses and resistant mutants. The use of a "universal" antibiofilm molecule for biofilm prevention and dispersal would be ideal, but this remains elusive. The most promising strategies would borrow from nature as they have evolved over millions of years and are still effective [15,16].

NO is a diatomic free radical produced endogenously and has a crucial role in wound healing and neurotransmission and is an innate host antimicrobial response against viruses, bacteria, parasites and fungi [17–20]. The mechanism of action of NO results from its interaction with superoxide and oxygen to form reactive nitrogen species that exhibit bactericidal properties through DNA cleavage, lipid peroxidation and protein dysfunction [19,21]. As a result of NO having several mechanisms of bacterial inactivation, it is regarded as a broad-spectrum antimicrobial with a low tendency towards developing resistance mechanisms [19,21]. Moreover, very low levels of NO (nM) have been shown to prevent biofilm formation and dispersal via a signalling pathway [22,23].

To be considered for use in the clinical setting, NO donors must be capable of controlled NO release at the required site and be stable for storage [24]. Despite the fact that NO is a potent therapeutic and antimicrobial agent, devising a means of storing NO is technically challenging due to its high reactivity and short half-life [24,25]. Several types of NO donors that are capable of releasing NO under physiological conditions have been reported: *N*-diazoniumdiolates, *S*-nitrosothiols (RSNOs), organic nitrates and nitrites and NO-metal complexes [19,26–32]. Out of these, *N*-diazoniumdiolates and RSNOs are the most widely-employed NO donors as they spontaneously decompose under physiological conditions. When exposed to proton sources, such as water or buffer, the *N*-diazoniumdiolates decompose to regenerate NO as seen in Figure 1 [32].

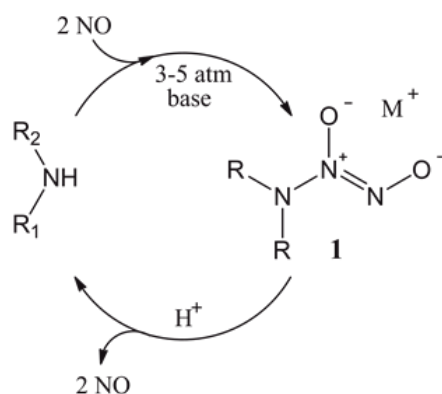


Figure 1. Synthesis and decomposition of diazeniumdiolates.

First identified by Drago, *N*-diazoniumdiolates (1) are compounds containing the functional group [N(O)NO], formed as a product of exposing secondary amines to high pressures of NO [33,34]. *N*-diazoniumdiolates have shown great potential in a variety of medical applications, requiring the rapid or gradual production of NO as they are stable as solid salts, but theoretically release two moles of NO when dissolved in aqueous solution at physiologically-relevant conditions, as seen in Figure 1 [35,36]. By varying the amine precursor, *N*-diazoniumdiolates can be synthesized with tuneable NO release rates with half-lives ranging from 2 s–20 h [37]. The addition of NO donors into polymeric materials has been demonstrated to be non-cytotoxic and non-haemolytic and preserves the mechanical properties of the underlying substrate polymer [38]; however, there is still a need to control the payload and external long-term release of the coating, whilst also preventing leaching. Meyerhoff's group has demonstrated that doping lipophilic dibutylhexyldiamine diazeniumdiolate into polymer films can be used as stable NO donors with minimal leaching [39]. The advantage of such a system is that the proton-catalysed release mechanism of NO creates free lipophilic amine species, which increases the pH, consequently slowing the NO release. Schoenfisch studied a range of NO-releasing xerogel and sol-gel polymers that are capable of inhibiting bacterial adhesion [40–42]. Unfortunately, the xerogels have had problems with stability due to the exposure of high pressures of NO during *N*-diazoniumdiolate formation, which appears to enhance sol-gel polycondensation, producing dense and non-permeable xerogel coatings [43]. Schoenfisch's group has also developed NO-releasing dendritic scaffolds using *N*-diazoniumdiolate derived from primary amine, secondary amine and amide functionalities. The secondary amine had the highest payload/storage capacity for NO owing to higher stability of the secondary amine diazeniumdiolates [44]. These macromolecular dendritic NO scaffolds had half-lives that significantly surpassed those for small molecule equivalents [44].

Herein, we report on the development and antimicrobial efficacy of stable NO-releasing polymer coatings on two medically-relevant polymers used for indwelling medical devices (poly(ethylene terephthalate) (PET) and silicone elastomer (SE)) and their efficacy in preventing *Pseudomonas aeruginosa* biofilm formation. The NO-releasing polymer coatings are synthesised as covalently tethered aminosilane-precursor diazeniumdiolates in order to yield a range of NO-release properties. The purpose of the study was to evaluate the relationship between the structure of the precursor aminosilane used and its relationship to decomposition rates and biofilm prevention. Much of the research looking at efficacy of antimicrobial coatings studies microbes in planktonic, nutrient-rich batch cultures, which is good for initial in vitro screening; however, in vivo infections are typically caused by bacterial biofilms [45,46]. In this study, we look at the antimicrobial efficacy by using overnight cultures of *P. aeruginosa* allowed to grow for 24 h at pH 7.4 under static conditions. Clinical isolate *P. aeruginosa* (PA14) was selected for biofilm prevention studies, as they are well-characterized medically-relevant opportunistic bacteria that form biofilms [47].

2. Materials and Methods

2.1. Preparation of Polymer Substrates for Analysis

Sheets of poly(ethylene terephthalate) (PET), 0.175 mm thick, and silicone elastomer (SE), 1 mm thick (Goodfellow, Cambridge, U.K.), were used as the substrate materials. Disks of each polymer, 6 mm in diameter, were used in NO release quantification experiments and bacterial assays. For all other analyses, substrates were cut into 15 × 15 mm squares. Pristine substrates were subjected to oxygen (BOC, Guildford, U.K.) plasma treatment at a gas flow rate of 14 standard cubic centimetres per minute (sccm) and a pressure of 0.75 mbar using a HPF100 plasma treatment system (Henniker Plasma, Warrington, U.K.).

2.2. Preparation of Aminosilanised Substrates

Substrates were aminosilanised using *N*-(3-(trimethoxysilyl)propyl)diethylenetriamine (DET3) and *N*-(3-(trimethoxysilyl)propyl)aniline (PTMSPA) (Sigma-Aldrich, St. Louis, MO, USA), (Figure 2).

Briefly, pristine PET and SE were subjected to oxygen (BOC, Guildford, U.K.) plasma for optimum treatment times of 7 and 2 min, respectively, as determined from preliminary experiments. Immediately after treatment, substrates were immersed in 10% solutions of either DET3 or PTMSPA in EtOH for 2 h. Substrates were rinsed in anhydrous EtOH, dried in air and cured for 4 h at 80 °C.

2.3. Preparation of Diazeniumdiolate-Tethered Substrates

Diazeniumdiolate tethering was carried out using a stainless steel reactor built in-house. Silanised substrates were placed into the reactor and the system purged with 6 bar of argon (BOC, Guildford, UK) for 3 × 5 min and 3 × 10 min. The reactor was then filled with 5 bar of nitric oxide (NO) (BOC, Guildford, UK) for 96 h. Upon release of NO from the system, the system was purged with 6 bar of argon for 2 × 5 min and 2 × 10 min. Substrates were removed from the reactor and stored at −20 °C prior to use.

2.4. Contact Angle Analysis

Static contact angles of water were used to determine changes in surface wettability following each step of the synthesis, using an Attension ThetaLite optical tensiometer (Biolin Scientific, Västra Frölunda, Sweden). The sessile drop method was used, and contact angles were taken at 17 frames per second for 10 s and data recorded using OneAttension software (Biolin Scientific, Västra Frölunda, Sweden). At least three readings were performed per sample type and the results recorded as the mean average ± the standard deviation.

2.5. XPS Analysis

XPS analysis was carried out on an Axis-Supra instrument (Kratos Analytical, Manchester, UK) using a monochromated Al K α X-ray source operating at a power of 225 W. Charge compensation was performed using a low-energy electron flood source. Survey and narrow region scans were carried out at pass energies of 160 and 20 eV and step sizes of 1 and 0.1 eV, respectively. Hybrid lens mode was used in both cases. Data were converted to vamas (*.vms) format and analysed using CasaXPS 2.3 software (Casa Software, Devon, UK). Spectra were calibrated to 284.6 and 285.0 eV for SE and PET, respectively, corrected with linear background removal and fitted using Gaussian-Lorentzian line curves.

2.6. Atomic Force Microscopy

AFM was used to observe changes in surface topography occurring during synthesis. A Bruker Multimode 8 (Bruker, Billerica, MA, USA) system fitted with a NanoScope V controller was used, and samples were imaged in air in ScanAsyst mode using a silicon RTESPA-150A tip operating at a scan rate of 0.9 Hz. Third order flattening was used to correct any errors whilst processing the image. 5 × 5 μm^2 images were taken and root mean square roughness (R_q) and average roughness (R_a) measured using NanoScope Analysis 1.7 software.

2.7. Electrochemical NO Detection

NO detection was carried out using an ISO-NOPF200 NO-specific electrochemical sensor (WPI, Hitchin, UK). The NO probe was maintained as per the instruction manual by routinely equilibrating it in distilled water for the purpose of acquiring stable background current measurements before samples were tested. S-nitroso-N-acetylpenicillamine (SNAP) was used to calibrate the sensor and has been recommended by WPI to be suitable for calibrating the system for long- and short-term donors [48,49]. Briefly, the sensor was left to polarise in 20 mL of 0.1 M CuCl₂ solution. Following polarisation, calibration was carried out on a daily basis owing to the fact that these types of electrochemical sensors measure small changes in voltage and are therefore extremely sensitive to temperature fluctuations and external noise [50,51]. Upon achieving a steady baseline, aliquots of 10 μM SNAP solution (20, 40, 80, 160 and 320 μL) were added sequentially to the CuCl₂ solution to give final concentrations

of 6, 12, 24, 48 and 96 nM of NO in the solution as outlined by WPI [48,49]. Each aliquot of SNAP addition increased the voltage rapidly, followed by a plateau, which decayed before the next volume was added. SNAP releases NO with a 60% efficiency, and this conversion yield is used to create a calibration curve of voltage vs. NO concentration. For substrate measurements, the NO probe was placed in either 2 mL acetate buffer (pH 4) or PBS (pH 7), until the baseline was stable (5–10 min). Substrate disks were then placed into the solution, and measurements were taken for 30 min (pH 4) and 24 h (pH 7). All experiments were conducted in a temperature controlled room at 25 °C. In order to confirm that the electrochemical sensor was measuring NO release, 100 μ M of the NO scavenger 2-4-carboxyphenyl-4,4,5,5-tetramethylimidazole-1-oxyl-3-oxide (cPTIO, Sigma, Dorset, UK) was added after the NO release measurements. The addition of this NO scavenger resulted in a decrease of the response back to the baseline establishing that only NO was measured.

2.8. Biofilm CFU Assay

Antimicrobial tests were carried out against the *P. aeruginosa* laboratory reference strain PA14 [52]. Overnight cultures of *P. aeruginosa* were diluted to McFarland Standard 0.5 in Luria-Bertani (LB) broth. Substrate disks were placed in 24-well plates and 2 mL of the bacterial solution added before incubating at 37 °C for 24 h to allow biofilm formation. At the end of this time, substrate disks were transferred to sterile well plates and washed with PBS to remove any non-adhered planktonic bacteria. Substrates were then placed in fresh wells and repeatedly washed and agitated vigorously to remove and re-suspend the attached biofilm. A serial dilution was performed on LB agar using the Miles and Misra method in order to enumerate the bacteria from the biofilm. All samples were studied in triplicate and repeated five times.

2.9. Statistical Analysis

The statistical analysis of bacterial numbers was performed using the data analysis package, SigmaPlot 13.0 (Systat Software, San Jose, CA, USA). One-way analysis of variance (ANOVA) was used to establish differences between group means and thus variance between treatment types. Significance between treatment types was determined using the Student–Newman–Keuls (SNK) method. A value of $p < 0.05$ was taken as statistically significant.

3. Results

The synthesis of diazeniumdiolates onto PET and SE is outlined in Figure 2. Briefly, pristine PET and SE were plasma treated to introduce oxygen functionalisation onto the surfaces. This was followed by silanization with the monoamine (PTMSPA) and the triamine (DET3). The aminosilane surfaces were then exposed to a high pressure of NO for 96 h to form the *N*-diazeniumdiolate.

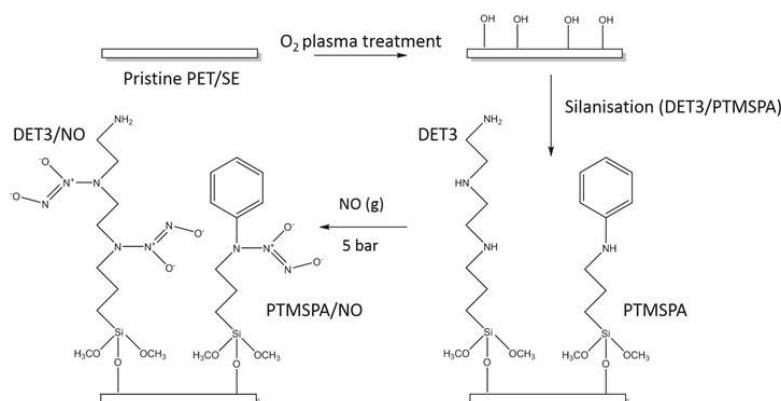


Figure 2. Reaction scheme for tethering of diazeniumdiolates onto PET and silicone elastomer (SE). DET3, *N*-[3-(trimethoxysilyl)propyl]diethylenetriamine; PTMSPA, *N*-[3-(trimethoxysilyl)propyl]aniline.

3.1. Surface Wettability: Contact Angle

The average contact angle values after each synthesis step are recorded in Table 1. A steep reduction in contact angle was observed on both substrates after plasma treatment, when compared with the corresponding pristine controls, confirming an increase in wettability as a result of the oxygen functionalisation of the surfaces. An increase in contact angle was also observed on all substrates following silanisation of PET-DET3 (90.2°), PET-PTMSPA (88.5°), SE-DET3 (116.6°) and SE-PTMSPA (119.2°) (Table 1), which confirmed functionalisation. After tethering the diazeniumdiolate, there was a slight decrease from the aminosilane control surfaces for both PET (PET-DET3/NO (79.0°), PET-PTMSPA (81.6°)) and SE surfaces (SE-DET3/NO (108.8°), SE-PTMSPA (108.6°)). This minor increase in wettability is most likely due to the diazeniumdiolates being more polar, as well as decomposition products (NO_2^- and NO_3^-) caused by the water droplet of the contact angle measurement.

Table 1. Static water contact angle measurements of silanised and diazeniumdiolate-tethered PET and SE.

Surface	Contact Angle (°)	
	PET	SE
Pristine	88.1 ± 1.0	113.0 ± 2.3
Plasma treated	19.7 ± 1.8	11.0 ± 1.2
DET3	90.2 ± 0.9	116.6 ± 1.8
DET3/NO	79.0 ± 0.4	108.8 ± 2.0
PTMSPA	88.5 ± 0.3	119.2 ± 1.5
PTMSPA/NO	81.7 ± 1.9	108.6 ± 2.8

3.2. XPS Analysis

3.2.1. PET

The success of each synthetic step for PET as a substrate was followed by XPS, and the resulting quantitative data are given in Tables 2 and 3. Curve fitting of the C 1s envelope of PET samples gave three components: C–C/C–H at 285.0 eV, O–CH₂CH₂ at 286.5 eV and O=C–O at 288.9 eV. PETox C 1s spectra were fitted in the same way. After plasma treatment, an increase in the O 1s peak was observed from 27–34 at %. This is attributed to an increase in oxygen functionalisation as evidenced from the curve fitting of the C1s envelope, which showed a decrease in the aromatic/aliphatic components commensurate with an increase in ether and ester type functional groups as seen in Table 3 (increase of 13.4% for O–CH₂CH₂ and 15.0% for O=C–O). Immobilisation of the aminosilanes onto PETox was confirmed by the appearance of the N 1s and Si 2p peak. Tethering of the diazeniumdiolate on the surface did not change the overall elemental compositions. However, curve fitting the high resolution N1s spectra clearly shows an additional component at 402.5 eV indicative of an N–O bond from the diazeniumdiolate moiety (Table 3, Figure 3a,b).

3.2.2. SE

The success of each synthetic step for SE as a substrate was followed by XPS, and the resulting quantitative data are given in Tables 2 and 4. The C 1s envelope of SE was curve fitted to give one component at binding energy 284.6 eV characteristic of C–H/C–C/C–Si. The high resolution Si 2p peak was curve fitted at 102.1 and 103.0 eV, indicative of R₂–Si(O)₂ and R–Si(O)₃. Upon plasma treatment, the at % of oxygen goes up slightly, from 32.3%–35.1%. Peak fitting of the C 1s envelope shows two components, one at 284.6 and one at 285.7 eV (C–O). The Si 2p spectra now have an extra component at 104.0 eV characteristic of Si(O)₄ groups. SE is known to undergo rapid hydrophobic recovery after plasma treatment [53]. The most widely-accepted mechanism for hydrophobic recovery is the formation of an inorganic silica layer, which is covered by low molecular weight species that have

diffused from the polymer bulk, which is consistent with what is observed here [53]. Similarly to PET, immobilisation of the two aminosilane molecules is observed by the introduction of the N 1s peak. Tethering of the diazeniumdiolate is confirmed by the appearance of a new peak in the N 1s spectrum at 403.1 eV, which is indicative of the N–O bond in the (Table 4, Figure 3c,d).

Table 2. XPS derived at% of C 1s, O 1s, N 1s and Si 2p regions for PET and SE surfaces.

Sample	at %			
	C 1s	O 1s	N 1s	Si 2p
PET	73.0 ± 0.4	27.0 ± 0.4	-	-
PETox	66.0 ± 0.2	34.0 ± 0.2	-	-
PET-DET3	56.0 ± 1.1	22.5 ± 0.2	4.7 ± 0.3	16.8 ± 1.2
PET-DET3/NO	57.2 ± 0.3	26.9 ± 0.1	5.7 ± 0.7	10.2 ± 0.4
PET-PTMSPA	61.7 ± 1.1	25.4 ± 0.2	3.3 ± 0.3	9.6 ± 0.6
PET-PTMSPA/NO	59.6 ± 0.6	25.5 ± 0.6	4.5 ± 0.9	10.4 ± 1.4
SE	38.2 ± 1.5	32.2 ± 1.2	-	29.6 ± 0.3
SEox	35.4 ± 1.5	35.1 ± 1.6	-	29.6 ± 0.5
SE-DET3	41.3 ± 1.2	28.4 ± 1.0	3.7 ± 0.5	26.6 ± 0.7
SE-DET3/NO	33.8 ± 0.9	35.1 ± 0.7	2.4 ± 0.2	29.4 ± 0.7
SE-PTMSPA	40.5 ± 1.5	30.0 ± 1.3	1.8 ± 0.0	27.7 ± 0.3
SE-PTMSPA/NO	37.1 ± 0.4	33.4 ± 0.4	1.6 ± 0.1	28.0 ± 0.0

Table 3. XPS-derived curved-fitted C 1s and N 1s components for PET surfaces.

Sample	at %					
	C 1s			N 1s		
	C–H, C–C	O–CH ₂ CH ₂	O=C–O	N–H	N+	N–O
PET	59.6 ± 0.2	24.0 ± 0.2	16.5 ± 0.2	-	-	-
PETox	41.1 ± 0.6	37.4 ± 0.6	21.5 ± 0.1	-	-	-
PET-DET3	54.8 ± 3.7	40.4 ± 3.4	4.8 ± 0.7	52.0 ± 0.9	48.0 ± 0.9	-
PET-DET3/NO	62.0 ± 2.7	26.4 ± 2.1	11.6 ± 0.6	34.7 ± 0.5	32.7 ± 0.2	32.7 ± 0.3
PET-PTMSPA	69.9 ± 0.3	19.4 ± 0.8	10.7 ± 0.7	68.7 ± 1.2	31.3 ± 1.2	-
PET-PTMSPA/NO	66.2 ± 1.7	25.4 ± 0.9	8.6 ± 0.9	28.1 ± 3.1	35.9 ± 1.5	35.9 ± 1.5

Table 4. XPS-derived curved-fitted C 1s and N 1s components for SE surfaces.

Sample	at %				
	C 1s		N 1s		
	C–H, C–C, C–Si	C–O	N–H	N+	N–O
SE	100.0 ± 0.0	-	-	-	-
SEox	82.2 ± 2.9	17.8 ± 2.9	-	-	-
SE-DET3	62.0 ± 6.2	38.0 ± 6.2	54.8 ± 3.2	45.2 ± 3.2	-
SE-DET3/NO	77.3 ± 5.3	22.7 ± 5.3	39.3 ± 0.2	30.4 ± 0.1	30.4 ± 0.1
SE-PTMSPA	70.9 ± 2.6	29.1 ± 2.6	66.6 ± 0.2	33.4 ± 0.2	-
SE-PTMSPA/NO	79.0 ± 2.5	21.0 ± 2.5	43.8 ± 4.5	28.1 ± 2.2	28.1 ± 2.2

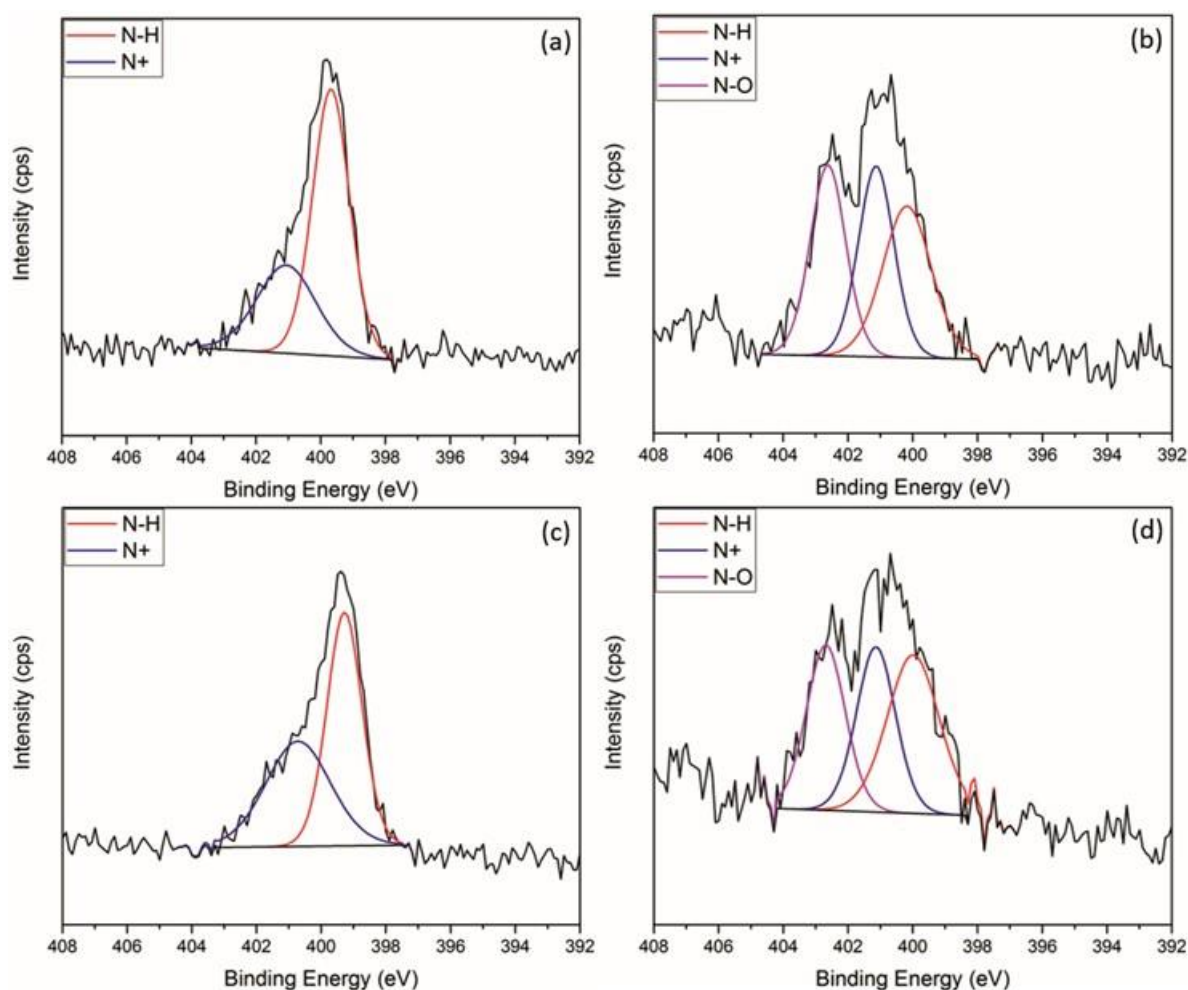


Figure 3. Curve-fitted N 1s XPS spectra for (a) PET-DET3, (b) PET-DET3/NO, (c) SE-DET3 and (d) SE-DET3/NO.

3.3. Atomic Force Microscopy

3.3.1. PET

The surface topography of the PET, PETox, PET-DET3, PET-DET3/NO, PET-PTMSPA and PET-PTMSPA/NO surfaces was examined by AFM, and representative images with associated roughness values are displayed in Figure 4. Pristine PET has a fairly smooth topography ($R_a = 3.2$ nm). After plasma treatment, plasma-induced etching of the surface is observed by an increase in the roughness values. Upon silanisation, a decrease in roughness was seen for PET-DET3 in comparison to PETox. A large variation in roughness values was observed for PET-PTMSPA; which is hypothesised to be due to the ease of aminosilanes forming inhomogeneous layers through solution phase deposition [54]. The roughness of both diazeniumdiolate tethered PET surfaces decreased in comparison to silanised surfaces.

3.3.2. SE

The surface topography of the SE, SEox, SE-DET3, SE-DET3/NO, SE-PTMSPA and SE-PTMSPA/NO surfaces was examined by AFM, and representative images with associated roughness values are displayed in Figure 5. Pristine SE has a fairly rough surface ($R_a = 23.0$ nm). After plasma treatment, large cracks in the polymer can be seen (Figure 5b). This is consistent with the XPS analysis indicating that the SE forms a brittle inorganic silica outer layer, which can form cracks as

previously reported in the literature [53,55–58]. Although silanised and diazeniumdiolate-tethered SE surfaces exhibited no significant difference ($p < 0.05$) in surface roughness, a less uniform array of peaks and troughs can be seen when compared to pristine SE. This is due to agglomerates of silane and resulting diazeniumdiolate found on the surface.

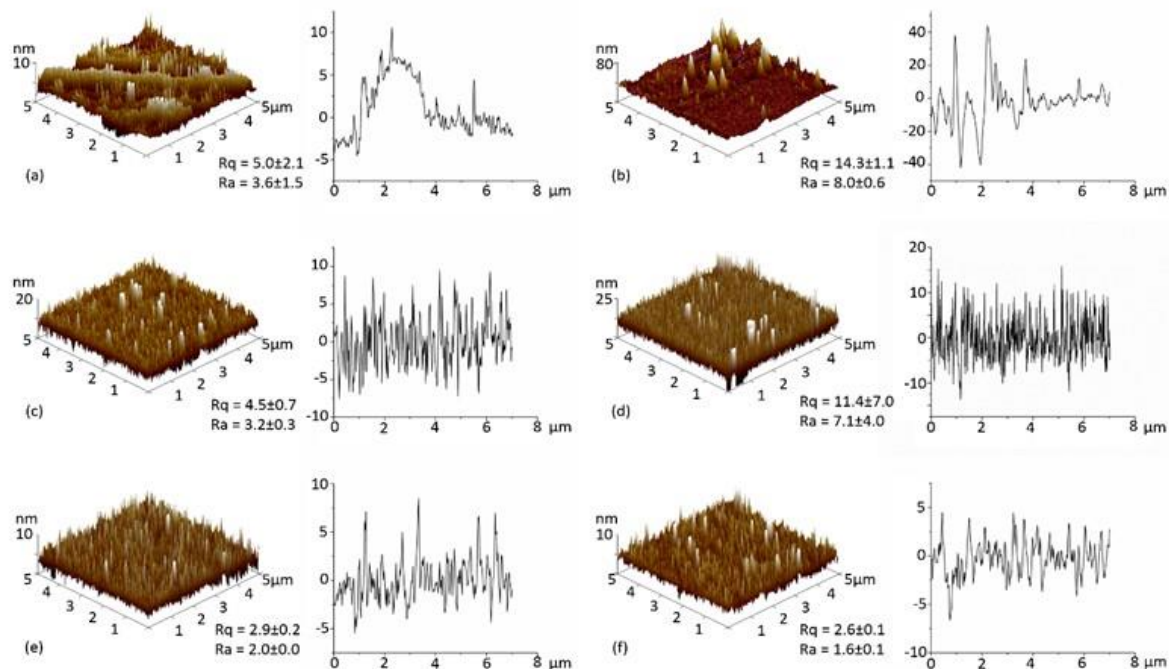


Figure 4. AFM 3D images ($5 \times 5 \mu\text{m}^2$) and depth profiles of (a) PET; (b) PETox; (c) PET-DET3; (d) PET-PTMSPA; (e) PET-DET3/NO and (f) PET-PTMSPA/NO. Rq and Ra values are given in nm.

3.4. NO Release: Electrochemical Detection

3.4.1. PET

Nitric oxide release was monitored for PET-DET3/NO and PET-PTMSPA/NO at ambient temperature (25°C) in real time via electrochemical detection at pH 4 and 7.4, as shown in Figure 6. Not all pristine substrates and silanised control substrates release NO. At pH 4, a difference was observed for the NO payload, which was dependent on the nature of the silane precursor (DET3 vs. PTMSPA). For PET-DET3/NO, an initial burst release was observed with 3250 nM of NO measured in under 2 min. Two smaller bursts of NO release were observed immediately after, each to a maximum of approximately 1000 nM. A steady, continuous rise was then observed for the remainder of the analysis. PET-PTMSPA/NO released less NO over a longer period of time, gradually rising to a peak of 560 nM after 7 min and then flattening out at approximately 250 nM after 16 min. Lower, steadier rates of release were observed over 24 h at pH 7.

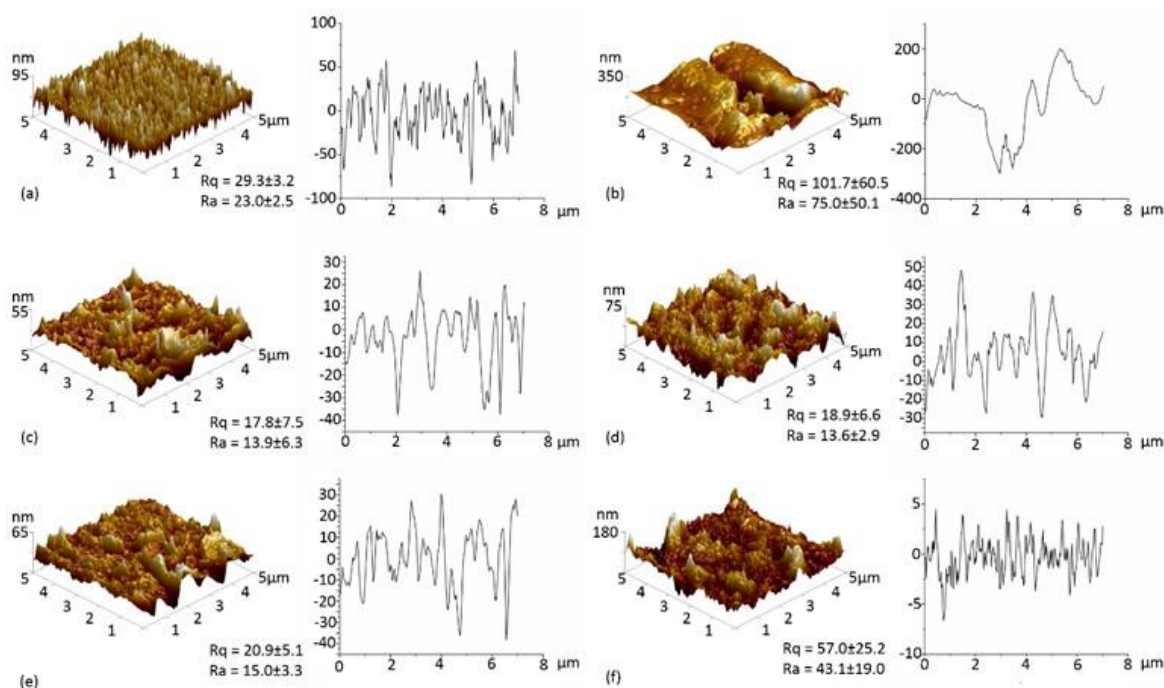


Figure 5. AFM 3D images ($5 \times 5 \mu\text{m}^2$) and depth profiles of (a) SE; (b) SEox; (c) SE-DET3; (d) SE-PTMSPA; (e) SE-DET3/NO and (f) SE-PTMSPA/NO. R_q and R_a values are given in nm.

3.4.2. SE

Nitric oxide release was monitored for SE-DET3/NO and SE-PTMSPA/NO at ambient temperature ($25 \text{ }^\circ\text{C}$) in real time via electrochemical detection at pH 4 and 7.4 as shown in Figure 7. Not all pristine substrates and silanised control substrates release NO. Again for SE-DET3/NO, at pH 4, a continuous initial burst release led to a measurement of 5000 nM of NO just after 4 min. In the same manner as PET-DET3/NO, a steady continuous rise of NO was then observed for the remainder of the measurement. For SE-PTMSPA, NO was released steadily, reaching a peak of 1600 nM after 17 min. Lower, steadier rates of release were observed over 24 h at pH 7.

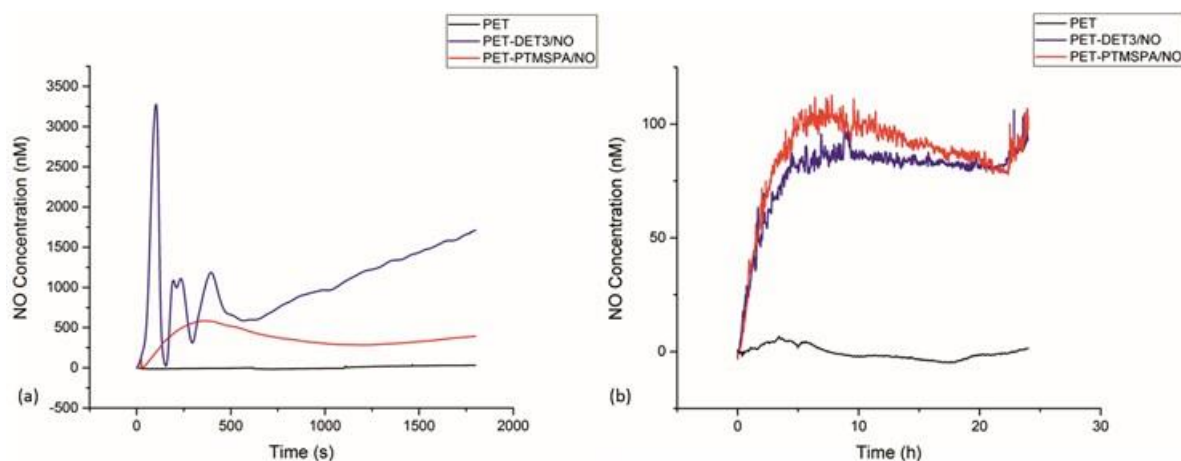


Figure 6. NO release profiles for diazeniumdiolate-tethered PET at (a) pH 4 and (b) pH 7 determined by electrochemical detection.

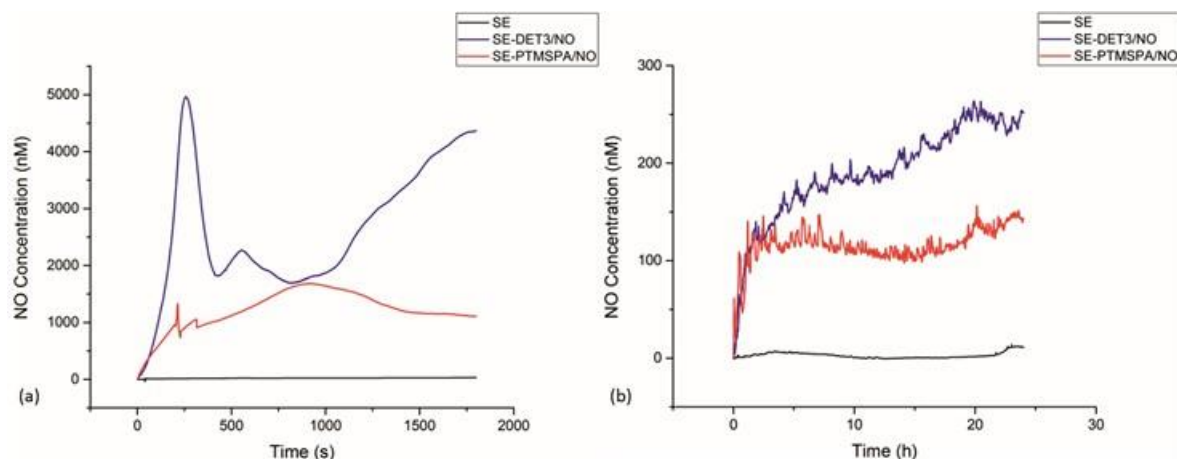


Figure 7. NO release profiles for diazeniumdiolate-tethered SE at (a) pH 4 and (b) pH 7 determined by electrochemical detection.

3.5. Bacterial Response

To investigate the antibacterial activity against *P. aeruginosa*, a colony forming unit (CFU) biofilm assay was carried out. The bacteria were incubated with the surfaces for 24 h in LB broth to allow a biofilm to form. Remaining viable bacteria from the surface were then counted to test the efficacy of the NO-releasing surfaces in biofilm prevention. The results are given in Figures 8 and 9 for PET and SE, respectively. For all diazeniumdiolate-tethered polymers, a statistically-significant ($p < 0.05$) reduction in CFU count, compared to pristine, plasma-treated and corresponding silane-tethered control substrates demonstrates that all NO-releasing polymers are capable of disrupting *P. aeruginosa* biofilms. Specifically, in the case of PET-DET3/NO and PET-PTMSPA/NO, 83% and 62% reduction in viable bacteria was observed. Similarly, for the SE surfaces, 92% reduction was observed for both SE-DET3/NO and SE-PTMSPA/NO.

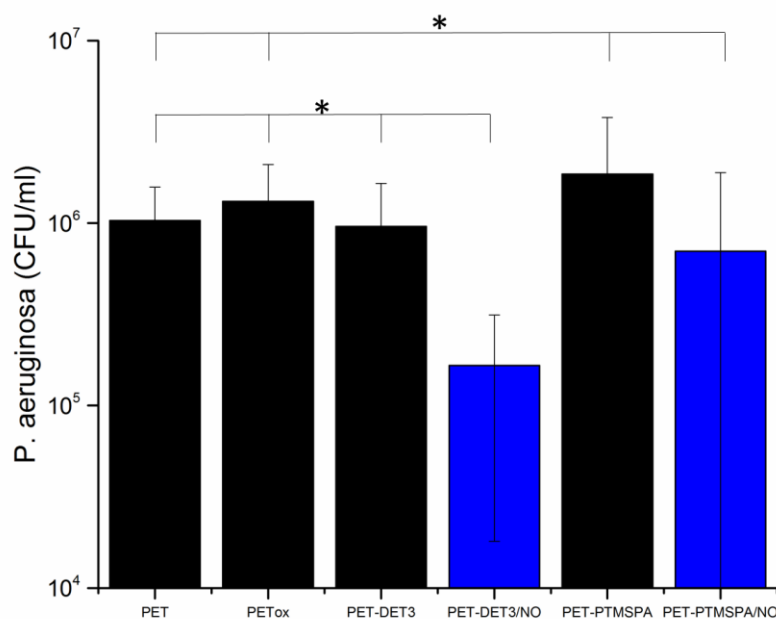


Figure 8. Viable *P. aeruginosa* cell counts (CFU/mL) after 24 h of biofilm growth on PET surfaces. Black bars indicate control surfaces; blue bars indicate NO-releasing surfaces. The symbol * indicates that all NO-releasing surfaces are statistically significantly different from all corresponding control surfaces at $p < 0.05$.

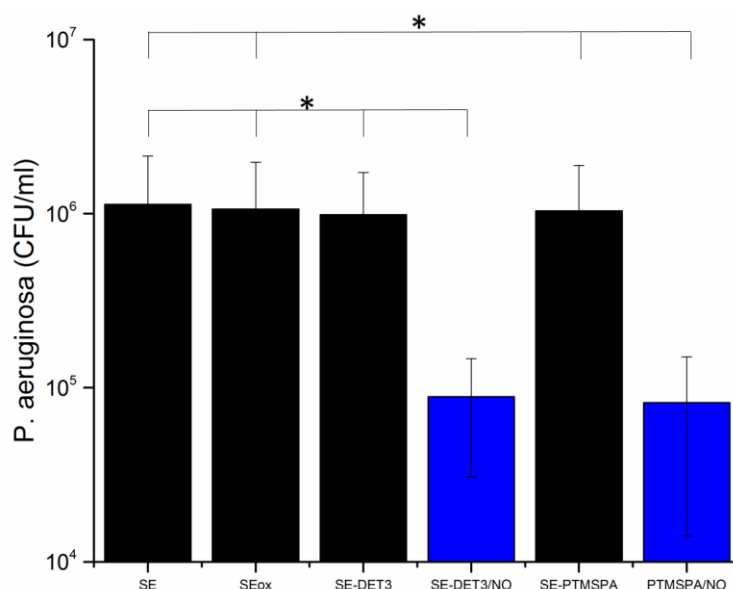


Figure 9. Viable *P. aeruginosa* cell counts (CFU/mL) after 24 h of biofilm growth on SE surfaces. Black bars indicate control surfaces; blue bars indicate NO-releasing surfaces. The symbol * indicates that all NO-releasing surfaces are statistically significantly different from all corresponding control surfaces at $p < 0.05$.

4. Discussion

NO is an endogenously produced molecule that plays an important role in the host antimicrobial response [25]. Once bacterial infection occurs, cytokines signal macrophages to produce NO, which acts as a potent oxidising agent causing oxidative stress via a plethora of reactive nitrogen intermediates. For example, NO reacts with superoxide (also produced by macrophages) to produce peroxynitrite ($^-\text{OONO}$), which can damage the cell membrane due to lipid peroxidation [59]. The reactive nitrogen species formed by NO are also able to damage DNA and denature proteins [60]. The antimicrobial effects of NO in solution-based assays was first observed by Raulli and co-workers who showed low molecular weight diethylenetriamine-derived diazeniumdiolate (DETA/NO) to have a bactericidal efficacy against a range of Gram-positive and Gram-negative species [61]. Schoenfisch and Meyerhoff doped LMW diazeniumdiolates into hydrophobic polymers [62,63]. However, there were concerns of leaching of by-products and their potential toxicity.

To circumvent the issue of leaching and toxic metabolites, several research groups have covalently tethered diazeniumdiolates into NO-releasing coatings. Schoenfisch's group has developed a series of sol-gel and xerogel coatings that are loaded with diazeniumdiolates [40–42,64,65]. These covalently-tethered diazeniumdiolate coatings were found to be effective in decreasing bacterial adhesion of *S. aureus*, *Escherichia coli* and *P. aeruginosa*. The studies showed that the maximal flux of NO released from the coatings occurred shortly after immersion in buffer followed by a gradual release over time. The duration and amount of release was based on the quantity and type of aminosilane used in the xerogel/sol-gel coating. For instance, the 40% *N*-(6-aminohexyl)aminopropyltrimethoxysilane/Isobutyltrimethoxysilane coatings released detectable quantities of NO up to 20 days [42]. While promising, increasing the aminosilane concentration to increase the NO release was limited by the xerogel stability [42].

The experimental approach taken in this study was to determine whether a simple aminosilane coating on polymer surfaces could be tethered with diazeniumdiolates and whether the release could be controlled in terms of the type of aminosilane used. For our surfaces, we found that the type of aminosilane used and indeed the substrate had an effect on the flux and payload of NO released. The DET3 silane has a triamine precursor (diethylenetriamine) with two secondary amines that can

be used to tether diazeniumdiolates. The PTMSPA has only one secondary amine that can be used to tether the diazeniumdiolate. Indeed, the NO release from the PET-DET3/NO and SE-DET3/NO was higher than PET-PTMSPA/NO and SE-PTMSPA/NO at pH 4 as seen in Figures 6 and 7. From Figure 7a, it can also be seen that at pH 4, SE-DET3/NO had an initial burst release of 5000 nM compared with a lower initial release concentration by PET-DET3/NO (Figure 6a). This is attributed to SE being porous, and as a result, it is hypothesised that some of the aminosilane precursor is doped within the subsurface of the polymer. As the diazeniumdiolate reaction occurs under high pressure, NO is able to reach the doped aminosilane precursor and form a diazeniumdiolate. This would account for the significant increase in the concentration of NO on SE vs. PET. The shelf-life or stability of the NO-releasing coating was analysed over a 14-day period after storage in air and at -20°C . The payload of NO release was significantly reduced when the substrates were left in air, indicating limited stability under atmospheric conditions. Substrates left in the freezer showed a slight decrease in payload up to 14 days, indicating that the samples may be stored cold. Additional experiments exploring ways of increasing the stability of these coatings is the focus of another study.

Diazeniumdiolate dissociation to NO is the reverse of its formation as shown in Figure 1 [66]. Therefore, the decomposition is based on the initial protonation of the amine functionality of the diazeniumdiolate, which yields up to 2 mol of NO. As such, the decomposition of the diazeniumdiolate moiety is dependent on the pKa of the secondary amine that is used to form the diazeniumdiolate, and the decomposition reaction is accelerated when the molecule comes into contact with water or another proton source (protonation of the amino nitrogen) [66], an increase in temperature [67] or a shift in the equilibrium towards the aminosilane precursor vs. the diazeniumdiolate (Figure 1) [66]. The pKa of diethylenetriamine (the precursor used to form the DET3/NO) is 10.45, while the pKa of aniline (the precursor of PTMSPA/NO) is 4.6. Based on the approximate pKa values, DET3 is more easily protonated and will decompose faster at pH 4 than PTMSPA. This is evident from the NO releasing profiles of PET-DET3/NO and SE-PTMSPA/NO at pH 4 (Figures 6a and 7a), which show DET3/NO surfaces to have a faster burst release followed by slower release than the PTMSPA/NO surfaces. Furthermore, Nablo et al. have shown that DET3/NO xerogels exhibited an enhanced diazeniumdiolate conversion efficiency due to the improved deprotonation resulting from the additional amines [64]. Nablo et al. have also shown that a hydrophobic substrate such as PVC can hinder the diffusion of water, which affects the decomposition rate, by reducing the initial NO flux and prolonging the release duration of NO [41].

Although studying microbes in planktonic, nutrient-rich batch cultures is useful for antimicrobial screening, *in vivo* infections are typically caused by bacterial biofilms [45,46]. In this study, more persistent cultures of *P. aeruginosa* (PA14) grown for a 24-h incubation period have been utilised. This assay more closely represents biofilm formation than the more commonly-used 30-min assay, which only represents the very early stages of bacterial attachment. All four diazeniumdiolated surfaces, PET-DET3/NO, PET-PTMSPA/NO, SE-DET3/NO and SE-PTMSPA/NO, reduced bacterial colonisation and biofilm formation over 24 h. The reduced bacterial load after growth for the SE surfaces was probably due to the higher initial rate of NO release, which may be crucial for fighting the early stages of bacterial colonisation and biofilm formation. It is envisaged that a prolonged and extended NO release in the slower phase can be effective for avoiding the recovery of bacterial growth, and this is the focus of subsequent studies.

5. Conclusions

This paper reports on the antibacterial nature of nitric oxide, which herein has shown to actively prevent *P. aeruginosa* biofilm formation when administered through different NO-releasing polymers on PET and SE. The NO payload and release were controlled by the aminosilane precursor, as DET3 has two secondary amine sites and PTMSPA only one. All NO-releasing coatings in this study were shown to significantly reduce *P. aeruginosa* adhesion over 24 h with the efficacy being a function of the aminosilane modification and the underlying substrate. These NO-releasing polymers demonstrate

the potential and utility of this facile coating technique for preventing biofilms for indwelling medical devices. Future work will report on broadening the utility of these coatings in order to lengthen and optimise release under physiological conditions.

Acknowledgments: This work has been supported by an EPSRC DTA studentship (EP/MO27325/1).

Author Contributions: George Fleming performed majority of the experiments and contributed to writing of the paper; Jenny Aveyard conceived and designed the experiments and contributed to the interpretation of the results; Joanne L. Fothergill contributed to the microbiology experiments and interpretation; Fiona McBride and Rasmita Raval contributed to the XPS analysis; and Raechelle A. D'Sa contributed to the interpretation and discussion of the results and writing of the paper.

Conflicts of Interest: The authors declare no conflict of interest.

References

1. Wells, R.K.; Badyal, J.P.S.; Drummond, I.W.; Robinson, K.S.; Street, F.J. A comparison of plasma-oxidized and photooxidized polystyrene surfaces. *Polymer* **1993**, *34*, 3611–3613. [[CrossRef](#)]
2. National Audit Office (NAO). *The Management and Control. of Hospital Acquired Infection in Acute nhs Trusts in England*; The Stationery Office: London, UK, 2000.
3. Donlan, R. Biofilms on central venous catheters: Is eradication possible? In *Bacterial Biofilms*; Springer: Berlin, Germany, 2008; pp. 133–161.
4. Public Health England (HPA). *Healthcare-Associated Infection and Antimicrobial Resistance: 2010–2011*; Public Health England: London, UK, 2012.
5. Garrett, T.R.; Bhakoo, M.; Zhang, Z. Bacterial adhesion and biofilms on surfaces. *Prog. Nat. Sci.* **2008**, *18*, 1049–1056. [[CrossRef](#)]
6. Reid, G. Biofilms in infectious disease and on medical devices. *Int. J. Antimicrob. Agents* **1999**, *11*, 223–226. [[CrossRef](#)]
7. Fedtke, I.; Götz, F.; Peschel, A. Bacterial evasion of innate host defenses—The staphylococcus aureus lesson. *Int. J. Med. Microbiol.* **2004**, *294*, 189–194. [[CrossRef](#)] [[PubMed](#)]
8. Sousa, A.M.; Pereira, M.O. Pseudomonas aeruginosa diversification during infection development in cystic fibrosis lungs—A review. *Pathogens* **2014**, *3*, 680–703. [[CrossRef](#)] [[PubMed](#)]
9. Wagner, V.E.; Filiatrault, M.J.; Picardo, K.F.; Iglewski, B.H. Pseudomonas aeruginosa virulence and pathogenesis. In *Pseudomonas: Genomics and Molecular Biology*; Caister Academic Press: Norfolk, UK, 2008.
10. Lister, P.D.; Wolter, D.J.; Hanson, N.D. Antibacterial-resistant pseudomonas aeruginosa: Clinical impact and complex regulation of chromosomally encoded resistance mechanisms. *Clin. Microbiol. Rev.* **2009**, *22*, 582–610. [[CrossRef](#)] [[PubMed](#)]
11. World Health Organization (WHO). *Global Priority List of Antibiotic-Resistant Bacteria to Guide Research, Discovery, and Development of New Antibiotics*; WHO: Geneva, Switzerland, 2017.
12. Donadio, S.; Maffioli, S.; Monciardini, P.; Sosio, M.; Jabes, D. Antibiotic discovery in the twenty-first century: Current trends and future perspectives. *J. Antibiot.* **2010**, *63*, 423. [[CrossRef](#)] [[PubMed](#)]
13. Fazeli, H.; Solgi, H.; Havaei, S.A.; Shokri, D.; Norouzi Barogh, M.; Zamani, F.Z. Carbapenem and fluoroquinolone resistance in multidrug resistant pseudomonas aeruginosa isolates from al-zahra hospital, isfahan, iran. *J. Med. Microbiol. Infect. Dis.* **2014**, *2*, 147–152.
14. Campoccia, D.; Montanaro, L.; Arciola, C.R. The significance of infection related to orthopedic devices and issues of antibiotic resistance. *Biomaterials* **2006**, *27*, 2331–2339. [[CrossRef](#)] [[PubMed](#)]
15. De Nys, R.; Givskov, M.; Kumar, N.; Kjelleberg, S.; Steinberg, P. Furanones. In *Antifouling Compounds*; Springer: Berlin/Heidelberg, Germany, 2006; pp. 55–86.
16. McDougald, D.; Rice, S.A.; Barraud, N.; Steinberg, P.D.; Kjelleberg, S. Should we stay or should we go: Mechanisms and ecological consequences for biofilm dispersal. *Nat. Rev. Microbiol.* **2012**, *10*, 39–50. [[CrossRef](#)] [[PubMed](#)]
17. Moncada, S.; Higgs, A. The l-arginine-nitric oxide pathway. *N. Engl. J. Med.* **1993**, *329*, 2002–2012. [[PubMed](#)]
18. Seabra, A.B.; Martins, D.; Simões, M.M.S.G.; Da Silva, R.; Brocchi, M.; De Oliveira, M.G. Antibacterial nitric oxide-releasing polyester for the coating of blood-contacting artificial materials. *Artif. Organs* **2010**, *34*, E204–E214. [[CrossRef](#)] [[PubMed](#)]

19. Carpenter, A.W.; Schoenfisch, M.H. Nitric oxide release: Part ii. Therapeutic applications. *Chem. Soc. Rev.* **2012**, *41*, 3742–3752. [[CrossRef](#)] [[PubMed](#)]
20. Backlund, C.J.; Worley, B.V.; Schoenfisch, M.H. Anti-biofilm action of nitric oxide-releasing alkyl-modified poly(amidoamine) dendrimers against streptococcus mutans. *Acta Biomater.* **2016**, *29*, 198–205. [[CrossRef](#)] [[PubMed](#)]
21. Schairer, D.O.; Chouake, J.S.; Nosanchuk, J.D.; Friedman, A.J. The potential of nitric oxide releasing therapies as antimicrobial agents. *Virulence* **2012**, *3*, 271–279. [[CrossRef](#)] [[PubMed](#)]
22. Barraud, N.; Kelso, J.M.; Rice, S.A.; Kjelleberg, S. Nitric oxide: A key mediator of biofilm dispersal with applications in infectious diseases. *Curr. Pharm. Des.* **2015**, *21*, 31–42. [[CrossRef](#)] [[PubMed](#)]
23. Barraud, N.; Schleheck, D.; Klebensberger, J.; Webb, J.S.; Hassett, D.J.; Rice, S.A.; Kjelleberg, S. Nitric oxide signaling in pseudomonas aeruginosa biofilms mediates phosphodiesterase activity, decreased cyclic di-gmp levels, and enhanced dispersal. *J. Bacteriol.* **2009**, *191*, 7333–7342. [[CrossRef](#)] [[PubMed](#)]
24. Weller, R.B. Nitric oxide-containing nanoparticles as an antimicrobial agent and enhancer of wound healing. *J. Investig. Dermatol.* **2009**, *129*, 2335–2337. [[CrossRef](#)] [[PubMed](#)]
25. Fang, F.C. Perspectives series: Host/pathogen interactions. Mechanisms of nitric oxide-related antimicrobial activity. *J. Clin. Investig.* **1997**, *99*, 2818–2825. [[CrossRef](#)] [[PubMed](#)]
26. Friedman, A.; Friedman, J. New biomaterials for the sustained release of nitric oxide: Past, present and future. *Expert Opin. Drug Deliv.* **2009**, *6*, 1113–1122. [[CrossRef](#)] [[PubMed](#)]
27. Riccio, D.A.; Schoenfisch, M.H. Nitric oxide release: Part i. Macromolecular scaffolds. *Chem. Soc. Rev.* **2012**, *41*, 3731–3741. [[CrossRef](#)] [[PubMed](#)]
28. Coneski, P.N.; Schoenfisch, M.H. Nitric oxide release: Part iii. Measurement and reporting. *Chem. Soc. Rev.* **2012**, *41*, 3753–3758. [[CrossRef](#)] [[PubMed](#)]
29. Keefer, L.K.; Nims, R.W.; Davies, K.M.; Wink, D.A. “Nonoates”(1-substituted diazen-1-ium-1, 2-diolates) as nitric oxide donors: Convenient nitric oxide dosage forms. *Methods Enzymol.* **1996**, *268*, 281–293. [[PubMed](#)]
30. Fitzhugh, A.L.; Keefer, L.K. Diazeniumdiolates: Pro- and antioxidant applications of the “nonoates”. *Free Radic. Biol. Med.* **2000**, *28*, 1463–1469. [[CrossRef](#)]
31. Wang, P.G.; Xian, M.; Tang, X.; Wu, X.; Wen, Z.; Cai, T.; Janczuk, A.J. Nitric oxide donors: Chemical activities and biological applications. *Chem. Rev.* **2002**, *102*, 1091–1134. [[CrossRef](#)] [[PubMed](#)]
32. Davies, K.M.; Wink, D.A.; Saavedra, J.E.; Keefer, L.K. Chemistry of the diazeniumdiolates. 2. Kinetics and mechanism of dissociation to nitric oxide in aqueous solution. *J. Am. Chem. Soc.* **2001**, *123*, 5473–5481. [[CrossRef](#)] [[PubMed](#)]
33. Drago, R.S.; Paulik, F.E. The reaction of nitrogen(ii) oxide with diethylamine. *J. Am. Chem. Soc.* **1960**, *82*, 96–98. [[CrossRef](#)]
34. Drago, R.S.; Karstetter, B.R. The reaction of nitrogen(ii) oxide with various primary and secondary amines. *J. Am. Chem. Soc.* **1961**, *83*, 1819–1822. [[CrossRef](#)]
35. Hrabie, J.A.; Keefer, L.K. Chemistry of the nitric oxide-releasing diazeniumdiolate (“nitrosohydroxylamine”) functional group and its oxygen-substituted derivatives. *Chem. Rev.* **2002**, *102*, 1135–1154. [[CrossRef](#)] [[PubMed](#)]
36. Abbott, C.A.; Carrington, A.L.; Ashe, H.; Bath, S.; Every, L.C.; Griffiths, J.; Hann, A.W.; Hussein, A.; Jackson, N.; Johnson, K.E.; et al. The north-west diabetes foot care study: Incidence of, and risk factors for, new diabetic foot ulceration in a community-based patient cohort. *Diabet. Med.* **2002**, *19*, 377–384. [[CrossRef](#)] [[PubMed](#)]
37. Keefer, L.K. Progress toward clinical application of the nitric oxide-releasing diazeniumdiolates. *Annu. Rev. Pharmacol. Toxicol.* **2003**, *43*, 585–607. [[CrossRef](#)] [[PubMed](#)]
38. Goudie, M.J.; Brisbois, E.J.; Pant, J.; Thompson, A.; Potkay, J.A.; Handa, H. Characterization of an s-nitroso-n-acetylpenicillamine—Based nitric oxide releasing polymer from a translational perspective. *Int. J. Polym. Mater. Polym. Biomater.* **2016**, *65*, 769–778. [[CrossRef](#)] [[PubMed](#)]
39. Batchelor, M.M.; Reoma, S.L.; Fleser, P.S.; Nuthakki, V.K.; Callahan, R.E.; Shanley, C.J.; Politis, J.K.; Elmore, J.; Merz, S.I.; Meyerhoff, M.E. More lipophilic dialkyldiamine-based diazeniumdiolates: Synthesis, characterization, and application in preparing thromboresistant nitric oxide release polymeric coatings. *J. Med. Chem.* **2003**, *46*, 5153–5161. [[CrossRef](#)] [[PubMed](#)]
40. Nablo, B.J.; Prichard, H.L.; Butler, R.D.; Klitzman, B.; Schoenfisch, M.H. Inhibition of implant-associated infections via nitric oxide release. *Biomaterials* **2005**, *26*, 6984–6990. [[CrossRef](#)] [[PubMed](#)]

41. Nablo, B.J.; Schoenfisch, M.H. Poly(vinyl chloride)-coated sol–gels for studying the effects of nitric oxide release on bacterial adhesion. *Biomacromolecules* **2004**, *5*, 2034–2041. [[CrossRef](#)] [[PubMed](#)]
42. Marxer, S.M.; Rothrock, A.R.; Nablo, B.J.; Robbins, M.E.; Schoenfisch, M.H. Preparation of nitric oxide (no)-releasing sol–gels for biomaterial applications. *Chem. Mater.* **2003**, *15*, 4193–4199. [[CrossRef](#)]
43. Shin, J.H.; Marxer, S.M.; Schoenfisch, M.H. Nitric oxide-releasing sol–gel particle/polyurethane glucose biosensors. *Anal. Chem.* **2004**, *76*, 4543–4549. [[CrossRef](#)] [[PubMed](#)]
44. Stasko, N.A.; Schoenfisch, M.H. Dendrimers as a scaffold for nitric oxide release. *J. Am. Chem. Soc.* **2006**, *128*, 8265–8271. [[CrossRef](#)] [[PubMed](#)]
45. Parsek, M.R.; Singh, P.K. Bacterial biofilms: An emerging link to disease pathogenesis. *Annu. Rev. Microbiol.* **2003**, *57*, 677–701. [[CrossRef](#)] [[PubMed](#)]
46. Hall-Stoodley, L.; Costerton, J.W.; Stoodley, P. Bacterial biofilms: From the natural environment to infectious diseases. *Nat. Rev. Microbiol.* **2004**, *2*, 95–108. [[CrossRef](#)] [[PubMed](#)]
47. O’Toole, G.; Kaplan, H.B.; Kolter, R. Biofilm formation as microbial development. *Annu. Rev. Microbiol.* **2000**, *54*, 49–79. [[CrossRef](#)] [[PubMed](#)]
48. Davies, I.R.; Zhang, X. Nitric oxide selective electrodes. In *Methods in Enzymology*; Elsevier: Amsterdam, The Netherlands, 2008; Volume 436, pp. 63–95.
49. Wadsworth, R.; Stankevicius, E.; Simonsen, U. Physiologically relevant measurements of nitric oxide in cardiovascular research using electrochemical microsensors. *J. Vasc. Res.* **2006**, *43*, 70–85. [[CrossRef](#)] [[PubMed](#)]
50. Simonsen, U.; Wadsworth, R.M.; Buus, N.H.; Mulvany, M.J. In vitro simultaneous measurements of relaxation and nitric oxide concentration in rat superior mesenteric artery. *J. Physiol.* **1999**, *516*, 271–282. [[CrossRef](#)] [[PubMed](#)]
51. Bradley, S.A.; Steinert, J.R. Characterisation and comparison of temporal release profiles of nitric oxide generating donors. *J. Neurosci. Methods* **2015**, *245*, 116–124. [[CrossRef](#)] [[PubMed](#)]
52. Lee, D.G.; Urbach, J.M.; Wu, G.; Liberati, N.T.; Feinbaum, R.L.; Miyata, S.; Diggins, L.T.; He, J.; Saucier, M.; Deziel, E.; et al. Genomic analysis reveals that pseudomonas aeruginosa virulence is combinatorial. *Genome Biol.* **2006**, *7*, R90. [[CrossRef](#)] [[PubMed](#)]
53. Kim, J.; Chaudhury, M.K.; Owen, M.J. Hydrophobic recovery of polydimethylsiloxane elastomer exposed to partial electrical discharge. *J. Colloid Interface Sci.* **2000**, *226*, 231–236. [[CrossRef](#)]
54. Zhu, M.; Lerum, M.Z.; Chen, W. How to prepare reproducible, homogeneous, and hydrolytically stable aminosilane-derived layers on silica. *Langmuir* **2011**, *28*, 416–423. [[CrossRef](#)] [[PubMed](#)]
55. Jokinen, V.; Suvanto, P.; Franssila, S. Oxygen and nitrogen plasma hydrophilization and hydrophobic recovery of polymers. *Biomicrofluidics* **2012**, *6*, 16501–1650110. [[CrossRef](#)] [[PubMed](#)]
56. Morra, M.; Occhiello, E.; Marola, R.; Garbassi, F.; Humphrey, P.; Johnson, D. On the aging of oxygen plasma-treated polydimethylsiloxane surfaces. *J. Colloid Interface Sci.* **1990**, *137*, 11–24. [[CrossRef](#)]
57. Fritz, J.L.; Owen, M.J. Hydrophobic recovery of plasma-treated polydimethylsiloxane. *J. Adhes.* **1995**, *54*, 33–45. [[CrossRef](#)]
58. Owen, M.J.; Smith, P.J. Plasma treatment of polydimethylsiloxane. *J. Adhes. Sci. Technol.* **1994**, *8*, 1063–1075. [[CrossRef](#)]
59. Rubbo, H.; Radi, R.; Trujillo, M.; Telleri, R.; Kalyanaraman, B.; Barnes, S.; Kirk, M.; Freeman, B.A. Nitric oxide regulation of superoxide and peroxynitrite-dependent lipid peroxidation. Formation of novel nitrogen-containing oxidized lipid derivatives. *J. Biol. Chem.* **1994**, *269*, 26066–26075. [[PubMed](#)]
60. Miranda, K.; Espey, M.; Jourd’heuil, D.; Grisham, M.; Fukuto, J.; Freilisch, M.; Wink, D. *Nitric Oxide: Biology and Pathobiology*; Ignarro, L.J., Ed.; Academic Press: New York, NY, USA, 2000; pp. 41–55.
61. Raulli, R.; McElhaney-Feser, G.; Hrabie, J.; Cihlar, R. Antimicrobial properties of nitric oxide using diazeniumdiolates as the nitric oxide donor. *Recent Res. Dev. Microbiol.* **2002**, *6*, 177–183.
62. Schoenfisch, M.H.; Mowery, K.A.; Rader, M.V.; Baliga, N.; Wahr, J.A.; Meyerhoff, M.E. Improving the thromboresistivity of chemical sensors via nitric oxide release: Fabrication and in vivo evaluation of no-releasing oxygen-sensing catheters. *Anal. Chem.* **2000**, *72*, 1119–1126. [[CrossRef](#)] [[PubMed](#)]
63. Mowery, K.A.; Schoenfisch, H.M.; Saavedra, J.E.; Keefer, L.K.; Meyerhoff, M.E. Preparation and characterization of hydrophobic polymeric films that are thromboresistant via nitric oxide release. *Biomaterials* **2000**, *21*, 9–21. [[CrossRef](#)]

64. Nablo, B.J.; Schoenfisch, M.H. In vitro cytotoxicity of nitric oxide-releasing sol-gel derived materials. *Biomaterials* **2005**, *26*, 4405–4415. [[CrossRef](#)] [[PubMed](#)]
65. Hetrick, E.M.; Schoenfisch, M.H. Antibacterial nitric oxide-releasing xerogels: Cell viability and parallel plate flow cell adhesion studies. *Biomaterials* **2007**, *28*, 1948–1956. [[CrossRef](#)] [[PubMed](#)]
66. Maragos, C.M.; Morley, D.; Wink, D.A.; Dunams, T.M.; Saavedra, J.E.; Hoffman, A.; Bove, A.A.; Isaac, L.; Hrabie, J.A.; Keefer, L.K. Complexes of ·NO with nucleophiles as agents for the controlled biological release of nitric oxide. Vasorelaxant effects. *J. Med. Chem.* **1991**, *34*, 3242–3247. [[CrossRef](#)] [[PubMed](#)]
67. Ragsdale, R.O.; Karstetter, B.R.; Drago, R.S. Decomposition of the adducts of diethylamine and isopropylamine with nitrogen(ii) oxide. *Inorg. Chem.* **1965**, *4*, 420–422. [[CrossRef](#)]



© 2017 by the authors. Licensee MDPI, Basel, Switzerland. This article is an open access article distributed under the terms and conditions of the Creative Commons Attribution (CC BY) license (<http://creativecommons.org/licenses/by/4.0/>).